The University of Nottingham
UNITED KINGDOM · CHINA · MALAYSIA

A Multi-Faceted Approach to Dye Remediation with Layered Double Hydroxides, Synthesised by Continuous Hydrothermal Method

Jacob Smith MChem

Thesis submitted to the University of Nottingham for the degree of Doctor of Philosophy

March 2022

EPSRC
Engineering and Physical Sciences
Research Council

Abstract

Pollution of fresh water by synthetic dyes from anthropogenic sources is of increasing global concern, due to the threat they pose to both aquatic and terrestrial ecosystems. Adsorption based treatment technologies offer simple and cost-effective means to remediate industrial dye wastewater effluent. Within this work layered double hydroxides (LDHs), synthesised by continuous flow hydrothermal synthesis (CFHS), were researched to evaluate their capability as adsorbents for synthetic dye remediation.

Within the first part of this research the effect of various reaction parameters (temperature, pressure, and NaOH concentration) on $Co_2Al\text{-}CO_3$ LDH synthesis and application was investigated. This was performed, not only to discern the influence these parameters have on structural, surface, and chemical properties of $Co_2Al\text{-}CO_3$, but also to compare to previous research and determine if a generalised method for all LDHs could be developed. Modifying reaction temperature and initial NaOH concentration resulted in changes to platelet size, surface area and particle size distributions, with higher temperatures resulting in larger platelets and lower surface areas. While pressure in of itself did not influence any crystal or surface properties, lower pressures exacerbated the temperature dependence. An inverse correlation between specific surface area and CDL measurements was attributed to a reduction in exposed surface sites as platelets stack on top of each other. Comparisons with previous LDHs synthesised by CFHS method indicated that optimal reaction parameters were highly dependent on the individual LDH, making a generalised method unapplicable. Application of calcined $Co_2Al\text{-}CO_3$ for adsorption of acid orange 7 (AO7) dye revealed synthesis temperature to influence adsorption capacity, with a maximum uptake of 599 mg g^{-1} reported at a temperature of 50 °C.

Six LDHs, commonly utilised in literature for synthetic dye adsorption, were synthesised to determine the role of M^{2+} and M^{3+} ions on adsorption of AO7 dye. The synthesis of $Ni_2Al\text{-}NO_3$, $Mg_2Fe\text{-}CO_3$ and $Ni_2Fe\text{-}CO_3$ by CFHS was reported for the first time. AO7 adsorption was best modelled by the Langmuir isotherm for all LDHs. Kinetics analysis revealed a greater fit for all LDHs to the pseudo 2nd order model. Intra-particle diffusion modelling indicated dye adsorption to occur by both intercalation into the interlayer and sorption onto the surface. $Ca_2Al\text{-}NO_3$ and $Mg_2Fe\text{-}CO_3$ exhibited the largest maximum uptake capacities of 1586 and 1603 mg g^{-1} respectively. A buffering phenomenon was observed for all LDHs whereby upon suspension in water, the pH was buffered near to the LDHs point of zero charge (pH_{PZC}), regardless of initial pH. Comparison of adsorption characteristics to physical properties of the six LDHs did not indicate correlation to any one specific physical attribute.

Due to their higher adsorption capacities, further analysis was conducted on $Ca_2Al\text{-}NO_3$ and $Mg_2Fe\text{-}CO_3$ to other dyes, to determine the effect dye properties (ionic nature, molecular size and chemical structure) have on adsorption. Maximum adsorption capacities of SY and EB onto $Ca_2Al\text{-}NO_3$ and $Mg_2Fe\text{-}CO_3$ were greatly reduced compared to AO7, attributed to their higher ionic valency and effects related to dye speciation and LDH pH buffering. Molecular size did not influence reaction kinetics, with reaction rates of AO7, SY and EB being of similar magnitude onto both $Ca_2Al\text{-}NO_3$ and $Mg_2Fe\text{-}CO_3$. Dye polarity influenced the adsorption mechanisms, with cationic MB adsorption being best modelled by the Freundlich isotherm, indicating surface adsorption to be the primary mechanism. Adsorption of cationic dyes appeared to be entirely dependent on pH effects, with Saf-O exhibiting negligible uptake onto both LDHs due to its neutral speciation at the pH_{PZC} of both $Ca_2Al\text{-}NO_3$ and $Mg_2Fe\text{-}CO_3$.

Based on experimental conditions from previous research, Mg_2Al-AO7 was successfully produced by CFHS, negating the need for traditional ion-exchange methods for AO7 intercalation post-synthesis. Intercalation of AO7 increased the interplanar spacing from 0.78 nm to 2.22 nm due to its larger molecular size compared to CO_3^{2-} or NO_3^{2-} ions. FTIR analysis revealed shifts in wavenumber of bonds associated with AO7 due to intercalation. Incorporation of AO7 into LDH structure enhanced its thermal stability. Similar dye intercalated syntheses were attempted with other dyes, with successful formation of Mg_2Al-SY and Mg_2Al-EB. While the crystal structure was hard to discern from XRD, ordered structures and fringes of LDH platelets were observed in TEM micrographs. Synthesis of Mg_2Al-AO7 attempted at lower concentrations, analogous to dye concentrations found in environmental dye effluent, were unsuccessful. Doping traditional $Mg_2Al\text{-}NO_3$ synthesis with 100 mg L^{-1} of dye resulted in near complete removal of AO7, SY and EB from solution. Over 90 % of the cationic dye MB was also removed by dye-doped synthesis, indicating the short residence times (~ 4s) within the CFHS reactor were sufficient for removal by surface adsorption. Dye doped $Mg_2Al\text{-}NO_3$ synthesis was just as effective at higher dye concentrations, with over 99 % AO7 removal from solution between 100 – 750 mg L^{-1}. XRD analysis confirmed removal of AO7 occurred by intercalation mechanism at high concentrations (> 500 mg L^{-1}), evidenced by a biphasic diffractogram of $Mg_2Al\text{-}NO_3$ and Mg_2AL-AO7.

Publications

I. Clark, J. Smith, R. L. Gomes and E. Lester, Continuous Synthesis of Zn2Al-CO3 Layered Double Hydroxides for the Adsorption of Reactive Dyes from Water, *J. Environ. Chem. Eng.*, , DOI:10.1016/j.jece.2019.103175

I. Clark, J. Smith, R. L. Gomes and E. Lester, Towards the continuous hydrothermal synthesis of zno@mg2 al-co3 core-shell composite nanomaterials, *Nanomaterials*, 2020, **10**, 1–15.

Conference Contributions

J. Smith, I. Clark, R. L. Gomes and E. Lester. The Synthesis and Application of Layered Double Hydroxides (LDHs) in Water Cleanup. 6th International Solvothermal and Hydrothermal Association Conference. August 8th - 12th, 2018. Sendai, Japan. Oral Presentation.

J. Smith, R.L. Gomes and E. Lester. The Synthesis and Optimisation of Cobalt-Aluminium Based LDHs via a Scalable Continuous Hydrothermal Method. 14th International Conference on Materials Chemistry. 8th – 11th July, 2019. Birmingham, UK. Poster Presentation.

J. Smith, R.L. Gomes and E. Lester. The Impact of Synthesis Parameters on Co_2Al-CO_3 Layered Double Hydroxide Crystallinity and the Subsequent Impact on Adsorption. 7th International Solvothermal and Hydrothermal Association Conference. 26th – 28th October, 2021. Virtual Conference. Oral Presentation.

Acknowledgements

First and foremost, I would like to express extreme gratitude to both Prof Rachel Gomes and Prof Ed Lester for their support and guidance. The completion of this work would not have been possible without their help.

I would also like to thank all my colleagues within the Gomes and Lester research groups for their input and advice over the past years, as well as for putting up with what I can only describe as my “orange chaos”.

Additionally, I would like to thank everyone within the CDT of Sustainable Chemistry for the support, assistance, and opportunities they offered throughout my PhD studies. A special thanks go out to Prof Pete License, Peri Williams, and Mandy Broniewski.

I would also like to express my gratitude to Dr Mike Fay for his assistance and expertise with TEM imaging, Vikki Archibald for ICP-OES analysis, Martin Roe for training of SEM and TEM, Dave Mee for the training of thermal analysis and BET methods, and to Hannah Constantin for her training and assistance of XRD analysis. I am also immensely appreciative to the staff over at Promethean Particles for opening their doors to me during the latter stages of the Covid-19 lockdown.

Finally, I would like to extend my deepest gratitude to all my friends and family for their support. I am immensely grateful towards Nash for her support and presence during the difficult periods of my PhD. Most of all I am indebted to my parents, I would not be where I am today if it was not for their unconditional support.

Table of Contents

List of Figures

List of Tables

Abbreviations

Dye Abbreviations

AO7 – Acid Orange 7

EB – Evan's Blue

MB – Methylene Blue

MO – Methyl Orange

SY – Sunset Yellow

Other Abbreviations

AC – Activated Carbon

AOP – Advanced Oxidation Processes

BET – Brunauer-Emmett-Teller

BOD – Biological Oxygen Demand

CED – Cumulative Energy Demand

CFD – Computational Fluid Dynamics

CFHS – Continuous Flow Hydrothermal Synthesis

CLDH – Calcined Layered Double Hydroxide

COD – Chemical Oxygen Demand

FTIR – Fourier-Transform Infrared

FWHM – Full Width Half Maximum

ICP-OES – Inductively Coupled Plasma Optical Emission Spectroscopy

ICSD – Inorganic Crystal Structure Database

ILDP – In-Line Dispersion Precipitation

LAI – Light Absorption Imaging

LDH – Layered Double Hydroxide

MMO – Mixed Metal Oxide

MOF – Metal Organic Framework

PSD – Particle Size Distribution

Pt-Co – Platinum-Cobalt Scale

PZC – Point of Zero Charge

RSD – Residence Time Distribution

scWHS – Supercritical Water Hydrothermal Synthesis

SEM – Scanning Electron Microscopy

SNAS – Separate Nucleation and Aging Steps

SSA – Specific Surface Area

STY – Space Time Yield

TEM – Transmission Electron Microscopy

TGA – Thermogravimetric Analysis

TOC – Total Organic Carbon

TSS – Total Suspended Solids

XRD – X-Ray Diffraction

1. Introduction

1.1. Thesis Overview

The focus of this study was on the synthesis of layered double hydroxides (LDHs) and the evaluation of their capabilities for remediation of dyes from water. A multi-faceted approach was taken, aimed at improving the understanding of various factors known to impact dye adsorption onto LDHs. A literature review was undertaken in Chapter 2, starting with an in-depth analysis of the anthropogenic nature of dye pollution. Within the review, various treatment technologies for dye remediation were also introduced, followed by an introduction into LDH materials and their utilization as adsorbents. Finally, background on continuous hydrothermal flow synthesis (CFHS), and its potential as an industrially viable method for LDH synthesis was also discussed. Chapter 3 outlines the experimental and analytical methods used. Chapter 4 to Chapter 6 were dedicated to results and discussion. Chapter 4 highlighted the effect of reaction variables such as temperature, pressure, and pH on the synthesis of $Co_2Al\text{-}CO_3$ LDHs. The impact of these variables was evaluated through characterisation of crystal structure, morphology, surface area and composition. Comparisons to previous literature were made to determine if a generalised method could be applied to all LDHs to optimise synthesis by CFHS. Chapter 4 also investigated how these changes to LDH structure affected the ability of $Co_2Al\text{-}CO_3$ to adsorb dye. Chapter 5 was aimed at discerning the effect of M^{2+} and M^{3+} on LDH structure and adsorption of synthetic textile dyes. Experiments were carried out with dyes of varying ionic charge, ionic valency and chemical structure, to determine their role in adsorption processes onto LDHs. Adsorption potential was investigated through analysis of kinetics, adsorption capacity and pH dependence. Chapter 6 explored the continuous synthesis of dye-intercalated LDHs. Experiments were conducted at various dye concentrations, to determine if LDH synthesis was possible at conditions more analogous to those found in environmental dye effluent. Conclusions drawn and recommendations for future research are outlined in Chapter 7 and Chapter 8.

1.2. Research Background

Due to increasing demand for dyes and pigments in various industries, [1,2] alongside globally poor management of fresh water, [3] water pollution from synthetic dyes is of growing concern. Among these dye pollutants, azo dyes are especially of concern due to their use in large quantities in textile, paint and food applications, and representing 70 % of all dyes used in industry. [4] Even at low concentrations, dissolution of dyes in water can be highly visible, disrupting many biological processes that require photochemical activity due to reduced light penetration. [5] In addition, many dyes have inherent toxicity which can cause harm to both aquatic and terrestrial ecosystems. [6–8] This is problematic when considering their recalcitrant and non-biodegradable nature, requiring the use of advanced treatment technologies for degradation and removal such as membrane filtration, advanced oxidation processes, microbial degradation, electrochemical treatment and adsorption. [9–14] Adsorption is often regarded as the most simple, effective and low-cost of these processes. [15] Adsorbents such as activated carbon from various agricultural and industrial solid wastes, [16] natural and modified zeolites, [17,18] and synthetic clays are commonly applied due to their low cost and high sorption capacities. [19,20]

LDHS are a type of anionic synthetic clay with the general formula $[M_{1-x}^{2+}M_x^{3+}(OH)_2]^{x+}(A^{n-})_{x/n}\cdot mH_2O$, where M indicates divalent and trivalent metal cations of molar ratio *x*, and *A* indicates the interlayer anion of valence *n.* The anion exchange characteristics of LDHs has resulted in considerable attention for many applications including catalysis, biomedicine, and adsorption. [20,21] In literature LDHs are most commonly synthesised by co-precipitation methods, [22,23] however their industrial scalability is limited due to its discontinuous nature and poor particle size distributions, as a result of long aging times. [24] Many authors have devised methods to counteract these issues with particle homogeneity, such as through Separate Nucleation and Aging Steps (SNAS) and controlled growth in reverse microemulsions. [25–27] Recently, CFHS, a rapid continuous scalable method more commonly used for metal oxide synthesis, has also been utilised for controlled LDH synthesis. [28,29] To date, only $Ca_xAl\text{-}NO_3$, $Ca_2Al\text{-}EDTA$, $MgAl\text{-}CO_3$ and $ZnAl\text{-}CO_3$ LDHs have been synthesised by this method. [9,28,30,31] Reaction parameters such as temperature, pressure and pH have also been found to influence structural and chemical properties of LDHs synthesised. However, there is still scope to expand the list of LDHs produced by CFHS, and further improve the understanding of how reaction parameters influence synthesis.

In recent years, the use of LDHs as adsorbents for dye remediation have been extensively researched within the literature, due to their high adsorption capacities and regenerative capabilities. [20,32] Adsorption onto LDHs occurs by several mechanisms including interlayer anion exchange, surface adsorption and a process known as the memory effect involving calcination, dehydroxylation and regeneration of the LDH structure. [33,34] While interlayer anion exchange is predominantly performed post-synthesis, a few authors have also reported direct intercalation of dyes during synthesis. [35,36] Many factors have been found to affect adsorption including temperature, [37,38] sorbent dose, [39] pH, [40] M^{2+}/M^{3+} ratio, [41] and interlayer anion choice. [20] A few authors have also highlighted a dependence of adsorption on dye structure and ionic valence, although research within this area is limited. [9,39] It is evident from literature comparisons that the choice of M^{2+} and M^{3+} ions play an important role in the adsorption capacities of LDH, however cross-comparison of separate studies to deduce the magnitude of effects becomes problematic due to inherent differences in experimental method.

1.3. Thesis Aims and Objectives

The aim of this research was twofold. Firstly, to improve the understanding of LDH synthesis by continuous hydrothermal flow (CFHS) synthesis and expand its scope (Objectives 1-3). Secondly, to both evaluate and improve understanding of the capability of LDHs as adsorbents for the remediation of dyes from water matrices (Objectives 4-6).

The specific objectives of this research are:

1. To further expand the list of LDHs that can be synthesised by CFHS.
2. To evaluate the effect various reaction parameters have on Co_2Al-CO_3 LDH synthesis, by identifying their impact on crystal, chemical, and surface properties.
3. To discern if the optimal LDH synthesis conditions for CFHS are independent of LDH components, in the hopes of developing a generalised method for all existing and future LDHs.
4. To evaluate and quantify LDHs capabilities for dye remediation using systematic batch adsorption experiments on various dyes.
5. To improve the understanding of various factors that impact adsorption of dyes onto LDHs: Synthesis parameters, M^{2+} and M^{3+} components, and dye structure.
6. To investigate an alternative method of dye removal by directly synthesising dye-intercalated LDHs via CFHS method and evaluate its potential in water matrices more analogous to environmental dye effluent.

2. Literature Review

2.1. Synthetic Dyes and Wastewater Pollution

2.1.1. The Use of Synthetic Dyes in Industry

While the Earth's water supply is constant, both demographic growth and increased industrial activity has resulted in an increased demand and consumption of fresh water. As a result of this, alongside the globally poor management of the water supply, the quality and availability of fresh water has decreased. [3] A recent report by the United Nations General Assembly (July 2021), stated that "Water should be managed in a way that guarantees the human right to water and sanitation and the sustainability of freshwater ecosystems." [42] One such water pollutant that is of growing global concern is that of organic dyes. Dyes and pigments are used extensively in a variety of different applications including automotive manufacture, coatings, construction, cosmetics, food, glass, paints, paper, plastics, printing and textiles. [1] In 2017 the current global market of dyes was estimated at 9.9 million tons, worth $26.53 billion. [2]

One of the major contributors of dye pollution is that of the textile industry due to the large quantities of aqueous waste and dye effluents generated. For example, while dyeing of 1 kg of cotton only uses 40 g of reactive dye, 150 L of water is required, which naturally generates large volumes of highly coloured effluent waste. [3] The release of these dyes into waste effluents is in part due to the low fixation rates of certain dyes onto fabrics during the dyeing process. While some dye types such as disperse and direct dyes have comparably lower losses of dyes during dyeing (2 – 10 % loss), this can be as high as 50 % for reactive dyes due to the hydrolysed form of the dye having no affinity for the fabric. [5] Without intervention this leads to severe contamination of both surface and ground waters surrounding dyeing facilities. In 2007 an estimated 280 000 of textile dyes were discharged as effluent every year, however over a decade later is likely to be much higher. [43]

2.1.2. Toxicity of Dyes to Humans and the Environment

Water pollution from dye effluents is mostly of concern due to both aesthetic and biotoxicity effects. The presence of very low quantities of dye (less than 1 mg L^{-1}) can still be highly visible, reducing the transparency of the water. This can disrupt many biological processes that require photochemical activity as it can reduce light penetration by absorption and reflection of sunlight. In addition, thin layers of dye can form on the surface of water, decreasing the amount of dissolved oxygen. [5] Alongside this, some dyes have reported toxicity in the form of carcinogens, genotoxins and/or mutagens. [44] For example, a toxicity assessment found increased incidence of bladder cancer in workers exposed to large quantities of azo dyes. [7] Workers handling or producing reactive dyes were also found to have potentially contacted dermatitis, allergic conjunctivitis, rhinitis, occupational asthma or allergic reactions as a result of exposure to the dye. [1] In addition, an estimated 40 % of dyes and pigments contain chlorine, a known carcinogen. [6] This is especially problematic when considering that many dyes have very low biodegradability due to inherently high thermal and photo stability, with some dyes exhibiting half-lives of 2-13 years. [45] Of the dyes that don’t have low biodegradability some can degrade into aromatic species, such as amines which can be carcinogenic in anaerobic conditions. [46] For example basic red 9 (a dye used in the textile, leather, paper and ink industries) breaks down under anaerobic conditions into aromatic amines. Its disposal in water bodies has been linked to allergic dermatitis, skin irritation, mutations and cancer in humans and produced local sarcomas and tumours when tests were performed on rats. [44]

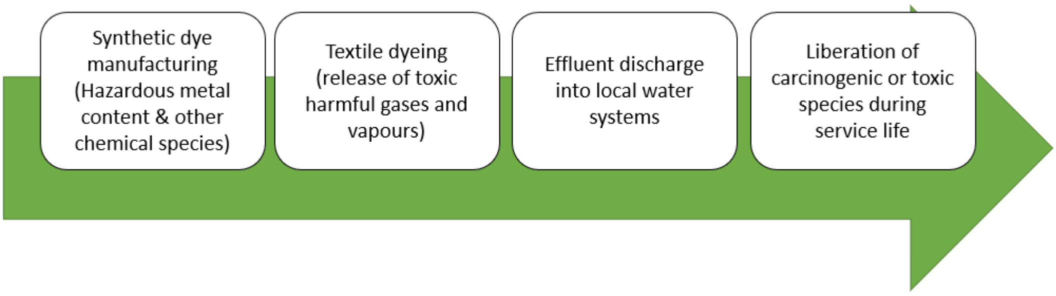

Figure 2.1. Sources of hazardous effects to the environment associated with textile dyeing adapted from Udden et al. [6]

It should be noted that the environmental impact of the release of dye effluent into water systems is not only as a result of the dye itself. For example, the dyeing process within the textile industry requires the use of a variety of other chemical species including salts and metals prior to (due to synthesis manufacturing) and discharge of effluent which have their own inherent environmental hazard associated with them upon their release (Figure 2.1). [6] A typical dye effluent can contain an increased concentration of suspended solids, chlorides, nitrates and various metals alongside high pH, biochemical oxygen demand (BOD) and chemical oxygen demand (COD) values. Many metal complexed dyes (e.g: chromium, copper, nickel or cobalt) are often used in dyeing as a means to modify surface chemistry between the molecule and the fabric. [5] These heavy metals are known to have associated health risks even at contamination levels below 1 mg L^{-1} (Table 2.1). [47] As a result of this various regulations, such as by the World Health Organisation and the European Commission, have been put in place to keep their contamination in environment below harmful levels. [48,49]

Table 2.1. Heavy metals found in dye wastewater and their associated toxicities

Heavy Metal	Toxicities	MCL (mg L^{-1})
Chromium	Headache, diarrhoea, nausea, vomiting and carcinogenic	0.05
Copper	Liver damage, Wilson disease and insomnia	0.25
Nickel	Dermatitis, nausea, chronic asthma, coughing, human carcinogen	0.20

2.1.3. Classification of Dyes

Dyes are most commonly classified in two ways: Chemical structure or industrial application. When classified by chemical structure their class is dictated by the common component within the molecule that is responsible for colour (i.e: Chromophore). [2] A list of common dye classifications with example dyes can be seen in Table 2.2. [50] For example, azo dyes are dictated by the occurrence of one or more Nitrogen-Nitrogen double bond (N=N), while the colour in phthalocyanine based dyes arises from a macrocyclic highly conjugated aromatic pi system. Azo dyes are the class with the largest production volume in dyestuff, representing ~ 70 % of all dyes used in industry. [4] Both the molar extinction coefficient (i.e: colour intensity) and adsorption bands are highly dependent on the chromophore, as are other factors such as photostability. [51]

Table 2.2. Classification of dyes according to chromophore

Class	Chromophore	Example Dyes
Anthraquinone	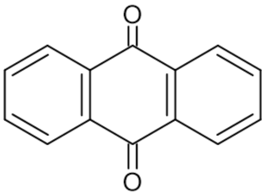	Reactive blue 4 and disperse red 60
Azo	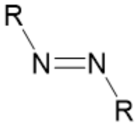	Acid orange 7, acid red 2, disperse yellow 7, direct black 22, evans blue, sunset yellow
Indigoid	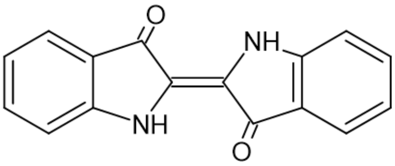	Indigo, indigo carmine, Tyrian purple, vat blue 35
Nitro	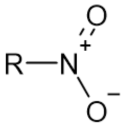	Disperse yellow 14, picric acid and acid yellow 24
Nitroso	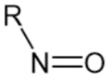	DNSBA-NO
Phthalocyanine	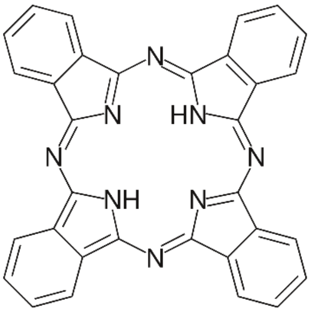	Direct blue 86, pigment green 7 and reactive blue 21
Phthalein	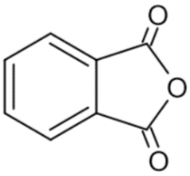	Phenolphtaleine
Triphenyl methyl	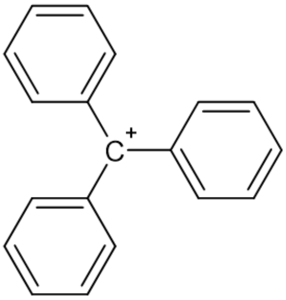	Basic violet 2 and basic violet 4

It should be noted that these classifications are by no means an exhaustive list, with many dyes pertaining unique chromophores that are not suited to any common classification regarding their chemical structure. A classification based on application is therefore often considered as more advantageous due to the complexity of chromophore nomenclature. As a result most literature classifies dyes in this manner. [1] In this instance dyes are often classified based off of their particle charge upon aqueous dissolution, such as cationic (basic dyes, anionic (direct, acid and reactive dyes) and non-ionic (dispersed dyes). [14] A summary of these classes and common substrates they are applied to in the textile industry can be seen in Table 2.3.

Table 2.3. Classification of dyes according to application adapted from Yagub et al. [14]

Class	Substrates	Common Chromophores
Acid	Wool, nylon, silk, inks, leather and paper	Anthraquinone, azo, nitro, nitroso and triphenylmethane
Basic	Inks, paper, polacrylonitrile, treated nylon and polyester	azo and triphenylmethane
Direct	Nylon, rayon, paper, leather and cotton	Azo and phthalocyanine
Disperse	Polyamide, acrylic polyester, acetate and plastics	Azo, anthraquinone and nitro
Reactive	Wool, cotton, silk and nylon	Azo, anthraquinone and phtalocyanine

2.1.4. Legislations and Regulations regarding Synthetic Dyes

In order to protect the quality of fresh water, many standards and legislations have been implemented around the globe to ensure its protection. In developed countries these environmental legislations tend to be very stringent covering a variety of different aspects: [48]

- Microbial aspects
- Disinfection
- Chemical aspects
- Radiological aspects
- Acceptability aspects

Within the textile industry the two most important parameters are that of chemical and acceptability aspects. Chemical aspects involve limiting the use of any chemical constituents that could cause adverse health effects (such as dyes or heavy metals), whether that be over prolonged periods or short-term exposures. Acceptability aspects covers parameters that, while not necessarily of health concern, may be objectionable to the consumer such as tastes, odours or colours. From a review highlighting the guidelines and legislations of dye house effluents it was noted that the most important legislative parameters for the textile industry was therefore BOD, COD, Total Suspended Solids (TSS), salinity (chloride or sulphate), colour and detergent or oil content. [3] A selection of the discharge limits for these parameters into the environment alongside characteristics of real wastewater can be seen in Table 2.4.

It was evident that wastewater from different industrial sites resulted in vastly differing effluent characteristics, as evidenced by parameters such as pH ranging from 4.3 – 11.9 and BOD_5 ranging from 61 – 3050. This was attributed to different levels of treatment and sourcing from different textile dye fabrics at different stages of their respective dyeing process. For many sources, such as the knit textile mills in India and textile effluents from Italy, BOD_5 and COD values appeared to exceed the legislative limits set for their location. It should however be noted that limit parameters are often lower for discharge into the environment than for discharge into municipal wastewater treatment plants due to their ability to conduct further treatment before releasing the effluent into the environment. [3]

Table 2.4. Comparison of real textile effluent characteristics to relevant legislative parameters, adapted from Hessel et al. and Yaseen et al. [3,52]

Country	Source	pH	Colour (Pt-Co)	BOD_5 / mg L^{-1}	COD / mg L^{-1}	TSS / mg L^{-1}	Chlorides / mg L^{-1}	Ref
Austria	Mixed textile polyester wastewater	6.36 – 9.67	1380 - 6033	177 - 720	-	75 - 220	- -	52
				20	150	30	-	3
China	Textile wastewater passed from activated sludge unit	8.0 – 8.3	310 - 325	61 - 75	6 - 10	-	-	53
				30	100	30		3
India	Knit textile mills	4.3-11.9	50 - 2500	195 - 3050	108 - 790	540 - 6510		54
			-	30	250	100	100	3
Italy	Textile Effluents from Dyeing Baths	9 ± 0.5	0.66	1078 ± 58	9.8 ± 1.3	-	38.6 ± 3.1	55
				40	160	80	1200	3
Malaysia	Textile mill wastewater	9 – 10.18	680 - 750	298 - 360	-	0.0076	-	18
				50	200	100	600	3
Mexico	Effluent from denim textile industry (rinsing)	6.84	330	344	91.91	-	338.19	56
				30	-	40	-	3
Spain	Textile mill wastewater from secondary treatment plant	7.6 – 7.8	0.39 – 0.54	200 – 315	-	15 - 46	200 - 365	57
				-	-	-	-	3
Thailand	Raw textile wastewater	-	2105 ± 13	2600 ± 3.78	520 ± 0.47	45 ± 0.73	-	58
				60	400	30	600	3

🟦 Real textile wastewater 🟩 Environmental discharge limits

Alongside differences in chemical aspects there also appeared to be differences in the effluent colours of different sources, ranging from 0.66 – 2500 in the Platinum-Cobalt scale (Pt-Co). The Pt-Co scale is the most common measure of colour used in literature and is used to compare the colour of wastewater to known concentrations of platinum cobalt dissolved in water. [59] While dye will be a contributing factor to the colour observed it is difficult to quantitatively measure the concentration of dye in environmental wastewater samples using this scale as the Pt-Co takes into consideration all dissolved and particulate materials in the water. A case study highlighting concentrations of dye in textile dye wastewater found the majority of dye concentrations cited values between 10 – 250 mg L^{-1}. [52] While two reports highlighted higher concentrations of 600 – 800 mg L^{-1} and 7000 mg L^{-1} these were noted to be anomalously high and most likely referred to direct effluent discharge of a specific textile industry.

In order to meet regulations and reduce the harmful effects of dye wastewater there are several short-term and long-term steps both government bodies and industries can take. One of the most effective method of achieving this has been cited to encompass many aims from a rapidly growing field of science known as green chemistry. [60] The 12 principles of green chemistry were introduced in 1998 by P. Anastas and J. Warner as a means to ensure the development of new chemical products and processes are performed in a manner to reduce hazards across all life-cycle stages. [61] Many of these principles can be directly related to dye industries such as through the improvement of atom economy in the production of dyestuff and reducing the toxicity and volume of waste products. However, while a sustainable model within these industries should be strived for in the future, these solutions do not solve the issues of already polluted eco-systems. As a result, short-term solutions to dye wastewater pollution through remediation via a variety of different process are required in conjunction with this.

2.2. Wastewater Treatment for Dye Removal

Due to the chemical stability of many dyes, traditional treatment technologies tend to be ineffective for dye wastewater. [62] As a result a wide range of technologies have been developed and utilised for the removal of synthetic dyes from wastewater. These consist of a variety of physical methods such as membrane-filtration and sorption techniques, chemical methods including coagulation and flocculation methods, and biological methods such as microbial degradation. [5] Herein some of the most commonly utilised methods are discussed. A summary of the advantages and disadvantages of treatment methods can be found on page 20 (Table 2.5).

2.2.1. Photocatalysis and Advanced Oxidation Processes (AOPs)

While many commercially available dyes tend to resist photodegradation they have been decolorized via the use of photocatalysts. Two commonly used photocatalysts are that of TiO_2 and ZnO semiconductors due to their high photosensitivity, stability and large band gap. [63] Upon exposure to visible/UV light these photocatalysts generate electron/hole pairs through the production of free radicals (Figure 2.2). These free radicals formed can then initiate various chemical reactions in the dye pollutant.

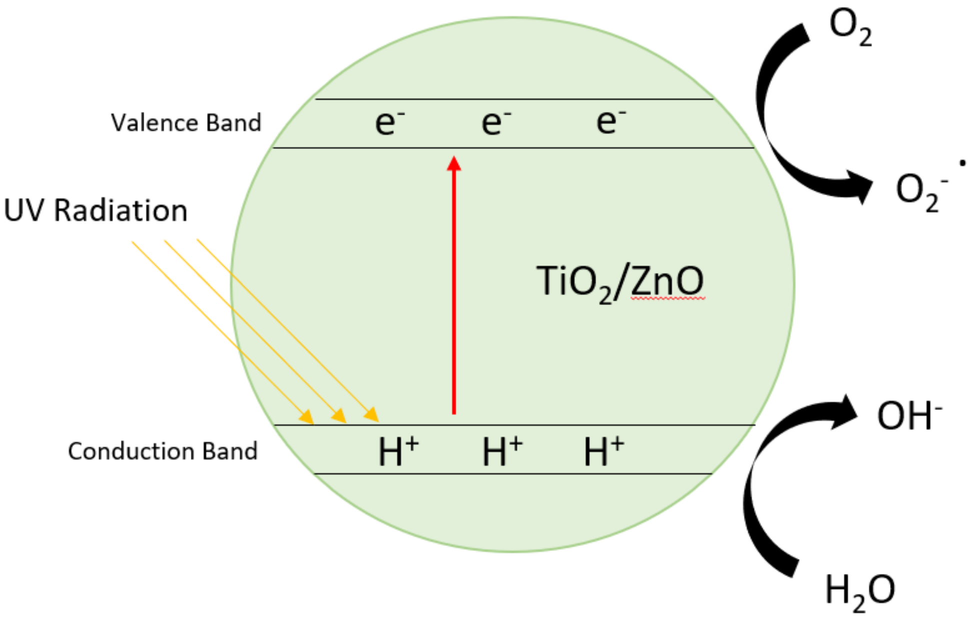

Figure 2.2. Radical formation by irradiation of photocatalysts with UV light

For example, acid orange 7 dye was successfully decomposed when deposited onto TiO_2 particles in the presence of oxygen. Upon excitation of the AO7 dye an electron is donated into the semi-conductor forming a cation radical of the dye. This cation formed then degrades to produce naphthoquinone and benzene sulfonic acid (Figure 2.3). Similar photocatalytic experiments were conducted comparing the oxidation of acid brown 14 by both TiO_2 and ZnO catalysts. [63] Of the two ZnO was found to have the highest photodegradation rate (7.48×10^4 s^{-1} compared to 3.08×10^4 s^{-1}), attributed to ZnO's larger band gap of 3.17 eV allowing for the adsorption of more light. Other studies comparing the UV degradation of various dyes with TiO_2 suggested that the kinetics depends very heavily on the molecular structure of the chromophore; As the number of azo linkages increases the oxidation rate decreases. [64]

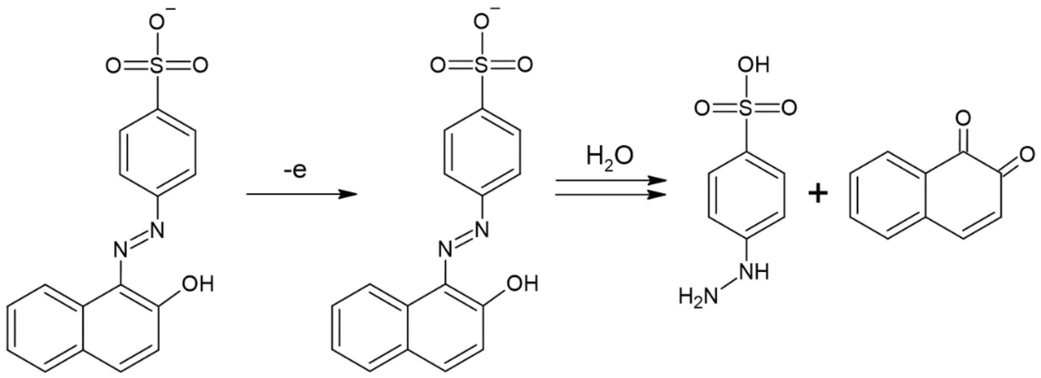

Figure 2.3. Photocatalytic degradation of acid orange 7 to naphthoquinone and benzene sulfonic acid

Other methods of photocatalytic degradation have also been employed, such as through the use of hydrogen peroxide (H_2O_2) via what is known as an Advanced Oxidation Process (AOP). AOPs are commonly used for decolouration of dyes due to the simplicity of the method. H_2O_2 acts as a strong oxidizing agent and in the presence of UV light can generate hydroxyl free radicals (Equation 2.1). This H_2O_2 AOP was utilized for a variety of dyes including for the treatment of Remazol black 5 dye and also a variety of anthraquinone sulfonate dyes when in the presence of TiO_2 . [65] One drawback noted with the use of H_2O_2 to generate free radicals was that optimal conditions for decolorization tended to be different for individual dyes, making development of a generalised oxidation method difficult. [62]

$$H_2O_2 + hv \rightarrow 2OH \cdot \qquad 2.1$$

Ozonation is another effective AOP method of dye treatment again through oxidation of dye chromophores by generated free radicals. Upon exposure of three azo dyes (reactive yellow 84, reactive red 120 and reactive blue 198) to ozone molecules, rapid decolorization of the dyes occurred within 30 minutes (initial concentration of 50 mg L^{-1}). [66] This was also accompanied with a reduction in solution pH due to the formation of acid products. One of the major disadvantages of AOPs is that incomplete degradation of dye molecules can result in production of toxic molecules such as aromatic amines. [5]

2.2.2. Bioremediation of Dyes

Microorganisms such as fungi, yeasts, bacteria and algae or enzymes can be used for biological decolourisation of dyes. As dyes are not typically biodegradable additional carbon and energy sources are required. [67] A common method of bioremediation is through activated sludge processes which can occur via a combination of both aerobic and anaerobic steps. [68] These biphasic processes are especially effective for degradation of azo dyes. The anaerobic step is firstly responsible for discoloration via the breakdown of azo bonds through azo reductase enzymes. This is subsequently followed by an aerobic phase that removes intermediary organic compounds such as aromatic amines, resulting in a non-toxic by-product. [69]

Biological treatment offers many advantages over other physical and chemical methods. Costs are inherently of low expense, both in terms of fixed and process costs, and mineralized end products tend to be of low toxicity. [67] In addition, alongside dyes over 70 % of other organic material responsible for high COD levels can also be decomposed. However, due to the xenobiotic nature of many dyes, many are recalcitrant. A study conducted to determine the partitioning effect of an activated sludge process on 18 acid and direct dyes found only 7 to be removed in any quantity by the waste sludge, with 4 being adsorbed onto the sludge and 3 being biodegraded. [70] In addition, even though mixed culture consortiums offer considerable advantages over the use of single-culture's, controlling the decomposition process can be difficult due to composition changes during the process. [12]

2.2.3. Membrane Filtration

Membrane filtration occurs via a permeable or semi-permeable barrier that prevents target components from permeating while allowing other components to move freely un-hindered through the membrane. Membranes are classified by their pore size and by the differing molecular weights that are retained: reverse osmosis (< 1 nm), nanofiltration (< 2 nm), ultrafiltration (1 – 100 nm) and microfiltration (0.1 – 5 μm). [5] While membrane filtration processes are one of the most effective wastewater treatment processes, operation costs are high as a result of the requirement for high-pressure pumps and specially prepared membranes. [71] In addition to this, costs are often driven higher by irreversible fouling of the membrane due to blocking of pores.

2.2.4. Electrochemical Treatment

Electrochemical treatment can occur by both electrooxidation and electrocoagulation, whereby chemical reactions occur as a result of an electric current sent through electrodes. Generally in electrooxidation, dye pollutants are oxidized either at the surface of the electrode or via oxidizing species generated by the current (direct and indirect). [13] These oxidized species can then be chemically reacted to evolve CO_2 gas through formation of various intermediary species. In order for good reaction efficiency of dye molecules, effective agitation of the electrolyte is required to ensure oxidizing species can move to the electrode surface. Electrocoagulation is a similar method that involves the dissolution of metal hydroxides (Iron/Aluminium) into the electrolyte. The resultant dissolved metal hydroxides that form act as coagulants that can form flocs to create a blanket of sludge that traps colloidal particles in the solution. [72] While these processes tend to be efficient and versatile in nature, applicable to a variety of dye contaminants, they suffer from high costs due to electricity consumption. Depending on the dyeing stage at which they are implemented, high sludge production can also be an issue. [73]

2.2.5. Coagulation and Flocculation

Coagulation and flocculation can also be performed without the use of an electrical current and is one of the most commonly used operations for conventional wastewater treatment. [74]. Coagulation is a complicated process and the coagulant type chosen plays a vital role in its effectiveness for dye remediation. The general approach involves pH adjustment and addition of salts to overcome repulsive forces between particles. The most commonly applied coagulants for dye removal tend to be aluminium, magnesium and ferric salts such as alum, aluminium chloride, magnesium chloride, ferric chloride and ferric sulphate. [75] However, due to human health implications of high aluminium concentrations in water, other more environmentally friendly coagulants such as chitosan (a renewable aminopolysaccharide produced from the deacetylation of chitin) have also been utilised for the removal of sulfonated azo based dyes. [76]

One major drawback of coagulation as a dye removal method is that effectiveness is heavily dependent on dye structure and charge. While dyes with few hydrophilic groups and more polar groups (such as disperse dyes) tend to easily coagulate and can be removed easily, dyes with more charged groups such as NH, NH_2 and SO_3H (such as azo dyes) tend to be more soluble and aren't as effectively removed. [77] In addition the production and disposal of sludge is an issue. Despite this, due to the cost effectiveness of the coagulation/flocculation method, some authors have suggested that it may still have some promise as an effective removal strategy for dyes via hybrid processes involving other treatment methods. For example, when utilized alongside nanofiltration, the generation of sludge was reportedly reduced and required a lower dosage of both coagulant and flocculants. [78] Similarly, a hybrid coagulation/adsorption method using activated carbon was utilised for effective decolourisation of two reactive dyes in wastewater, alongside over 90 % removal of COD and total organic carbon (TOC). [79] By combining these two treatment methods coagulant consumption was halved and a lower volume of sludge was formed.

2.2.6. Adsorbents & Ion-Exchange Materials

Adsorbents are widely regarded to be one of the most effective and economic treatment methods for dye removal due to their simplicity of application, selectivity, and cost effectiveness. Adsorption treatment methods involve the transfer of dye molecules from the liquid phase to the surface of a solid. Depending on the nature of the sorbent, adsorption can occur by either chemisorption or physisorption (Figure 2.4). Physisorption is indicative of weak van der Waals interactions between the adsorbate and adsorbent, whereas chemisorption involves the formation of chemical bonds between adsorbate ions/molecules and the adsorbent surface. [14]

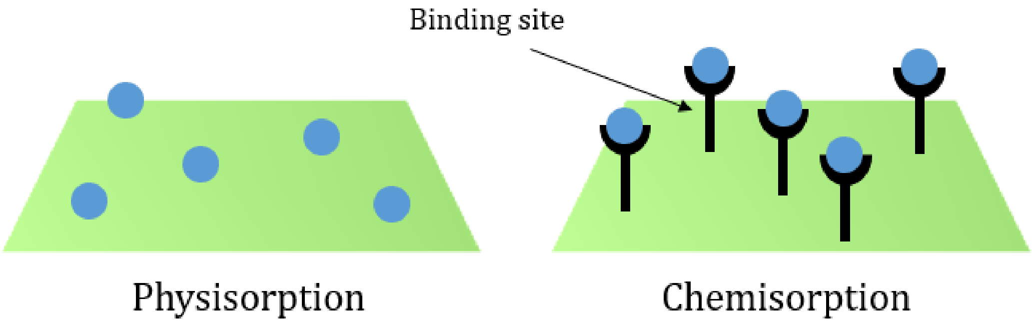

Figure 2.4. Methods of sorption: Physisorption (left) and Chemisorption (right)

A commonly applied sorbent for dye wastewater treatment is that of activated carbon (AC) due to its high porosity of various sizes, chemical and mechanical stability and high adsorption capacities. [16] AC is produced by heating a carbonaceous species to high temperature (~ 900 °C) to form a char, followed by physical or chemical activation. One major benefit of using AC adsorbents is the wide range of carbon sources that can be utilised as precursors. There has especially been growing interest surrounding the utilisation of renewable and cheap precursors for AC preparation. In fact AC generated from various waste products such as fruit kernels, fruit husks, sawdust, nut shells and wood have already been utilised for the remediation of both anionic and cationic dyes, as highlighted in a review by Foo et al. [16] The core challenge that prevents the use of AC sorbents industrially is the difficulties associated with regeneration. Current uses of AC involve its disposal in landfill when saturation is reached, which is neither environmentally acceptable nor economically feasible for large scale usage. [80]

Another treatment method under the umbrella term of adsorbents is that of ion-exchange materials. In ion-exchange processes there is a reversible interchange of ions between a solid resin and electrolytic liquid phase, releasing a stoichiometric amount of similarly charged ions in the process. [81] Unlike traditional sorbents like AC, ion-exchange materials can be fully regenerated following sorption. Zeolites, a class of aluminosilicate minerals, are commonly used for this purpose due to their cationic and zwitterionic nature and have been extensively studied for the removal of dyes due to their inherently high specific surface area (SSA) and high cation exchange capacity. [82] This cationic exchange capability arises from a three-dimensional framework of negative charged ions, balanced by cations. While Zeolites are both low cost and readily available for use due to their natural abundance, their dye removal efficiencies are not as comparable to other clay-based and AC sorbents. [83] In addition, due to their cationic nature, ion-exchange of anionic dyes (such as reactive azo dyes) is negligible without further modification. [84]

Another type of ion-exchange material that has gained attention are clay minerals. Similarly to Zeolites this arises from their natural abundance, low cost, high sorption, and exchangeable ions on their surface. [81] Naturally occurring clay minerals mainly exist in the form of layered hydrous aluminium phyllosilicates structures with variable amounts of other cations such as iron, magnesium and alkali metals. [85] Natural clays adsorption capacities are dependent on their net negative charge, aiding in cationic dyes by adsorption. In addition to this, clays can act as scavengers due to the presence of ions such as H^+, K^+, Na^+, Ca^{2+}, Mg^{2+}, Cl^-, SO_4^{2-}, PO_4^{3-} and NO_3^- on their surface that can be readily exchanged. [86] Furthermore they can be easily modified through calcination, magnetisation and acid/surfactant or polymer activation. [19] These modifications aid in dye removal through changes to surface area and/or addition of functional groups such as amine, carboxyl and alcohols that act as binding sites for cationic species. The work herein involves the development of a type of synthetic clay known as Layered Double Hydroxides (LDHs).

Table 2.5. A summary of wastewater treatment methods: advantages and disadvantages

Method	**Advantages**	**Disadvantages**
Photocatalysis and Advanced Oxidation Processes (AOPs)	Simple No sludge production	Different conditions required for different dyes Incomplete photodegradation can produce toxic intermediary species (aromatic amines)
Bioremediation	Low fixed and operation costs Non-toxic by-products	Many dyes are recalcitrant to biological treatment
Membrane Filtration	Selective and versatile	High production costs Irreversible membrane fouling can prevent regeneration
Electrochemical Treatment	Versatile (effective with a variety of dye contaminants) No consumption of chemicals	High operational costs due to electricity consumption Can produce high volumes of sludge
Coagulation and Flocculation	Cost effective	High sludge production Large concentrations of salts required
Adsorbents	Removal of a variety of dyes Low cost to produce/can be produced from renewable sources (AC)	Cannot be regenerated easily (disposed of in landfill)
Ion-Exchange	Low cost Can be readily regenerated	Selective to specific dyes without further modification

2.3. Synthesis of Layered Double Hydroxides

LDHs are a synthetic layered brucite-like material that have the general formula. $[M_{1-x}^{2+}M_x^{3+}(OH)_2]^{x+}(A^{n-})_{x/n}\cdot mH_2O$ where M indicates divalent and trivalent metal cations of molar ratio *x*, and *A* indicates the interlayer anion of valence *n* (Figure 2.5). The substitution of some ions from divalent to trivalent produces a positive charge excess which is balanced by the introduction of interlayer anions and water molecules. [87] LDHs can be synthesised using a variety of cations including but not restricted to aluminium, calcium, chromium, cobalt, iron, lithium, magnesium, nickel and zinc. [88] Generally cations must be of similar ionic radius to Mg^{2+} for sufficient intercalation into brucite-like layers however. [89] Likewise an array of interlayer species of varying size can be incorporated into the structure. [90] As there is no cross-linking between brucite sheets, the interlayer region can expand or contract to accommodate different anionic species. This unique and versatile structure allows for LDHs to have potential for many applications including catalysis [91], biomedicine, [92] and the removal of oxyanionic and cationic species from water.

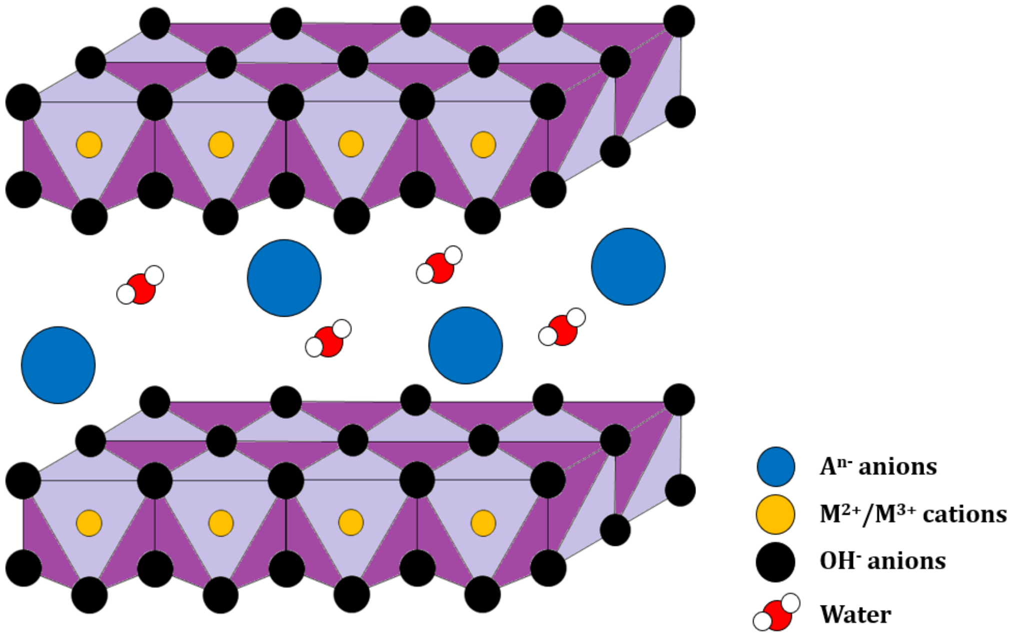

Figure 2.5. Schematic representation of LDH structure

2.3.1. Co-Precipitation Synthesis

The majority of synthetic LDHs found in literature are synthesised by a co-precipitation route, due to its simplicity, low expense and “one pot” method. [88] Co-precipitation involves the simultaneous precipitation of $M(OH)_2$ and $M(OH)_3$ from desired metal salts in the presence of base and an interlayer anion source. [93] Typically hydrated nitrate or chloride salts are used as metal precursors. As previously mentioned, there is a wide range of possible interlayer anions that can be intercalated, ranging from simple inorganic anions to more complex organics. Alkali sources such as sodium carbonate or sodium nitrate are used as precipitation agents to form carbonate (CO_3^{-2}) or (NO_3^-) interlayers. However due to high selectivity of CO_3^{2-} ions, and the presence of CO_2 in air, decarbonated water under nitrogen atmosphere is required to produce the pure nitrate form of LDH. [94]

Co-precipitation is typically done under low super-saturation conditions. [22] A mixed metal salt solution is slowly added to the anion solution under constant pH. The synthesis pH is of vital importance to ensure pure hydrotalcite phase is obtained. While co-precipitation is generally conducted between pH 7 – 10, optimal conditions are dependent on the choice of cations. [95] Co-precipitation can also occur under high super-saturation conditions, via variable pH due to complete base addition, but it is generally reported that a less crystalline LDH is formed as a result due to higher nucleation rates. [96] In comparison constant-pH synthesis tends to produce larger well-formed hexagonal crystals due to lower amounts of nuclei. [97]

2.3.2. The Role of Synthesis Conditions on the formation of LDHs by co-precipitation

Reaction conditions play an important role in physical characteristics of LDH material including surface area, crystallinity and morphology. One of the most studied reaction conditions is that of pH. An incorrect choice of pH for the cations of choice can result in impurities forming in preference to LDH. For example, an investigation into the pH effect of ZnAl-LDH found that pure hydrotalcite formed between pH 8-11, with impurities such as $Zn(OH)_2$, $Na[Al(OH)_4]$ and $Na_2[Zn(OH)_4]$ forming outside this range. [98] A similar study conducted on the synthesis of CaAl-LDH at pH 8.5, 10.5 and 12.5 found pristine LDH to form only at pH 8.5. [92] At higher pH's mixed phases comprising of both LDH and $CaCO_3$ polymorphs were observed, with the $CaCO_3$ phase becoming more predominant at higher pH.

Similar to pH, the ratio of M^{2+}:M^{3+} ions can influence the formation of LDH. It is generally reported in literature that a ratio of 2-4 is optimal for pure hydrotalcite formation, with impurities such as metal oxides forming outside this range. [96] Cation ratio has also been reported to affect the crystallinity of LDH product. A paper highlighting the effect of operating parameters on ZnAl-LDH synthesis found that by varying the Zn^{2+}:Al^{3+} ratio between 1-5 the intensity of the (00*l*) peaks, indicative of LDH stacking, decreased with increasing cationic ratio. [99] TEM analysis also revealed an increasing presence of ZnO nanorods at higher cation ratios. These nanorod impurities were not observed at lower Zn^{2+}:Al^{3+} ratios, which was attributed to the lower amount of zinc in the samples. A similar study investigated how changing the Mg/Al ratio between 1-20 impacts the synthesis of MgAl-CO_3 LDH by co-precipitation. [100] While LDH formation was evident from the presence of typical hydrotalcite phase in XRD at all starting ratios, relative crystallinity appeared lower at ratios of 1 and 2. This was attributed to actual Mg/Al ratios below 2, as measured by ICP-OES, outside the optimal range for hydrotalcite formation. Control of Mg/Al ratio also appeared difficult at higher ratios, with ratios not exceeding 3 despite higher initial Mg^{2+} concentrations. This was hypothesised to be due to low Mg^{2+} precipitation at chosen reaction pH (pH 9.5). Interestingly increasing pH to 10 – 11 resulted in greater incorporation of Mg^{2+} suggesting a co-dependency between the two factors.

Alongside co-precipitation many authors report hydrothermal treatment (aging) post-synthesis as a means of improving crystal characteristics. This hydrothermal treatment was utilised for the synthesis of Mg_3Al-CO_3 LDH by Yun et al. between temperatures of 40 – 100 °C and 2 – 13 h. [101] It was observed that both increasing aging time and aging temperature increased crystal growth in both the *a* and *c* direction, indicative of platelet stacking and growth. Interestingly the crystal growth appeared to be greater in the *a* direction with increasing aging time, which was attributed to phenomena related to periodic bond chain theory. Periodic bond chain theory states that the time required for bond forming is inversely related to bond energy. As crystallite growth in the *a* direction is related to chemical bonding between metal cations and OH^-, the growth rate will be larger than in the *c* direction (weak interactions of hydrogen bonding between platelets). Different aging methods have also been investigated to determine the effects on LDH synthesis. Three aging procedures, namely, room temperature stirring, hydrothermal and microwave-hydrothermal treatment were investigated following co-precipitation synthesis of $Mg_2Al\text{-}CO_3$ LDH. Similar to previously discussed aging studies, longer aging times and higher aging temperatures resulted in increased crystallite sizes. There also appeared to be a converse relationship between crystallinity and reported surface areas which was attributed to partial destruction of crystallite particles at high temperatures. Generally shorter treatment times were required for microwave hydrothermal treatment to produce LDH with high crystallinity.

As briefly discussed earlier the choice of interlayer anion (A^-) is important when considering further application of LDH. This is especially prevalent for applications such as drug delivery and pollutant remediation where selective intercalation and/or release of ionic species from the interlayer is key. For example, one author reported the influence of the interlayer anions NO_3^-, SO_4^{2-} and Cl^- on removal capabilities of MgAl-LDH for chromium (Cr^{6+}) in its oxyanionic form (CrO_4^{2-}). [102] It was observed that uptake of Cr increased with interlayer by the trend $NO_3^- > Cl^- > SO_4^{2-}$. This was attributed to weaker interaction between NO_3^- and brucite sheets than that of Cl^- and SO_4^{2-}. LDH materials have an affinity towards anions with higher charge density, of which common anions can be seen in Figure 2.6. As SO_4^{2-} has two negative charges that bind strongly with the hydroxide layer, ion-exchange with chromate ions is less favourable. Similar observations have been reported for literature surrounding LDHs for dye remediation whereby higher valence anions such as PO_4^{3-} and CO_3^{2-} have a larger impact on dye sorption than compared to monovalent anions such as Cl^- and NO_3^-. [20]

$$PO_4^{3-} > CO_3^{2-} > SO_4^{2-} > NO_3^- > Cl^-$$

Figure 2.6. Affinity of common anions into the interlayer region

This phenomenon is also important for drug delivery applications whereby drugs are encapsulated into LDH structure before controlled release. Upon attempting to intercalate ibuprofen into MgAl-LDH structure one author found that introducing the drug during co-precipitation synthesis resulted in reduced order in the structure, due to disruption of the stacking of cationic layers. [89] However, intercalation of ibuprofen via anion exchange with a prepared MgAl-Cl LDH resulted in an improved crystal structure attributed to the weak binding affinity of the Cl^- compared to ibuprofen. Choice of anionic species can also be utilized for improving the adsorption of cationic species such as heavy metals. [38] While anionic species can adsorb onto LDHs via both ion-exchange and surface binding, cationic species are limited to only surface binding due to electrostatic repulsion with brucite sheets. However, many authors have reported the introduction of chelating agents such as citrate, humic acid and EDTA to enhance adsorption. [103–105] This allowed for the removal of various heavy metals such as Cu^{2+}, Pb^{2+} and Cd^{2+} via a separate surface complexation mechanism. A summary of chelated LDHs for heavy metal removal can be seen in Table 2.6.

One organic anion intercalated LDH structure that was especially of interest was an acid orange 7 (AO7) Mg_2Al-LDH reported by Liu and Evans. [106] While LDH literature surrounding dye remediation applications predominantly removes dyes via a post-synthesis ion-exchange mechanism, AO7 was directly intercalated into LDH structure during synthesis via co-precipitation. This was evidenced by a left shift in XRD reflections, compared to Mg_2Al-CO_3, related to interlayer distance (003, 006 and 009) and a corresponding increase in galley height to 1.79 nm to accommodate the larger dye molecule. As stated by the author the synthesis of dye intercalated LDHs not only has considerable interest for photo-related applications such as molecular devices and optical storage as a result of their photochemical activity, but also a mechanism of wastewater treatment. Similar Zn_xAl-AO7 LDHs have also been reported suggesting AO7 intercalation is not restricted to MgAl based LDHs. [36]

Table 2.6. A summary of chelated LDHs found in literature for heavy metal removal

LDH	Chelating Agent	Heavy Metal Ions	Maximum Adsorption Capacity	Ref
MgAl	Citric Acid	Pb^{2+}	298.5 mg g^{-1}	[105]
ZnAl	Ethylenediaminetetraacetic Acid (EDTA)	Cu^{2+}	0.83 mmol g^{-1}	[103]
MgAl	Humic Acid	Cd^{2+} / Cu^{2+} / Pb^{2+}	0.35 / 0.75 / 0.48 mmol g^{-1}	[104]
MgAl	Sulfonated Lignin	Pb^{2+} / Cu^{2+}	123 / 64 mg g^{-1}	[107]
MgAl	MoS_4	Ag^{+} / Cu^{2+} / Pb^{2+} / Hg^{2+}	450 / 181 / 290 / 500 mg g^{-1}	[108]
		Ag^{+} / Hg^{2+} / Pb^{2+}	564 / 594 / 357 mg g^{1+}	[109]
NiCr	Diphenylamine-4-sulfonate	Cd^{2+} / Cu^{2+} / Pb^{2+} / Zn^{2+}	258 / 282 / 479 / 242 mg g^{-1}	[110]
	Dodecyl sulfonate		142 / 189 / 309 / 164 mg g^{-1}	
	Fumarate		92 / 110 / 176 / 112 mg g^{1}	
	Pentansulfonate		117 / 143 / 232 / 139 mg g^{-1}	
	Terephthalate		113 / 112 / 195 / 118 mg g^{-1}	
	2-ethylhexyl hydrogenphosphate		45 / 44 / 89 / 42 mg g^{-1}	

2.3.3. Control of Crystallite Size and Particle Size Distribution with Alternative Synthesis Methods

Synthesis of LDHs via co-precipitation route involves two main steps: nucleation and subsequent crystal growth through aging. While in Section 2.3.2 it was discussed that generally increased aging time results in larger crystallite sizes, the process of crystal growth is very complex involving many other processes including agglomeration, breakage and Ostwald Ripening. [24] In addition, aging times can be long (2 – 24 h) resulting in vastly differing aging times for separate nuclei depending on when in the addition process they were produced. The result of this is that with traditional co-precipitation methods crystallite sizes are difficult to control and can result in wide particle size distributions. A short nucleation step and controlled growth of LDH particles has been cited as the optimal method to produce monodisperse particles. [111]

As a result of this many authors have developed modifications to traditional syntheses to mitigate these issues. One such method was that of LDH synthesis by Separate Nucleation and Aging Steps (SNAS), developed by Zhao et al. [112] In the SNAS method MgAl-LDH precursors were rapidly mixed and nucleated for 2 minutes in a colloid mill at 3000 rpm. Particles were subsequently aged for 13 h at 100 °C. Compared to LDH synthesised by constant and variable-pH co-precipitation, synthesis via colloid mill resulted in smaller crystallite sizes with higher aspect ratios. More importantly however was the reduced particle size distribution that resulted. While co-precipitated LDH tended to have a bimodal distribution of particles varying between 0.05 – 10 µm, SNAS LDH had more uniform diameters around ~0.1 µm in diameter. These uniform particle sizes were not only attributed to separating out nucleation and aging but also the high-speed fluid shears and high pressures that occur when mixing at high velocity, inhibiting agglomeration of nuclei. The importance of rotor speed was further studied by Yang et al. who showed that increasing rotor speed from 2000 to 8000 rpm for synthesis of $Ca_2Al\text{-}NO_3$ LDH resulted in smaller platelet diameters. [113]

Another synthesis method developed to improve the quality of LDH nanomaterials was through the merging of co-precipitation and reverse microemulsion systems as a means to control crystal growth. [27] Dissolution of surfactants into organic solvents results in the formation of reverse micelles. Upon addition of water or aqueous solutions into these systems, the reverse micelles entrap water droplets at the polar cores. The result of this is that LDH precursors can be dispersed in “microreactors” with both limited space and reactants for crystal growth (Figure 2.7). This mechanism for LDH synthesis was initially published by Hu and O'Hare for the synthesis of Mg_2Al LDH using sodium dodecyl sulfate (NaDDS) as surfactant, resulting in nano-platelets ~ 40-50 nm in diameter. [26] The water:surfactant ratio is vital for controlling the size of water pools in reverse microemulsions/micelles. Further research by Hu et al. showed that adjusting the water content allowed for tuneable particle sizes. [27]

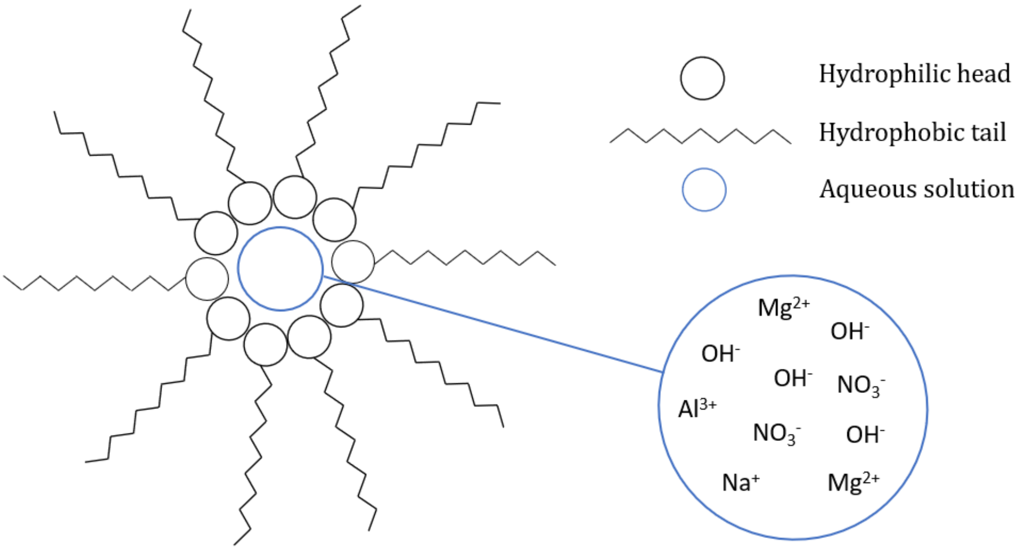

Figure 2.7. Schematic of microemulsion containing MgAl-LDH precursors adapted from Hu et al. [26]

2.3.4. Scaling LDH Synthesis

A further issue of co-precipitation methods of LDH synthesis is that they are operated as batch and/or multi-step processes. Batch processes often possess inconsistant product quality (control of particle size and morphology) due to discontinuous operation and variances in residence time and supersaturation between batches. [28] In addition, the long aging times often required (2 – 24 h) in many synthesis methods results in low product throughput (~mg h^{-1}). Some of these issues were recently highlighted by Bai et al. in a paper highlighting the scalability of SNAS synthesis for the production of monolayer LDH sheets. [25] While the authors highlighted an effective method of producing homogeneous exfoliated MgAl, CoAl and NiCo LDH sheets via rapid nucleation in a colloid mill for 2 minutes, a throughput of only 9 g h^{-1} was achieved. While this is a step-up compared to conventional co-precipitation methods, there was little evidence to suggest LDH particles of similar size uniformity and low thickness (~ 1 nm) could be achieved with use of an industrial colloid mill.

As a result of these batch processing issues, many authors have developed continuous flow methods to produce LDH nanoparticles with controlled size and morphology. [114] Abelló et al. utilized a continuous in-line dispersion precipitation (ILDP) method to produce MgAl, MgFe and NiAl LDHs. [115] Precipitation of LDHs occurred by pumping LDH precursors into a miniaturised reaction chamber with a high-shear homogeniser to ensure rapid mixing. Crystal size and surface area were controlled through adjusting the flow of the feed solutions, altering residence times between 1 – 75 s, and by pH control at the reactor outlet. While LDHs possessed comparable structures to those synthesised by conventional co-precipitation methods, the author noted that ILDP resulted in significant differences in mechanical, optical and density properties. In addition, LDHs synthesised at very low residence times (~ 1 s) resulted in very low surface areas (~0 – 10 m^2 g^{-1}) and low porosity due to particle agglomeration.

Another author developed a continuous steady state co-precipitation method of LDH synthesis through the use of a magnetically stirred vortex reactor. [116] During synthesis, metal cation and alkaline reactants were pumped into a cylindrical tank and stirred magnetically at 300 rpm. Residence time was varied between 5 – 15 minutes before collection of the effluent through an over-flow pipe (Figure 2.8). Compared to traditional “static” co-precipitation methods, smaller $Zn_2Al\text{-}CO_3$ LDH platelets (20 – 60 nm) were produced with larger surface areas of 16 – 62 m^2 g^{-1}. In addition, structural and textural properties could be tailored through altering operating conditions such as reactant concentrations, solvent mixture, residence time, pH and interlayer anion choice. [116] However it should be noted that finer control over particle size and PSD was limited by gradients of supersaturation that existed within the tank. Higher levels of supersaturation were suggested to be generated within the vortex region where nucleation occurred, with particle growth and agglomeration occurring on the periphery of these vortices, increasing particle size and reducing PSD.

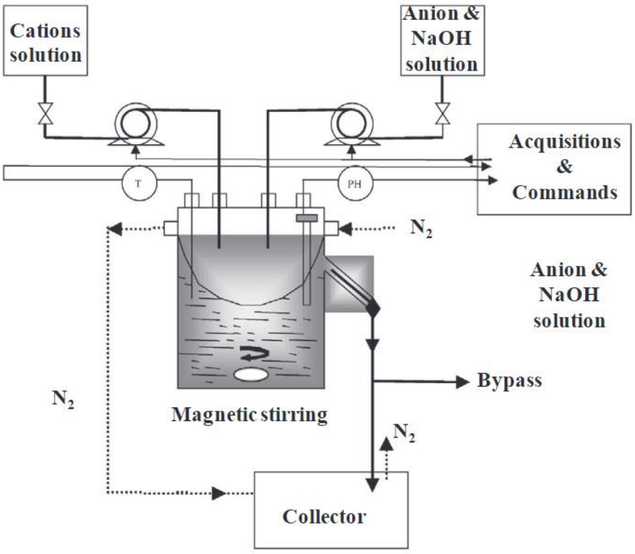

Figure 2.8. Experimental setup for the continuous co-precipitation of LDHs using a vortex reactor, developed by Chang et al. [116]

While continuous synthesis methods offer many benefits over batch methods, scale up of these processes can often result in poorer heat and mass transfer due to larger channels used, resulting in poorer surface-to-volume ratios. [117] As a result of this one author showed further control over particle size and aspect ratio could be achieved through the use of microreactors with channels in the sub-millimeter range (< 1 mm). [118] The greater surface-to-volume ratio observed for < 1 mm channels resulted in more effective dissipation of kinetic energy resulting in a more homogeneous composition and morphology of particles, as well as being less energy demanding. Scale up using narrow channels was easily achieved by simply increasing the number of channel reactors used.

Another issue commonly found with both batch and continuous LDH synthesis is the presence of residual precursor after reaction. The presence of electrolytes can result in the formation of macro-sized agglomerates; therefore, it is common practice to include additional washing steps post-reaction to remove these residual precursors. As a result of this, Flegler et al. developed a semi continuous process coupling synthesis with immediate cleaning to remove residual precursors and quench the reaction. [119] Mg_2Al LDHs were synthesised by a continuous co-precipitation method using a static spiral mixer. Upon precipitation, the product was directly fed into a semi-continuous tubular centrifuge. Upon comparison to conventional lab-scale centrifuges washing, using the semi-continuous washing procedure was found to be just as effective when using four consecutive washes. This was evidenced by the reduction of the hydrodynamic diameter of the agglomerates from 5 µm to 50 nm, paving the way for a one-step continuous process that includes washing.

More recently continuous-flow hydrothermal synthesis (CFHS), using a nozzle reactor design developed at the University of Nottingham, was also utilized for the synthesis of Ca_2Al-NO_3 and Mg_3Al-CO_3 LDHs. [120] While this reactor design was initially developed for the synthesis of metal oxide nanoparticles at supercritical conditions, Wang et al. reported that it possessed advantages of both SNAS and ILDP methods due to the short residence times (~4 s) limiting nucleation and crystal growth, alongside the continuous nature. [120] This CFHS method will be discussed in more detail in Section 2.4. It was also shown that by altering both temperature and pressure within the reactor between 75 – 400 °C and 50 – 240 bar. Temperature appeared to have a more significant impact on crystal growth than pressure, as evidenced by larger particle sizes observed in TEM at higher temperatures. However reductions in platelet growth and irregularity of Mg_3Al-CO_3, alongside the presence of impurities such as AlOOH and $Al(OH)_3$, were observed at temperatures exceeding 200 °C. This was attributed to decomposition and dissociation of LDH at high temperatures and preferential formation of oxides/hydroxide oxides under supercritical conditions. [121]

Clark et al. built on this research by further investigating the impact of reactor temperature (50 – 200 °C), pressure (50 – 200 bar) and initial NaOH concentration (0.1 – 1 M) on physical properties of Ca_2Al-NO_3 LDH synthesised by CFHS method. [87] from crystal domain length (CDL) calculations it was apparent that pressure had a larger influence on crystal growth in the (002) direction at temperatures of 75 and 100 °C, suggesting increased tuneability at lower temperatures. This was attributed to lower residence times and turbulent mixing at these conditions. [87] There did not appear to be any direct correlation with either temperature or pressure with crystal growth of the (030) domain, indicative of individual platelet growth in the *ab* lattice plane. NaOH concentrations around the stoichiometric 2;1 OH:(M^{2+}/M^{3+}) ratio dictated by LDH formula (described on page 21) appeared to provide larger crystallites, with $Ca(OH)_2$ impurities being present at high initial NaOH concentrations of 1 M. While no trends with surface area and reactor conditions were observed, this was most likely due to the very low surface areas (~5-7 $m^2\ g^{-1}$) inherent with Ca_2Al-NO_3 synthesised via this method.

One inherent advantage the CFHS method possesses over other LDH synthesis methods is proof of concept that it can be upscaled to larger reactor systems. While the research above highlighting CFHS use was conducted on a bench microreactor system with estimated space time yields (STY) of 6.3 $Kg^{-1}\ L^{-1}\ h^{-1}$, Clark et al. have reported successful Zn_2Al-CO_3 LDH synthesis in larger pilot and industrial systems, capable of producing upwards of 150 $Kg^{-1}\ L^{-1}\ h^{-1}$ (Table 2.7). [122] Scaling synthesis from bench to industrial did not appear to have any considerable effects on crystal size, with CDL of both (003) and (110) crystal planes for industrial Zn_2Al-CO_3 remaining comparable to bench scaled synthesis. More importantly however was that TEM micrographs revealed no reduction in particle size distribution at the industrial scale, suggesting that product quality can be maintained. All in all, CFHS appears to be one of the most promising methods to synthesis LDHs due to its scalability, continuous nature and controllable crystal characteristics.

Table 2.7. Comparison of flowrates and space-time yield (STY) of synthesis scales, adapted from Clark et al. [122]

Scale	**Flowrate / L h^{-1}**	**STY / kg^{-1} L^{-1} h^{-1}**
Bench	1.8	6.3
Pilot	35	5.2
Industrial	1050	157.3

2.4. Continuous Hydrothermal Synthesis

2.4.1. Supercritical Water Hydrothermal Synthesis (scWHS)

The significance of controlled crystal growth during synthesis is nothing unique to LDH synthesis. In recent years, as the demand for nanomaterials has increased, it has become increasingly evident that their applicability is heavily tied to their physical characteristics such as shape, size, surface chemistry and PSD. [123] For example the optical and electrical properties of quantum dots have a strong dependence on size and shape, with optimal sizes within the range 2 – 10 nm. Larger quantum dots tend to emit shorter wavelengths of light upon fluorescence (orange/red), with longer wavelengths associated to shorter wavelengths (blue/green). [124] As a result of this a variety of synthesis routes have been utilized for the production of controlled nanomaterials such as solvothermal, hydrothermal and sol-gel bottom-up approaches and other top-down approaches such as lithography and sputtering. [125] A review by Santamaria et al. highlighting many of these synthesis processes showed continuous hydrothermal synthesis to have the potential for large-scale synthesis of nanomaterials due to its affordability and green nature. [126]

Adschiri et al. originally developed continuous hydrothermal synthesis for the synthesis of metal oxide nanoparticles under supercritical conditions. [121] Conventional hydrothermal routes for producing metal oxides required the use of various additional chemicals in the form of precipitating agents, ligands for surface modification and surfactants as a means of size control. [127] However under supercritical conditions Adschiri et al. found that when water is heated to its critical point (i.e: 374 °C and 22.1 MPa) the polarity of the fluid changes to that of a fluid with a low dielectric constant and pH. [128] Under these conditions metal salts could be easily hydrolysed due to high concentrations of OH$^-$ and H$^+$ in solution, followed by immediate dehydration of metal hydroxide’s that formed:

$$Hydrolysis: ML_x + xOH^- \rightarrow M(OH)_x + xL^- \qquad 2.2$$

$$Dehydration: M(OH)_x \rightarrow MO_{x/2} + \frac{x}{2}H_2O \qquad 2.3$$

This supercritical water hydrothermal synthesis (scWHS) was, not only simpler than conventional routes that often required many process steps, but also negated the need for additional toxic and expensive chemicals. Since its discovery scWHS has been utilized for the production of a variety of nanomaterials including nitrides, [129] magnetic oxides, [130] and metal nanodispersions. [131] However, scWHS was not without its issues. In scWHS two feeds, an aqueous metal salt solution and pressurized/heated deionized water, were pumped into an apparatus and combined at a mixing point. Upon mixing, the aqueous metal salt solution was rapidly heated with the supercritical water resulting in the production of fine metal oxides, which were quenched, filtered and rapidly transported away from the reactor. [121] However synthesis via this method was often hindered by unreliability and poor reproducibility due to particle agglomeration. This particle agglomeration also resulted in a narrowing and eventual blocking of the inlets, which often resulted in premature shutdown and extensive cleaning of the apparatus. [128]

2.4.2. Reaction Engineering

The poor process reliability and reproducibility issues that were inherent with the initial scWHS apparatus design were investigated by Lester et al using Light Absorption Imaging (LAI). [132] Through dyeing (12 ppm methylene blue) of a pseudo-metal salt solution (40% w/w aqueous sucrose), in the presence of pseudo-scH_2O conditions (methanol), the path taken by the pseudo-metal salt solution could be monitored. This allowed for the observation of zones where strong mixing occurred within the reactor T-piece using a steady state concentration map. In order to conduct these experiments a section of the T-piece reactor was constructed out of transparent acrylic resin. From LAI analysis three non-optimal mixing phenomena were highlighted as the contributing factors of particle build-up:

- Inlet mixing – Large density differentials induced macro-mixing in the sucrose inlet (Figure 2.9).
- Stagnant zones – Product accumulation in areas of low net flow.
- Flow Partitioning – Differences in fluid density resulted in partitioning of the two flows and very poor mixing.

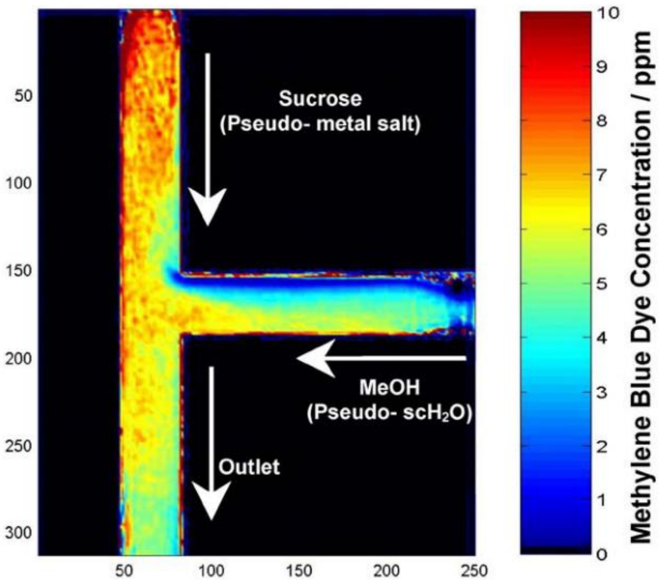

Figure 2.9. LAI steady state concentration map of the T-piece reactor, Flowrates: 270 cm^3 min^{-1} (MeOH) and 611 cm^3 min^{-1} (Sucrose). Used with permission from Blood et al. [132]

Further Computational Fluid Dynamics (CFD) modelling revealed that despite both inlet feeds pertaining to a highly laminar nature, the macro-mixing appeared to be highly turbulent due to the strong buoyancy forces that occurred as a result of the differences in fluid densities. [128] From this LAI/CFD analysis, it was concluded that the current T-piece design used within the scWHS reactor was ineffective at handling the current mixing processes. It was also concluded that a scWHS reactor should satisfy the following criteria for optimal mixing of two flows of significantly different densities to produce metal oxides:

- Instantaneous strong and uniform mixing – To produce small metal oxide nanoparticles
- Short residence times with narrow residence time distributions (RSD) – PSD is completely dependent on RSD, thus reducing RSD will reduce PSD. [133]
- Minimal pre-heating of metal salt stream followed by immediate and rapid heating upon mixing – Prevents premature precipitation and accumulation on reactor walls.
- Strong net downstream eddies – rapidly transports particles out of the reactor, further preventing particle accumulation on reactor walls.

These criteria subsequently led to the invention of a new pipe-in-pipe reactor design, whereby supercritical water is fed downwards through an internal pipe to meet the counter-current aqueous metal salt stream (Figure 2.10). [128] Upon mixing, metal oxide nanoparticles are then rapidly transported upwards through the outer pipe.

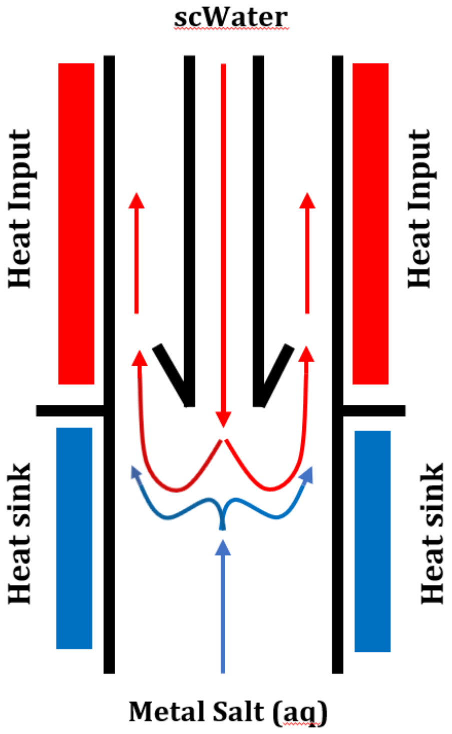

Figure 2.10. Schematic of pipe-in-pipe reactor design, adapted from Lester et al (2006).

Since the conception of the improved pipe-in-pipe nozzle design various papers have been released highlighting its applicability to produce tuneable continuous nanoparticles at supercritical conditions, without the issues of particle agglomeration and blockages apparent with the previous mixing regime. [29,127,134] For example, spherical ZrO_2 nanoparticle doped with Eu^{3+} were produced with fluorescent properties for potential biological applications. [134] While residence time had no impact on particle sizes, changing reaction temperature between 200 – 400 °C allowed for particle size to be controlled between 2 – 22.5 nm. In addition, highly controlled Co_3O_4 cubic spinels have been produced from hydrated acetate salts, without the requirement for additional precipitation agents or surfactants. [127] Once again the reaction temperature played an important role, with high temperatures (~400 °C) resulting in the highest conversion (~ 100 %) and largest particle sizes (~ 60 nm). A wide variety of metal sulphides have been produced including CdS, CuS, PbS and ZnS with superheated thiourea as HS^- source, again highlighting a relationship between nanoparticle size and temperature. [29] Continuous hydrothermal synthesis has also been demonstrated as a scalable one-step method for metal organic framework (MOF) synthesis and activation, such as ZIF-8, UiO-66, HKUST-1 and NOTT-400, which have applicability for gas storage, catalysis and drug delivery due to their ultra-high surface areas. [135–137] It should therefore be evident that continuous hydrothermal synthesis can be utilized for reproducible continuous synthesis of nanosized inorganic materials, with reaction temperature playing an important role in size and shape control. While there is great potential for expanding the scope of materials synthesised via CFHS further, as discussed in Section 2.3, the main interest within this literature review lies in the synthesis and application of layered double hydroxide materials for application for dye remediation. [30,37,138]

2.5. Dye Removal Studies with Layered Double Hydroxides

Due to the high ion-exchange and sorption capacities of LDHs, they have attracted substantial attention in the literature for the remediation of dyes, with numerous papers highlighting their potential for adsorption of a wide variety of both cationic and anionic dyes. In this section, the mechanisms of removal, analysis techniques and subsequent factors that affect dye adsorption have been explored. While many papers have highlighted the potential for photocatalytic degradation of dyes with LDHs, the primary focus of the research within was aimed at the use of LDHs as sorbents. [139–141] As a result the photocatalytic properties of LDHs has not been included within this review.

2.5.1. Sorption Mechanisms

LDH adsorption is a complex process with removal occurring via several mechanisms: interlayer anion exchange, memory effect, surface adsorption, electrostatic attraction and hydrogen bonding. [34] Of these, anion exchange and surface adsorption are the most well documented in the literature for conventional LDHs. [20] Generally surface sorption is dictated by electrostatic interactions between charged surface sites and dye molecules of opposite charge. [142] Ion-exchange capabilities are more complex and can depend on various factors such as the affinity of the interlayer anion (discussed indepth in Section 2.3.2), substitute anion and the M^{2+}/M^{3+} ratio. [143,144] The presence of swelling agents have also been documented to assist in dye intercalation of CO_3^{2-} based LDHs, a notoriously stubborn interlayer anion due to its high charge density. [41]

A common method utilized for determining the dye removal mechanism is through XRD analysis. The interplanar spacing (d_{003}) is dictated by the size of the interlayer molecule. For common interlayer anions such as Cl^-, NO_3^- or CO_3^{2-} this is typically in the region of 0.70 – 0.80 nm. [145,146] Upon ion-exchange, these anions are typically expelled and replaced by the dye molecules of similar charge resulting in an expansion of the interlayer region to accommodate larger dye molecules. As the 2θ position (°) of reflections in XRD is directly related to the distance between repeating planes, if a dye molecule has been intercalated it should be evident by a left shift of peaks associated with this interplanar spacing. [147] For example, CaAl-Cl based LDH was utilized for the adsorption of two dyes, methyl orange (MO) and acidic scarlet GR. [148] Initially the d-spacing between brucite sheets of the CaAl-LDH was 0.78 nm, however following dispersion in solution of MO for 24h, the d-spacing increased to

2.45 nm suggesting the dye had been intercalated. Conversely, upon dispersion in acidic scarlet no changes to basal reflections occurred suggesting surface sorption to be a more appropriate mechanism for its removal. [148] Similarly intercalation of three dyes, evan's blue, chicago sky blue 6b and niagara blue 3B, into Zn_2Al-Cl was confirmed by the left shift of (003) reflections to lower 2θ angles. [149]

2.5.2. Calcination and the Memory Effect

Another mechanism of dye adsorption commonly utilised in literature is through a phenomenon known as the "memory effect". Upon heating of LDH to a critical temperature, generally in the region of 400 – 600 °C, both the interlayer anion and water molecules within the interplanar spacing are expelled. [33] Further dehydroxylation of brucite layers results in the formation of a mixed metal oxide (MMO). Upon dispersion of this MMO structure in a solution of the anion of choice, the original lamellar structure can be regenerated (Figure 2.11). Generally temperatures exceeding 600 °C are not utilized due to the formation of irreversibly formed spinel structures that cannot reform LDH structure. [150]

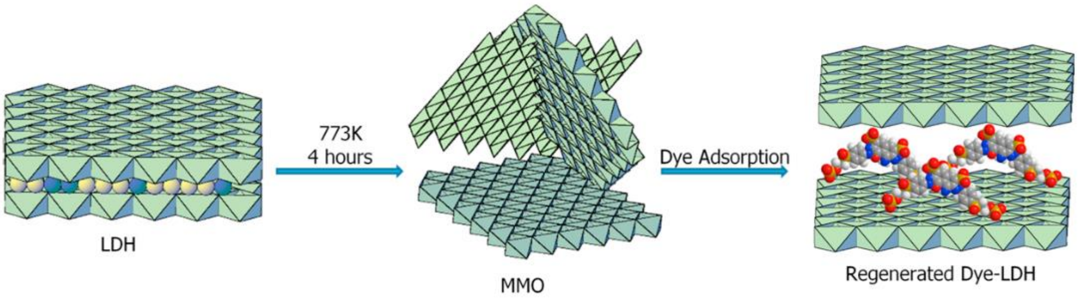

Figure 2.11. Adsorption of dyes by the memory effect, used with permission by Clark et al.[37]

Calcined LDHs (CLDHs) often exhibit higher removal efficiencies compared to the parent LDH. This is attributed to the structural reconstruction, higher surface areas and greater ion-exchange capacities due to loss of charge-compensating anions. [37,151] For example, one author compared calcined and uncalcined MgAl-CO_3 LDH for the adsorption of the azo dye acid green 68. [152] While no surface areas were reported, calcination at 550 °C for 4h resulted in an increase in uptake capacity of over 50 %, from 99.1 to 154.8 mg g^{-1}. Similarly another author utilized uncalcined and calcined ZnAl, MgAl and ZnMgAl LDHs for the adsorption of remazol brilliant blue. [34] Prior to calcination, the surface areas of all LDHs remained between

40 – 50 $m^2 g^{-1}$ which increased to above 100 $m^2 g^{-1}$ upon heating in a furnace at 500 °C for 4 h. Considerably higher uptake of remazol brilliant blue was observed for CLDHs, with the greatest adsorption capacity reported for ZnMgAl-CLDH at 263 mg g^{-1}. This was attributed to its large specific surface area (156 m^2 g^{-1}), hierarchical pore structure and enhanced electrostatic interactions due to greater positive charge. Many other authors have reported similar findings, of which have been summarised in Table 2.8.

One inherent bias that is rarely discussed in the literature regarding the higher removal efficiencies of CLDHs is the inherent mass loss that occurs upon dehydroxylation and expulsion of the LDHs interlayer. A standard LDH mass loss profile in TGA generally has an initial loss of around 1 – 2 % below 100 °C due to water loss, with a further 30 – 45 % mass loss occurring as the LDH structure is broken down to form spinels. [153] This becomes problematic when considering that adsorption capacities of LDHs and CLDHs are generally compared by mass of dye (mg) removed per gram of sorbent (g^{-1}). The result of this is that literature often overstates the potential of CLDHs for dye remediation. For example, one author highlighted the use of MgAl-LDH for the removal of congo red (CR) both in its calcined and uncalcined form. [154] It was reported that the CLDH had an improved adsorption capacity for CR of 143.27 mg g^1 compared to 129.9 mg g^{-1}. However, TGA analysis conveyed over 40 % weight loss occurring at the calcination temperature of 700 °C. Taking into consideration this mass loss in the conversion of LDH to MMO, it can be calculated that the effective adsorption capacity is closer to ~86 mg g^{-1}, considerably lower than that of the pristine LDH.

Table 2.8. A comparison of surface areas and adsorption capacities of calcined and uncalcined LDHs for dye removal

LDH	Calcination Conditions		Form	Dye(s)	Specific Surface Area (SSA) / $m^2\ g^{-1}$	Adsorption Capacity / $mg\ g^{-1}$	Ref
	Temperature / °C	Time / h					
MgFe	-	-	Uncalcined	Acid brown 14	35.4	370.0	155
	500	3	Calcined		131	41.7	
MgAl	-	-	Uncalcined	Acid green 68	-	99.1	152
	550	4	Calcined		-	154.8	
MgAl	-	-	Uncalcined	Congo red	24.74	129.9	154
	700	3.5	Calcined		165.07	143.27	
NiMgAl	-	-	Uncalcined	Congo red	101	286	156
	600	2	Calcined		179	1250	
MgNiAl	-	-	Uncalcined	Methyl orange	137.4	118.5	157
	500	4	Calcined		246.5	375.4	
MgAl	-	-	Uncalcined	RBB	41.34	220	34
	500	4	Calcined		117.6	247	
ZnAl	-	-	Uncalcined	RBB	44.24	191	34
	500	4	Calcined		109.5	236	
ZnMgAl	-	-	Uncalcined	RBB	50.17	164	34
	500	4	Calcined		156.2	263	

2.5.3. Adsorption Isotherms & Kinetics

Equilibrium studies in the form of isotherm & kinetic experiments are considered to be standard procedures for evaluating sorbents. [158] Equilibrium defines the point at which a dynamic balance has been reached between adsorbate concentration in bulk solution and on the adsorbent surface. By varying initial adsorbate concentration at constant pH and temperature, information regarding how the adsorbate and adsorbent interact can be elucidated. [159] Alongside this, at high adsorbate concentrations maximum adsorption capacities can be calculated, which acts as a powerful tool to compare sorbents. Observing the time-dependence of sorption helps describe the rate of sorption. Previous literature reviews on the use of LDHs/CLDHs for dye removal have highlighted that both the Langmuir and Freundlich models are most commonly utilized to study sorption isotherms. [20] Similarly pseudo-first and pseudo-second order models tend to fit kinetic data well. However, it should be noted that due to the complex nature of the dye sorption mechanism many authors have found that a single kinetic model cannot always fully describe the sorption process. [37,160] As the mechanism can involve a combination of external mass transfer from the bulk to the sorbent surface and intraparticle diffusion to internal sites, the intraparticle diffusion model has also been cited to be best suited to describing sorption onto LDHs and CLDHs. These isotherm and kinetic models have been discussed in more depth in the Materials and Methods (Chapter 3). A summary of dye removal studies by LDHs discussed within this literature review, and relevant adsorption properties, can be found in Section 2.5.5.

2.5.4. Factors affecting Dye Adsorption onto LDHs

2.5.4.1. Sorbent Dosage

There are several factors affecting dye removal by LDHs. The optimal adsorbent dosage (i.e: the sorbent to volume ratio at a fixed adsorbate concentration) is crucial for ensuring the removal effectiveness of the sorbent is as high as possible. By increasing the adsorbent dose, the amount of active sites available for the dye to be adsorbed on increases. [39] Increasing adsorbent dose of a MgAl-Cl LDH between 400 – 1200 mg L^{-1} resulted in an increase in the dye removal efficiency (%) of reactive brilliant red. [161] This was especially prevalent at higher dye concentrations of 400 mg L^{1}, whereby dye removal increased from ~45 % to over 90 % from a dose of 400 to 1200 mg L^{-1}. Similarly, the maximum removal capacities of MgAl and

MgFe LDHs for reactive red 120 was reached at an adsorbent dose of 3.5 g L^1, with removals of 93 and 96 % respectively. [162] Despite this, it appeared that substantially lower adsorbent doses of LDH (0.5 g L^{-1}) could still yield up to 78.8 % removal of dye at saturation.

2.5.4.2. Temperature

Temperature plays an important role in dye uptake due to changes in mobility, solubility of the dye, and equilibrium adsorption capacity (q_e). [37,38] Generally at higher temperatures equilibrium dye uptake is reached quicker, as was observed by one author for the uptake of yellow GX dye onto MgFe-LDH. [163] Upon increasing temperature from 25 to 55 °C the reaction rate, as calculated from the pseudo-second order kinetic model, increased from 9×10^{-4} to 2.5×10^{-3} g mg^{-1} min^{-1}. In real terms, this equated to equilibrium being reached after approximately 120 minutes at 55 °C, compared to almost 200 minutes at room temperature. Most reactions involving dye uptake onto LDHs tend to be endothermic, suggesting favourable adsorption at higher temperatures. [20] This was evidenced by one author whereby q_e of benzopurpurine 4B onto MgAl-CO_3 LDH increased from 120 to 160 mg g^{-1} increasing temperature from 10 to 50 °C. [164] This was further confirmed by thermodynamic analysis that described a spontaneous and endothermic process, as indicated by a negative Gibbs free energy ($\Delta G°$) and positive system enthalpy ($\Delta H°$). It should be noted however that, while the thermodynamic nature of a sorption system is paramount for improving an understanding mechanistically, mimicking temperature conditions of environmental dye effluent would be more beneficial for industrial application.

2.5.4.3. pH

pH is of great importance for the sorption of dyes onto LDHs as it impacts many phenomena including the sorbent surface charge, degree of ionization, dissociation of functional groups on actives sites and the solubility of the dye. [165] The magnitude of the effect of pH is dependent on the point of zero charge, pH_{PZC}. The pH_{PZC} is the pH at which the net particle charge is zero. When the pH exceeds pH_{PZC} the surface of the sorbent becomes negatively charged, due to the high concentration of OH^- in solution:

$$Sur - OH + OH^- \rightarrow Sur - O^- + H_2O \qquad 2.4$$

If the pH < pH_{PZC} the surface of the sorbent becomes positively charged, due to the high concentration of H^+ in solution.

$$Sur - OH + H_3O^+ \rightarrow Sur - OH_2^+ + H_2O \qquad 2.5$$

It should therefore be evident that when the pH < pH_{PZC}, anionic dye sorption can occur by both electrostatic forces with the positively charged surface, and via ion-exchange within the interlayer. When the pH > pH_{PZC}, not only is surface sorption no longer favourable due to electrostatic attraction, but the anionic dye is also in competition with OH^- for ion-exchange within the interlayer anion. One author found that a low pH (pH 4) was optimal for the uptake of sunset yellow FCF (SY) dye onto CaAl-NO_3 LDH. [165] This was attributed to a protonated and positively charged surface, due to the pH being lower than the PZC calculated of 7.29. Upon dissolution of the dye in solution, the sulfonate groups (R-SO_3^-) of SY could associate with this positively charged surface. Similar findings were found within an investigation of Co_4Al-Cl LDH for the adsorption of MO. [166] Between pH range of 4-10 removal of MO remained around 98 %, with significant drops noted at pH 2 and 12. The drop in MO removal at pH 12 was attributed to pH exceeding the pH_{PZC} of 11.3. The lower removal of MO at very acidic conditions (pH = 2) was ascribed to a destruction of LDH structure as H^+ reacts with OH^- ions in the brucite layers. [166] Interestingly this relationship between pH and LDH pH_{PZC} did not appear to encompass all sorption systems, with many authors highlighting an independent relationship between pH and sorption due to buffering. [167,168] This has been attributed to hydrogen ions being neutralized by hydroxyl groups in the brucite layer at low pH, and deprotonation of the LDH surface at higher pHs. [20] Due to the variable nature of environmental dye wastewater, with pH varies varying from strongly acidic to alkaline (pH 4 – 12), further investigation into this buffering mechanism could be of interest as it allows for the utilization of LDH sorbents in a variety of wastewater streams.

2.5.4.4. Dye Structure

One factor that tends to be overlooked within literature is the importance of the dye structure on sorption. While many papers highlight differences in the sorption capacities of dyes onto LDHs, the reasoning behind these are rarely reported. [149,169] Different dyes can have vastly different adsorption capacities with LDHs depending on their size, shape, charge and chemical structure. [170] One author reported the uptake of reactive black 5 (RB5) and reactive orange 16 (RO16) onto Zn_2Al-CO_3 CLDHs. [37] Adsorption capacity of reactive orange 16 (q_m = 895 mg g^1) appeared to be considerably greater than reactive black 5 (589 mg g^{-1}) due to the reduced number of R-SO_3^- functional groups. In addition, it was thought that the increased size of reactive black 5 molecules reduced its interactions with the sorbent surface due to steric hindrance. As environmental dye effluents are likely to contain a multitude of dye contaminants, understanding the relationship between the uptake of dyes and structure is of vital importance. Further studies revolving around dye structure should be considered.

2.5.4.5. Structural Effects and Composites

The composition of the LDH has also been reported to play a role in the sorption of dyes. One author noted a Mg/Al ratio between 3.1 – 4.4 to be optimal for the adsorption of acid blue 9 due to increased surface area and phase purity. [41] Similar observations were observed for the removal of acid blue 9, acid red 37 and acid yellow 23 dyes where optimal uptake was achieved at ratios between 2.2 – 4.0. [168] Interestingly this appears to correlate with the optimal conditions for pure hydrotalcite formation discussed in Section 2.3.2. Gao et al. showed that both the structure and surface area of CoAl-LDH affected the adsorption capacity for MO. 3D hollow and solid spheres, alongside 2D hexagonal platelet structures of CoAl were found to have vastly differing surface areas that significantly influenced their adsorption capacity. Flower-like hollow spheres possessed the largest uptake for MO at 2189.23 mg g^{-1}, almost double that of the 2D structure (1217.31 mg g^{-1}). [171]

Another growing area of research is the use of LDH-composites and hybrids for dye removal. Many authors have modified LDH materials with various other nanoparticles such as to increase surface area and porosity, add additional functionality and/or induce magnetism for easy removal. [172–174] However, as the work herein highlights the use of pure-LDH materials, and such composites have been discussed in other reviews, these will not be discussed in depth. [19,20,33,175]

2.5.5. Summary of Dye Removal Studies by LDHs

Table 2.9. Summary of the removal of dyes by LDHs

LDHs	Synthesis	Dyes	Q_m / mg g^{-1}	Isotherm Model	Kinetic Model	Thermodynamics	Ref
CaAl	Co-precipitation	Acidic scarlet	N/A (Mechanistic study)				148
CaAl	Co-precipitation	Methyl orange	N/A (Mechanistic study)				148
CaAl	Co-precipitation	Methyl orange	-	L	-	-	176
CaAl	Co-precipitation	Sunset yellow	398.41	L	-	-	165
3D-CoAl	Urea Co-precipitation	Methyl orange	2189.23	L / Sips	2nd / IPD	Endothermic	171
2D-CoAl	Urea Co-precipitation	Methyl orange	1217.31	L / Sips	2nd / IPD	Endothermic	171
CoAl	Acid-salt treatment	Methyl orange	801.08	L	2nd	Endothermic	166
3D-MgAl	Ultrasonication	Acid orange 7	485.6	L / F	Elovich / IPD	Endothermic	39
3D-MgAl	Ultrasonication	Methylene blue	58.3	L / F	Elovich / IPD	Endothermic	39
MgAl	Co-precipitation	Acid blue 9	49.9	L	-	-	168
MgAl	Co-precipitation	Acid green 68:1	154.8	L	2nd	-	152
MgAl	Co-precipitation	Acid red 37	82.2	L	-	-	168
MgAl	Co-precipitation	Acid yellow 23	43.5	L	N/A	-	168
MgAl	Co-precipitation	Benzopurpurine 4B	153.88	L / F	-	Endothermic	164
MgAl	Hydrothermal	Congo red	129.9	L	2nd	-	154
MgAl	Hydrothermal	Methyl orange	148	L / F	2nd	-	157

Table 2.9. (continued)

LDHs	Synthesis	Dyes	Q_m / mg g^{-1}	Isotherm Model	Kinetic Model	Thermodynamics	Ref
MgAl	Co-precipitation	Reactive brilliant red	657.5	L / F	2^{nd}	Endothermic	[161]
MgAl	Co-precipitation	Remazol brilliant blue	220	R-P	2^{nd}	-	[34]
MgAl	Co-precipitation	Reactive red 120	108.83	L	2^{nd}	-	[162]
MgFe	Co-precipitation	Metanil yellow	42.72	L / F	2^{nd}	Endothermic	[163]
MgFe	Co-precipitation	Methylene blue	4.01	L	2^{nd}	Exothermic	shi
MgFe	Co-precipitation	Reactive red 120	82.59	L	2^{nd}	-	[162]
NiAl	Sonochemical	Congo red	120.5	L	2^{nd}	Endothermic	[177]
NiAl	Co-precipitation	Reactive brilliant red X-3B	14	L	2^{nd}	Exothermic	[178]
NiFe	Co-precipitation	Methyl orange	205.76	L	2^{nd}	-	[143]
NiMgAl	Hydrothermal	Congo red	262	L	2^{nd}	Endothermic	[156]
NiMgAl	Co-precipitation	Methyl orange	118.5	L / R-P	2^{nd}	Endothermic	[157]
ZnAl	Co-precipitation	Evan’s blue	491.93	L	-	Endothermic	[149]
ZnAl	Co-precipitation	Chicago sky blue	501.36	L	-	Endothermic	[149]
ZnAl	Co-precipitation	Niagara blue	536.13	L	-	Endothermic	[149]
ZnAl	Co-precipitation	Remazol brilliant blue	191	R-P	2^{nd}	-	[34]
ZnFe	Co-precipitation	Methylene blue	2.78	L	2^{nd}	Exothermic	[179]
ZnMgAl	Co-precipitation	Remazol brilliant blue	164	R-P	2^{nd}	-	[34]

Notes: Q_m = Maximum adsorption capacity, L = Langmuir, F = Freundlich, R-P = Redlich-Peterson, 2^{nd} = Pseudo second, IPD = Intra-particle diffusion

2.6. Gaps within the Literature

The literature has identified that while CFHS appears to be a promising method for producing homogeneous continuous LDH nanoparticles with controllable properties, it is not yet fully understood. To date only three types of LDHs synthesised by CFHS method have been reported: CaAl, [30,180] MgAl, [28] and ZnAl. [37] There is scope to expand this list to create a large catalogue of LDHs. In addition, while both Clark et al. and Wang et al. have identified how synthesis parameters effect physical properties of CaAl and MgAl LDHs, [28,30] it is not yet known if optimal synthesis conditions are dependent on the individual LDH material. If synthesis conditions have the same effect irrespective of metal components (M^{2+}/M^{3+}) this would allow for the development of a generalised method that could be utilized for all existing and new LDH systems produced by CFHS. Therefore, further analysis should be conducted to corroborate if this is the case.

Alongside this, there appears to be a disconnect between literature surrounding LDH synthesis and application for dye removal. Many environmental and external factors have been shown to impact both capacities and kinetics of dye sorption onto LDHs, however, the role of structural impacts has largely been undiscussed. Therefore, there is an opportunity to improve understanding of how synthesis conditions (e.g., temperature, pressure, pH) and the subsequent changes in physical properties (e.g., Surface area, morphology and particle size) impact dye sorption.

There is also an argument to include the impact of different metals in this study. Few studies have directly analysed the impact of substituting different divalent or trivalent metals has on dye sorption. Cross-comparison of separate studies to deduce these effects becomes problematic due to the inherent differences in the experimental methods. For example the adsorption of MO onto ZnMgAl and MgAl LDHs has been studied, reporting adsorption capacities of 883.24 and 329.27 mg g^{-1} respectively. [167,181] While this may suggest that the incorporation of Zn into MgAl structure results in a superior adsorption capacity, there is an inherent bias in this observation due to differences in synthesis conditions (Table 2.10). While both LDHs were synthesised by co-precipitation, different aging times and temperatures were utilized which have been reported to impact crystal growth. Therefore, it is possible that the choice of synthesis conditions will have also factored into the differences in adsorption capacity observed. Furthermore, a lack of consistency between physical properties reported, such as surface area, makes conclusive arguments between papers even harder to justify. Therefore, there is merit for further experimentation on the role LDH metal cation choice plays on dye sorption, under more controlled conditions.

Table 2.10. Comparison of papers highlighting adsorption of MO

	Synthesis Method	**Synthesis Conditions**	**Surface Area / $m^2\ g^{-1}$**	**Adsorption Capacity / mg g^{-1}**	**Ref.**
Mg-Al-CO_3	Co-precipitation	200 °C, 20 h	Not reported.	329.27	[167]
Zn-Mg-Al-CO_3	Co-precipitation	100 °C, 25 h	82.13	883.24	[181]

Finally, previous literature by Liu and Evans has shown that AO7 dye can be directly intercalated into LDH structure during synthesis by a batch co-precipitation method. [35] This has potential as an alternative mechanism for wastewater treatment whereby, instead of remediating dyes from wastewater through adsorption onto LDHs, the wastewater is used directly as a feedstock to produce LDH-AO7 materials. Due to issues with scaling batch processes, further investigations into the synthesis of LDH-AO7 by continuous method (CFHS), is of interest. Conducting synthesis under conditions more realistic to environmental wastewater would further aid the feasibility of this approach. Furthermore, expanding the scope of dyes that can be incorporated into LDH structure during synthesis would highlight a greater potential for a wide variety of wastewater feedstocks.

3. Materials and Methods

This chapter highlights the experimental methodology used during layered double hydroxide (LDHs) synthesis and adsorption analysis. In addition, analytical techniques used to characterise LDHs are also discussed.

3.1. Reagents and Chemicals

All chemicals used during layered double hydroxide synthesis and adsorption experiments were of reagent grade and used as received. Solutions were made fresh in deionised water prior to synthesis. Calcium nitrate hexahydrate (≥ 99 %), evans blue (EB, ≥ 75 %), iron nitrate nonahydrate (≥ 98 %), magnesium nitrate hexahydrate (98+ %), methylene blue (MB, ≥ 95 %), nickel nitrate hexahydrate (98 %), orange II sodium salt (acid orange 7, dye content > 85 %), safranin-O (Saf-O, ≥ 85 %), sodium carbonate (> 97 %), sodium nitrate (≥ 99 %), sodium hydroxide (> 97 %), sunset yellow FCF (SY, ≥ 90 %), and zinc nitrate hexahydrate (98 %) were all purchased from Sigma Aldrich (Devon, UK). Cobalt nitrate hexahydrate (> 98 %) was purchased from Fisher Scientific (Loughborough, UK) while aluminium nitrate hexahydrate (> 98 %) was purchased from Alfa Aesar (MA, USA).

3.2. Layered Double Hydroxide Synthesis

3.2.1. Continuous Hydrothermal Synthesis

Various LDH syntheses were performed using a prototype counter continuous hydrothermal reactor, originally designed at the University of Nottingham, constructed by Promethean Particles (Figure 3.1). [182,183] The base solution (downflow), containing NaOH and interlayer anion precursors, was fed into the reactor via a Gilson pump (HPLC) at 20 mL min^{-1}. The downflow feed was heated to the desired temperature by a 2kW band heater (20 – 400 °C) before being fed into the inner tube of the pipe-in-pipe reactor. The mixed metal salt solution (upflow), containing the desired M^{2+} and M^{3+} precursors, was also fed into the reactor via a Gilson pump (HPLC) at 10 mL min^{-1}. This upflow stream entered the bottom of the reactor t-piece at ambient temperature. Upon reaction of the counter-current flows within the reactor t-piece (resident time *ca*. 4 s), [184] the resulting product suspension was rapidly transported out of the reactor and cooled by a counter-current heat exchanger. To ensure no heat loss during the reaction an additional band heater was placed around the reactor t-piece. Reaction temperature was monitored and maintained by two thermocouples positioned directly before and after the reaction occurred (T1 and T2 in Figure 3.1 schematic). The pressure of the system was maintained as desired between 1-240 bar by a Swagelok back-pressure regulator. To remove residual counter ions and precursors, upon collection product suspensions were centrifuged and washed with deionised water. Washed samples were subsequently oven dried overnight at 80 °C unless otherwise stated. A variety of different LDHs were synthesised during this research at varying conditions based on previous literature. These are summarised in Table 3.1.

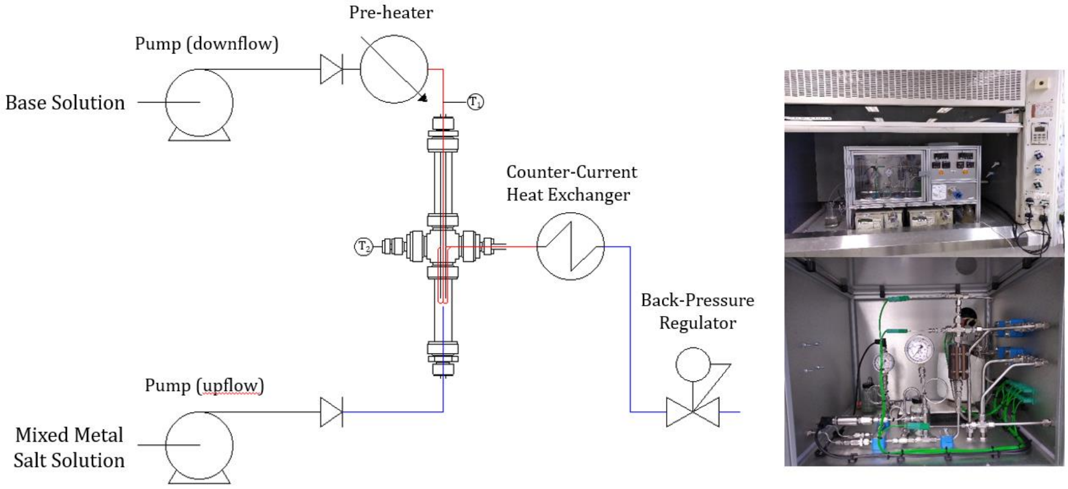

Figure 3.1. Counter-current flow reactor schematic (left). Rig exterior (top right) and rig interior (bottom right)

Table 3.1. Conditions used during layered double hydroxide synthesis

Chapter	LDH	Downflow (Base Solution)		Upflow (Mixed Metal Salt Solution)		Temperature / °C	Pressure / Bar
		Precursors	Concentration / mol L^{-1}	Precursors	Concentration / mol L^{-1}		
4	Co_2Al-CO_3	NaOH	0.05 – 1.00	$Co(NO_3)_2$	0.066	20 - 400	1 - 240
		Na_2CO_3	0.0165	$Al(NO_3)_3$	0.033		
5	Ca_2Al-NO_3	NaOH	0.125	$Ca(NO_3)_2$	0.066	50	100
		Na_2NO_3	0.033	$Al(NO_3)_3$	0.033		
	Mg_2Al-CO_3	NaOH	0.125	$Mg(NO_3)_2$	0.066		
		Na_2CO_3	0.0165	$Al(NO_3)_3$	0.033		
	Zn_2Al-CO_3	NaOH	0.125	$Zn(NO_3)_2$	0.066		
		Na_2CO_3	0.0165	$Al(NO_3)_3$	0.033		
	Ni_2Al-NO_3	NaOH	0.125	$Ni(NO_3)_2$	0.066		
		Na_2NO_3	0.033	$Al(NO_3)_3$	0.033		
	Mg_2Fe-CO_3	NaOH	0.125	$Mg(NO_3)_2$	0.066		
		Na_2CO_3	0.0165	$Fe(NO_3)_3$	0.033		
	Ni_2Fe-NO_3	NaOH	0.125	$Ni(NO_3)_2$	0.066		
		Na_2NO_3	0.033	$Fe(NO_3)_3$	0.033		

Table 3.1 (continued)

Results Chapter	**LDH**	**Downflow (Base Solution)**		**Upflow (Mixed Metal Salt Solution)**		**Temperature / °C**	**Pressure / Bar**
		Precursors	**Concentration / mol L^{-1}**	**Precursors**	**Concentration / mol L^{-1}**		
6	Mg_2Al-dye	NaOH	0.125	$Mg(NO_3)_2$	0.066	93	1
		Acid orange 7	0.033				
		Sunset yellow	0.0165				
		Evan’s blue	0.0082				
		Methylene blue	0.033	$Al(NO_3)_3$	0.033		
		Safranin-O	0.033				
	Mg_2Al-NO_3	NaOH	0.125	$Mg(NO_3)_2$	0.066		
		$NaNO_3$	0.033	$Al(NO_3)_3$	0.033		
		Dye*	0 – 1500 mg L^{-1}				

**Dyes include acid orange 7 (AO7), sunset yellow (SY), evans blue (EB), methylene blue (MB) and safranin-O (Saf-O)*

3.2.2. Synthesis of Co_2Al-CO_3 LDHs

The effect of synthesis temperature and pressure on Co_2Al-CO_3 LDHs synthesis was carried out between 1-240 bar and 20-400 °C (Figure 3.2). All other variables such as flowrates and precursor concentrations were maintained to prevent bias. Once washed and dried, product collected was analysed by a variety of characterization techniques for determining any changes in physical properties.

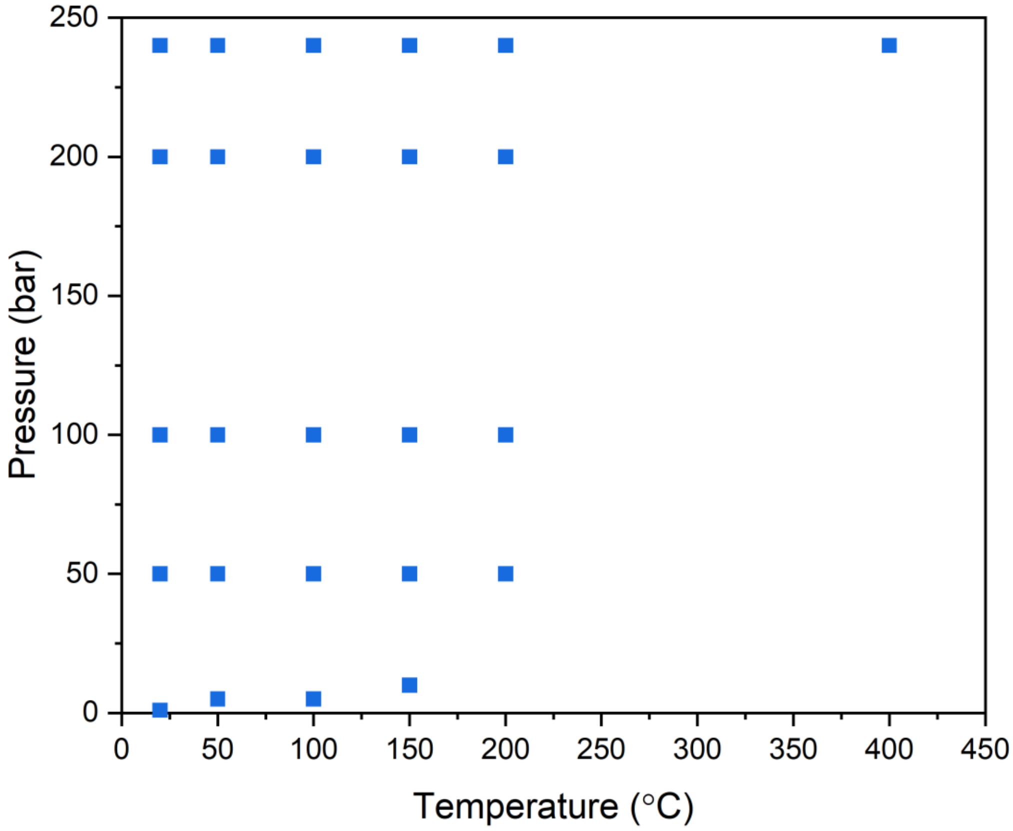

Figure 3.2. Matrix of Co2Al-CO3 LDHs synthesised

Reaction yields of Co_2Al-CO_3 were calculated using the reaction equation below (3.1). A water content of 15 % was assumed in LDH product (85 % dehydrated mass), based on water loss observed in TGA analysis. Prior to centrifugation and drying, the total volume of product collected was measured in a measuring cylinder.

$$2\,NaOH + 0.167\,Na_2CO_3 + 0.66\,Co(NO_3)_2 + 0.33\,Al(NO_3)_3 \rightarrow [Co_{0.66}^{2+}Al_{0.33}^{3+}(OH)_2](CO_3)_{0.165}{}^{2-} \cdot xH_2O + 2.33\,NaNO_3 \quad 3.1$$

In addition to temperature and pressure effects, the role of pH and NaOH concentration on physical properties were observed. Based on the general LDH formula, $[M_{1-x}^{2+}M_x^{3+}(OH)_2](A^{n-})_{x/n} \cdot mH_2O$, it can be seen that a stoichiometric ratio of 2:1 (NaOH:Metal Salts) is optimal to balance the amount of reagents required for synthesis. [93] As the mixed metal feed is pumped at half the flowrate (10 mL min^{-1}, upflow) of the base feed (20 mL min^{-1}, downflow), this equates to a practical ratio of 1:1. For the variable NaOH experiments, LDHs were synthesised at NaOH concentrations between 0.05 M and 1 M while maintaining metal salt concentrations, temperature and pressure (Table 3.2). This allowed for the comparison of how properties such as surface area and crystallinity change at concentrations where NaOH is deficient (0.05 M) and in excess (> 0.10 M).

Table 3.2. Variable NaOH experiments synthesis parameters.

Temperature / °C	**Pressure / Bar**	**[M^{2+}] / mol dm^{-3}**	**[M^{3+}] / mol dm^{-3}**	**[NaOH] / mol dm^{-3}**	**Stoichiometric Ratio (NaOH:Metal Salts)**
100	100	0.066	0.033	0.05	1:1
				0.10	2:1
				0.20	4:1
				0.50	10:1
				1.00	20:1

3.2.3. Synthesis of LDHs with varying M^{2+} and M^{3+} ions

In Chapter 5 six different LDHs, commonly utilized in literature for adsorption, were synthesised to determine the role of metals on acid orange 7 adsorption:

- $Ca_2Al\text{-}NO_3$
- $Mg_2Al\text{-}CO_3$
- $Zn_2Al\text{-}CO_3$
- $Ni_2Al\text{-}NO_3$
- $Mg_2Fe\text{-}CO_3$
- $Ni_2Fe\text{-}NO_3$

To present an unbiased comparison of the impact of M^{2+} and M^{3+} on dye uptake, the same experimental conditions were used for the synthesis of all LDHs (Table 3.1). In addition to this nitrate salts were used for all M^{2+} and M^{3+} precursors. Flow rates and precursor concentrations were based off those used in previous work by Clark et al. [87] Synthesis temperature and pressure were chosen due to previous literature suggesting these conditions allow for greater surface area and tuneability at these conditions (lower temperatures). [28]

3.2.4. Synthesis of Dye Intercalated Mg_2Al LDHs

Synthesis of dye intercalated Mg_2Al LDHs were carried out at conditions based on previous work by Liu and Evans et al (conventional synthesis - Table 3.3). [106] The concentrations of dye during Mg_2Al-SY, Mg_2Al-EB, Mg_2Al-MB and Mg_2Al-Saf-O were stoichiometrically based off ionic charge and $Al(OH)_3$ concentration. For example, as EB has an ionic charge of -4, a concentration four times lower than AO7 was utilized. Upon scaling Mg_2Al-AO7 synthesis down to concentrations of dye more typically found in environmental wastewater, all precursors were scaled down equally to ensure Mg:Al:OH:AO7 ratios were maintained (Table 3.3). During dye-doped $Mg_2Al\text{-}NO_3$ synthesis, conventional concentrations were used with an additional 100 – 1500 mg L^{-1} dye added to the downflow solution.

Table 3.3. Concentrations used during CFHS synthesis

	Concentrations / mol dm^{-3}	
	Conventional	**100 mg L^{-1} Dye**
NaOH	0.125	1.15 x 10^{-3}
AO7 or NO_3	0.033	3.06 x 10^{-4}
$Mg_2(NO_3)_2$	0.066	6.12 x 10^{-4}
$Al(NO_3)_3$	0.033	3.06 x 10^{-4}

3.2.5. Calcination of Co_2Al-CO_3

In Chapter 4 Co_2Al-CO_3 LDHs were calcined for subsequent adsorption experiments with AO7 to determine the effect of synthesis temperature on sorption. Five LDH samples synthesised at 100 bar and varying temperature (20 – 200 °C) were calcined based on experimental method by Clark et al. [9] Initially samples were calcined in air for 4 hours at varying temperature (100 – 500 °C) for 4 hours to determine the optimal temperature of calcination for Co_2Al-CO_3. Calcination temperature experiments revealed 200 °C to be the optimal temperature for adsorption experiments. Further calcination experiments were therefore conducted at 200 °C for 4 hours.

3.2.6. Control Experiments with AO7

Prior to synthesis of Mg_2Al-AO7, control experiments were conducted with AO7 to ensure no degradation of the dye occurred upon pumping through the continuous-flow reactor system (Table 3.4). Control experiments were conducted at 93 °C and 1 bar to mimic the conditions used during LDH synthesis. Aliquots were taken every minute and centrifuged to separate any solids that may have formed. The concentration of the aliquots was observed through quantified dilution and subsequent UV-vis analysis. As analysis showed that homogeneous dispersion of AO7 occurred after 9 minutes, subsequent control experiments were also conducted with SY, EB, MB and Saf-O, with aliquots taken between 10 – 12 minutes to confirm dyes did not degrade.

Table 3.4. Experimental conditions used during AO7 control experiment

Temperature / °C	95
Pressure / Bar	1
Time Intervals / min	1-15 (sample every minute)
Downflow	AO7 dye (20 mL min^{-1})
Upflow	Deionised water (10 mL min^{-1})
Initial AO7 Concentration / mg dm^{-3}	1000

3.2.7. Stability of Mg_2Al-AO7 in Water

The stability of Mg_2Al-AO7 was conducted to determine if dissolution of the dye (AO7) occurred upon suspension in water. Experiments were conducted at 20 °C within an incubator. 1 g L^{-1} of the LDH was suspended in two separate 250 mL solutions containing DI water. A further 0.0165 M Na_2CO_3 was dissolved in one solution to observe any additional ion exchange properties of the LDH. 3 x 1 mL aliquots were taken once a day for 7 days, centrifuged and quantitively diluted. The concentration of AO7 leachate was subsequently calculated through UV-vis spectrophotometry.

3.3. Materials Characterization

3.3.1. X-Ray Diffraction Crystallography (XRD)

Powder x-ray diffraction (PXRD) is one of the most common techniques for characterizing inorganic materials. For PXRD analysis An x-ray beam, generally in the range of 1 keV – 120 keV, is generated from an x-ray tube and fired into a crystalline powder sample. [147] A powder sample allows for random orientation of crystal domains within the sample. The x-rays fired collide with the electrons of atoms within the sample, resulting in photons from the incident beam to get scattered away (Figure 3.3). If the wavelength of the scattered x-rays remains unchanged it is known as *Thompson Scattering.*

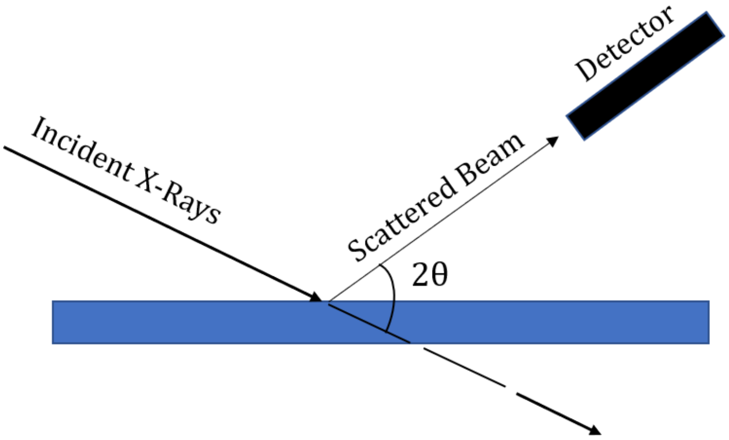

Figure 3.3. Detection of scattered X-rays by reflection

Diffracted waves from different atoms can interfere with each other, resulting in an increased intensity of x-rays detected. If atoms are arranged in a periodic fashion (i.e., long range crystal order) these diffracted waves can result in very sharp interference "peaks" with the same symmetry as the distribution of atoms. If two x-ray beams of identical wavelength are scattered off two different atoms within a crystalline structure, the length the additional x-ray beam travel is related to the scattering angle (θ) and the distance between these two atoms (d). As a result, when constructive interference is observed the scattering angle at which it occurs can be used to calculate the distance between these atoms (d-spacing). This is known as Bragg's law and can be defined as followed: [147]

$$2dsin\theta = n\lambda \qquad 3.2$$

Where *d* is the interplanar distance, θ the scattering angle, λ the x-ray wavelength and *n* an integer representing the order of the diffraction peak. As this law holds true for any periodic distribution of electron density, it can be applied to LDHs to calculate the distance between metal ions within the brucite sheets, and the interlayer distance. As different crystalline phases produce unique diffraction patterns, due to differing atomic arrangements, diffraction patterns can be used to identify what phases are present (by comparing to reference materials).

In addition to calculating distances between periodic crystalline phases, the d-spacing can be used to calculate lattice parameters of a unit cell. The unit cell of a crystal phase can be described by three vectors *a, b* and *c* and three interaxial angles α, β and γ (Figure 3.4).[147] LDHs exhibit hexagonal crystal structure with three equilateral axes (120 °) and one axes perpendicular to the others. In addition, the vectors *a* and *b* are of equal length (a=b≠c). In order to show a crystal plane Miller indices are employed, defined as the fractional intercepts that the plane makes with crystallographic axes. [147] If a plane is described as having Miller Indices of (*h, k, l*), the plane makes intercepts of 1/*h*, 1/*k* and 1/*l* with the axes *a, b* and c.

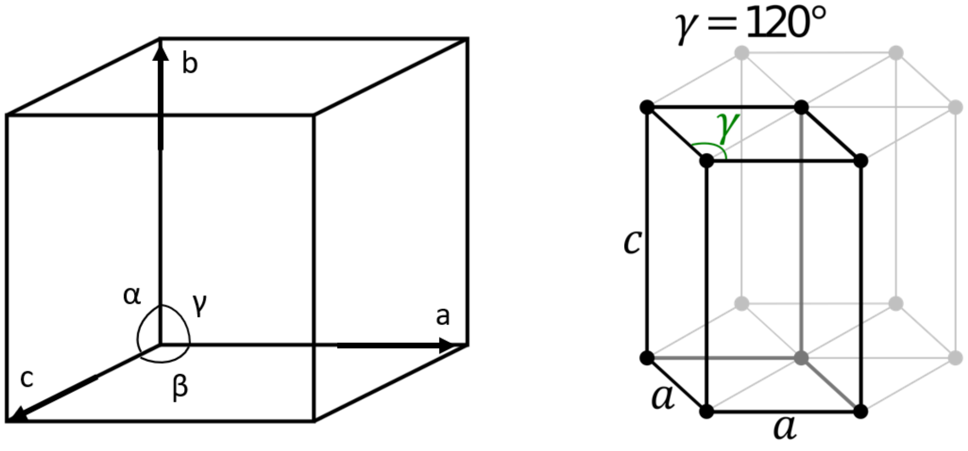

Figure 3.4. Vectors and interaxial angles of a crystals unit cell (left), hexagonal unit cell (right)

For a hexagonal system the relationship between miller indices, lattice parameters (*a* and *c*) and Bragg's law can be described as followed:

$$\frac{4\sin^2\theta}{\lambda^2} = \frac{1}{d^2} = \frac{4}{3}\frac{4h^2 + hk + k^2}{a^2} + \frac{l^2}{c^2} \qquad 3.3$$

Therefore, if the specific miller indices of x-ray diffraction peaks are known of a powder with hexagonal system, the lattice parameters can be calculated from those specific peaks. For example, an LDH spectra with two reflections relating to (003) and (110) would allow for *a* and *c* to be calculated from the following equations:

$$c^2 = l^2 d^2 = 9d^2 \tag{3.4}$$

$$a^2 = \frac{4}{3}(h^2 + hk + k^2)d^2 = 4d^2 \tag{3.5}$$

In conjunction with this, the Scherrer equation allowed us for the calculation of the crystal domain length (CDL) of specific crystal planes. This is calculated from the width of a diffraction peak at half its maximum intensity, full width half maximum (FWHM) and is expressed as:

$$CDL = \frac{k\lambda}{Bcos\theta} \tag{3.6}$$

Where k is the shape factor calculated at 0.9, λ is the wavelength of the x-ray beam, B is the FWHM and θ is the scattering angle. It should be noted however that crystallite size in a specific plane is not the only factor that causes peak broadening. Uniform distribution in all directions of crystallites is required to provide accurate calculations of crystallite diameter. In reality however additional broadening will occur due to strain broadening, small crystallite sizes (< 0.1 µm) and instrumental broadening. [147]

X-ray Diffraction analysis within this work was performed on a Bruker (Coventry, UK) D8 Advance Diffractometer with Da Vinci using copper kα radiation (λ = 1.5418 Å) and Bragg-Brentano geometry. Analysis was conducted at a scanning rate 6.0 ° min^{-1} over a 2θ range of 2 – 70 °. In CDL calculations instrumental broadening was accounted for using a LaB_6 reference material that contained no peak broadening due to crystallite size or micro-strain. [185] Calculation of *a* and *c* parameters and CDL of LDHs utilised *(002) / (003)* and *(030) / (110)* reflections from XRD analysis.

3.3.2. Specific Surface Area and Pore Size Measurements (BET)

Determination of specific surface area (SSA) within a sample are commonly done by manometric method. [186] A known amount of pure gas, such as Nitrogen, is admitted into a confined, calibrated volume at constant temperature containing the material of interest. As adsorption of the gas occurs the pressure in this space falls. The amount of gas adsorbed at equilibrium pressure can then be calculated as the difference between the amount of gas admitted and the amount of gas required to fill the dead volume around the sample. The most commonly applied method of calculating surface area is the Brunauer, Emmett and Teller (BET) theory which allows for the consideration of multilayer adsorption, seen in Equation 3.7: [187]

$$\frac{p/p_0}{V\left(1-\frac{p}{p_0}\right)} = \frac{C-1}{V_m C}\left(\frac{p}{p_0}\right) + \frac{1}{V_m C} \qquad 3.7$$

Where (p/p_0) is the relative pressure, v the volume adsorbed at relative pressure, V_m the monolayer capacity and C a constant related to the energy of monolayer adsorption. The specific surface area (S_{BET}) can then be calculated from V_m with the following equation (3.8):

$$S_{BET} = \frac{\left(\frac{V_m N \sigma}{V}\right)}{a} \qquad 3.8$$

Where v_m is the monolayer adsorbed gas volume, N is Avogadro’s number, σ the cross sectional area of a single adsorbate molecule ($\sigma(N_2) = 0.162$ nm) and V the volume of one mol of vapor. [188] In order to convert total surface to specific surface area (S_{BET}), this is then divided by mass of the sample (*a*). It should be noted however that the BET equation only stands over limited regions of physisorption isotherms due to dependence on system, operational temperature, and isotherm type. As a result BET surface area measurements were conducted over a range that conformed to Rouquerol’s criteria: [186]

- BET C value should be positive.
- $V(1-p/p_0)$ should be increasing with partial pressure (p/p_0).
- The pressure corresponding to monolayer coverage (V_m) should be within the linear BET range.

For the purpose of this research, Nitrogen was used for adsorption at 77 K. Prior to surface area analysis samples were outgassed overnight at 80 °C. Samples were subsequently analysed on a Micromeritics Tristar II 3020 instrument (Micromeritics, UK) between relative pressures of 0.006 – 0.999. Pore size distribution of the sample was analysed from the desorption branch of the nitrogen adsorption-desorption isotherm using the BJH model.

3.3.3. Thermogravimetric Analysis (TGA)

Thermogravimetric analysis (TGA) is a characterization technique that allows for the determination of mass change as a function of temperature. A pre-weighed pan containing sample is loaded onto a precision balance, residing in a furnace. Sample environment is then controlled by a purge gas which can either be reactive (Air) or inert (Nitrogen/Argon). As a sample is heated up mass change can occur for a variety of reasons such as water evaporation, oxidation or thermal composition. [189] Detection and analysis of evolved gases can also be incorporated through simultaneous thermal analysis and mass spectrometry (MS).

Within this study the thermal stability and water content of LDHs synthesised was determined using a TA Q500 TGA instrument (Cheshire, UK). Analysis was conducted between 25 – 800 °C at a heating rate of 10 °C min^{-1} and Nitrogen flow of 100 mL min^{-1}. Detection of evolved gases via TGA-MS was conducted on a separate TA Q500 TGA instrument between 25 – 800 °C, heating rate of 5 °C min^{1} and Argon flow of 40 mL min^{-1}. A variety of signals were observed at m/z 16 (O^{2-}), m/z, m/z 17 (OH^{-}) 18 (H_2O), m/z 30 (NO) and m/z 44 (CO_2).

3.3.4. Fourier-Transform Infrared Spectroscopy (FTIR)

Fourier-Transform Infrared Spectroscopy was used as a qualitative method to observe chemical bonds in dye intercalated LDHs, synthesised in Chapter 1. As infrared radiation passes through a sample, some of this radiation is absorbed by covalent bonds within the sample. Different covalent bonds within a sample will selectively absorb this infrared radiation at specific wavelengths, resulting in changes to the vibrational energy of the bond (stretching or bending). As a result, each molecular structure will produce a unique spectrum in infrared radiation. A Bruker Tensor 27 was used during analysis in attenuated total reflection mode, between 600 – 4000 cm^{-1}.

3.3.5. Inductively Coupled Plasma Optical Emission Spectrometry (ICP-OES)

Inductively Coupled Plasma Optical Emission Spectrometry (ICP-OES) is an analytical technique commonly used to detect and quantify chemical elements in a nebulized sample. An inductively coupled plasma is used to excite elements electrons from the ground state to an excited state. As these excited electrons return to the ground state, they emit electromagnetic radiation at a specific wavelength (Figure 3.5). As this wavelength is dependent on both the atom and the energy levels the electron is moving between, the presence of different elements can be detected.

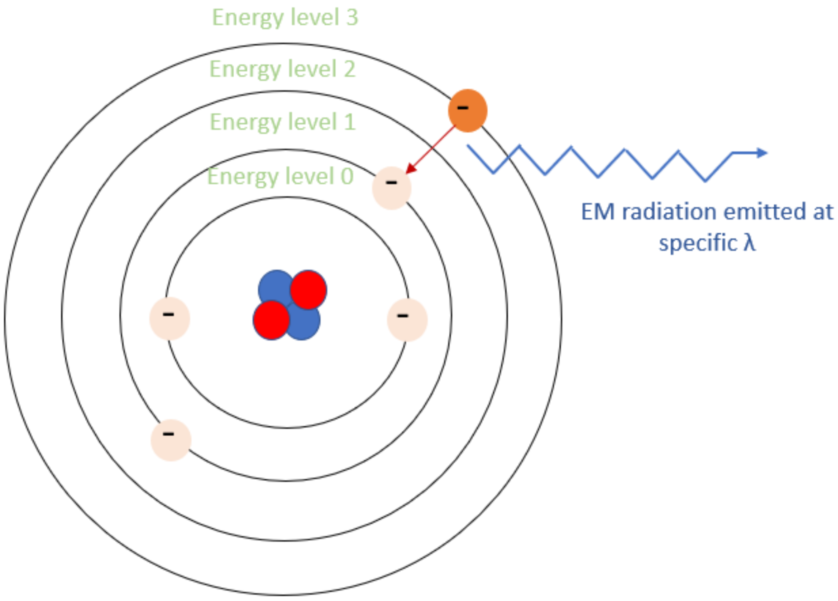

Figure 3.5. Emission of EM radiation at specific radiation upon transition of electrons to lower states, adapted from Agilent Technologies website [190]

As the Beer Lambert law states that the intensity of light emitted is directly proportional to the concentration within the sample, the quantity of individual elements in a sample can be quantified. This is done by comparison of samples to known calibration standards. The Beer Lambert law can be expressed as followed (Equation 3.9):

$$A = \varepsilon c l \qquad 3.9$$

Where A is the absorbance, ε the molar extinction coefficient (M^{-1} cm^{-1}), *c* the concentration (mol dm^{-3}) and *l* the path length (cm). ICP-OES was conducted for multi-element analysis to determine M^{2+}/M^{3+} content of LDHs using an Agilent 5110 VDV. Operating parameters used can be seen in Table 3.5.

Table 3.5. Operating parameters for ICP-OES analysis

Parameter	Description
Rf Power	1.20 kW
Plasma gas flow rate	12.0 L min^{-1}
Auxiliary gas flow rate	1.00 L min^{-1}
Nebulizer gas flow rate	0.7 L min^{-1}
Torch type	Easy fit torch one piece (1.8 mm, quartz)
Nebulizer type	C-Spray
Spray chamber type	Double pass s/c insert + ball joint
Viewing mode	Radial
Read time	5s

LDHs were prepared based on previous literature by dissolving in aqua regia (3:1 molar ratio of hydrochloric acid:nitric acid) at a ratio of 1 g LDH to 10 mL aqua regia. [191] Once digested samples were diluted to ensure aqua regia was 10 % v/w. Prior to analysis, multi-element calibration standards were prepared from Romil 10 000 ppm single element standards. The elements used and their respective wavelengths/calibration ranges can be found in Table 3.6.

Table 3.6. Element wavelength and calibration range during ICP-OES analysis

Element	Wavelength / nm	Calibration Range / mg L^{-1}
Al	396.152	0 – 130
Ca	422.673	0 – 300
Fe	260.709	0 - 250
Mg	383.829	0 - 250
Ni	216.555	0 - 400
Zn	472.215	0 - 500

3.3.6. Scanning Electron Microscopy and Energy Dispersive Spectroscopy (SEM-EDS)

Scanning Electron Microscopy (SEM) was used for observation of surface morphology and agglomeration of LDH particles. Unlike TEM analysis, samples can be observed as they are and do not require any thinning prior to analysis. [192] Electrons emitted from an electron gun are irradiated onto a sample. Unlike TEM, secondary electrons are recorded from scanning electron beams across the sample surface (incidence depth of ~10 nm). Secondary electrons are emitted by excitation from their ground electron state to that of a higher energy level.

Alongside morphological analysis, Energy Dispersive Spectroscopic Analysis (EDS) was used for the determination of element ratios in LDHs. Specifically, SEM-EDS analysis was conducted to determine if AO7 dye had been successfully intercalated into Mg_2Al-based LDHs in Chapter 1. Similar to that of ICP OES (Section 3.3.5) SEM-EDS analyses the energy intensity of x-rays emitted from the sample, which is dependent on both the atom and energy states the electrons were excited between. [95] Prior to analysis, samples were adhered to a carbon tab and a platinum coating was applied via a sputter coater (Palaron), ~ 15 nm thick. For analysis a Siemens XL30 FEG ESEM was used at an acceleration voltage of 20 kV, with an Oxford Instruments EDS detector being used for EDS analysis.

3.3.7. Transmission Electron Microscopy (TEM)

Much like SEM, Transmission Electron Microscopy (TEM) is a imaging tool that was used to observe microstructural features on the surface of LDH nanoparticles, alongside particle size distribution image analysis. [193] During TEM imaging a sample is irradiated with electrons which are transmitted through the sample, creating an image under the sample from the transmitted electron beams. [192] Both scattered and transmitted electrons pass through the atoms when the sample is irradiated (Figure 3.6). [192] While transmitted electrons give no information on atomic arrangement, scattered electrons can give information on atomic densities from elastic-scattered electrons (interact with electric field of atomic nucleus) and inelastic-scattered electrons (electrons emitted upon transferral of energy to electrons in atoms). These elastic scattered electrons are used for TEM observations. [192]

TEM imaging was conducted using a JEOL 2100+ TEM at an acceleration voltage of 200 kV. Prior to analysis samples were suspended (~0.1 mg mL^{-1}) and sonicated in deionised water for 15 minutes, before being dropped onto lacy carbon films on mesh copper grids. Particle size distribution analysis was conducted on micrographs using ImageJ software (100 – 400 particles observed per sample).

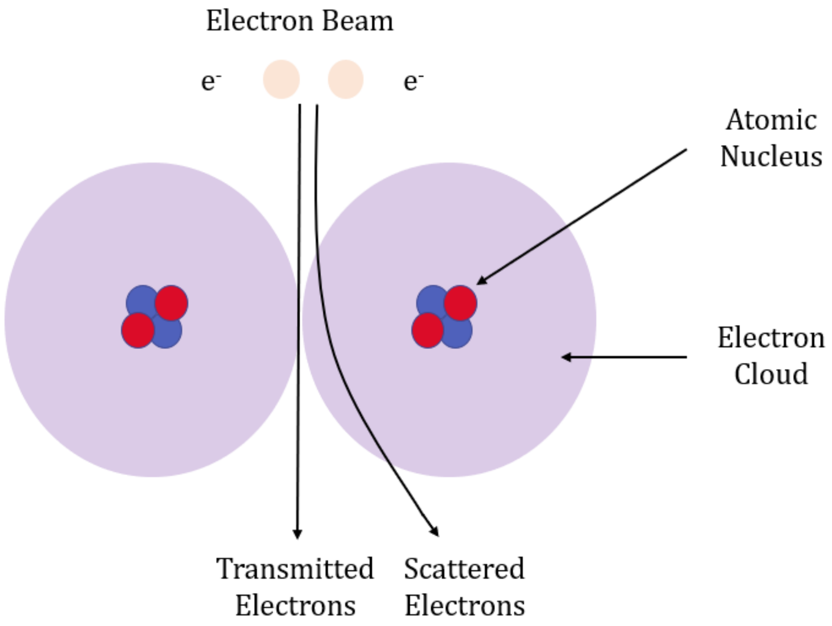

Figure 3.6. Schematic illustrating the interaction between electrons and atoms, adapted from Oku. [192]

3.4. Adsorption of Dyes onto LDHs

3.4.1. Adsorbate Dyes

Adsorption of dyes onto LDHs and calcined LDHs utilised five different dyes: AO7, SY, EB, MB and Saf-O. All dyes were obtained from Sigma Aldrich (Devon, United Kingdom). Dye solutions were made fresh before each experiment. In Chapter 4 only AO7 dye (Figure 3.7) was utilized for adsorption onto calcined Co_2Al-CO_3 LDH. In Chapter 5 AO7 was utilized for adsorption onto LDHs with varying M^{2+}/M^{3+} ions. Due to promising adsorption properties Ca_2Al-NO_3 and Mg_2Fe-CO_3 LDH were taken forward for further adsorption onto SY, EB, MB and Saf-O (Figure 3.8). Dyes were chosen to determine the effect of particle charge, chemical structure and molecular mass on dye uptake.

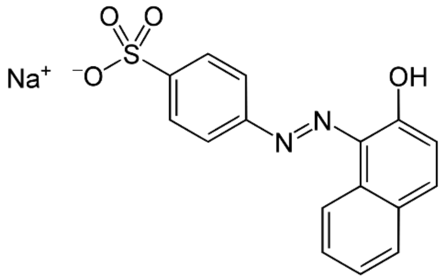

Figure 3.7. Molecular structure of acid orange 7 (AO7) dye

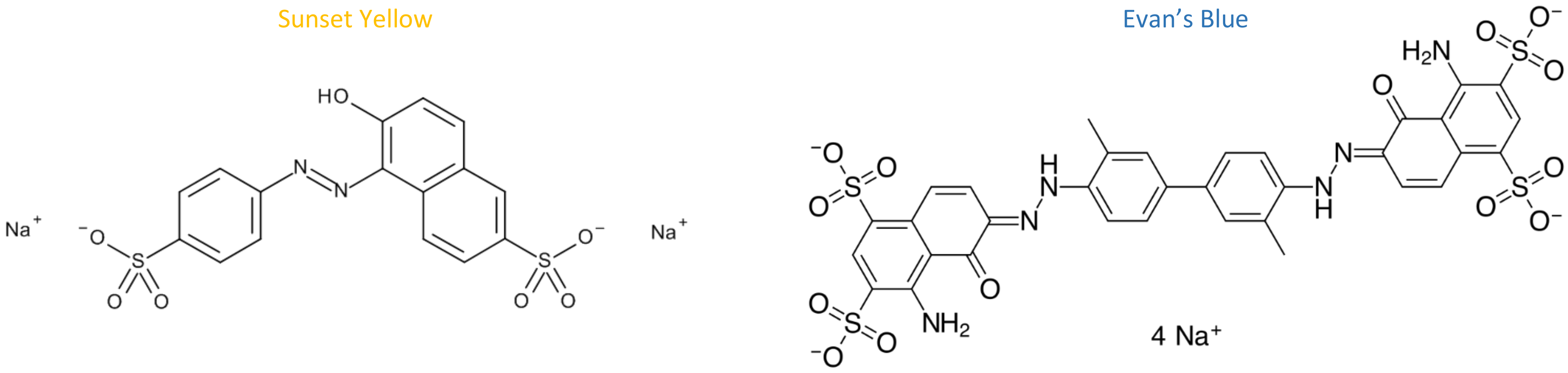

Sunset Yellow

Evan's Blue

Methylene Blue

Safranin-O

Figure 3.8. Molecular structure of sunset yellow (top left), evans blue (top right), methylene blue (bottom left) and safranin-O (bottom right)

3.4.2. Adsorption Studies

Analysis of adsorption experiments were carried out by quantification of dye concentration using an Agilent Cary 60 UV-vis spectrophotometer (Cheadle, UK). Prior to analysis, calibration curves were produced of AO7, SY, EB, MB and Saf-O using their respective dye powders. On a balance (± 0.01 mg) stock solutions at a concentration of 1000 mg L^{-1} were made using deionised water. This stock solution was then used to produce diluted samples for the calibration range within the linear range of 0.2 mg L^{1} and 15 mg L^{-1}. Calibration curves for each dye can be found in the Appendix (Appendix A - Appendix J). For all batch adsorption experiments an adsorbent dosage of 1 g L^{-1} was used and prepared using deionised water. Adsorption experiments were conducted in an incubator at a temperature of 20 °C (293 K) and were equilibrated for 30 minutes prior to analysis with constant stirring. Uptake of dye was calculated from the following (eq. 3.10): [194]

$$q = \frac{(C_0 - C) \times V}{m} \qquad 3.10$$

Where q (mg g^{-1}) is the uptake, C_0 is the initial dye concentration and C is the dye concentration (mg L^{-1}) of the sample at any given time. V is the volume of the solution (L) and *m* the mass of sorbent (g). For all sorption experiments three aliquots were taken for every sample and centrifuged. After centrifuging the supernatants were quantitatively diluted and analysed by UV-vis Spectrophotometry. An average concentration was taken between the three readings. Control solutions containing dye in deionised water, with no adsorbent loading, were also conducted to determine any changes in dye concentration with time. UV-vis analysis was conducted at the λ_{max} of the different dyes (Table 3.7).

Table 3.7. λ_{max} for different dyes used during UV-vis analysis

Dye	**Λ_{max} / nm**	**Ref**
Acid Orange 7	485	[195]
Sunset Yellow	480	[165]
Evan's Blue	620	[196]
Methylene Blue	664	[179]
Safranin-O	520	[197]

3.4.3. Adsorption Kinetics

Kinetic studies were conducted to determine adsorption rates and equilibrium uptake of dye. Adsorbent dose was fixed at 1 g L^{-1} and an initial dye concentration of 1500 mg L^{-1} was used, based off previous literature. [31,194] The initial volume of dye solution was 250 mL. Kinetics experiments were conducted in an incubator at 20 °C (293.15 K) with constant stirring. At selected time intervals 3 sample aliquots were taken (3 x 1 mL), centrifuged, quantitatively diluted and measured by UV-vis spectrophotometry. Analysis of kinetic data was compared against pseudo-first order, pseudo-second order and intra-particle diffusion rate models. [198,199] Pseudo first order and pseudo second order models were chosen based on their common use within literature and most relevant for the adsorption of dyes onto both LDHs and CLDHs. [20] The intra-particle diffusion model was applied due to its applicability to sorption mechanisms involving diffusion of sorbents into internal sites, such as ion exchange into the interplanar region of LDHs. All models were used in their linear forms for regression analysis. The pseudo first order model is expressed as: [198]

$$\ln(q_e - q_t) = \ln(q_e) - k_1 t \qquad 3.11$$

Where q_e (mg g^{-1}) and q_t (mg g^{-1}) are the adsorption at equilibrium and t (min) respectively. k_1 (min^{-1}) is the pseudo-first order rate constant. The pseudo second model is expressed as following: [198]

$$\frac{t}{q_t} = \frac{1}{k_2 q_e^2} + \frac{t}{q_e} \qquad 3.12$$

Where k_2 (g mg^{-1} min^{-1}) is the pseudo-second order rate constant. The final model used for linear regression analysis was the intra-particle diffusion model, a model developed by Weber and Morris, and is expressed as: [199]

$$q_t = k_{id}\sqrt{t} + C_i \qquad 3.13$$

Where k_{id} is the intra-particle diffusion constant and C_i a constant related to the boundary thickness.

3.4.4. Adsorption Isotherms

While kinetic experiments give an idea of both adsorption rate and equilibrium uptake (q_e), isotherm studies were conducted to compliment this for a determination of adsorption capacity. Initial dye concentrations of 100 – 1500 mg L^{-1} were chosen based on concentrations observed in literature and those required for complete saturation of the LDH sorbents. For the purpose of AO7 uptake onto calcined Co_2Al-CO_3 LDH, higher concentrations of 2000 and 3000 mg L^{-1} were also conducted due to incomplete saturation of the sorbents at 1500 mg L^{-1}. Analysis was conducted using an adsorbent dose of 1 g L^{-1} within an incubator at 20 °C (293.15 K). For each sample three aliquots were taken after 24 h, centrifuged and quantitatively diluted prior to UV-vis spectrophotometry analysis. Experimental data was analysed using both the Langmuir and Freundlich models due to their common use in literature and simplicity of non-linear and linear regression methods. [200] The Langmuir model can be expressed in either its linear (3.14) or non-linear (3.15) form:

$$\frac{C_e}{q_e} = \frac{C_e}{q_m} + \frac{1}{k_L q_m} \qquad 3.14$$

$$q_e = \frac{q_m k_L C_e}{1 + k_L C_e} \qquad 3.15$$

Where C_e (mg L^{-1}) is the adsorbate concentration at equilibrium, q_e the adsorbed amount at equilibrium (mg g^{-1}), q_m the maximum amount adsorbed (mg g^{-1}) and k_L the Langmuir constant (L mg^{-1}). The Freundlich model can be expressed in either its linear (3.16) or non-linear form (3.17):

$$\ln(q_e) = \ln(k_f) + \frac{1}{n}\ln(C_e) \qquad 3.16$$

$$qe = k_F C_e^{\frac{1}{n}} \qquad 3.17$$

Where k_F ($L^{1/n}$ $mg^{1-1/n}$ g^{-1}) is the Freundlich constant and n is the constant heterogeneity factor.

3.4.5. The Effect of Initial pH Studies

Initial pH experiments were conducted at an initial dye concentration of 1500 mg L^{-1} and adsorbent dose of 1 g L^{-1} within an incubator (20 °C, 293.15 K). Prior to sorbent addition, the pH of the dye solution was adjusted between pH 4-10 with 0.05 M HCl and 0.05 M NaOH solutions. Solution pH was measured using a pH probe that had been calibrated with buffer solutions (pH 4, 7 and 10) prior to use. After 24 h three aliquots (1 mL) were taken, centrifuged and quantitatively diluted. Samples were analysed by UV-vis spectrophotometry.

3.4.6. Point of Zero Charge (PZC) pH Calculations

Prior to pH analysis, the pH_{PZC} of LDHs were calculated to aid in the understanding of the surface charge at different pHs. This was calculated by the pH drift method, a simple and reproducible method of calculating pH_{PZC} by suspending the sorbent in pH adjusted solutions (pH 4 – 11.5) and observing the change in pH after 24 h. [158] This pH range was chosen due to the propensity for dissolution of LDHs at very high and very low pH's. pH_{PZC} was calculated using the following:

$$pH_{diff} = mpH_0 + C \qquad 3.18$$

Where pH_0 is the initial pH, pH_{diff} is the difference in pH after 24 hours, and *m* and *C* are arbitrary gradient and constant values. The pH_{PZC} was calculated as the point at which the change in pH was 0 (pH_{diff} = 0). pH drift plots of the individual LDHs can be seen in Figure 3.9. pH_{PZC} measurements at high pH (> 11) were not used for calculations due to an inability for the LDHs to buffer at these alkaline conditions.

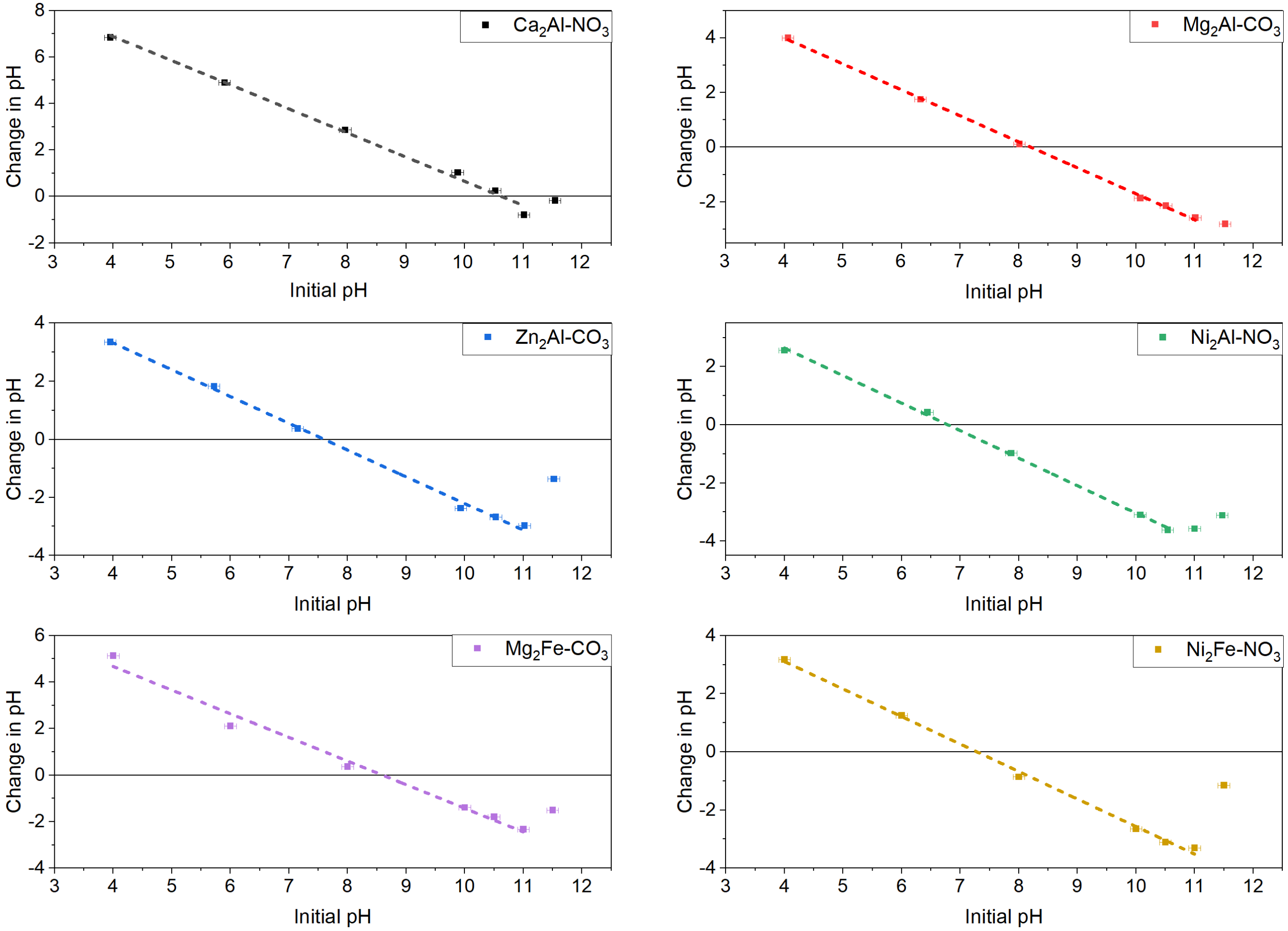

Figure 3.9. Determination of pHPZC by pH drift method

3.4.7. pH Buffering Experiments

While many papers have reported pH dependence for dye sorption onto LDHs, many others have reported that sorption is independent of pH due to buffering effects that occur for uncalcined LDHs. [167,168] As a result, alongside pH studies, an investigation into pH buffering effects was conducted. For pH buffering experiments LDHs (adsorbent loading = 1 g L^{-1}) were placed in a pH adjusted (pH = 4) solution of deionised water. Experiments were conducted with constant stirring within an incubator at 20 °C (293.15 K). To determine the speed at which buffering occurs, the pH of solution was monitored at various time (t) intervals over the initial hour (t = 1, 5, 10, 20, 30 and 60 mins). To determine buffering effectiveness over multiple cycles the pH was monitored with a pH probe every 24 hours and adjusted back to pH = 4. pH was cycled seven times over the course of seven days (t = 0, 24, 48, 72, 96, 120 and 144 hours).

4. Results and Discussion: The Impact of Synthesis Parameters on Co_2Al-CO_3 Layered Double Hydroxide Physical Properties and the Subsequent Impact on Adsorption

4.1. Introduction

LDHs are commonly synthesised by batch co-precipitation syntheses, however these methods become problematic with the consideration of scale-up due to long reaction and aging times, and large particle size distributions that occurs as a result of Ostwald Ripening. [201] Continuous-flow Hydrothermal Synthesis (CFHS) has been shown to be a scalable alternative option to synthesise LDHs, due to its short residence times (~ 4s), rapid mixing of precursors and homogeneous product quality. To date synthesis of three different LDHs, with varying interlayer anions, have been reported by CFHS: CaAl, MgAl and ZnAl. [9,30,138] In addition, previous research has shown that CFHS allows for tuneable crystal properties through alterations of reactor conditions such as temperature, pressure and NaOH concentration. One of the most promising applications for LDHs is the remediation of anionic and cationic contaminants from water such as metals, pharmaceuticals and dyes via adsorption/ion exchange. [38] However one factor that has been vastly ignored in literature is the role that tuneable synthesis parameters and the subsequent influence on physical properties have on adsorption onto LDHs, which is of great importance if LDHs are to ever be used industrially.

In this work the synthesis of a Co_2Al-CO_3 LDH is highlighted for the first time by this continuous-flow hydrothermal method. Co_2Al-CO_3 was chosen as, in comparison to other LDHs, its synthesis has been relatively unreported in literature despite its potential application in semiconductors due to its electrochemical properties. [202,203] Synthesis temperature, pressure and NaOH concentrations were investigated to determine their influence on morphology, crystal size, surface area and stability. The influence of synthesis conditions on physical properties was also compared to previous literature to observe any similarities and determine if a generalised method of CFHS could be developed. In addition, brief adsorption studies were conducted using AO7 dye to determine the impact of synthesis conditions on dye removal capabilities.

4.2. Highlights

- First reported synthesis of Cobalt-Aluminium LDH by continuous hydrothermal method.
- Synthesis temperature, pressure and NaOH all impact crystal domain length, particle sizes and specific surface area.
- Stoichiometric ratios of NaOH with metal salts (2:1) were optimal for achieving the highest surface area of Co_2Al-CO_3 (92.0 m^2 g^{-1}).
- Upon calcination of Co_2Al-CO_3 a maximum equilibrium uptake of 599 mg g^{-1} were reported for the uptake of acid orange 7 dye.
- Lower synthesis temperature resulted in higher uptakes of acid orange 7 dye, due to a synergy between crystal stacking and surface area.

4.3. The Effect of Synthesis Temperature and Pressure on Co_2Al-CO_3 Physical Properties

4.3.1. X-Ray Diffraction (XRD) Analysis

For all Co_2Al-CO_3 LDHs synthesised between 1-240 bar and 20-200 °C XRD analysis revealed the presence of intense symmetrical peaks at low 2θ angles, with broader asymmetrical peaks at higher 2θ angles which is indicative of LDH formation (Figure 4.1). [204] Peaks occurring at 11.6 ° and 60.2 ° correspond to 003 and 110 crystal planes respectively. The 003 plane is indicative of the thickness of one layer (i.e. One brucite layer and one interlayer), while the 110 plane is characteristic of the average distance between metal ions within the brucite sheet. [204] All LDHs synthesised at varying temperature and pressure had the following lattice parameters: a = 0.31 nm, c = 2.28 nm, which was in agreement with previously reported Co_2Al-CO_3 syntheses. [205]

For the Co_2Al-CO_3 LDH synthesised at 240 bar 400 °C (i.e., supercritical conditions), while there were peaks present indicating the formation of LDH, there were also additional reflections suggesting the presence of impurities (Figure 4.2). Upon comparison to structures within the inorganic crystal structure database (ICSD), these were concluded to be due to cobalt oxide, which are known to preferentially form under supercritical conditions. [206] Previous literature suggests that Aluminium hydroxide oxide (AlOOH) and Aluminium Hydroxide ($Al(OH_3)$) impurities are also likely to be present however they are undetectable via XRD due to being amorphous. [184] As a result of said impurities, further analysis on supercritically synthesised Co_2Al-CO_3 was not conducted.

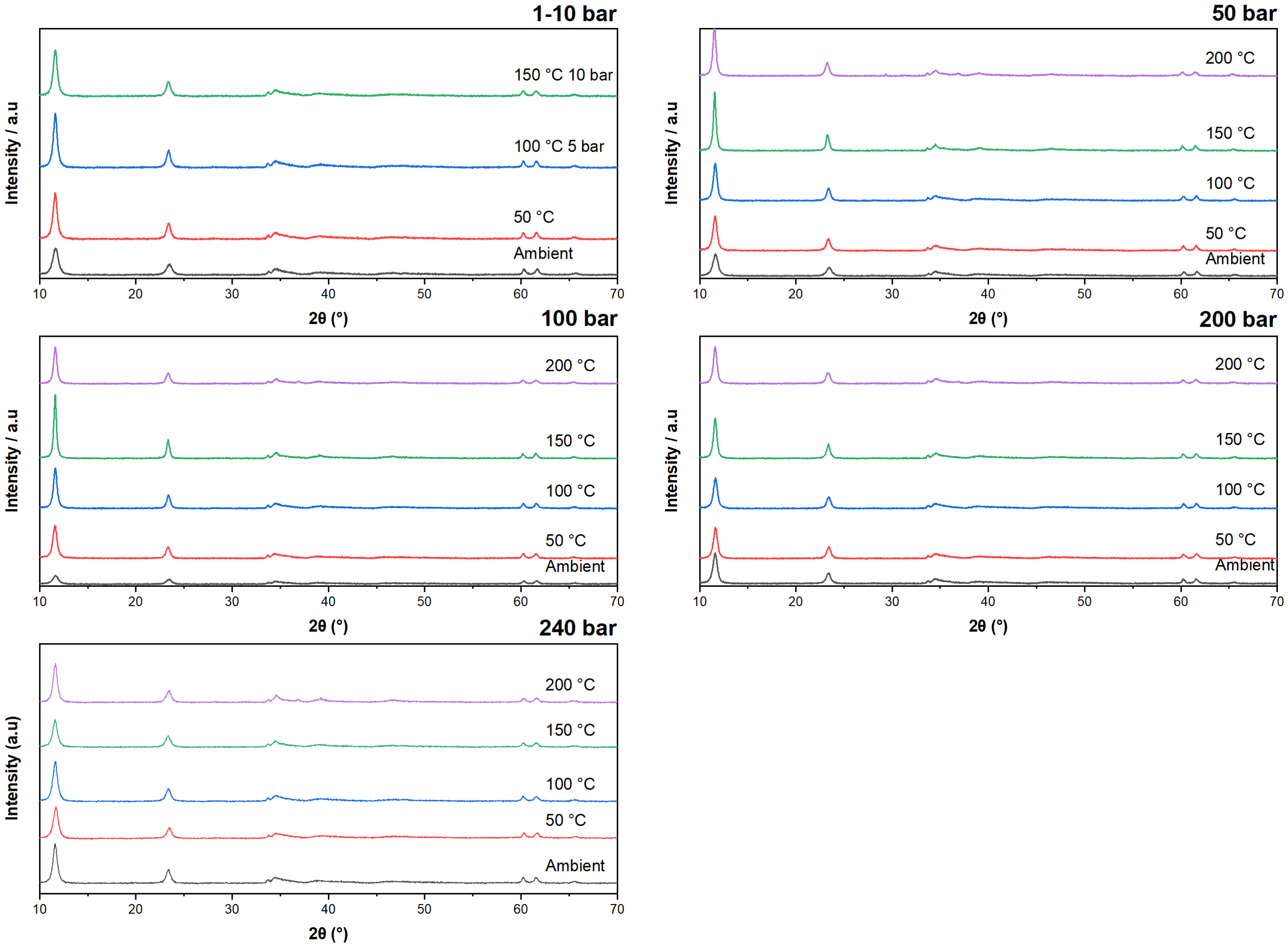

Figure 4.1. XRD plots of Co_2Al-CO_3 LDHs synthesised at varying temperature and pressure: 1-10 bar (top left), 50 bar (top right), 100 bar (centre left), 200 bar (centre right) and 240 bar (bottom left)

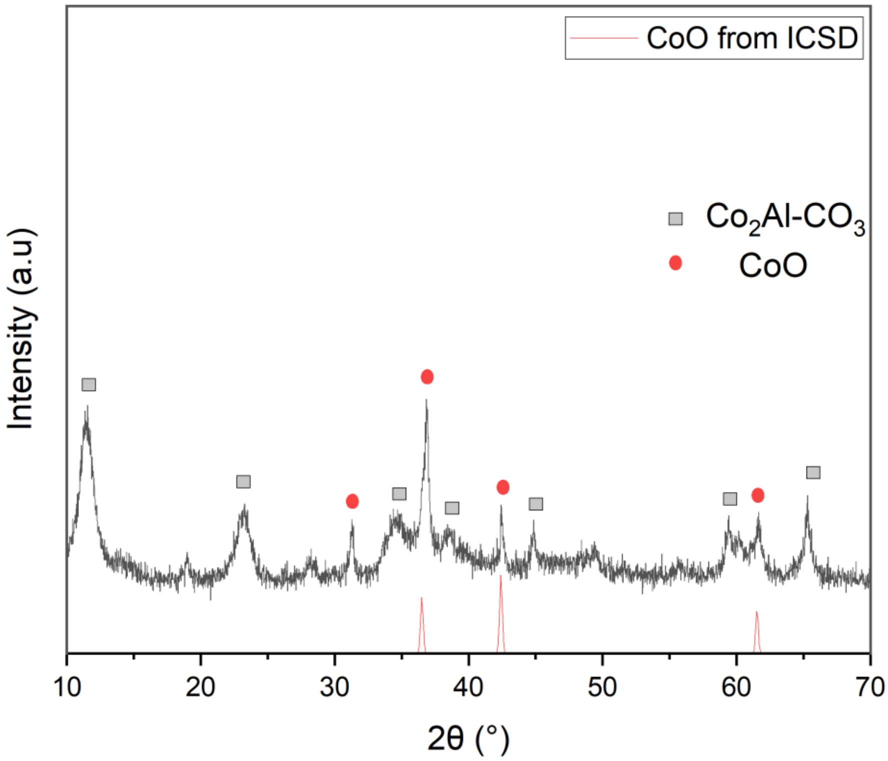

Figure 4.2. X-Ray diffraction pattern of Co_2Al-CO_3 synthesised at supercritical conditions: 240 bar 400 °C

Changes in crystal domain length (CDL) for the 003 and 110 crystal planes were calculated using the Scherrer equation to determine the effects of temperature and pressure on crystal growth. (Figure 4.3). A general increase in CDL (003) was observed with increasing synthesis temperature up to 150 °C for all LDHs synthesised below 240 bar, indicating an increased amount of platelet stacking. A reduction in CDL (003) was then observed for LDHs synthesised at 200 °C. It is evident that the most tuneability of CDL (003) occurs for LDHs synthesised at 50 and 100 bar, where we see large variances in crystal stacking with temperature. These changes in CDL (003) became less prominent at both high and low synthesis temperatures (1-10 bar and 240 bar), suggesting a lack of tuneability at these conditions. At low temperature (20 – 50 °C) there was little change in CDL (003) with pressure, however these changes became more prominent at higher temperatures (150 and 200 °C). LDHs synthesised at 150 °C had the greatest degree of tuneability, varying between 13 – 26 nm with changing pressure.

There did not appear to be any correlation with synthesis temperature and pressure with CDL (110). While this would suggest that crystal growth of individual platelets in the a/b plane is likely tied to other synthesis parameters such as residence time, it is difficult to say for certain due to larger errors that resulted due to weaker peak intensities at higher 2θ angles. This is an issue that has been observed in literature, specifically when attempting to measure crystallite sizes of NiZnFe-LDH, whereby the weak intensity of the (110) reflection resulted in high errors. [207] This makes any trends in platelet growth with temperature or pressure difficult to observe. A reduction in CDL (110) above 150 °C was once again observed, suggesting reduced platelet growth at high temperatures.

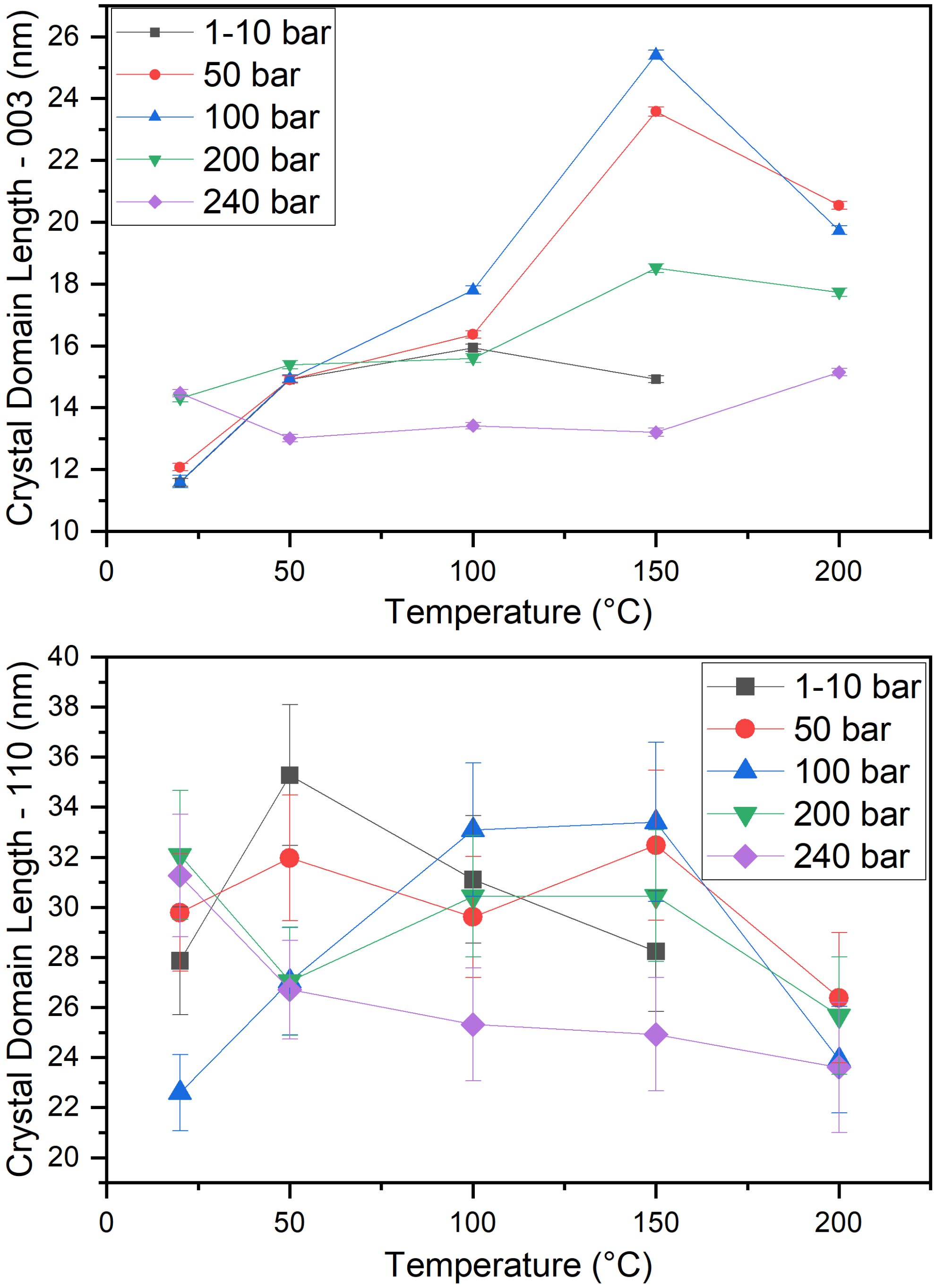

Figure 4.3. Changes in CDL of 003 (top) and 110 (bottom) planes for Co_2Al-CO_3 at varying synthesis temperature and pressure

4.3.2. Thermogravimetric Analysis (TGA)

Thermogravimetric analysis revealed three distinct regions of mass loss for all Co_2Al-CO_3, regardless of synthesis conditions (Figure 4.4). During the first mass loss stage a 3 % mass loss was observed below 150 °C. The second mass loss stage occurred between 160 - 210 °C with a total mass loss of 12 %, while the third mass loss stage occurred between 220 – 300 °C with a total mass loss of around 18 %. There did not appear to be any changes to either the intensity of onset of these mass loss stages, suggesting neither temperature nor pressure impacted the thermal stability of Co_2Al-CO_3 LDHs. Generally, LDHs exhibit three distinct regions of mass loss: [87]

- Stage 1: Evaporation of surface bound water
- Stage 2: Dehydroxylation of brucite sheets.
- Stage 3: Breakdown of the layered structure and evolution of interlayer anion.

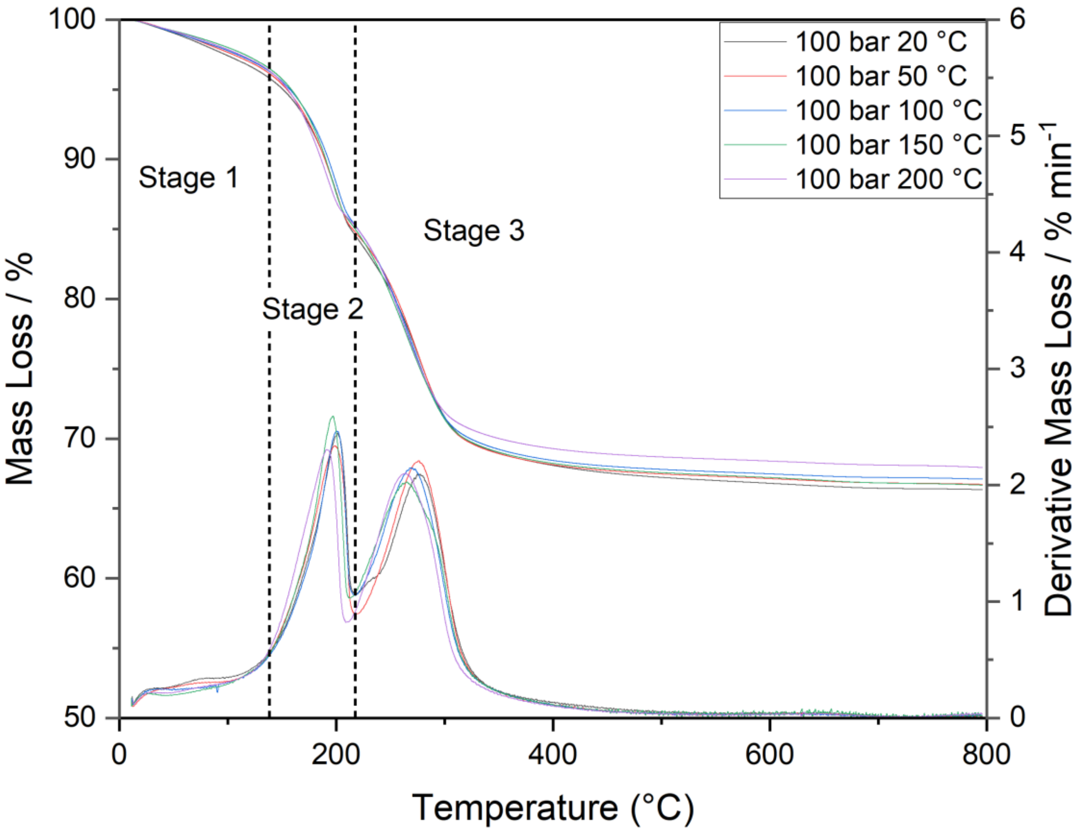

Figure 4.4. Thermogravimetric analysis of Co_2Al-CO_3 LDHs synthesised at 100 bar and varying temperature

To corroborate this, TGA-MS analysis was conducted to investigate the volatile components produced during each mass loss stage. From Figure 4.5 it can be seen that the mass loss observed in the 2nd stage is predominantly associated with a *m/z* 18 signal, suggesting evaporation of surface bound water. During the 3rd stage of mass loss a variety of signals are observed at different m/z values indicating evolution of OH^-, H_2O, NO^- and CO_2. This explains why only two regions of mass loss are observed. Not only does dehydroxylation of the brucite layers occur, as evidenced by loss of H_2O and OH^- ions, but also a breakdown of the layered structure and evolution of the carbonate interlayer. Interestingly, the presence of NO^- volatiles in this second mass loss stage suggests that the interlayer comprises not just of carbonate ions, but also of nitrate ions present from the nitrate salt precursors. This mass loss profile may explain why a reduction in CDL (003 and 110) occurs at higher synthesis temperatures (200 °C). At this temperature breakdown of the layered structure starts to become favourable and competes with crystal growth.

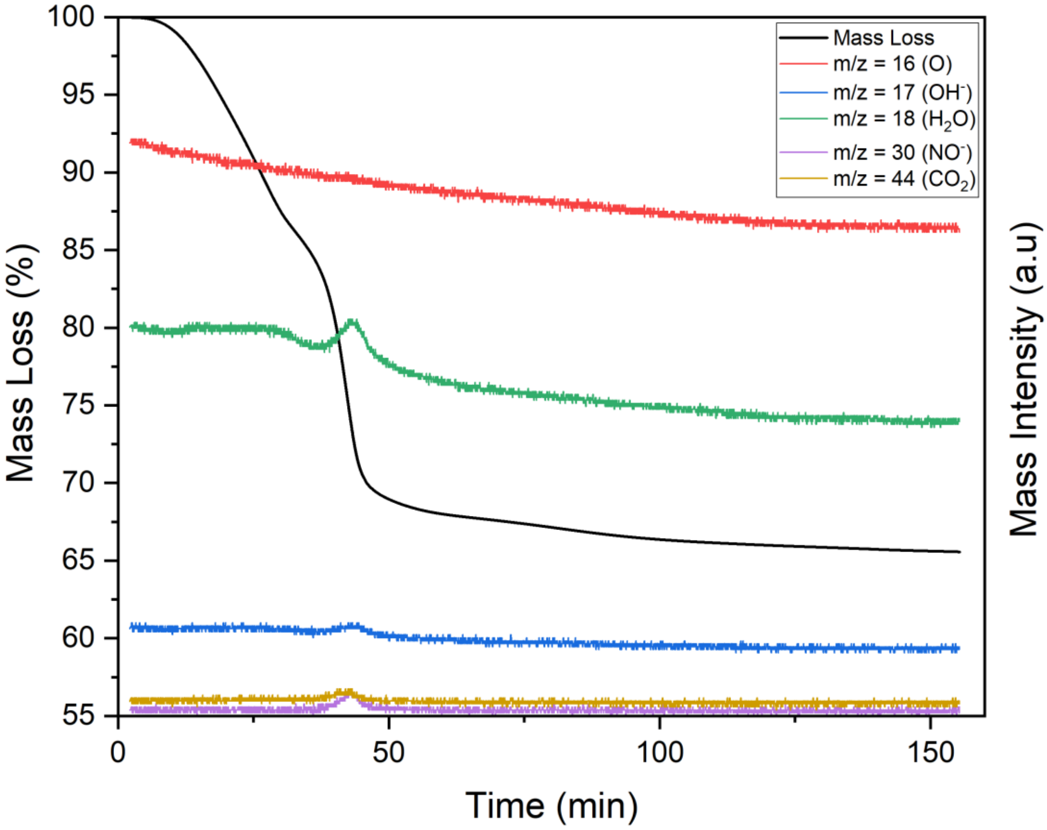

Figure 4.5. TGA-MS analysis of Co_2Al-CO_3 synthesised at 100 bar, 100 °C

4.3.3. Transmission Electron Microscopy (TEM) Analysis

Morphological analysis via TEM (Figure 4.6) revealed the presence of hexagonal platelets, indicative of LDH formation. [208] In addition, platelets appeared to agglomerate together, with a significant degree of face-to-face stacking.

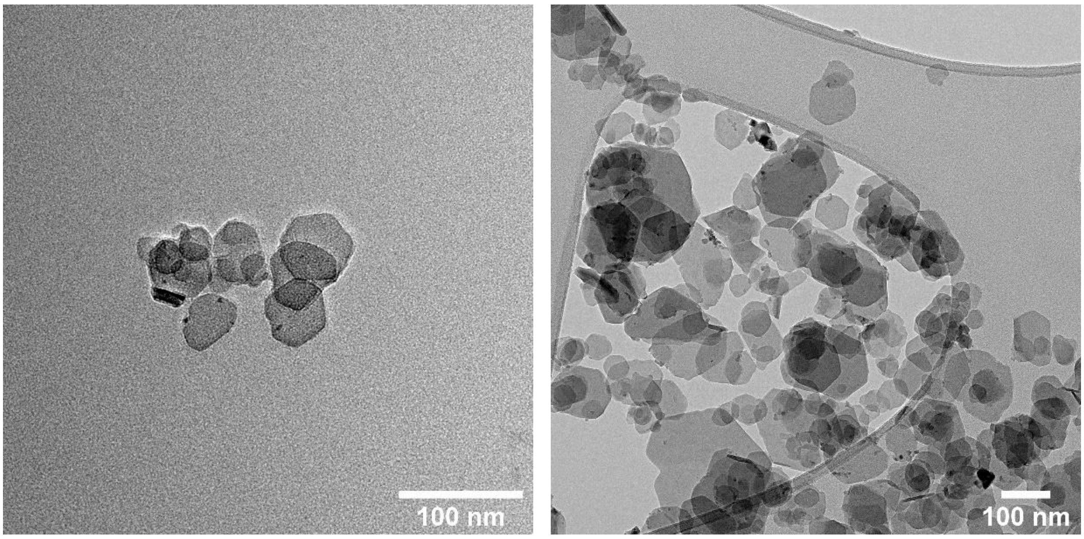

Figure 4.6. TEM of Co_2Al-CO_3 LDHs synthesised at 100 bar 20 °C (left) and 100 bar 150 °C (right)

Particle size analysis revealed an increase in average diameter with increasing synthesis temperature, with the highest diameter observed for Co_2Al-CO_3 synthesised at 150 °C (Table 4.1). These observations can most likely be attributed to the temperature dependence on the kinetics of nucleation and crystal growth processes. [209] In addition to this, in Figure 4.7 it can be seen that larger particle sizes at high temperature (above 100 °C) also resulted in a larger distribution, ranging from 5 – 200nm. In comparison, LDHs synthesised at 20 °C and 50 °C respectively had a narrower distribution of particle sizes, ranging from 5 – 125 nm. This is thought to be due to Ostwald Ripening being more favourable at higher temperatures, resulting in smaller particles being more readily dissolved and deposited onto larger particles. [210] For all LDHs platelets observed in TEM appeared to be larger than CDL's calculated from XRD suggesting some disruptions within the long range order occur. [95]

Table 4.1. A comparison of average particle diameter (TEM) and crystal domain length (CDL)

Synthesis Pressure / bar	Synthesis Temperature / °C	Average Particle Diameter / nm	Crystal Domain Length (110) / nm
100	20	40.0 ± 2.7	22.6 ± 1.5
100	50	43.1 ± 2.8	27.0 ± 2.1
100	100	65.6 ± 3.9	33.1 ± 2.7
100	150	73.9 ± 5.4	33.4 ± 3.2
100	200	70.7 ± 4.2	23.9 ± 2.1
10	150	41.1 ± 2.4	28.3 ± 2.4
50	150	78.7 ± 5.1	32.5 ± 3.0
100	150	73.9 ± 5.4	33.4 ± 3.2
200	150	59.7 ± 3.6	30.5 ± 2.6
240	150	39.3 ± 2.6	24.9 ± 2.3

Changing synthesis pressure also appeared to have an impact on both crystal size and homogeneity. LDHs synthesised at 50 and 100 bar appeared to produce the largest platelets, with an average particle diameter over 70 nm. In contrast LDHs produced at both low and high pressure (10 and 240 bar) produced the smallest platelets, averaging 40 nm respectively. In addition, these conditions also produced more homogeneous particle sizes, with a range of 5 – 125 nm. While no direct correlation could be observed with pressure and particle size/distribution, it was clear that smaller particles resulted in more homogeneous particle size distributions. From this it should be evident that both pressure and temperature can be used to control both the size and homogeneity of $Co_2Al\text{-}CO_3$. Low temperatures at 10 and 240 bar are optimal for platelet homogeneity, whereas high temperatures at 50-200 bar favour's larger platelets.

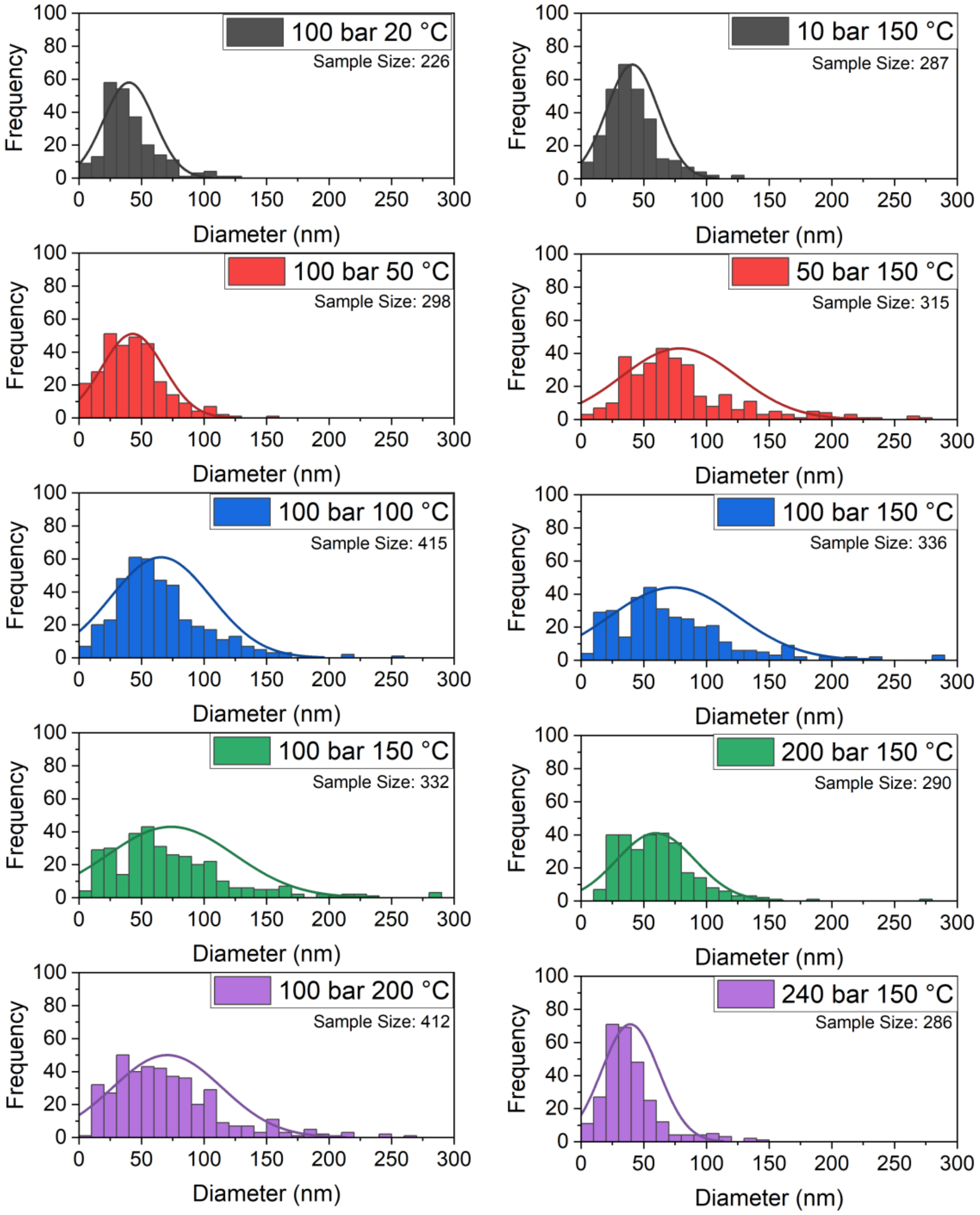

Figure 4.7. The impact of synthesis temperature (left) and pressure (right) on particle diameter distribution

4.3.4. Surface Area and Isotherm Analysis (BET)

Surface area analysis of Co_2Al-CO_3 LDHs most resembled a Type IVa Isotherm, suggesting the presence of mesopores (Figure 4.8). [186] Much like Type II isotherms, the sharp knee at low relative pressures (P/P_0) indicates near complete filling of the monolayer, which is followed by condensation of gas onto mesopore walls. [186,187] The hysteresis most resembles H2 hysteresis due to the well-defined plateau at high P/P_0. [211] While surface areas were relatively low compared to other sorbents, between 39 – 70 $m^2\,g^{-1}$ (Table 4.2), these were in line with surface areas of CoAl-LDHs reported in literature. [212] A general reduction in surface area was observed with increasing temperature, while a U-shaped trend was observed with pressure – where the highest surface areas were observed at low (10-20 bar) and high (240 bar) pressures.

Table 4.2. The impact of synthesis temperature and pressure on surface area

Synthesis Pressure / bar	Synthesis Temperature / °C	BET Surface Area / $m^2\,g^{-1}$
100	20	56.1 ± 0.6
100	50	59.1 ± 0.6
100	100	48.0 ± 0.5
100	150	39.3 ± 0.4
100	200	43.9 ± 0.5
10	150	67.1 ± 0.7
50	150	44.9 ± 0.5
100	150	39.3 ± 0.4
200	150	48.0 ± 0.5
240	150	66.3 ± 0.7

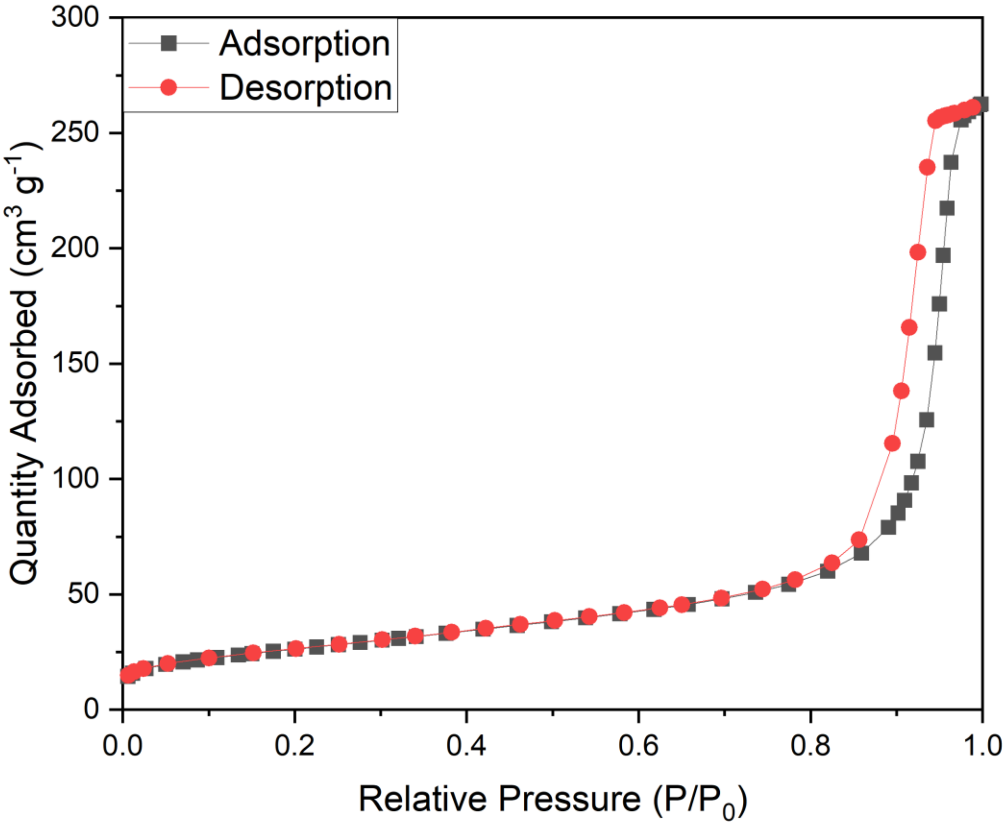

Figure 4.8. Nitrogen adsorption isotherm of $Co_2Al\text{-}CO_3$ LDH synthesised at 100 bar 20 °C

Interestingly there was an inverse correlation between the SSA and the CDL in the 003 plane (Figure 4.9-Figure 4.10) As previously mentioned the 003 plane is indicative of the distance between brucite sheets, and thus an increasing CDL (003) suggests an increased amount of face-face platelet stacking. The correlation observed is therefore rather intuitive; as the amount of face-face platelet stacking increases less of the individual platelets surface is exposed, resulting in a lower SSA.

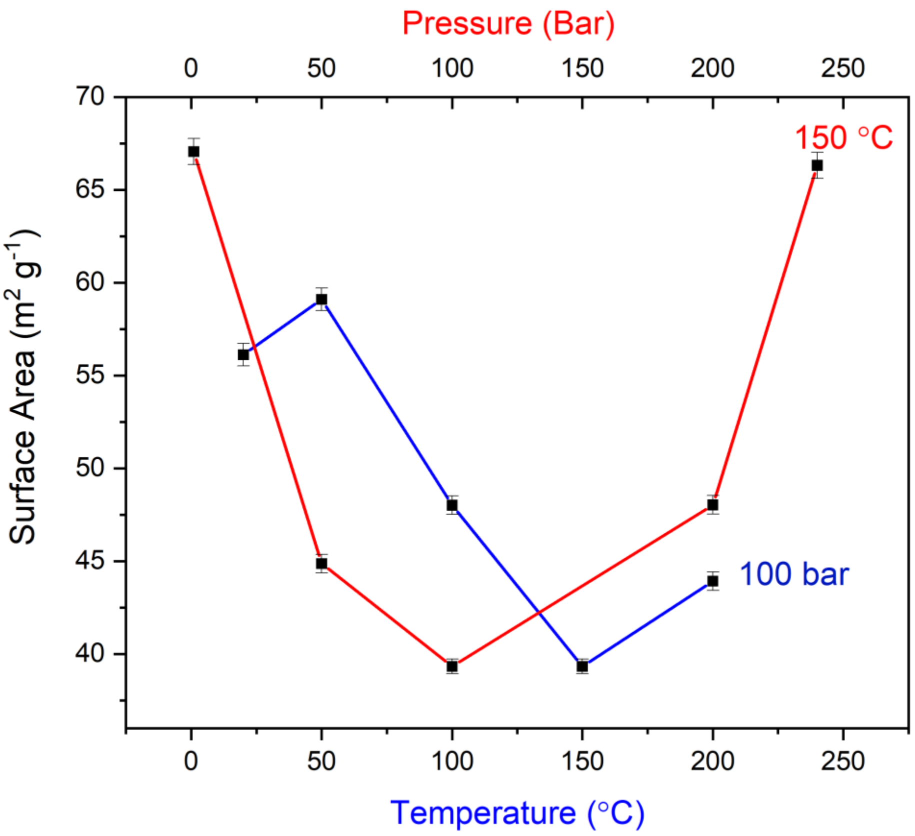

Figure 4.9. Comparison of specific surface area (SSA) with synthesis temperature and pressure

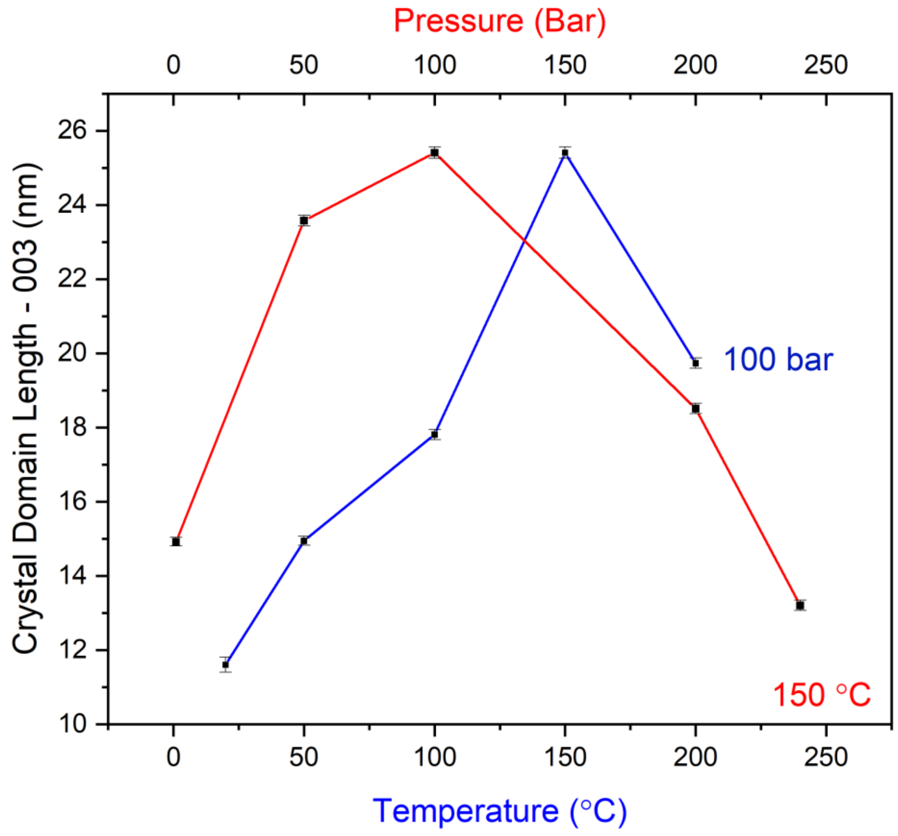

Figure 4.10. Comparison of crystal domain length (CDL) in the 003 plane with synthesis temperature and pressure

4.3.5. Yields and Repeatability

Analysis of product yields revealed considerable fluctuations at different synthesis conditions (Figure 4.11). Yield fluctuated from 47 – 76 % with no discernible correlation with either synthesis temperature or pressure. The only trend that was observed at different pressures was a 5-10 % decrease in yield as synthesis temperature was increased from 150 to 200 °C, due to the tendency for Co_2Al-CO_3 LDHs to breakdown and dissociate at high temperature.

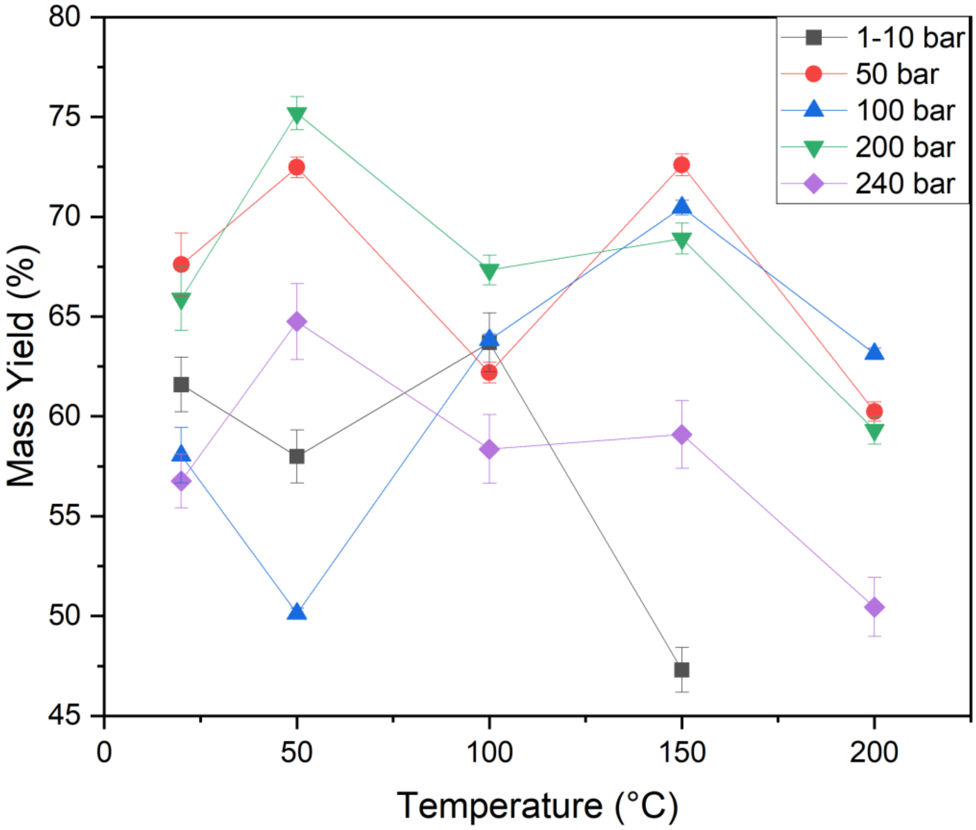

Figure 4.11. Comparison of product yield with synthesis temperature and pressure

To determine whether or not low yields were as a result of unreacted precursors the synthesis of Co_2Al-CO_3 (100 °C, 100 bar) was repeated and the waste product after centrifugation collected and dried. XRD analysis of this solid waste product and comparison to ICSD structures, revealed it to contain reflections consistent with the formation of sodium nitrate, a biproduct of LDH synthesis (Figure 4.12). In addition, other minor peaks of low intensity were observed over the 2θ range of 20-50 °, suggesting the presence of unreacted precursors in small quantities. It is thought that the very low intense and broad peak observed at 12-15 ° is due to residual LDH. This could be because of either insufficient centrifugation or low quantities of unreacted precursors still reacting.

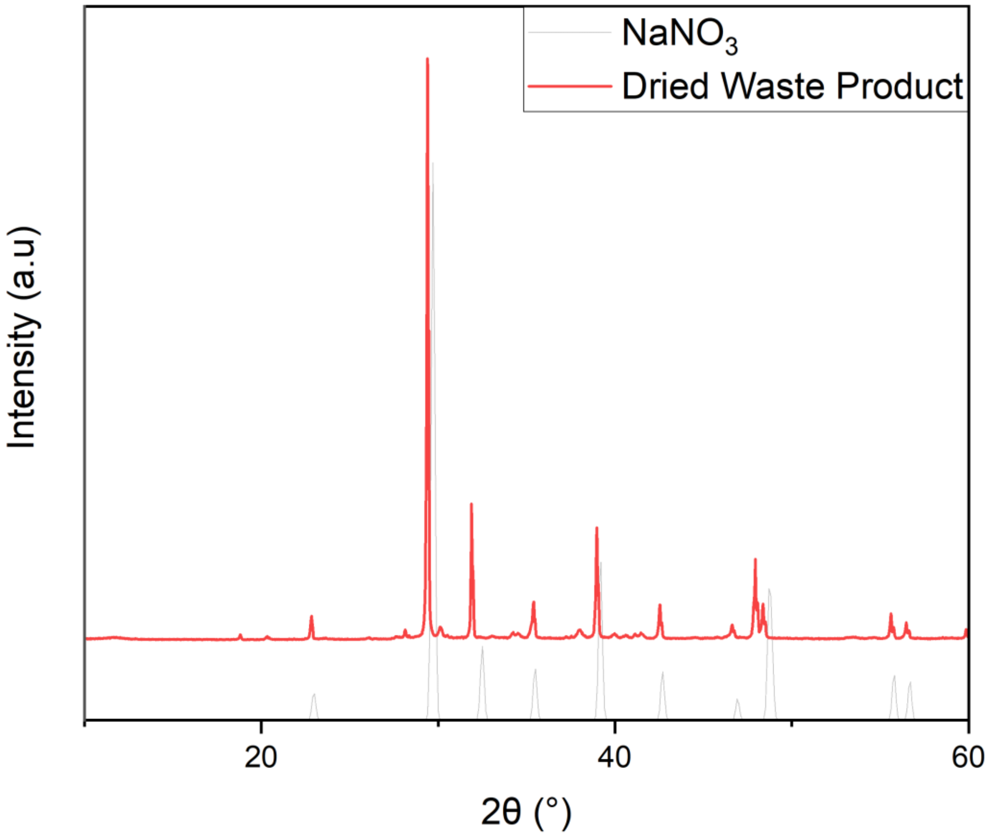

Figure 4.12. XRD analysis of dried waste product from Co_2Al-CO_3 synthesis (100 °C, 100 bar)

ICP was conducted on the solid waste product to check this hypothesis (Table 4.3). Over 35 % of the total mass comprised of Sodium, as expected from the notable presence of $NaNO_3$ in XRD. Both Cobalt and Aluminium were present at quantities of 0.8 and 1.1 % respectively confirming the presence of residual precursors/LDH. The other ~62 % of mass unaccounted for in ICP analysis can most likely be attributed to the anionic portion of metal salts that would have crystallised upon drying, such as hydroxide (OH^-) and nitrate (NO_3^-). It can therefore be concluded that, while some precursors remain unreacted after flowing through the CFHS rig, it cannot be the sole reason for reduced yields as evidenced by the low concentration of Co and Al in the waste product. It is therefore reasonable to assume that considerable amounts of LDH product are lost either during the work up processes (weighing, grinding, transferal and centrifugation) or within the rig. It is likely that, due to the turbulent mixing of the two aqueous streams within the reactor, some LDH particles may have accumulated on reactor walls resulting in further particle growth. [213] Previous analysis of residence time distributions for nanoparticle synthesis by continuous hydrothermal synthesis has shown that the presence of temperature gradients in specific areas of the reactor can result in the formation of "dead volumes". [133] These "dead volumes" within the reactor can, not only result in uncontrolled growth of nanoparticles, but also result in the formation of eddies that greatly increase residence time of the fluid trapped in these areas. It is therefore possible that any LDH nanoparticles that have nucleated within these regions of the reactor may exit when product collection has concluded. This was something regularly observed after finishing a run – despite a total residence time of around 5-6 minutes within the rig, product (in the form of a cloudy precipitate) would often be observed for up to 10-15 minutes after the pumps were swapped from precursor to DI water for washing.

Table 4.3. Metal content of solid waste product from ICP

	% of Total Mass	**Moles / mol**
Co	0.8	1×10^{-4}
Al	1.1	4×10^{-4}
Na	35.9	1.5×10^{-2}

Following on from this analysis the natural question that arose was whether these dead volumes with uncontrollable crystal growth affect repeatability. As a result, four different synthesis conditions were repeated twice more to observe any changes in yield and/or crystallinity (Table 4.4). It was immediately evident that there were large deviations in % yield upon repeating runs. The standard deviation of yields for each synthesis condition fluctuated between 1.5 – 8.9. This was much larger than the errors in the individual measurements, which resulted in yield errors of at maximum 2-3 %, indicating external factors were causing additional uncertainty.

Table 4.4. Changes in product yield with repeated synthesis

Synthesis Conditions		**Product Yield / %**			**Standard Deviation**
Temperature / °C	**Pressure / Bar**	**Run #1**	**Run #2**	**Run #3**	
20	1	61.6 ± 2.2	67.9 ± 2.8	68.8 ± 2.9	3.9
50	50	72.5 ± 0.7	55.5 ± 0.9	61.8 ± 0.9	8.9
100	100	63.8 ± 0.5	60.8 ± 3.0	62.1 ± 2.2	1.5
200	200	59.3 ± 1.2	58.0 ± 2.3	67.1 ± 2.4	4.9

While this initially did not allow for a determination of the cause of the additional uncertainty, changes in relative peak intensity and height of reflections analogous to LDH formation were observed upon XRD analysis (Figure 4.13). CDL calculations (Table 4.5) again revealed deviations in crystal size in both the 003 plane (platelet stacking) and 110 plane (platelet growth). The standard deviation of the three repeated samples generally exceeded the error in individual samples that arose during gaussian peak fitting (Table 4.6), once again suggesting external factors were causing additional uncertainty in crystallite sizes. While other factors such as aging time are known to result in differences in crystallinity due to processes such as Ostwald ripening, work-up procedures were kept the same for purpose of these experiments, suggesting they were unlikely to be the cause. [214] As a result, these additional deviations were determined to be caused by phenomena (such as "dead volumes" discussed previously) occurring during the reactions within the rig.

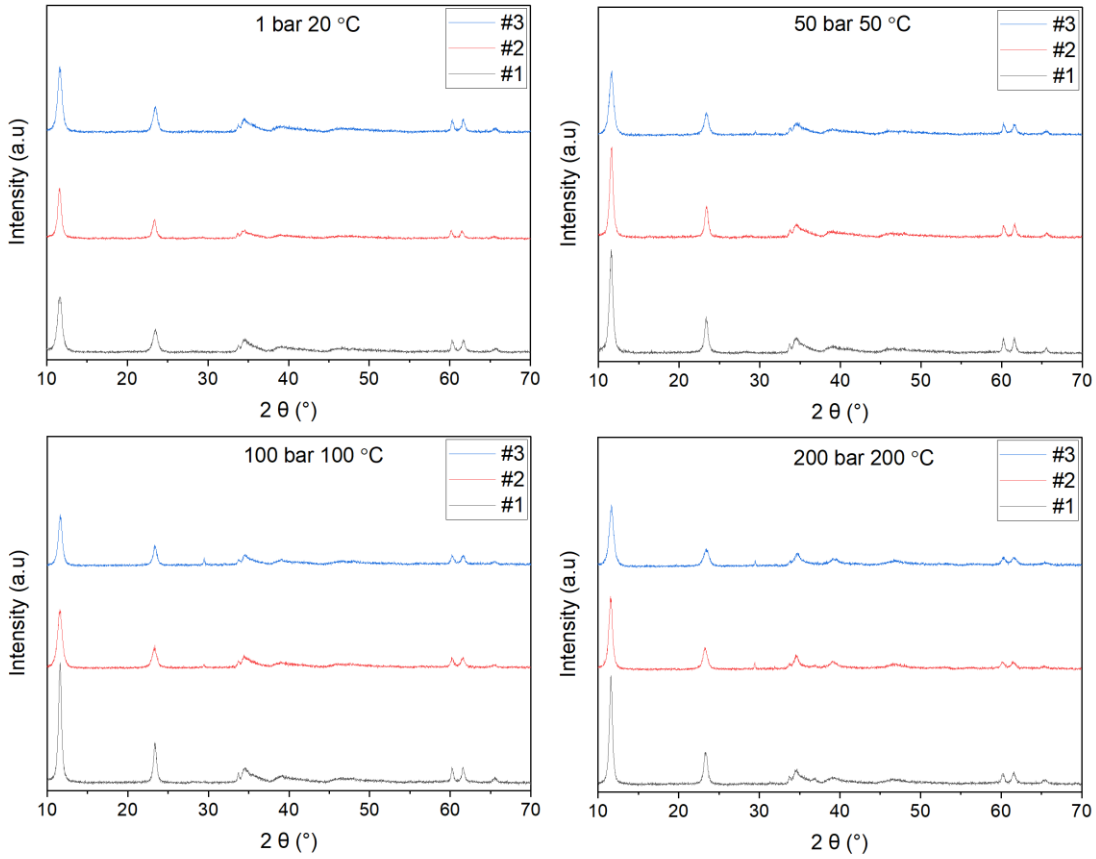

Figure 4.13. XRD graphs of repeated Co_2Al-CO_3 synthesis: 1 bar 20 C (top left), 50 bar 50 C (top right), 100 bar 100 C (bottom left) and 200 bar 200 C (bottom right)

Table 4.5. Crystal domain length calculations of repeated Co_2Al-CO_3 synthesis

Synthesis Conditions		Crystal Domain Length (003) / nm			Crystal Domain Length (110) / nm		
Temperature / °C	Pressure / Bar	#1	#2	#3	#1	#2	#3
20	1	11.58 ± 0.12	14.47 ± 0.12	12.08 ± 0.12	27.86 ± 2.16	30.95 ± 2.23	29.79 ± 2.35
50	50	14.91 ± 0.12	12.35 ± 0.12	9.27 ± 0.10	31.97 ± 2.51	21.42 ± 1.96	24.33 ± 2.08
100	100	17.81 ± 0.13	13.52 ± 0.12	11.04 ± 0.11	33.09 ± 2.67	23.18 ± 2.01	27.80 ± 2.22
200	200	17.71 ± 0.13	14.64 ± 0.12	11.33 ± 0.12	25.66 ± 2.23	20.30 ± 1.88	19.42 ± 1.90

Table 4.6. Standard deviation (CDL) of repeated Co_2Al-CO_3 synthesis

Synthesis Conditions		Standard Deviation (σ)	
Temperature / °C	Pressure / Bar	CDL (003) / nm	CDL (110) / nm
20	1	1.54	1.56
50	50	2.82	5.45
100	100	3.43	4.96
200	200	3.19	3.38

While these findings do not entirely diminish the temperature and pressure correlations discussed in Section 78, it does reduce the accuracy of the conclusions drawn. For example, when synthesised at a pressure of 100 bar a general increase in the CDL (003) was observed with temperature, increasing from 11.5 nm to 25 nm between 20 – 150 °C. While the variance in standard deviations reported ($\sigma = 1.5 - 3.4$) does not exceed this difference, there is a possibility that the magnitude of these temperature effects are either exaggerated or understated.

However, it should be noted that there were other unquantifiable rig factors that could also play a role in the repeatability of experiments. Initial synthesis experiments conducted at variable temperature and pressure were performed between January – March 2020. During this time the CFHS rig was operated solely for the synthesis of LDHs. The repeated synthesis experiments were performed at a later date, during the summer of 2021. By this time not only had the active users of the CFHS rig increased, but the rig was also being used for the synthesis of a variety of other nanomaterials including calcium apatite and titanium dioxide, alongside the conversion of biomass at supercritical conditions. While thorough cleaning is performed between runs, it is common for next users to observe contaminant product from the previous runs either before or during their subsequent run. From this it is evident that residual contaminant particles may have been present during repeatability rig experiments, which could result in changes in crystal nucleation and growth.

While no investigations of this were conducted during synthesis of Co_2Al-CO_3, evidence of this contamination has been observed in synthesis of other LDHs. Upon SEM analysis of Mg_2Al-CO_3 a large degree of small nanoparticles was observed, deposited on the surface of LDH (Appendix K). SEM-EDX analysis revealed high degrees of contaminant elements present such as Fe. Ti, Ba and Ce, which was attributed to Fe_3O_4, CeO_2 and $BaTiO_3$ (Appendix L). Further experimentation would therefore provide valuable insight on whether the repeatability issues discussed above are as a result of distributions in residence time due to dead spacing, or contaminant species from other nanoparticle syntheses. This could be performed through:

- Synthesis on a CFHS rig used solely for the purpose of LDH synthesis.
- Synthesis of Co_2Al-CO_3 on a CFHS rig made from transparent tubing such as PFA (While pressure and temperature ratings would be lower, any residual contaminants could be seen and removed prior to analysis).

4.3.6. Comparisons to Literature

Calcium-Aluminium,[30,138,180] Magnesium-Aluminium and Zinc-Aluminium based LDHs have all been synthesised in literature via the CFHS method. [30,138,180,194] Of these, the impact of synthesis parameters (temperature, pressure and pH) have been studied for Ca_2Al-NO_3 and Mg_3Al-CO_3 between 75-400 °C and 50-240 bar by Clark et al. [30] (Ca_2Al-NO_3) and Wang et al. [138] (Ca_2Al-NO_3 and Mg_3Al-CO_3).

Wang et al. reported that temperature had a greater impact on platelet size and morphology than pressure. While no changes were observed for the CDL (003) with temperature or pressure, it was reported that Mg_3Al-CO_3 nanoplatelets enlarged with increasing temperature, as evidenced by TEM imaging. This is similar to what is reported herein, whereby platelet diameter increased with temperature up to 150 °C. No direct correlation with temperature and platelet size was observed by Clark et al. Both Wang et al. and Clark et al. reported there to be a lower degree of tuneability in CDL at high temperatures for Ca_2Al-NO_3 and Mg_3Al-CO_3. This was thought to be due to low residence times and turbulent mixing within the reactor at these conditions. This is in direct contrast to what was observed with Co_2Al-CO_3 where a higher degree of tuneability was observed at high temperature for particle size and stacking. This was evidenced by both CDL (003) and particle size analysis in sections 4.3.1 and 4.3.3.

Interestingly there did appear to be correlation between the work herein and papers highlighting the impact of aging temperature on crystallinity of LDHs when synthesised via co-precipitation methods. Previous research highlighted that upon increasing the aging temperature of Mg_3Al-CO_3 LDH synthesis between 40 – 100 °C crystallite sizes increased in both the a and c direction. [101] This was confirmed by similar analyses to calculate CDL from the Full Width Half Maximum (FWHM) values of (003),(006) and (110) reflections. However higher errors were observed in the calculations of crystallite sizes from the (110) reflection due to the weaker intensity of the peak, an issue that was also discussed in Section 4.3.1.

One agreement in findings with CFHS based literature is that LDH synthesis is optimal at low temperatures. Both Clark et al. and Wang et al. reported the presence of impurities at high temperatures (200 and 400 °C), thought to be due to the presence of amorphous AlOOH and $Al(OH)_3$. Similar impurities were observed herein, alongside the presence of Cobalt Oxide in XRD spectra. Wang et al. also concluded that reduction in platelet growth and irregularity at high temperatures was due to the decomposition and dissociation of the LDH, which was evidenced to also be the case for $Co_2Al\text{-}CO_3$ through TGA-MS analysis (Section 4.2). This suggests that optimal conditions are for the most part dependent on the individual LDH being synthesised, suggesting no general method can be derived, although high temperatures above 200 °C should generally be avoided. Unfortunately, no comparisons could be made with surface area observations due to the low surface areas reported for $Ca_2Al\text{-}NO_3$ (<10 m^2 g^{-1}) and none reported for $Mg_3Al\text{-}CO_3$, although the work herein suggests there is a clear link between crystal growth and a reduction in surface area.

4.4. The Impact of NaOH Concentration

4.4.1. Changes in Physical Properties

XRD analysis (Figure 4.14) revealed the presence of intense symmetrical peaks at low 2θ angles, and broader asymmetrical peaks at higher 2θ angles, for all LDHs synthesised between 0.1 – 1 M NaOH. This indicated successful formation of LDH. Synthesis attempted at 0.05 M NaOH resulted in no product formation and as a result further analysis was concluded. Interestingly it appeared that increasing the amount of excess NaOH resulted in greater crystallinity of the product, as evidenced by the intensity of 003 and 006 peaks at 11° and 23° respectively. From CDL calculations it appeared that there was increased crystal growth for 0.2 – 1 M NaOH in both the 003 and 110 plane (Table 4.7), indicative of both increased crystal stacking and growth of individual platelets. Unfortunately, due to low peak intensity and overlap of 110 and 112 peaks, no CDL calculations could be performed on the LDH synthesised at 0.1 M NaOH. NaOH concentration did not appear to affect the interplanar distance (d_{003}) between brucite layers suggesting that carbonate anions do not change position or symmetry. No peaks correlating to impurities such as $Co(OH)_2$ or CoO were identified indicating hydrotalcite was the only crystalline phase formed at all NaOH concentrations.

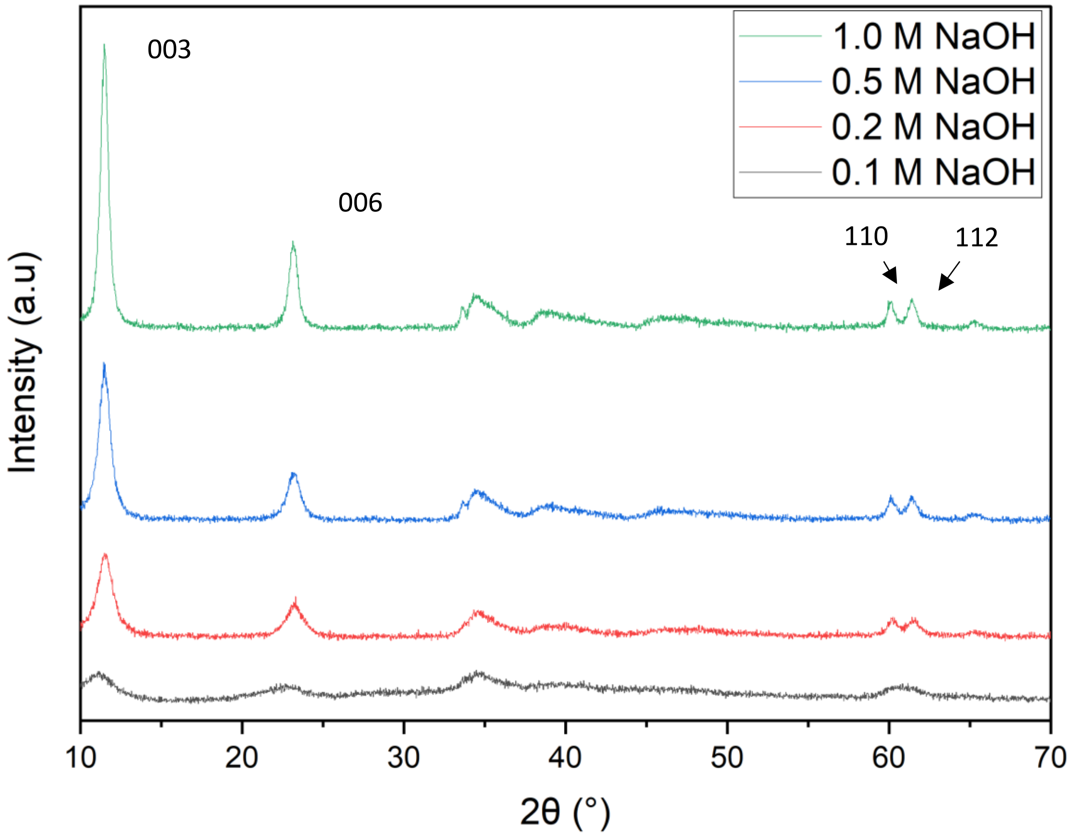

Figure 4.14. XRD patterns of samples prepared at varying initial NaOH concentrations.

Table 4.7. Crystal parameters of variable NaOH experiments

Initial NaOH Concentration / mol dm^{-3}	**D_{003} Spacing / nm**	**CDL_{003} / nm**	**CDL_{110} / nm**
0.05	No product Formation.		
0.10	Peak intensities too low.		
0.20	0.77	6.41 ± 0.09	14.89 ± 1.63
0.50	0.77	8.54 ± 0.08	17.04 ± 1.76
1.00	0.77	13.13 ± 0.09	21.50 ± 2.13

TGA analysis revealed no noteworthy differences between mass loss profiles of LDHs synthesised with varying NaOH concentrations (Figure 4.15). Like the variable synthesis temperature and pressure experiments, all LDHs exhibited three major mass loss stages between 140 – 220 °C and 220 – 330 °C respectively. The first mass loss stage was attributed to evaporation of surface bound water while the second mass loss stage was due to dehydroxylation, evolution of the interlayer and breakdown of the layered structure (Section 4.3.2). Total mass loss appeared to be between 32 – 33 % for all LDHs which is in agreement with TGA profiles of other CoAl based LDHs found in literature. [153] While there did appear to be some temperature differences in the onset of the two mass loss stages started (~10 – 20 °C), no discernible correlation could be deduced.

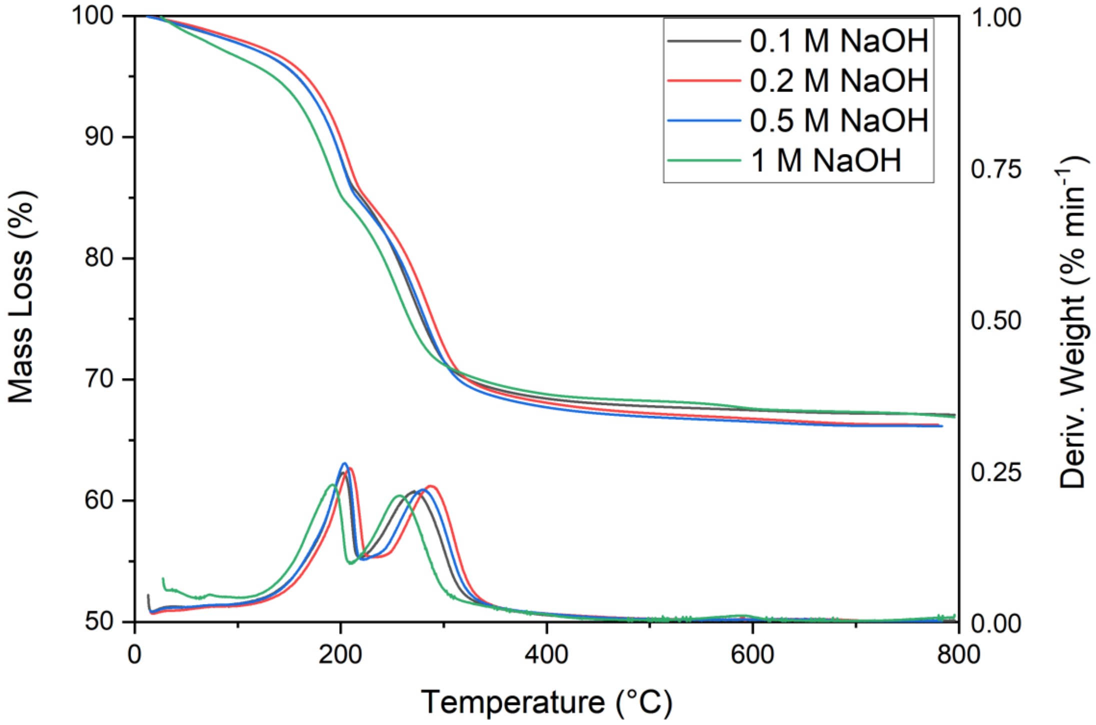

Figure 4.15. Thermogravimetric analysis of Co2Al-CO3 LDHs synthesised at varying NaOH concentration

All LDHs, synthesised at varying NaOH concentration (0.1 – 1 M) once again exhibited Type IVa isotherm behaviour with H1 hysteresis, according to IUPAC classifications (Figure 4.16-Figure 4.17). [186] This was evidenced by a saturation plateau at high relative pressure (P/P_0) indicating mesoporous nature. The initial knee indicates monolayer adsorption followed by subsequent condensation of gas in mesopores. For a solely mesoporous adsorbent the isotherm should remain completely horizontal over the upper range of 0.95 (P/P_0) due to complete filling of mesopores. [215] The presence of non-horizontal plateau regions suggests the presence of some macropores (50 – 100 nm in size) which were observed in pore size distribution analysis (onset Figure 4.16-Figure 4.17). As a result of the presence of macropores, which are incompletely filled at high P/P_0, total pore volume could not be evaluated.

BET surface area (Table 4.8) appeared to decrease with increasing NaOH concentration from 64.6 to 92.0 $m^2 g^{-1}$. This was once again attributed to a relationship with platelet stacking observed in Section 4.3. An increased amount of face-face platelet stacking observed with increasing NaOH concentration, as evidenced by increased CDL in the 003 plane, results in less exposed surface and a lower SSA. High C values observed (C > 100) indicate monolayer adsorption can be well defined and occurs on high energy surface sites. [186]

Table 4.8. The effect of NaOH concentration on surface area parameters

Synthesis NaOH Concentration / mol dm^{-3}	**BET Surface Area / $m^2 g^{-1}$**	**BET C value**	**CDL (003) / nm**
0.1	92.0 ± 1.1	117.8 ± 1.5	N/A
0.2	83.8 ± 1.1	202.3 ± 2.0	6.41 ± 0.09
0.5	70.8 ±1.1	109.9 ± 0.9	8.54 ± 0.08
1.0	64.6 ± 1.0	117.8 ± 1.5	13.13 ± 0.09

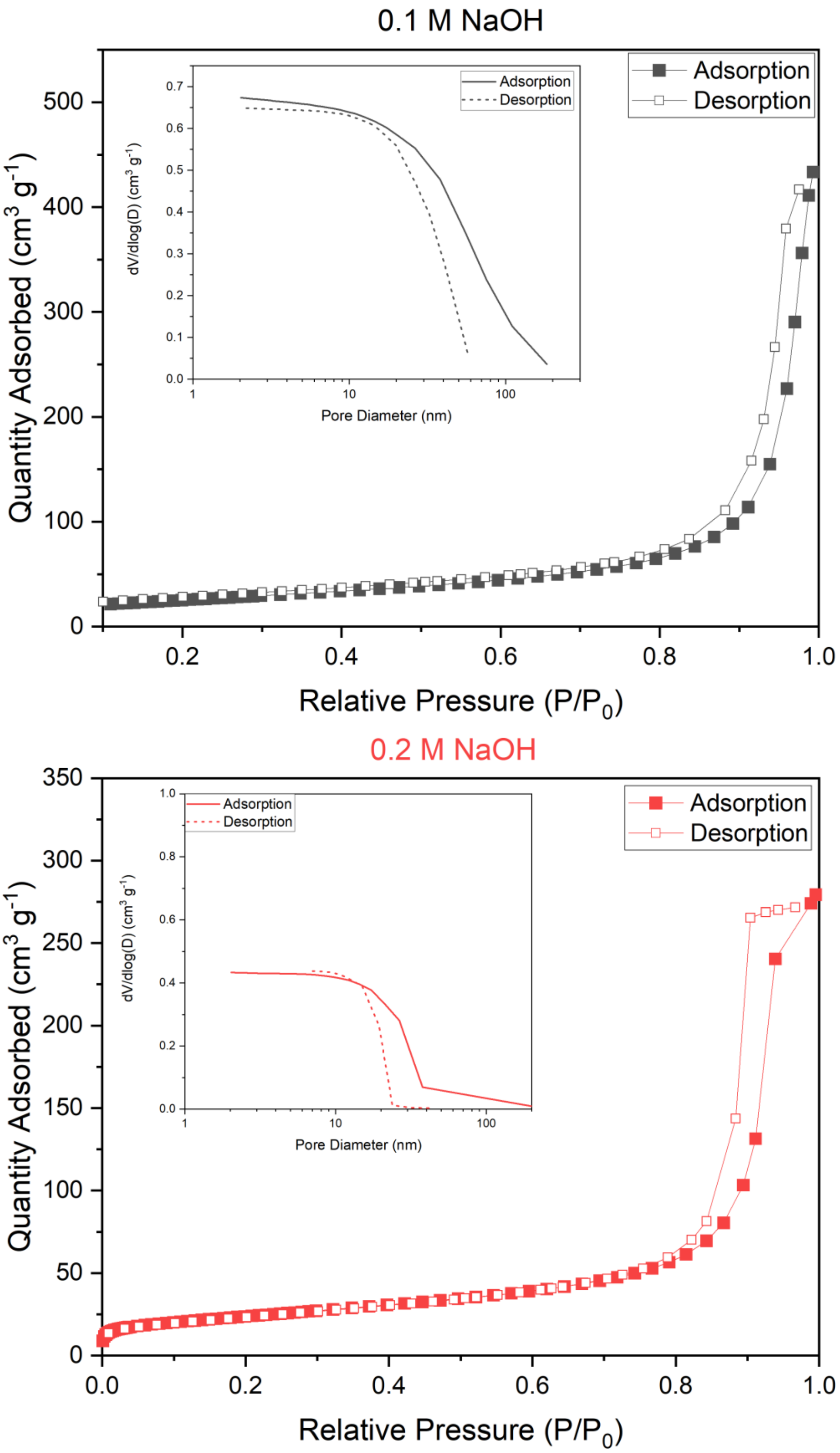

Figure 4.16. N_2 adsorption/desorption isotherm of Co_2Al-CO_3 and pore size distribution (inset): 0.1 M NaOH (top) and 0.2 M NaOH (bottom)

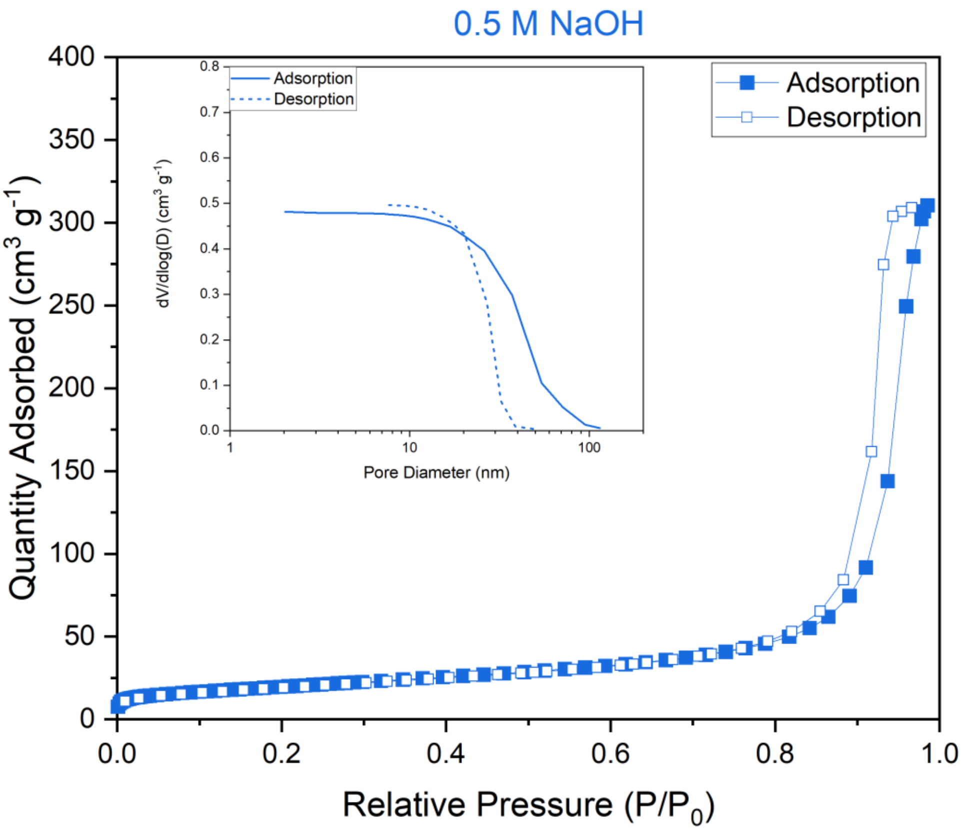
0.5 M NaOH

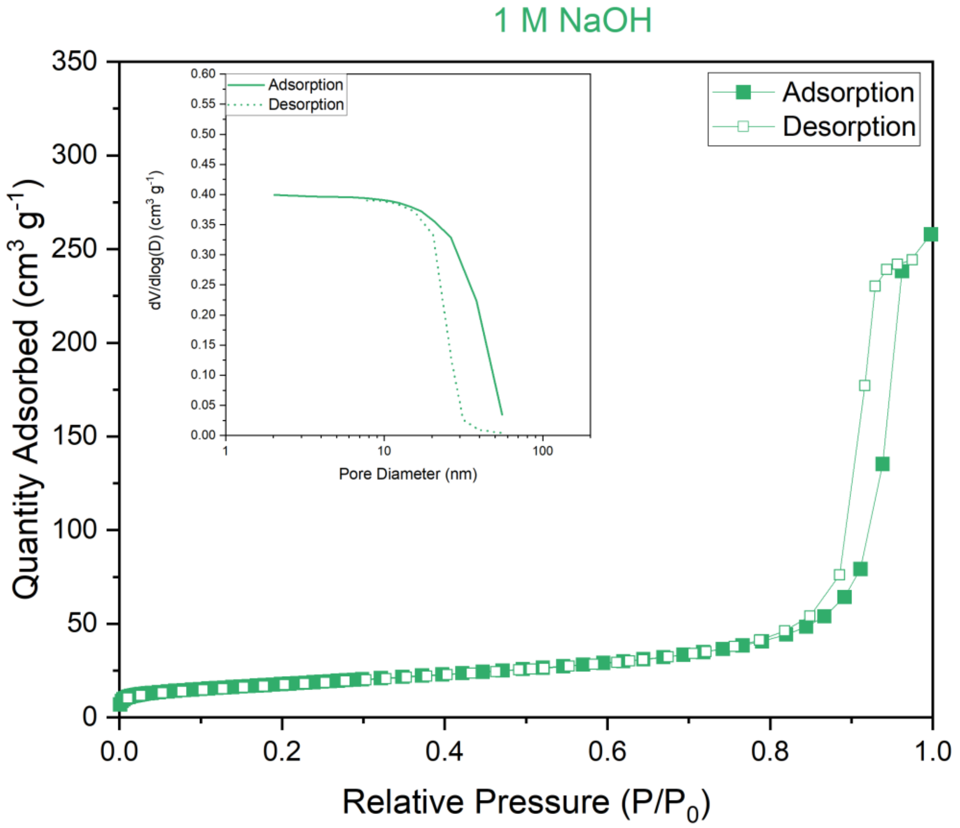
1 M NaOH

Figure 4.17. N_2 adsorption/desorption isotherm of Co_2Al-CO_3 and pore size distribution (inset): 0.1 M NaOH (top) and 0.2 M NaOH (bottom)

4.4.2. Further Comparisons to Literature

Interestingly these observations were in direct contrast with those by Clark et al. [208] Increasing the OH^- excess during Ca_2Al-NO_3 synthesis, not only resulted in lower crystallinity, but also resulted in the preferential formation of impurities such as $Ca(OH)_2$. This reduction in crystallinity corresponded with a reduction in the CDL (002), which was explained to be due to the inhibition of crystal growth in favour of nucleation. It was concluded that a NaOH concentration around stoichiometric was ideal for LDH formation. However a previous review highlighting the effect of alkaline solution concentration on LDH formation found that there did not appear to be any clear trend with the concentration of base solution. [216] While many of the papers reviewed also recommended a base solution containing a stoichiometric amount of NaOH, other papers (such as work highlighting the formation of CuZnAl-LDH) instead recommended an excess to ensure complete precipitation of metal ions occurred. [217] This lack of influence was interpreted to be due to resulting changes in pH which often occur when altering NaOH concentrations.

pH is known to play a vital role in not only the formation of hydrotalcite LDH phases, but also formation of other impurities such as hydroxides. It is generally agreed upon that basic conditions are required for hydrotalcite formation. [218] For example one author found that varying the reaction pH for the synthesis of ZnAl LDH by co-precipitation resulted in the formation of $Zn(OH)_2$ and $Al(OH)_3$ impurities at low pH (7-8). [219] At higher pH's (pH > 12) aluminium hydroxide dissolved to form sodium aluminates. Similar findings were also reported elsewhere, whereby in highly alkaline conditions (pH > 12) the redissolution of hydrotalcite resulted in ZnO formation. [220] Interestingly however it was also reported that the intensity of XRD reflections increased with pH up to 11.5-12 corresponding with increased crystallinity. pH domains where LDH formation is favourable, alongside their respective hydroxides, have been well reported in literature for many commonly used LDHs such as ZnAl, MgAl, NiAl and ZnCr however no such reports were found highlighting pH conditions optimal for the synthesis of Cobalt-Aluminium based LDHs. [221]

Upon increasing concentration of NaOH the initial reaction pH increased from 12.75 to a maximum of 13.75 (Table 4.9). It is therefore probable that increased crystal growth may instead be attributed to Co_2Al-CO_3 formation being more favourable at higher pH's. It is evident from previous research however that further pH increase may result in dissolution of hydrotalcite phases formed. Further experimentation, in the form of fixed-pH LDH synthesis, could therefore improve the understanding of the pH dependence on Cobalt-Aluminium LDH synthesis. Regardless of this, it was evident that optimal NaOH concentrations for LDH synthesis by CFHS is likely to vary depending on the choice of metal ions due to the subsequent impact it has on pH.

Table 4.9. NaOH concentration and resulting reaction pH

NaOH Concentration / mol dm^{-3}	**Reaction pH**
0.05	12.75
0.10	13.05
0.20	13.28
0.50	13.60
1.00	13.75

4.5. The Importance of Drying Method

As discussed previously the experimental method within this work was based on similar research conducted by Clark et al. to understand the role of synthesis conditions on Ca_2Al-NO_3 LDH production. [87] While in this paper oven drying was used post-synthesis, other papers reporting synthesis of LDHs by continuous hydrothermal method had dried samples via freeze-drying method. [194] The drying process is a critical step during LDH nanoparticle production and has been found to affect physicochemical properties of LDH. For example one author found that freeze drying increased the surface area of $MgAl-NO_3$ based LDHs from 39 m^2 g^{-1} to 154 m^2 g^{-1} when compared to conventional oven drying (100 °C). [222] In addition to increased surface area, it has been reported that freeze-drying results in a reduced crystallinity and lower particle size distribution of $MgAl-SO_4$ based LDHs. [223] This was attributed to exposure to additional stresses during the freezing, primary and secondary drying stages. During oven drying water exerts capillary forces upon walls during evaporation causing them to collapse. [224] As freeze drying involves sublimation of ice to water vapour these capillary forces do not occur. As a result of this, a brief study into the effect of freeze drying on Co_2Al-CO_3 LDH physical properties was conducted. Freeze drying and oven drying analysis was performed on Co_2Al-CO_3 synthesised at 100 bar 100 °C. Oven drying was performed at 80 °C overnight (12 h).

BET surface area analysis of the LDH revealed an increase in surface area from 55.6 m^2 g^{-1} to 78.5 m^2 g^{-1} when freeze dried, an increase of approximately 40 % (Table 4.10). This increase was of lower magnitude than other papers within literature, who reported increases in surface area of 300-400 %. [222,223] While BET Isotherms (Figure 4.18) exhibited Type II behaviour suggesting a non-porous or macroporous nature, [186] pore size distribution insets revealed a large distribution of pore sizes ranging from 2 – 140 nm suggesting a mixture of macro and mesoporosity.

Table 4.10. BET Surface area of oven dried and freeze dried Co_2Al-CO_3 LDH

Drying method	**Surface Area / m^2 g^{-1}**
Oven Drying	55.6 ± 0.6
Freeze-Drying	78.5 ± 0.8

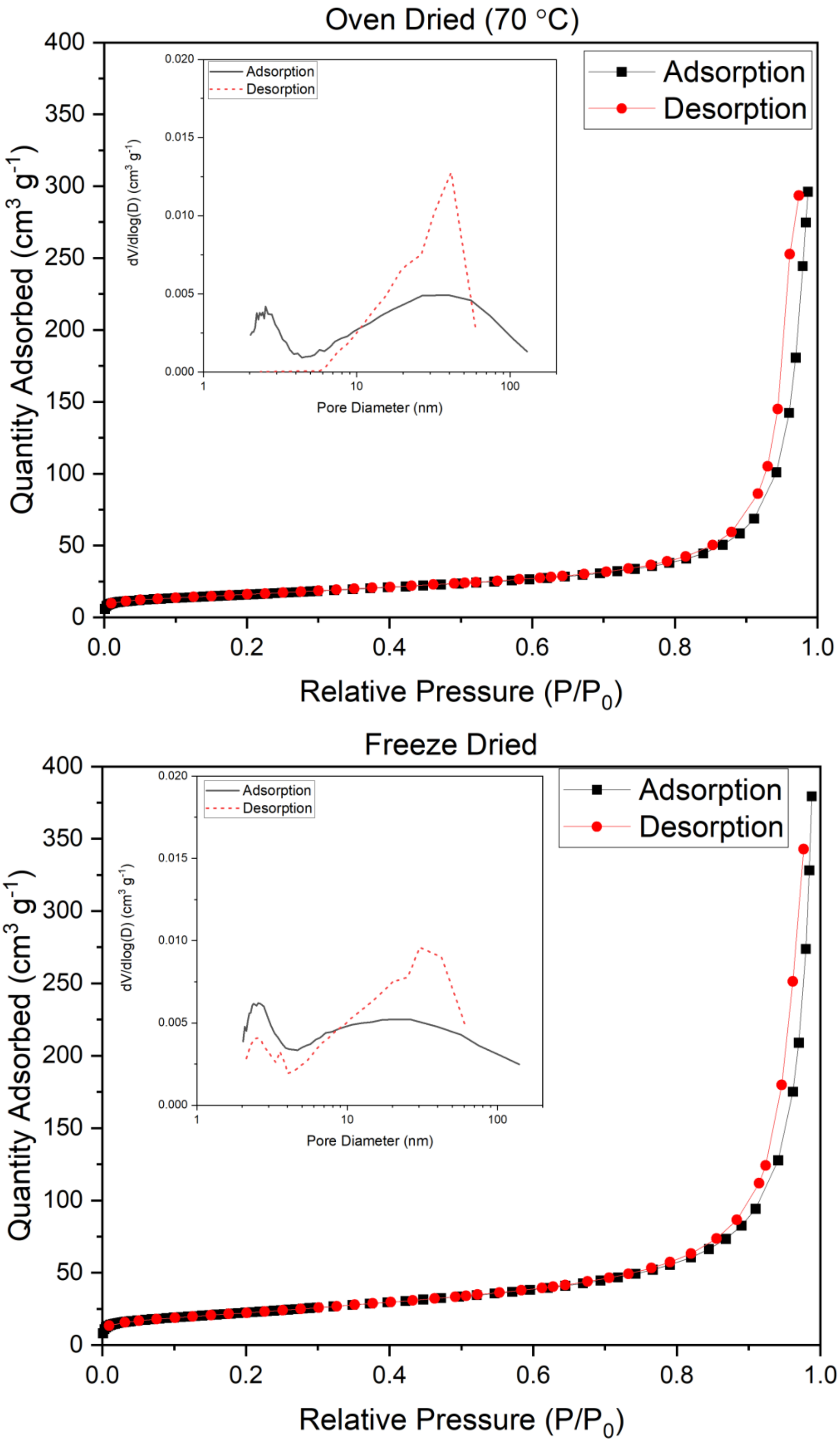

Figure 4.18. BET analysis of oven dried (top) and freeze dried (bottom) Co_2Al-CO_3 with pore size distribution (inset)

While in appearance freeze dried samples had a fluffier, less dense texture than its oven dried counterpart, there did not appear to be any observable changes in morphology in SEM analysis (Figure 4.19). Despite previous literature suggesting freeze dried LDH exhibited smaller and narrower particle size distributions (~200 nm) than the aggregates formed in oven drying, this did not appear to be the case. [223] Both oven dried and freeze dried samples exhibited large distribution of particles and agglomerates, 1 – 150 µm in size.

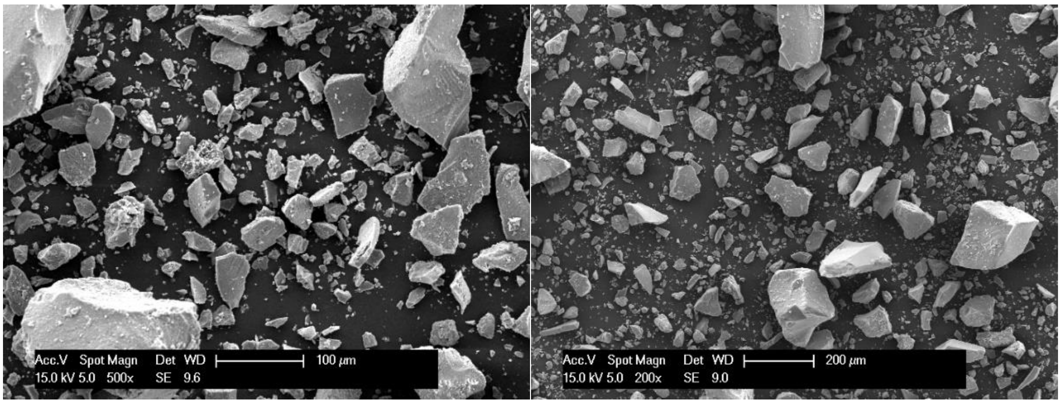

Figure 4.19. SEM image analysis of freeze dried (left) and oven dried (right) $Co_2Al\text{-}CO_3$ LDH

Similarly, XRD analysis showed minimal visual differences in the spectra of oven dried and freeze dried $Co_2Al\text{-}CO_3$ LDH (Figure 4.20). Both LDHs portrayed lattice parameters representative of $Co_2Al\text{-}CO_3$ LDH formation (a = 0.31 nm, c = 2.29 nm). [205] It was expected that the interplanar d-spacing between brucite sheets (d_{003}) may increase upon freeze drying due to the expansion of water within the interlayer, however this was not the case with both LDHs exhibiting d_{003} spacings of 0.77 nm (Table 4.11). There did appear to be some differences in crystallite sizes, as evidenced by CDL in both 003 and 110 lattice planes, however these were minor.

Table 4.11. Crystal parameters of oven dried and freeze dried $Co_2Al\text{-}CO_3$ LDH

Drying Method	**Lattice Parameters**		**D_{003} Spacing / nm**	**Crystal Domain Length (CDL)**	
	a / nm	**c / nm**		**CDL_{003} / nm**	**CDL_{110} / nm**
Oven drying	0.31	2.29	0.77	14.03 ± 0.10	21.71 ± 2.46
Freeze-drying	0.31	2.29	0.77	16.76 ± 0.15	23.71 ± 2.28

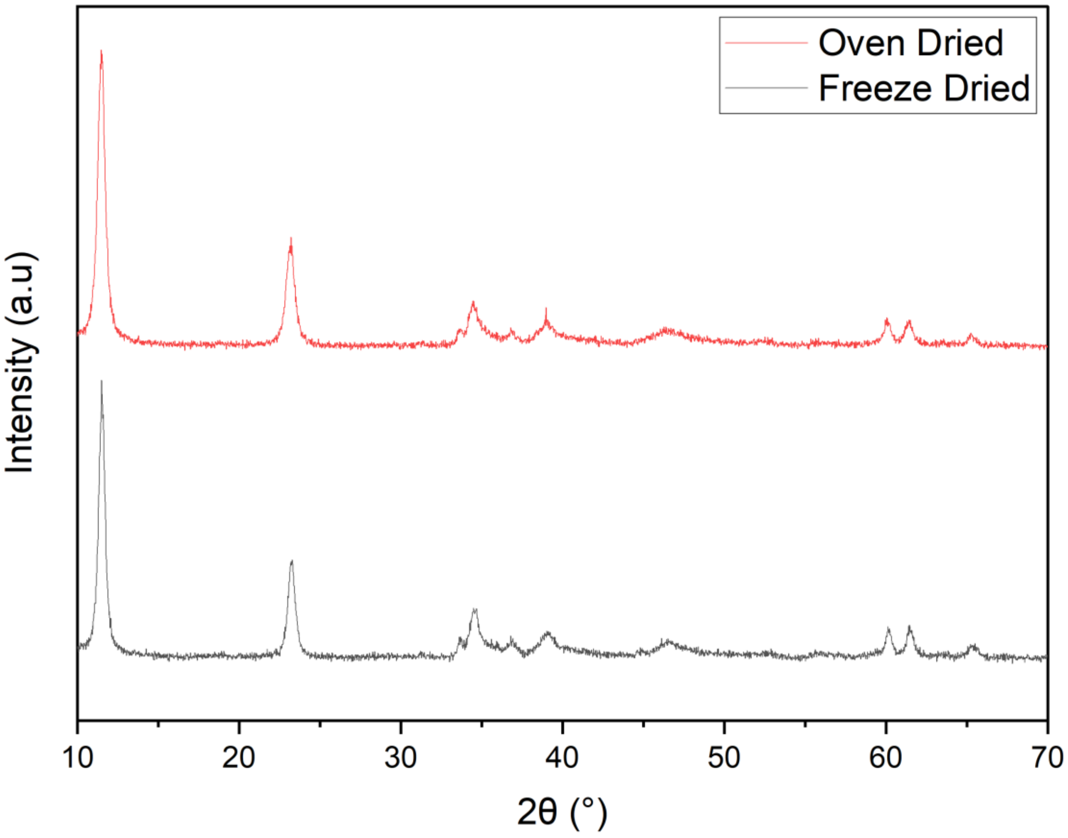

Figure 4.20. XRD spectra of oven dried and freeze dried Co_2Al-CO_3

While freeze drying may appear to be the preferable drying method for Co_2Al-CO_3, due to its higher surface areas and slighter crystallite sizes, when compared to other drying methods it has less industrial potential. Compared to oven drying freeze-drying exhibits lower throughputs and is a more expensive process due to higher investment, operation and maintenance costs. [225] While the benefits of freeze-drying in other industries may still outweigh these costs, such as in the food industry where it can aid in enhancing and/or maintaining flavour, [226] depending on application this may not be the case for Co_2Al-CO_3 LDH synthesis. In addition other drying methods including spray drying and supercritical drying have also been utilized during LDH preparation. [227] For example Olusegun et al. reported increased uptake of methylene blue dye onto calcined Co_2Fe-LDH using spray drying (compared to oven-drying), which was attributed to its higher SSA (138 $m^2\ g^{-1}$ compared to 47 $m^2\ g^{-1}$ for oven drying). [228] Further research on these drying methods during Co_2Al-CO_3 synthesis should be considered before any concrete conclusions about the optimal drying method can be made.

4.6. The Impact of Synthesis Temperature on Dye Adsorption

While learning how synthesis parameters impact LDH characteristics such as crystal size and surface area is of great importance for synthesis optimisation, learning how these changes affect subsequent application of LDHs is also required if they are to be used industrially. As a result, a brief kinetic study was conducted to determine the effect of synthesis temperature on adsorption of a commonly used dye in textile industries, Acid Orange 7. [20] Synthesis temperature was chosen due to the clear correlation between it and platelet stacking/surface area observed in XRD and BET.

4.6.1. Initial Experiments

As no previous literature could be found highlighting the use of $Co_2Al\text{-}CO_3$ for the adsorption of AO7 dye, before conducting experiments to determine the effect temperature had on adsorption, preliminary adsorption tests were conducted to determine if any adsorption occurred (Table 4.12).

Table 4.12. Preliminary adsorption analysis with AO7 dye

	Sorbent Loading / g L^1	**Initial dye concentration / mg L^{-1}**	**Adsorption time / h**	**AO7 Uptake / mg g^{-1}**
$Co_2Al\text{-}CO_3$ LDH	1	1500	24	20

After 24 hours, minimal uptake of AO7 dye was observed by the $Co_2Al\text{-}CO_3$ adsorbent. It is well known within literature that the interlayer anion plays a vital role in the ability of LDHs to adsorb dyes. Anions with higher valence and charge density tend to have an interfering effect and compete with dye molecules, resulting in little or no uptake. [229] Carbonate ions (CO_3^{2-}) are known to have a strong affinity with the hydrotalcite layers and it is therefore most likely the reason as to why no AO7 could be adsorbed. [230]

4.6.2. Calcination

As a result of this, calcined LDHs (CLDHs) were investigated as an alternative adsorption route. Upon heating LDHs to high temperature they can be converted to mixed metal oxides (MMO) by expulsion of the interlayer and oxidation of the brucite sheets. These MMOs possess a unique phenomenon known as the “memory effect” which allows them to reconstruct their initial LDH structure upon rehydration in an aqueous solution of anions. [20] This anionic solution does not need to contain the initial anion that formed the LDHs interlayer, and instead can be used as a mechanism to introduce a new anionic species, such as a contaminant dye, into the interlayer region.

The temperature of calcination is extremely important if a CLDH is to retain the ability to reconstruct their initial structure. Too low of a calcination temperature and the LDH structure will not be broken down, too high a temperature and spinel’s will form that cannot undergo rehydration. [9] As a result, calcination experiments were conducted between 100 – 500 °C to determine the optimal temperature for Co_2Al-CO_3 CLDH formation. From XRD analysis of Co_2Al-CO_3 CLDHs (Figure 4.21) it can be seen that the initial LDH structure is retained when calcined at 100 °C. Above this temperature (200 – 500 °C) reflections analogous to LDH can no longer be observed, in its place reflections associated with the formation of Co_3O_4 and thus the MMO occur. [231] Any Al_2O_3 present is assumed to be amorphous in nature. In addition, it can also be seen that with increasing calcination temperature, reflections associated to Co_2O_3 become more intense suggesting a greater degree of spinel formation.

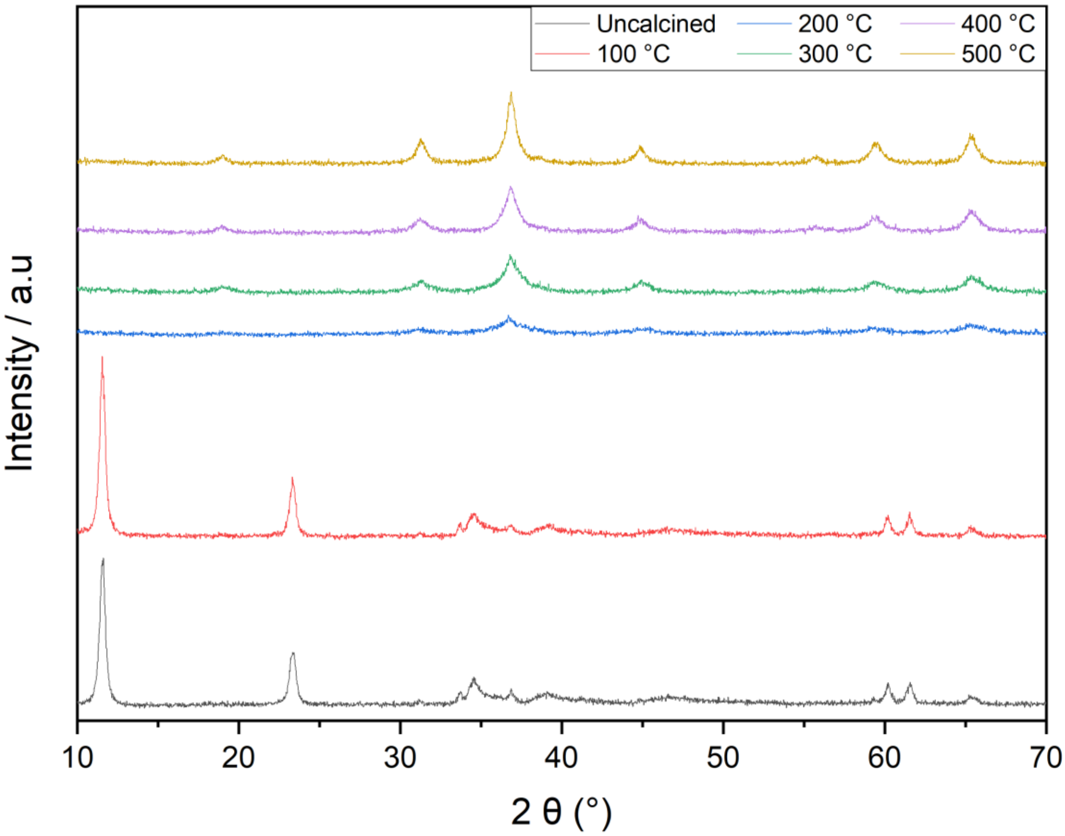

Figure 4.21. XRD analysis of Co_2Al-CO_3 LDHs calcined between 100 - 500 °C

Going forward with adsorption experiments, a calcination temperature of 200 °C was therefore used due to it being the lowest temperature at which LDH structure was observed to be broken down. XRD analysis revealed complete breakdown of the layered structure, as evidenced by the loss of intense symmetrical peaks at 11° and 23.5°, corresponding to Co_2Al-CO_3 formation (Figure 4.22). Reflections associated with Co_3O_4 were once again present between 10 – 60 °. While the broad peak at ~66 ° was not included in the reference Co_3O_4 material, this was still attributed to cobalt oxide formation due to the reference article only reporting peaks between 10 – 60 °. [231]

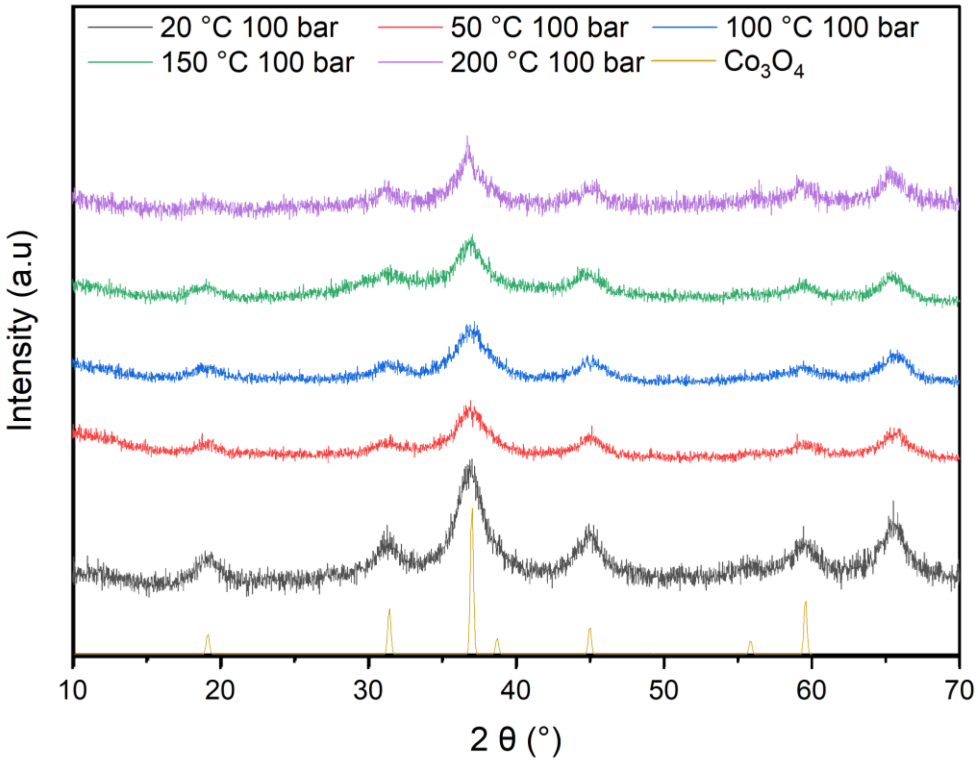

Figure 4.22. XRD analysis of Co_2Al-CO_3 LDHs calcined at 200 °C

One reason calcined LDHs are often attributed to having greater adsorption capabilities than uncalcined LDHs is due to their higher surface area. [34] BET measurements of Co_2Al-CO_3 CLDH's revealed a substantial increase in surface area compared to their uncalcined counterparts (Table 4.13). Prior to calcination surface area remained between 39 – 60 m^2 g^{-1}, compared with 180 – 192 m^2 g^{-1} afterwards. Interestingly there did not appear to be any correlation between uncalcined and calcined surface areas, suggesting that any synthesis temperature effects on surface area were nullified upon calcination.

Table 4.13. BET Surface area measurements of calcined and uncalcined LDH

Synthesis Conditions		**Surface Area / m^2 g^{-1}**	
Temperature / °C	**Pressure / Bar**	**LDH (uncalcined)**	**CLDH (calcined)**
20	100	56.1 ± 0.6	184.1 ± 1.8
50	100	59.1 ± 0.6	180.5 ± 1.9
100	100	48.0 ± 0.5	186.2 ± 1.9
150	100	39.3 ± 0.4	182.4 ± 1.8
200	100	43.9 ± 0.5	192.0 ± 2.0

4.6.3. Kinetic Study

A kinetic study was conducted on CLDHs to determine any changes in AO7 dye uptake and the speed of uptake with changing synthesis temperature. Synthesis temperature was chosen as the main parameter due to its links with platelet growth/stacking and surface area discussed earlier in Section 4.3. In Figure 4.23 the kinetic plots of AO7 adsorption for oven-dried Co_2Al-CO_3 synthesised at varying temperatures (20 - 200 °C) can be seen. From the plots it is evident that the highest uptake after 96 h is observed for Co_2Al-CO_3 synthesised at a temperature of 50 °C (599 mg g^{-1}), which decreases inversely with temperature to a low of 270 mg g^{-1} at 200 °C. Interestingly, while these findings correlated once again with that of the BET surface areas and platelet stacking from XRD, the same conclusions could not be drawn. In section 4.3 it was discussed that platelet stacking becomes more favourable at higher synthesis temperature, resulting in lower surface areas. Upon calcination however the differences in surface area were nullified, with all LDHs exhibiting surface areas between 180 – 192 m^2 g^{-1}. Previous authors have suggested that pore size plays an important role in adsorption mechanisms, with diffusion channels at least three times the size of the sorbent molecule being most suitable for sorption. [142,232] Therefore if the pore structure is maintained upon calcination this may explain the differences observed. Unfortunately, full isotherms of calcined Co_2Al-CO_3 LDHs were not obtained so this could not be corroborated.

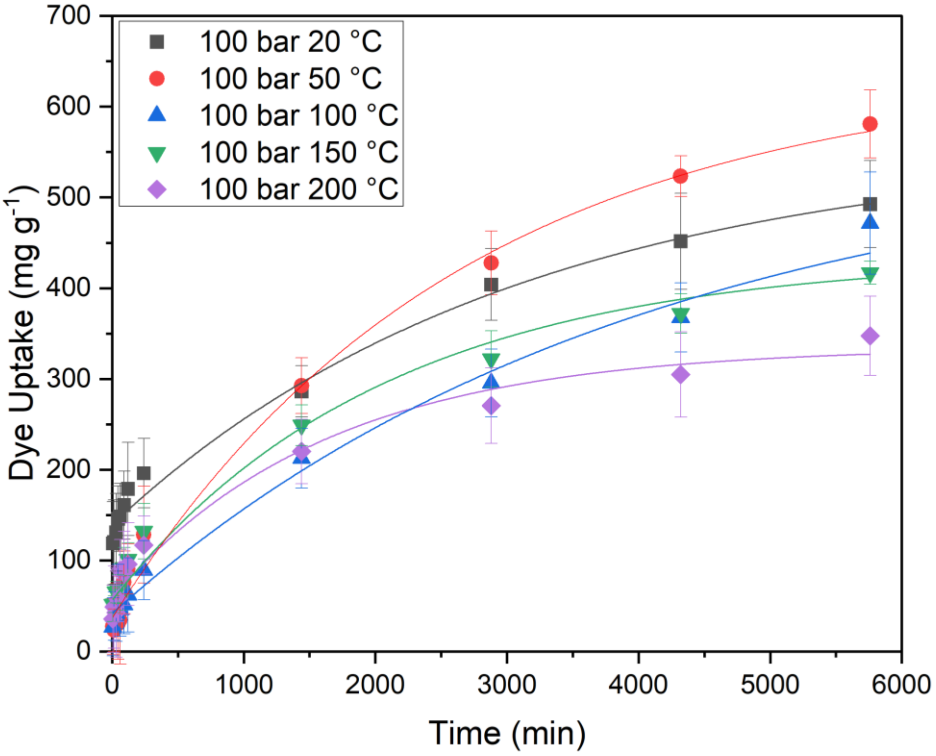

Figure 4.23. The effect of Co_2Al-CO_3 synthesis temperature on the adsorption of AO7 dye (C_0 = 1500 mg L^{-1}; V_{dye} = 250 mL; adsorbent dose = 1 g L^{-1}; T = 20 °C

From kinetic modelling (Table 4.14) it can be seen that generally the experimental data has a better fit with that of a pseudo 1st order model, as evidenced by the higher R^2 values and smaller deviations of $q_{e,exp}$ away from $q_{e,cal}$. However, there did also appear to be a good fit towards the pseudo 2nd order model, with R^2 values exceeding 0.9 at all temperatures. A reduction in $q_{e,cal}$ was also observed with increasing synthesis temperature for the pseudo 1st order model, however these $q_{e,cal}$ values did not match up as well for the pseudo 2nd order model. This is in disagreement with literature where the pseudo-second order model is commonly found to be a better fit for the adsorption of dyes onto LDHs due to the rate limiting step involving chemisorption processes such as chelation and/or complexation. [20] The 1st order model is generally associated with physisorption based mechanisms, with diffusion processes (such as external diffusion and intra-particle diffusion) being the rate limiting steps. [233] As the pseudo 1st order models often fit better during the initial stages of adsorption, compared with the entire period for pseudo 2nd order, it is possible that it is being favoured within this study due to a lack of equilibrium being reached within the system (as evidenced by adsorption uptake lacking a plateau region).

Table 4.14. Kinetic constant from pseudo-first and pseudo-second order model fitting for adsorption of AO7 onto Co_2Al-CO_3 LDHs

Sample		**$q_{e,exp}$ / mg g^{-1}**	**Pseudo 1st order**			**Pseudo 2nd order**		
Synthesis Pressure / bar	**Synthesis Temperature / °C**		**k_1 / min^{-1}**	**$q_{e,cal}$ / mg g^{-1}**	**R^2**	**k_2 / g mg^{-1} min^{-1}**	**$q_{e,cal}$ / mg g^{-1}**	**R^2**
100	20	556	3.25×10^{-4}	416	0.996	1.293×10^{-5}	442	0.976
100	50	639	3.77×10^{-4}	599	0.996	2.907×10^{-6}	556	0.948
100	100	562	2.31×10^{-4}	516	0.994	6.206×10^{-6}	370	0.951
100	150	434	4.16×10^{-4}	365	0.993	9.999×10^{-6}	370	0.980
100	200	335	5.11×10^{-4}	270	0.989	1.495×10^{5}	303	0.987

Table 4.15. Intra-particle diffusion model parameters and rate constants for adsorption of AO7 onto Co_2Al-CO_3 LDHs

Synthesis Temperature / °C	**K_{dA} (mg $h^{-1/2}$ g^{-1})**	**C_A (mg g^{-1})**	**$(R_A)^2$**	**K_{dB} (mg $h^{-1/2}$ g^{-1})**	**C_B (mg g^{-1})**	**$(R_B)^2$**
20	39.99	109.3	0.995			
50	61.07	-4.04	0.997			
100	44.27	6.49	0.991			
150	39.75	4.52	0.994			
200	50.87	20.85	0.898	28.79	67.17	0.992

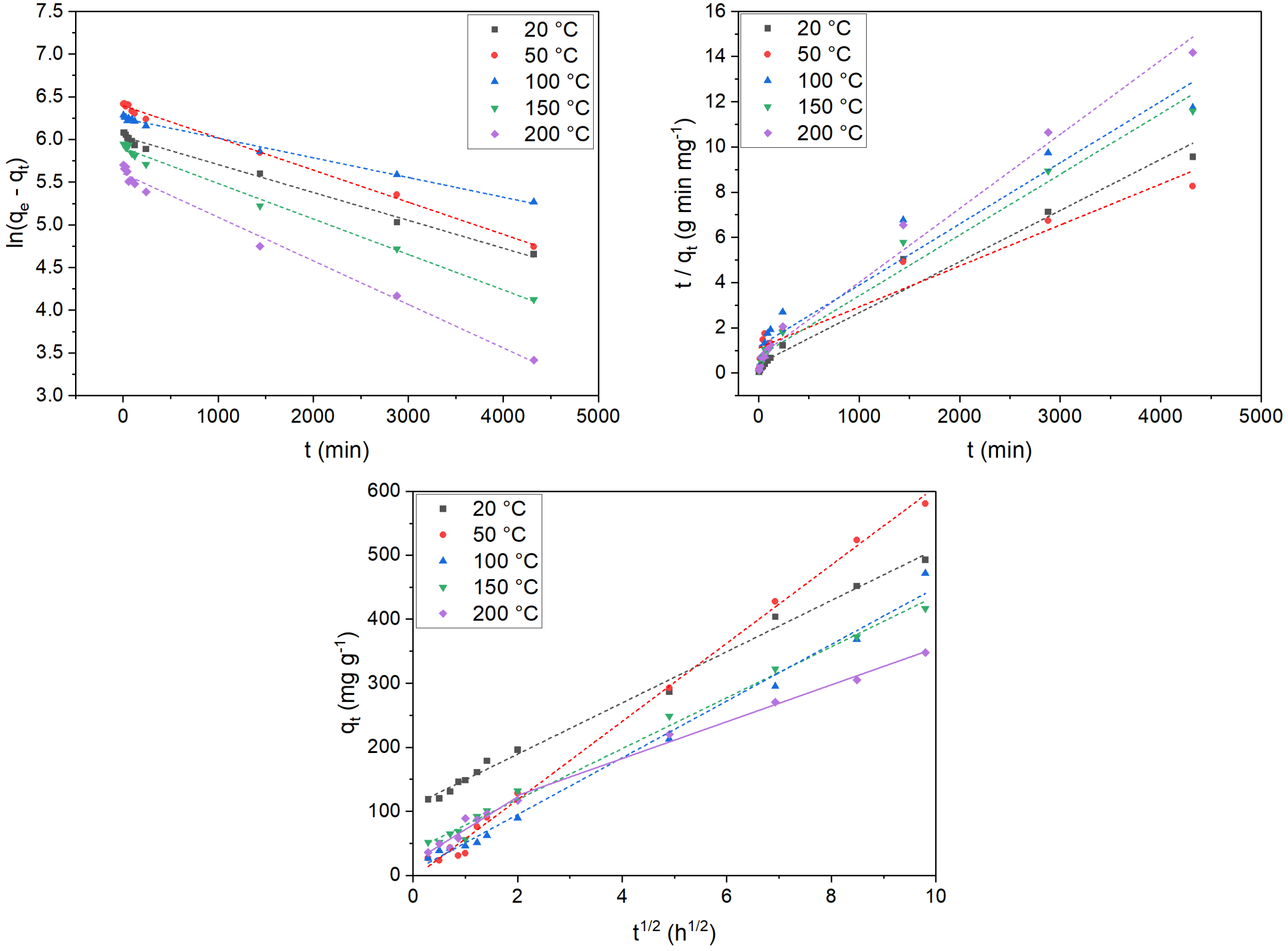

Figure 4.24. Kinetic models for the adsorption of AO7 dye at different synthesis temperatures: Linear pseudo 1st order (top left), linear pseudo 2nd order (top right) and intra-particle diffusion (bottom)

Upon observation of linear pseudo 1st and pseudo 2nd plots (Figure 4.24) it was apparent that the data had an inferior fit during the initial stages of adsorption, as evidenced by its non-linear nature. While this could be explained by the model favouring data points at the latter stages of the experiment (> 24 h), it was also hypothesised that it could be because of the rate determining step changing throughout the course of the kinetic experiment. As a result of this the intra-particle diffusion model was also applied to experimental data. This model, proposed by Weber and Morris, [199] describes a complex adsorption rate that is dependent on different factors:

A) Diffusion of the solute from the solution to the sorbent surface.

B) Diffusion from the surface to internal sites (such as the interlayer region).

C) Saturation of the sorbent as equilibrium is reached and/or low adsorbate concentrations in solution. [234]

Therefore if the adsorption rate of AO7 onto $Co_2Al\text{-}CO_3$ is a multi-faceted process, different rate limiting regions would be observed in linear intra-particle modelling corresponding to external diffusion, intra-particle diffusion and saturation. [37] Interestingly linear intra-particle diffusion plots (Figure 4.24) for LDHs synthesised at 20, 50, 100 and 150 °C portrayed only one linear region suggesting this was not the case. The only LDH that appeared to have two distinct regions of adsorption was the LDH synthesised at 200 °C. Rate constants (K_{dA}) of all LDHs appeared to be of similar magnitude regardless of synthesis temperature, suggesting changes in surface area and crystallinity did not play a role in adsorption rate (Table 4.15). In the intra-particle diffusion model C_i is indicative of the boundary layer thickness. A C_i of 0 indicates the rate is entirely determined by intra-particle diffusion. C_A values for LDHs synthesised between 50 – 200 °C were very low, between 0 and 21 mg g^{-1} suggesting very little external surface adsorption occurs and that adsorption rate is predominantly controlled by intra-particle diffusion. The C_A value for $Co_2Al\text{-}CO_3$ synthesised at 20 °C was 109.3 mg g^{-1}, suggesting that some external surface adsorption occurs.

4.6.4. Regeneration of LDH Structure Post Adsorption

Following adsorption of AO7, XRD analysis was performed on the MMO structures. It was expected that, if the mechanism of AO7 adsorption involved rehydration and reformation of the layered structure, reflections analogous to LDH would be visible. [194] In Figure 4.25 it can be seen that all MMOs exhibited broad reflections associated with Co_3O_4, indicating the MMO structure was maintained. No reflections indicative of LDH reformation were present indicating surface adsorption to be the predominant mechanism for AO7 removal This explains why a greater fit was observed to the pseudo-first order model during kinetic analysis. The slow adsorption rates, and findings from intra-particle diffusion modelling, suggested that diffusion processes were involved with the rate limiting step. Therefore, the bulk of the dye is thought to be adsorbed onto the surface of internal sites.

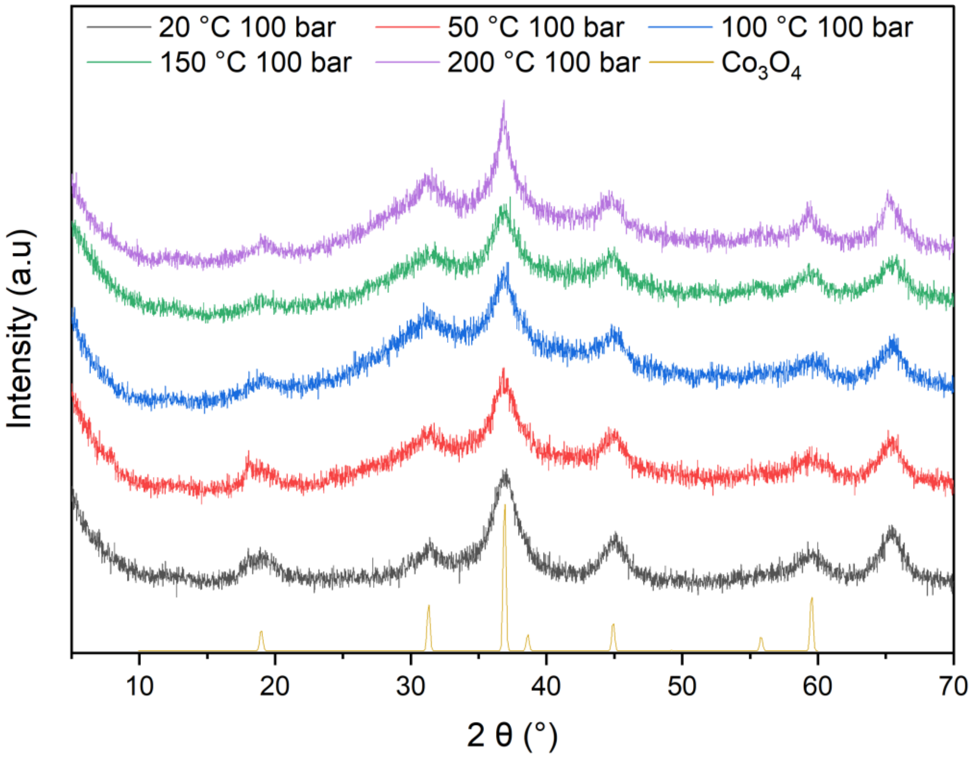

Figure 4.25. XRD patterns of MMOs post-adsorption of AO7

4.6.5. Comparison of Co_2Al-CO_3 MMO to Other Sorbents

Upon initial comparison with literature (Table 4.16) Co_2Al-CO_3 CLDH appears to be a promising candidate for the sorption of AO7, with only chitosan-based sorbents having a q_m value that exceeds the maximum uptake values observed in this work. However, Co_2Al-CO_3 CLDH's are unlikely to ever have industrial use for the removal of AO7 from wastewater due to their low adsorption rate. Despite exceeding 500 mg g^{-1} uptake capacity, Co_2Al-CO_3 CLDH took 96 hours to reach these values, with only ~300 mg g^{-1} of this occurring in the first 24 hours (Figure 4.23). Even after 4 days of suspension the sorption curve did not appear to plateau completely, suggesting equilibrium uptake had not been reached. As a result of this, rate constants (k_1 and k_2) were orders of magnitude lower than other sorbents found in literature (Table 4.16). In addition to this changing synthesis temperature did not appear to alter the speed of AO7 uptake by any order of magnitude indicating this could not be improved by the tuneable physical properties inherent in LDH synthesis.

While sorption capacity is of great importance for the production of a high-quality effluent during wastewater treatment, it should go hand in hand with sorption kinetics that allow for as low sorption residence times as possible to allow for a greater throughput of wastewater treated. Due to the continuous nature of wastewater generation any application of LDHs for dye remediation would need to occur in continuous processes. Fixed-bed columns are typically used for ion-exchange and adsorption processes due to their simplicity, ease of operation and handling. [235] In powder form LDHs are not suitable for this type of water treatment due to issues with sludge production and pressure drops as a result of their small particle size/diameter, and porosity. [236] As a result of this LDHs often require immobilization onto other larger sized and more porous substrates (such as polymeric materials) for use in fixed bed columns, which results in poorer adsorption performance. [236]

Another issue hindering the application of Co_2Al-CO_3 for dye adsorption is the necessity for calcination. While many LDHs in literature have shown promise for adsorption in their uncalcined form, negligible uptake of AO7 was reported for Co_2Al-CO_3 prior to calcination. Therefore the requirement for additional heating to temperature's exceeding 200 °C to calcine the LDH would greatly increase the cumulative energy demand (CED) of their production, and subsequently their cost and CO_2 emissions. [237] From this it is evident that there is little merit advocating for Co_2Al-CO_3's use as an adsorbent for dye remediation from wastewater due to:

- Poor kinetics due to its nanosize, low surface area and porosity.

- Ineffective scale-up to continuous adsorption processes.
- Increased CED from the calcination of the LDH.

Regardless of this, within this work it was clear that synthesis conditions, and the subsequent effect on physical properties, play an important role in adsorption capabilities of LDHs. Naturally, the choice of synthesis conditions should be considered for future research involving other LDH/sorbent systems.

Table 4.16. Maximum uptake (q_m), rate constants and surface areas of other sorbents in literature utilized for AO7 sorption

Adsorbent	**Maximum Uptake / mg g^{-1}**	**Pseudo-first order rate constant (k_1) / min^{-1}**	**Pseudo-second order rate constant (k_2) / g mg^{-1} min^{-1}**	**Surface Area / m^2 g^{-1}**	**Reference**
$Co_2Al\text{-}CO_3$ CLDH	639	3.77×10^{-4}	2.907×10^{-6}	59	*This Study*
Mg_2Al-SDS LDH	485.6	5.039	0.021	Not reported.	[39]
Activated Carbon	440.0	-	0.1809	Not reported.	[238]
ZIF-8 MOF	16.9	-	-	1080	[239]
UiO-66 MOF	106.6	-	-	902	[239]
Modified Pumice	1.08	0.017	0.007	Not reported.	[240]
TiO_2 Nanotube	137	N/A		279	[144]
Polymer Modified Bentonite	208.6	0.0301	0.0266	Not reported.	[241]
Magnetic Biochar (sewage Sludge & Woodchip)	110.27	-	0.014	99.83	[195]
Chitosan	2352.99	0.0198	3.4×10^{-5}	Not reported.	[242]

5. Results and Discussion: The Impact of LDH Metal Ions on Dye Sorption Characteristics

5.1. Introduction

Within literature many authors have highlighted the effectiveness of many LDHs, both in their calcined and uncalcined forms, for the adsorption of numerous dyes. Many of these papers have been highlighted in previous reviews, compiling extensive lists of LDH and CLDH sorbents for the adsorption and photocatalysis of dyes. [20,142] In addition, in-depth discussion on many aspects of LDH dye sorption including adsorption capacities, kinetics, adsorbent dose, adsorption factors and the impact on LDH calcination have been discussed. While these reviews act as a great steppingstone towards drawing a comparison between the effectiveness of LDHs containing various M^{2+}/M^{3+} ions for dye removal, few studies have directly discussed their impact. Similarly, few papers have discussed the role of dye choice on sorption capabilities. Cross-comparison of papers to deduce observations is also problematic due to inherent differences in experimental method, such as synthesis method and conditions, that introduces bias.

The work herein aimed to synthesis six LDHs by CFHS ($Ca_2Al\text{-}NO_3$, $Mg_2Al\text{-}CO_3$, $Zn_2Al\text{-}CO_3$, $Ni_2Al\text{-}NO_3$, $Mg_2Fe\text{-}CO_3$ and $Ni_2Fe\text{-}NO_3$), to deduce the effect of metal cation choice on both physical properties, and adsorption of AO7 dye. In addition, this work aimed to expand the scope of LDHs that can be synthesised by this method, with $Ni_2Al\text{-}NO_3$, $Mg_2Fe\text{-}CO_3$ and $Ni_2Fe\text{-}NO_3$ being reported for the first time. To mitigate bias, all LDHs were synthesised under identical experimental conditions. Following on from this, further sorption analysis was conducted on the most promising LDHs, quantified through adsorption capacities and sorption rate, with four additional dyes: SY, EB, MB and Saf-O. These were chosen to determine the effects of ionic charge, molecular size and chemical structure on dye uptake, and to see if high sorption capacity of AO7 translates over to other dyes.

5.2. Highlights

- $Ni_2Al\text{-}NO_3$, $Mg_2Fe\text{-}CO_3$ and $Ni_2Fe\text{-}NO_3$ LDH nanomaterials synthesised by continuous flow hydrothermal method (CFHS) for the first time.
- Altering M^{2+}/M^{3+} ions had a profound effect on AO7 adsorption, with adsorption capacities varying between 182 – 1603 mg g^{-1}. $Ca_2Al\text{-}NO_3$ and $Mg_2Fe\text{-}CO_3$ LDHs exhibited the highest adsorption capacities for AO7 dye, at 1586 and 1603 mg g^{-1} respectively.
- Comparison of physical properties of the six LDHs to adsorption of AO7 found no correlation with any one specific physical attribute. Adsorption was concluded to be dependent on multiple factors such as crystallinity, surface area, pH effects and interlayer anion, that are all altered upon varying M^{2+} and M^{3+} ions.
- Further adsorption experiments conducted with $Ca_2Al\text{-}NO_3$ and $Mg_2Fe\text{-}CO_3$ on SY, EB, MB and Saf-O dyes resulted in lower adsorption capacities than AO7, attributed to the valency, polarity and speciation of the dye, alongside pH buffering effects by the LDHs.

5.3. Continuous Synthesis of LDHs Containing Different M^{2+} and M^{3+} Ions

In this work six LDHs were synthesised for the adsorption of Acid Orange 7 dye: Ca_2Al-NO_3, Mg_2Al-CO_3, Zn_2Al-CO_3, Ni_2Al-CO_3, Mg_2Fe-CO_3 and Ni_2Fe-NO_3. These LDHs were chosen based on a study of LDHs utilized for removal of dye contaminants from water within the literature review. While other LDHs such as Cu_2Al-CO_3, [141] Ni-Zn-Cr-CO_3 and Zn-Mg-Al-CO_3 were also found in literature, these tended to be one-off papers and had not been experimented on many different dyes. [243,244] It was assumed that these LDHs most commonly found in literature would represent the LDHs that were easiest to produce and/or most effective for dye removal. In addition, it was hoped that any differences in adsorption properties could be correlated to physical characteristics, that occurred due to the choice of M^{2+} and M^{3+} ion.

To present an unbiased comparison of the impact of M^{2+} and M^{3+} on dye uptake, the same experimental conditions were used for the synthesis of all LDHs (Table 5.1). In addition to this, nitrate salts were used for all M^{2+} and M^{3+} precursors. Flow rates and precursor concentrations were based off those used in previous work by Clark et al. [87] Synthesis temperature and pressure were chosen due to previous literature suggesting these conditions allow for greater surface area and tuneability at these conditions (lower temperatures). [28]

For Ca_2Al-NO_3, Mg_2Al-CO_3 and Zn_2Al-CO_3 the interlayer anion was chosen based on previous synthesis of these LDHs by CFHS. [9,28,87] As this chapter highlights the first reported synthesis of Ni_2Al-NO_3, Mg_2Fe-CO_3 and Ni_2Fe-NO_3 by CFHS, their interlayer anion was chosen based on the most commonly incorporated anion in literature. pH is important for the precipitation and phase composition of LDH during synthesis and presence of different ions within the base solution (such as Na_2CO_3 and $NaNO_3$) can play a pivotal role on the formation of said LDH. [245] It was assumed that the anion most represented in literature would be most effectively incorporated into the interlayer region.

Table 5.1. Experimental conditions for LDH synthesis

Synthesis Temperature / °C	50
Synthesis Pressure / Bar	100
Flow Rate / mL min^{-1}	20 (downflow) + 10 (upflow)
[M^{2+}] / mol dm^{-3}	0.066
[M^{3+}] / mol dm^{-3}	0.033
[NaOH] / mol dm^{-3}	0.125
[Na_2CO_3] / mol dm^{-3}	0.0167
[$NaNO_3$] / mol dm^{-3}	0.033

5.4. The Effect of Metal Ions on Physical Properties

5.4.1. Crystal Characteristics

For all LDHs, XRD analysis was performed to determine if LDH formation was successful during synthesis, and to compare crystal characteristics of each individual LDH. LDHs have a distinct diffraction pattern XRD whereby intense symmetrical reflection are observed at low 2θ angles, becoming broader and more asymmetrical at higher 2θ angles. [96] The diffraction patterns of each LDH can be seen in Figure 5.1. $Ca_2Al\text{-}NO_3$, $Mg_2Al\text{-}CO_3$, $Zn_2Al\text{-}CO_3$ and $Mg_2Fe\text{-}CO_3$ LDHs exhibited intense symmetrical peaks at lower 2θ angles, becoming broader at high 2θ angles, indicating the formation of LDH was successful. For $Ni_2Al\text{-}NO_3$ and $Ni_2Fe\text{-}NO_3$ LDHs formation was not as obvious due to low relative peak intensities and peak broadness. Initially this was thought to be due to a lower degree of crystallinity within these two samples however, as the six LDHs contain different metal ions a direct comparison cannot be made. The relative intensity of the diffraction peak is dependent on both the relative amount of phase and the ability of individual phases to diffract X-rays (e.g: An equal amount of Ca_2Al and Mg_2Al phase would not give equal peak heights due to differences in the ability of Calcium and Magnesium phases to diffract). [246] The peak broadening occurring in Nickel containing LDHs may also indicate: [147]

- Comparatively smaller crystallite sizes
- Stacking faults
- Microstrains and/or defects within the long-range order.

Upon comparison of the peak positions to reference literature it was confirmed that all six LDHs had been formed (Table 5.2). As expected LDHs displayed a hexagonal crystal system, with $Ca_2Al\text{-}NO_3$ having a space group of $P\bar{3}c1$ and all others a space group of R3mH. Small additional reflections were observed in all samples due to unknown crystalline impurity phases. These were thought to be due to the formation of metal oxides such as CaO and MgO. This is due to the fact that CoO oxide impurity was observed during the synthesis of $Co_2Al\text{-}CO_3$ in Chapter 4, and it is known that oxide formation is favourable at supercritical conditions. [182]

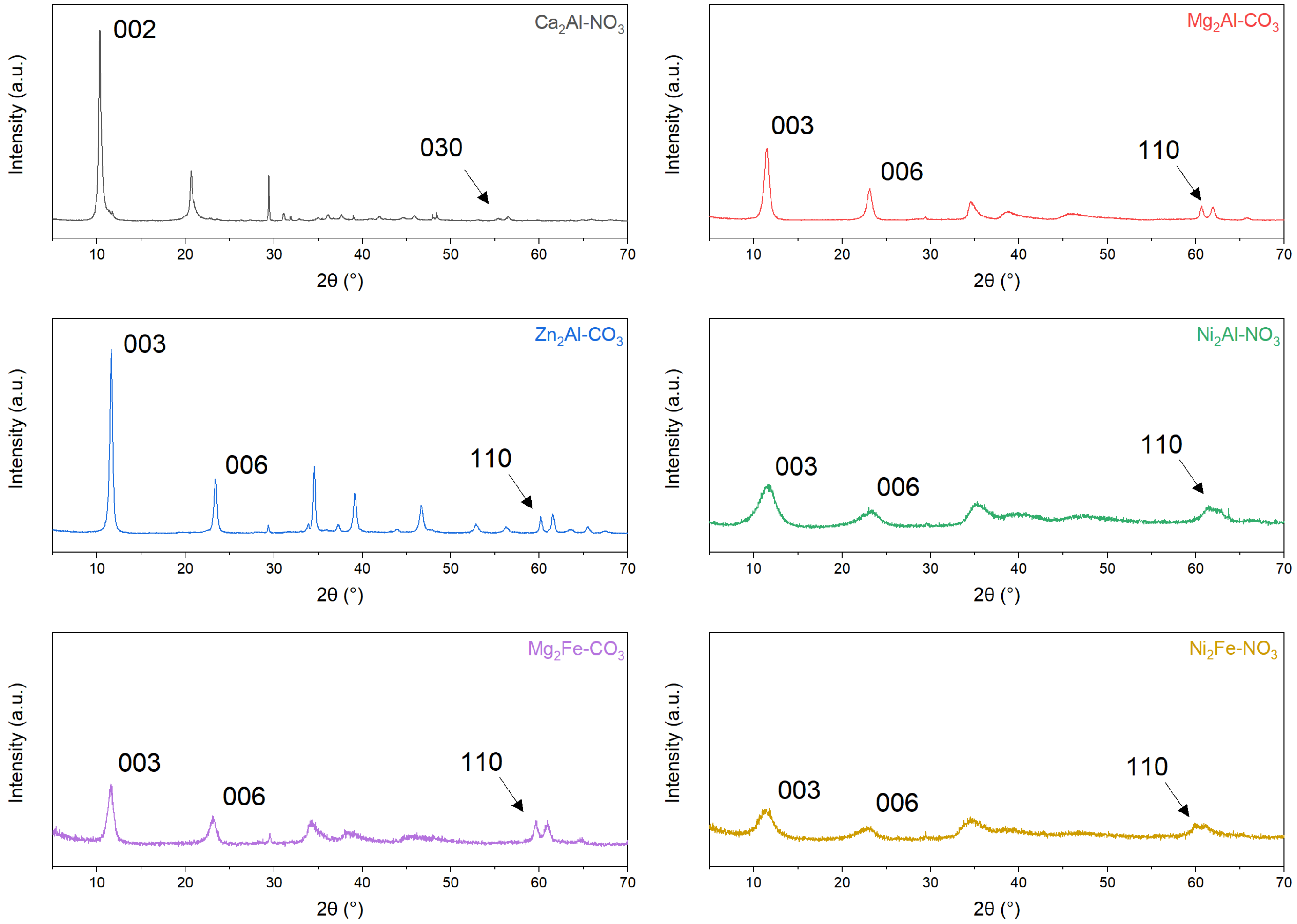

Figure 5.1. X-Ray Diffraction Patterns of Ca_2Al-NO_3 (top left), Mg_2Al-CO_3 (top right), Zn_2Al-CO_3 (centre left), Ni_2Al-NO_3 (centre right), Mg_2Fe-CO_3 (bottom left) and Ni_2Fe-NO_3 (bottom right)

Table 5.2. Crystallographic data from XRD analysis

	Crystal System	Symmetry	D-spacing (d_{002}) / nm	Lattice Parameters		CDL (002) / nm	CDL (030) / nm	Ref
				a / nm	c /nm			
Ca_2Al-NO_3	Hexagonal	P 3 c 1	0.85	0.57	1.71	22.17 ± 0.73	61.52 ± 90.21	[247]
			D-spacing (d_{003}) / nm			**CDL (003) / nm**	**CDL (110) / nm**	
Mg_2Al-CO_3	Hexagonal	R 3 m H	0.77	0.30	2.28	11.70 ± 0.13	23.84 ± 1.84	[248]
Zn_2Al-CO_3	Hexagonal	R 3 m H	0.76	0.31	2.32	20.60 ± 0.24	35.51 ± 5.95	[249]
Ni_2Al-NO_3	Hexagonal	R 3 m H	0.77	0.30	2.26	3.89 ± 0.08	7.36 ± 1.59	[250]
Mg_2Fe-CO_3	Hexagonal	R 3 m H	0.77	0.31	2.35	10.00 ± 0.12	18.80 ± 1.37	[251]
Ni_2Fe-NO_3	Hexagonal	R 3 H	0.78	0.31	2.28	4.58 ± 0.13	17.41 ± 5.16	[252]

For all LDHs that exhibited R3mH symmetry, lattice parameters were 0.30 ± 0.01 and 2.31 ± 0.04 nm for *a* and *b* respectively. Ca_2Al-NO_3 exhibited lattice parameters of 0.57 nm and 1.71 nm for *a* and *b*. These lattice parameters were in agreement with syntheses of LDHs published in literature. [253–258] D-spacing of individual platelets in the 002 (P3̅c1) and 003 (R3mH) reflections corresponds to the thickness of one layer, which constitutes a brucite-like sheet and an interlayer. [208,259] Conversely, the d-spacing of the 030 (P3̅c1) and 110 (R3mH) reflections corresponds to the metal ion-metal ion distance within the brucite sheet. D spacing for all LDHs with R3mH symmetry did not appear to change substantially (0.77 ± 0.01 nm), indicating that the presence of either CO_3^{2-} or NO_3^- did not appear to change the width of the interlayer region. While a slightly higher d_{002} of 0.85 nm was seen for Ca_2Al-NO_3, this was attributed to the different symmetry (P3̅c1).

From CDL calculations in Table 5.2 it was evident that Ca_2Al-NO_3 synthesis produced the largest crystals, evidenced by their CDL_{003} and CDL_{110} of 22.17 and 61.52 nm. While Zn_2Al-CO_3 had a similar degree of platelet stacking (CDL_{003} of 20.60 nm) its individual platelet size was smaller (CDL_{110} of 35.51 nm). Although it should be noted that, due to the low intensity of the 030 reflection in Ca_2Al-NO_3, there was a large degree of error within the CDL_{030} measurement making any platelet size comparisons from XRD analysis hard to justify. Interestingly both Ni_2Al-NO_3 and Ni_2Fe-NO_3 had the lowest CDL_{110} values of 7.36 and 17.41 nm respectively, indicating either smaller crystallite sizes or reduced long range order within the structure due to defects or impurities. [208]

The large variations in CDL values indicated that the choice of M^{2+} and M^{3+} ions had a large impact on crystal growth. It is well documented in literature that in order for metal cations to be introduced into LDH structure they must be of similar ionic radius to Mg^{2+} ions. For example, due to its smaller ionic radius and greater charge density compared to Mg^{2+}, incorporation of Ni^{2+} into LDH structure is more difficult. [260] Similarly, Fe^{3+} ions are known to distort layers due to its larger atomic radius, resulting in strain broadening. These differences result in lower crystallinities observed for Ni_2Al-NO_3, Mg_2Fe-CO_3 and Ni_2Fe-NO_3 LDHs.

5.4.2. Structural & Chemical Characteristics

Morphological analysis was performed on all six LDHs by TEM analysis (Figure 5.2). Images of all LDHs synthesised appeared to show the presence of individual nanoplatelets. While the indicative LDH hexagonal platelets were present, most platelets were irregularly shaped.

The largest platelets were observed for Ca_2Al-NO_3, in the range of 0.25 – 1 µm in lateral diameter, which is in agreement with other Ca_xAl LDHs synthesised by continuous hydrothermal method and previous CDL calculations. [208] There also appeared to be a large amount of agglomeration of platelets, which is expected to result in a lower overall surface area. Along the edges of agglomerates there appeared to be much smaller primary nanoparticles present, which has been previously reported to be due to the short residence time (~4s) and rapid quenching of nanoparticles by cold water. [28] Much smaller platelets were observed for Mg_2Al-CO_3 and Zn_2Al-CO_3, ranging from 20 – 100 nm and 50 – 200 nm in lateral diameter respectively. The smallest nano-platelets were observed for Ni_2Al-NO_3, with lateral diameters in the range of 5-25 nm, explaining why the diffraction pattern appeared to have a greater degree of peak-broadening due to smaller crystallite sizes. Finally, the lateral diameters of Mg_2Fe-CO_3 (10 - 50 nm) and Ni_2Fe-NO_3 (5 – 100 nm) also appeared to be comparable to others synthesised in literature. One author reported the synthesis of MgFe LDH for the adsorption of indigo carmine dye. [261] Despite synthesising the LDHs via a sol gel method, the dimensions of nanoplatelets were in the region of 6 – 22 nm. Similarly, previous syntheses of NiFe LDH reported average particle diameters below 100 nm. Aggregation of platelets, forming a “house-of-cards” type agglomerate, was attributed to a reduced surface area.

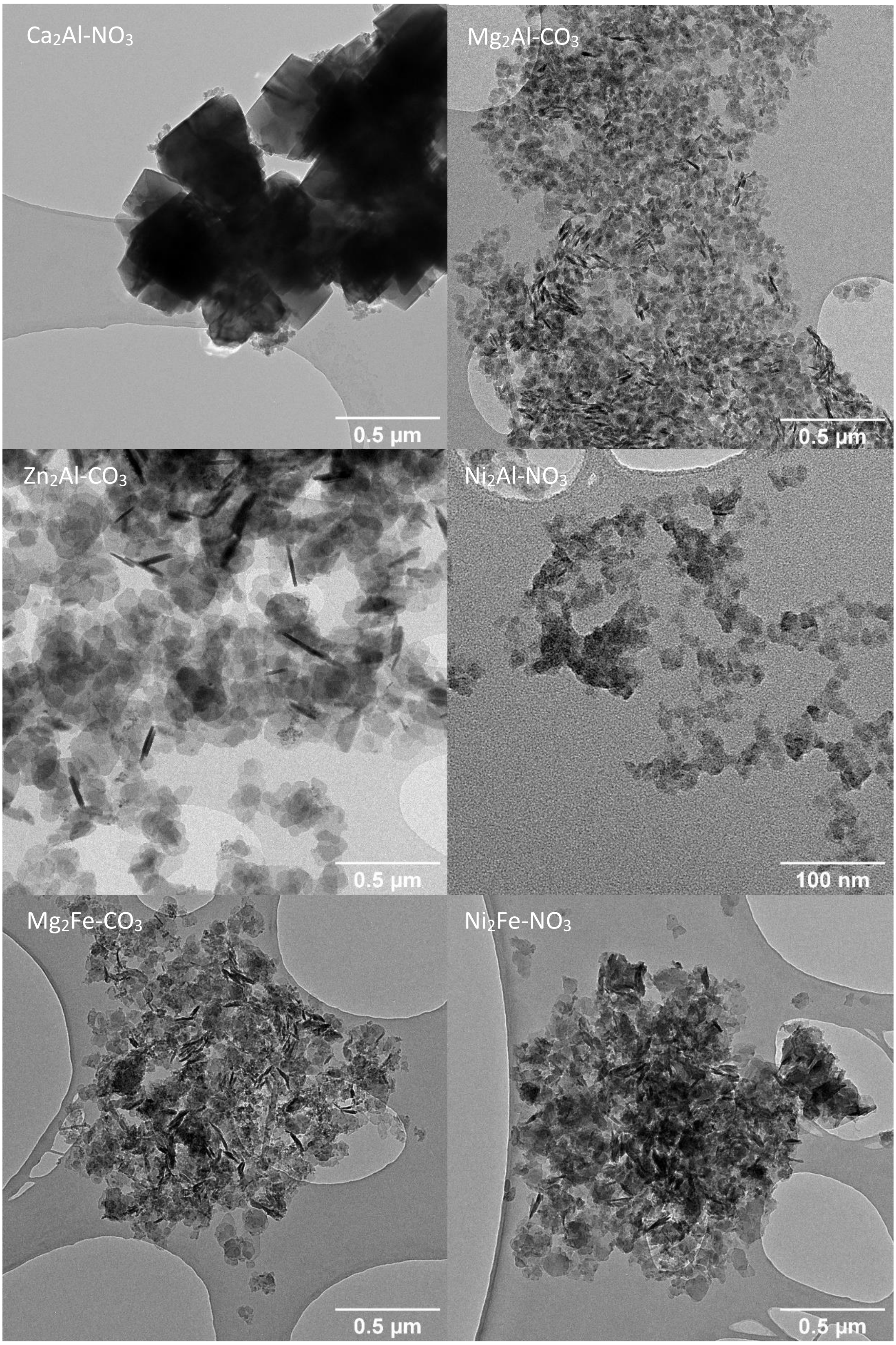

Figure 5.2. TEM images of LDHs: Ca_2Al-NO_3 (top left), Mg_2Al-CO_3 (top right), Zn_2Al-CO_3 (centre left), Ni_2Al-NO_3 (centre right), Mg_2Fe-CO_3 (bottom left) and Ni_2Fe-NO_3 (bottom right)

While there appeared to be a correlation of LDH lateral diameters and crystallite size from CDL calculations in XRD, the platelets appeared to be much greater in size (Table 5.3). For example, while a CDL_{110} of 35.51 nm was observed in Zn_2Al-CO_3, platelet sizes from TEM imaging far exceeded this (50 – 200 nm). CDL tends to be lower than platelet sizes observed in TEM due to the presence of internal disorder within the platelets such as microstrains and defects. [246] Unfortunately due to poor imaging resolution at the required magnification, and the tendency for LDHs to agglomerate, an assessment into particle size distribution was not conducted.

Table 5.3. Comparison of CDL (003) to particle diameters observed in TEM

LDH	**CDL (030) / nm**	**Particle Diameters / nm**
Ca_2Al-NO_3	61.52 ± 90.21	250 - 1000
	CDL (110) / nm	
Mg_2Al-CO_3	23.84 ± 1.84	20 – 100
Zn_2Al-CO_3	35.51 ± 5.95	50 - 200
Ni_2Al-NO_3	7.36 ± 1.59	5- 25
Mg_2Fe-CO_3	18.80 ± 1.37	10 - 50
Ni_2Fe-NO_3	17.41 ± 5.16	5 - 100

TGA analysis was performed to determine the thermal stability of LDHs. Generally it is seen in the literature that LDHs have two or three regions of mass loss. [93] The first of these occurs broadly around 100 °C and is associated with the evaporation of surface bound water. At higher temperatures (200 – 400 °C), dehydroxylation of the brucite sheets occurs. Finally, above 400 °C complete breakdown of the layered structure occurs, and the interlayer is evolved.

Mass loss and derivative mass loss profiles for all six LDHs can be seen in Figure 5.3. Ca_2Al-NO_3 exhibited three distinct regions of mass loss, similar to what was observed by Clark et al: [208] evaporation of surface bound water up to 100 °C, dehydroxylation of brucite sheets at ~250 °C and breakdown of the layered structure/evolution of the interlayer ions above ~500 °C. Mg_2Al-CO_3, Zn_2Al-CO_3, Ni_2Al-NO_3 and Ni_2Fe-NO_3 all portrayed profiles with two distinct regions of mass loss, as seen in their respective literature (Table 5.4). These were attributed to 1) evaporation of physisorbed and surface bound water and 2) dehydroxylation, collapse and desorption of interlayer ions as gas (N_2, NO_x and CO_2). [262] While no literature could be found highlighting the thermal degradation of $Mg_2Fe\text{-}CO_3$, it had a very similar profile to that of $Ni_2Fe\text{-}CO_3$ indicating the presence of iron plays an important role in its thermal stability.

Of the 6 six LDHs prepared, dehydroxylation occurred at similar temperatures, starting around ~200 – 250 °C. As $Ca_2Al\text{-}NO_3$ was the only LDH with a 3rd mass loss region above 450 °C, it appeared to be the LDH that had the greatest thermal stability for complete structural collapse. Although having said this, no further XRD or TGA-MS characterization was performed to determine if the other LDHs did have any substantial degree of breakdown of the layered structure during thermogravimetric analysis. Typically, environmental wastewater containing dyes is between 20 – 45 °C, far below temperatures at which structural breakdown of LDH occurs. [2]

Table 5.4. Comparison of TGA mass loss profile with literature

	This Research		**Literature**		
	Mass Loss Regions	**Total Mass Loss / %**	**Mass Loss Regions**	**Total Mass Loss / %**	**Ref**
$Ca_2Al\text{-}NO_3$	3	59	3	40-45	[208]
$Mg_2Al\text{-}CO_3$	2	56	2	42	[262]
$Zn_2Al\text{-}CO_3$	2	41	2	~26	[263]
$Ni_2Al\text{-}NO_3$	2	33	2	40-45	[151]
$Mg_2Fe\text{-}CO_3$	2	44	N/A		
$Ni_2Fe\text{-}NO_3$	2	54	2	35	[264]

Interestingly all LDHs exhibited a 10-15 % difference in total mass loss compared to similar literature. This was deduced to be due to a combination of different factors such as bound water content, TGA parameters and M^{2+}:M^{3+} ratio within the LDH. For example Clark et al. [208] reported ~25 % mass loss during the initial mass loss stage, 5 % less than the $Ca_2Al\text{-}NO_3$ synthesised in this study, suggesting a difference in bound water content. In addition to this, despite mass loss still occurring the temperature ramp was stopped 100 °C earlier at 700 °C. Similarly, other authors also reported 5 – 10 % less mass loss during this first region associated to bound water content. [262,263] Finally differences in the TGA profile of $Ni_4Fe\text{-}NO_3$, was attributed to the 4:1 ratio of Ni^{2+}:Fe^{3+} used. [143] In LDH structure the additional charge on the M^{3+} ion (Fe^{3+}) is counteracted by anions ($CO^{2-}{}_3$ or NO_3^-) and water within the interlayer region. Therefore, the reduced amount of Fe^{3+} within the LDH structure when using a 4:1

M^{2+}:M^{3+} ratio would result in less ions and water within the interlayer, and an overall reduction in mass loss observed.

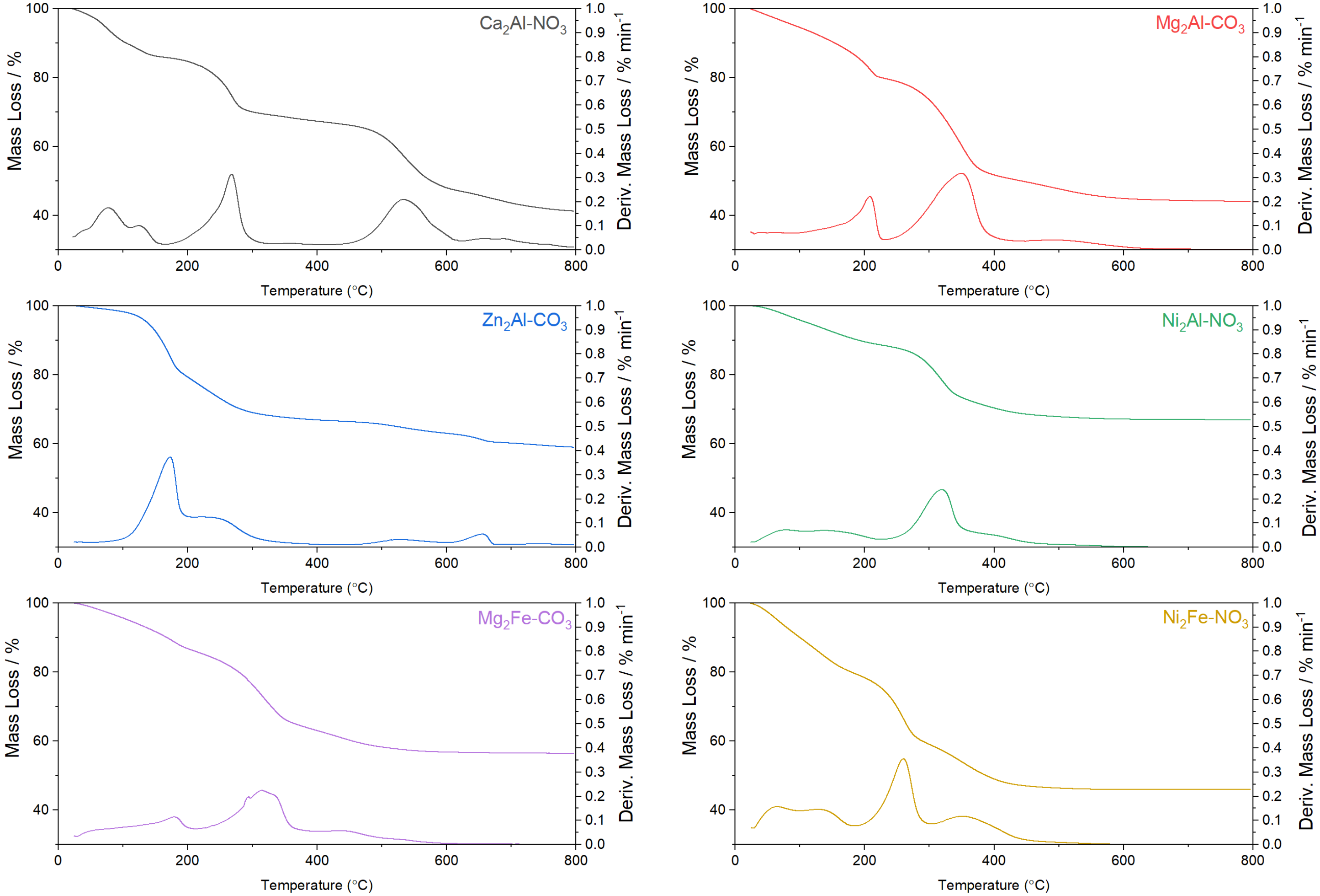

Figure 5.3. TGA mass loss and derivate mass loss of LDHs - Ca$_2$Al-NO$_3$ (top left), Mg$_2$Al-CO$_4$ (top right), Zn$_2$Al-CO$_3$ (centre left), Ni$_2$Al-NO$_3$ (centre right), Mg$_2$Fe-CO$_3$ (bottom left) and Ni$_2$Fe-NO$_3$ (bottom right)

The M^{2+}:M^{3+} ratio is known to alter the formation of LDH, and it is generally regarded that the ratio should lie between 2-4 to obtain a pure hydrotalcite phase. [96] Changing this ratio can affect the physical properties and has been reported to alter the crystallinity and purity of LDH material, [99] alongside porosity due to a breakdown in uniformity at lower molar ratios. [95] For this purpose, LDHs were synthesised using a 2:1 M^{2+}:M^{3+} ratio of precursors (nitrate salts) to take advantage of this increased porosity. It can be seen in Table 5.5 that the metal content in $Ca_2Al\text{-}NO_3$, $Mg_2Fe\text{-}CO_3$ and $Ni_2Fe\text{-}NO_3$ did not deviate far from the 2:1 ratio expected, reporting M^{2+}:M^{3+} ratios between 1.90-2.00. On the other hand, metal ratios of $Mg_2Al\text{-}CO_3$, $Zn_2Al\text{-}CO_3$ and $Ni_2Al\text{-}NO_3$ appeared to be 20-30 % above the 2:1 ratio expected, suggesting incomplete precipitation of Al^{3+} ions. [100] While this is still within the 2-4 ratio required for pure hydrotalcite formation, the crystallinity and porosity may have been affected as a result. Therefore, these deviations should be taken into consideration when comparing the characteristics of different LDHs.

Table 5.5. M^{2+}:M^{3+} ratio of LDHs, as determined by ICP

Sample	M^{2+}:M^{3+} ratio (X:1)
$Ca_2Al\text{-}NO_3$	1.98
$Mg_2Al\text{-}CO_3$	2.61
$Zn_2Al\text{-}CO_3$	2.32
$Ni_2Al\text{-}NO_3$	2.67
$Mg_2Fe\text{-}CO_3$	1.99
$Ni_2Fe\text{-}NO_3$	1.90

5.4.3. Surface Area Characteristics

It is well studied in literature that SSA is one of many factors that plays a vital role in the performance of adsorbents. [265] Many adsorbents such as zeolites and activated carbon are attractive not only due to their low cost of production, but also their high specific surface areas. [14] In addition, pore size has been reported to play an important role in adsorption mechanisms, with larger diffusion channels being most suitable for sorption. [142,232] As a result, N_2 (77 K) adsorption and desorption isotherms, and their corresponding pore size distributions, were carried out on each LDH (Figure 5.4 to Figure 5.9).

$Mg_2Al\text{-}CO_3$ (Figure 5.5) and $Mg_2Fe\text{-}CO_3$ (Figure 5.8) exhibited both Type II and Type IVa isotherms behaviour, according to the IUPAC isotherm classifications. [186] This was evidenced by the saturation plateau at high relative pressure (P/P_0) and indicated mesoporous nature. The initial knee is indicative of monolayer adsorption and is followed by subsequent condensation of gas in the mesopores. However, for a solely mesoporous adsorbent the isotherm should remain horizontal over the upper range of p/p^0 (0.95 and above) due to the complete filling of mesopores. [215] In this instance, both $Mg_2Al\text{-}CO_3$ and $Mg_2Fe\text{-}CO_3$ exhibited non-horizontal plateau regions suggesting the presence of some macropores. These macropores were evidenced in the pore size distribution insets where pore diameters were observed between 20 – 100 nm. The presence of H1 hysteresis during the desorption branch suggests that the pores are larger than the critical width (dependent on the adsorption system but generally wider than ~4 nm).

$Ca_2Al\text{-}NO_3$ (Figure 5.4), $Zn_2Al\text{-}CO_3$ (Figure 5.6), $Ni_2Al\text{-}NO_3$ (Figure 5.7) and $Ni_2Fe\text{-}CO_3$ (Figure 5.9) exhibited Type II behaviour suggesting they are non-porous/macroporous in nature. The shape is a result of initial monolayer coverage (the knee) followed by unrestricted monolayer/multilayer adsorption up to high P/P_0. The knee observed for $Ni_2Al\text{-}NO_3$ was less distinct and more gradual suggesting an overlap between monolayer coverage and when multilayer adsorption occurs. From the pore size distribution insets, it can be seen that all LDHs of Type II were predominantly macroporous in nature, with some mesoporosity, as evidenced with pores of 20 nm and larger. Due to this macroporosity an assessment of pore volume (V_p) could not be conducted as the multilayer pore filling is unrestricted. The desorption branches of $Ca_2Al\text{-}NO_3$, $Zn_2Al\text{-}CO_3$, $Ni_2Al\text{-}NO_3$ and $Ni_2Fe\text{-}CO_3$ appeared to mimic the shape of a Type II isotherm suggesting H3 hysteresis. This occurs as a result of multilayer metastability and delayed capillary condensation due to low pore curvature. [211] Type H3 hysteresis are often seen by plate-like particles that form non-rigid aggregates.

An interesting phenomenon observed for Ni_2Al-NO_3, Mg_2Fe-CO_3 and Ni_2Fe-NO_3 was a sharp drop in adsorbed gas during the desorption branch at saturation pressures of around 0.4 – 0.5 p/p^0. In the pore size distribution plots this appears to be due to presence of a narrow band of mesopores, 20-30 nm in diameter, however this is unlikely to be the case. This low-pressure hysteresis can instead be attributed to expansion and contraction of non-rigid aggregates, or structural transformations that occur during adsorption. These structural transformations have been observed for similar adsorbents such as “breathing” Metal-Organic frameworks (MOFs) whereby multiple hysteresis loops are observed during desorption due to the expansion and contraction of the material at varying temperature. [266]

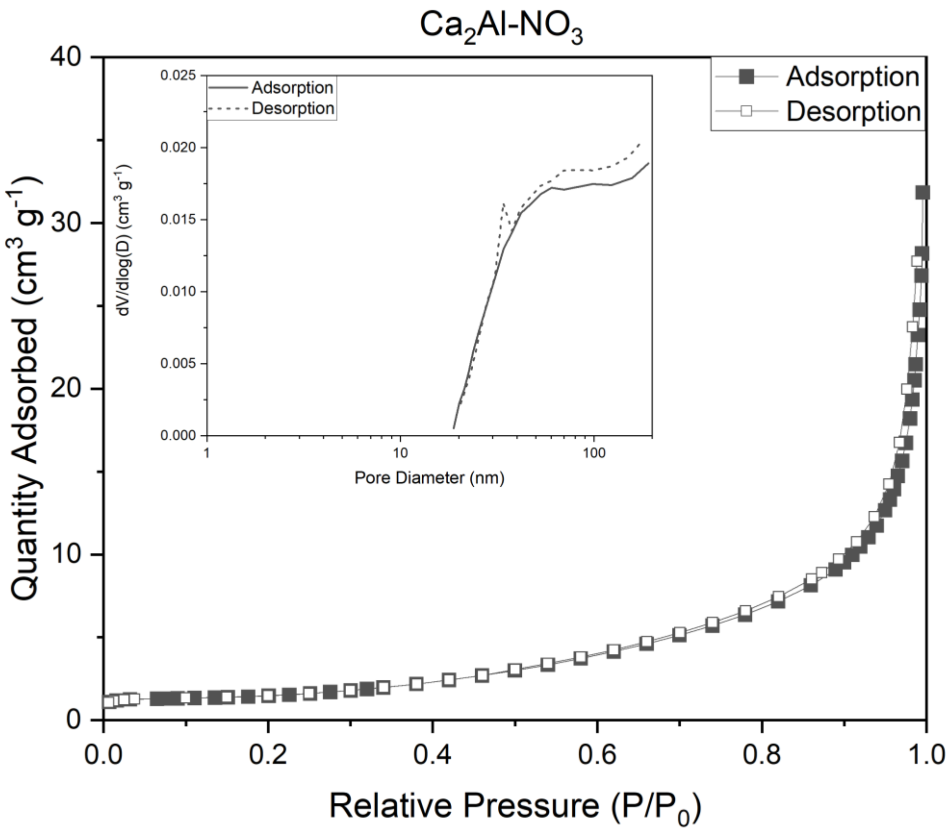

Figure 5.4. N_2 adsorption/desorption isotherm of $Ca_2Al\text{-}NO_3$ and pore size distribution (inset).

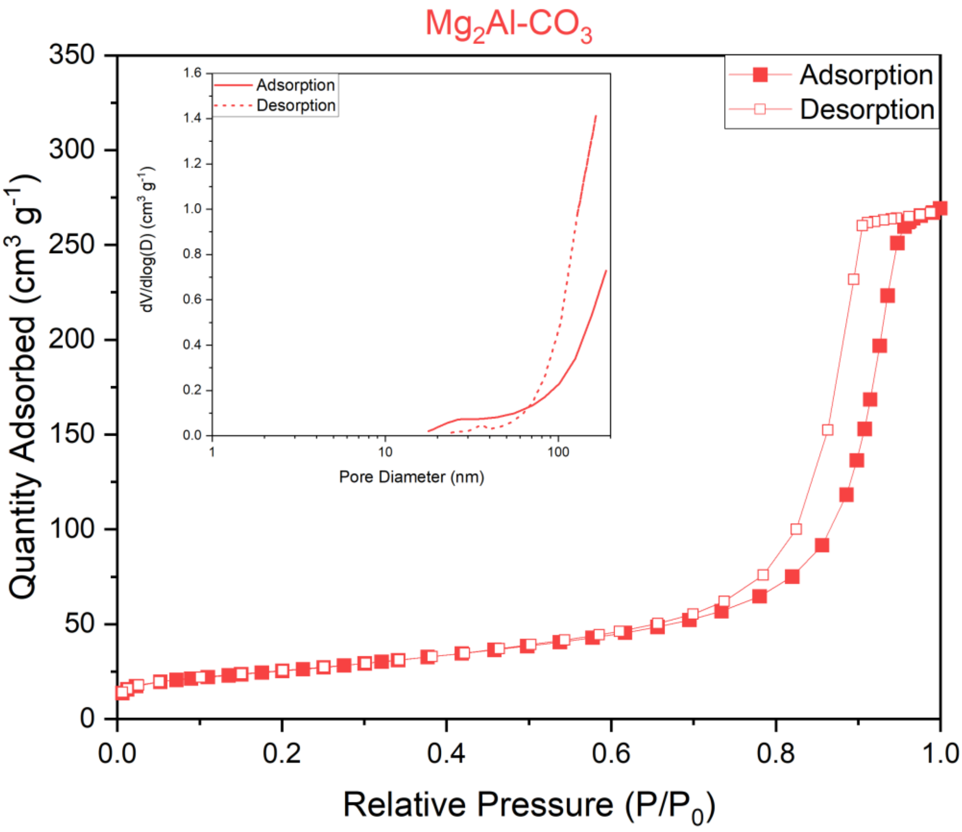

Figure 5.5. N2 adsorption/desorption isotherm of $Mg_2Al\text{-}CO_3$ and pore size distribution (inset).

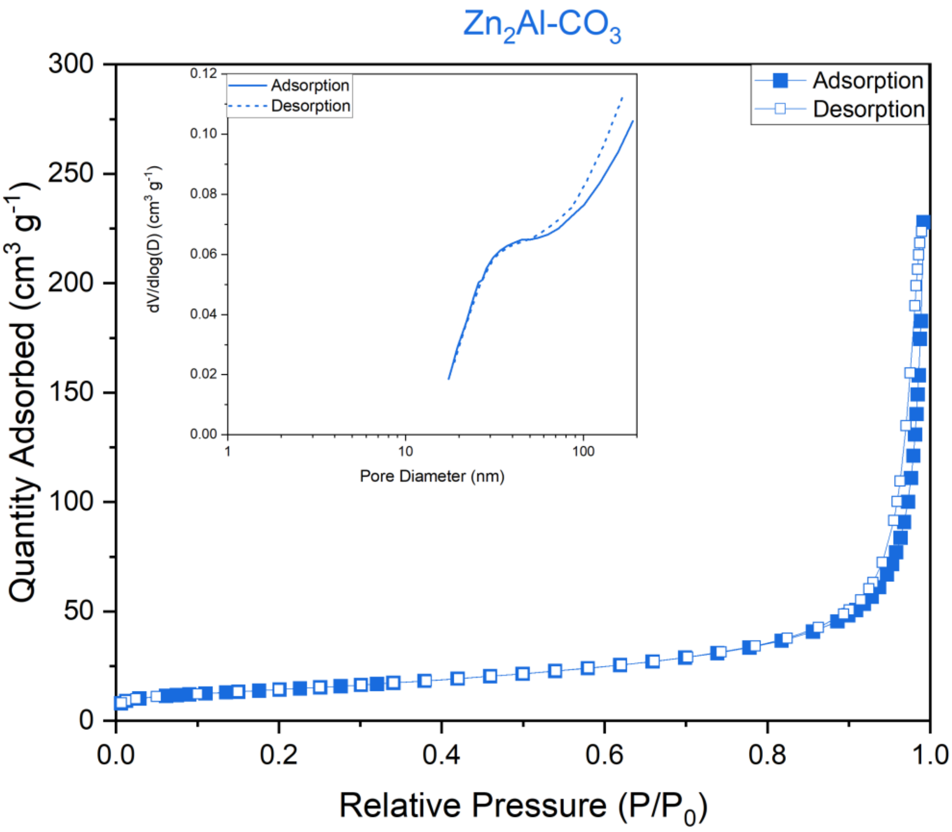

Figure 5.6. N2 adsorption/desorption isotherm of Zn_2Al-CO_3 and pore size distribution (inset).

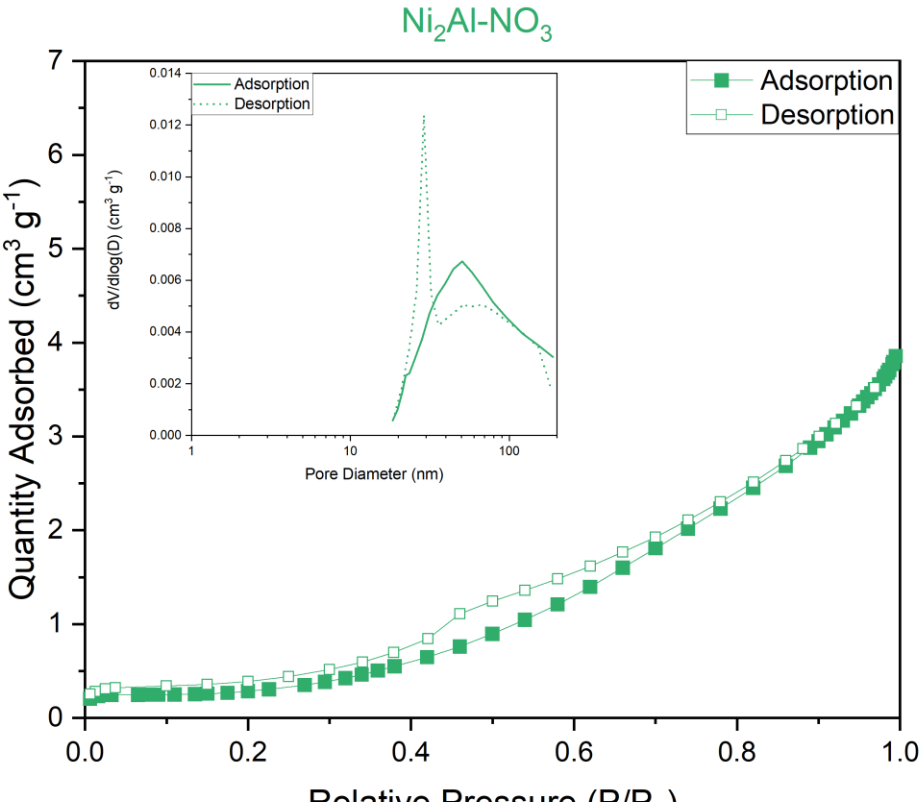

Figure 5.7. N2 adsorption/desorption isotherm of Ni_2Al-NO_3 and pore size distribution (inset).

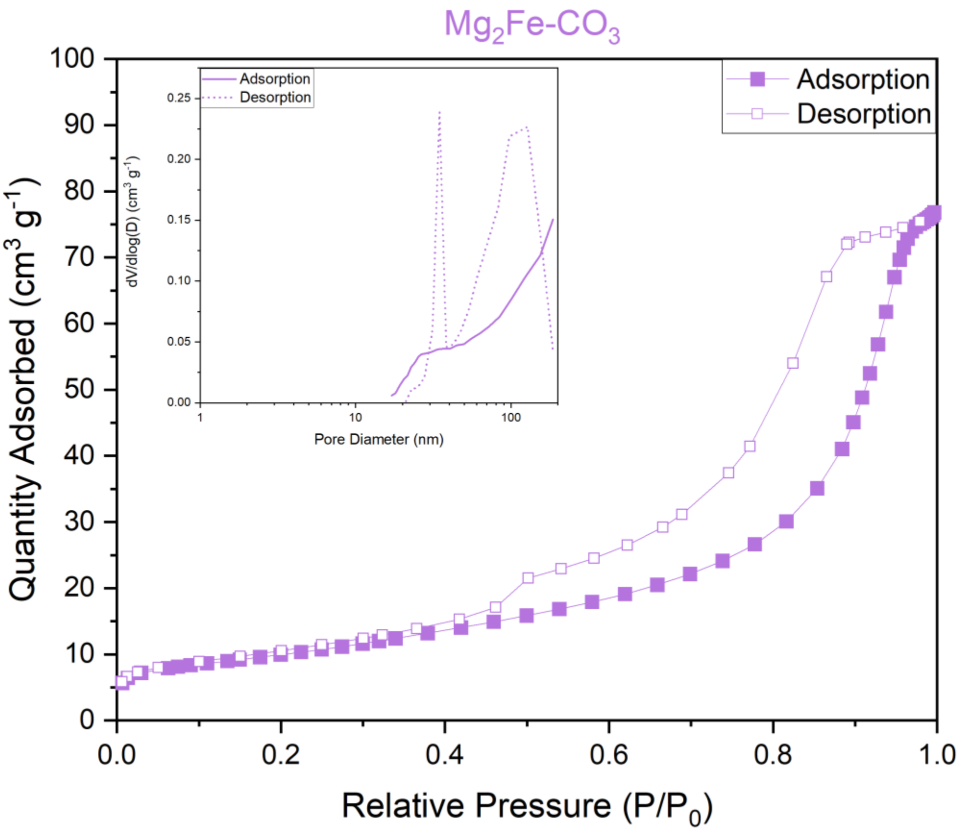

Figure 5.8. N2 adsorption/desorption isotherm of Mg_2Fe-CO_3 and pore size distribution (inset).

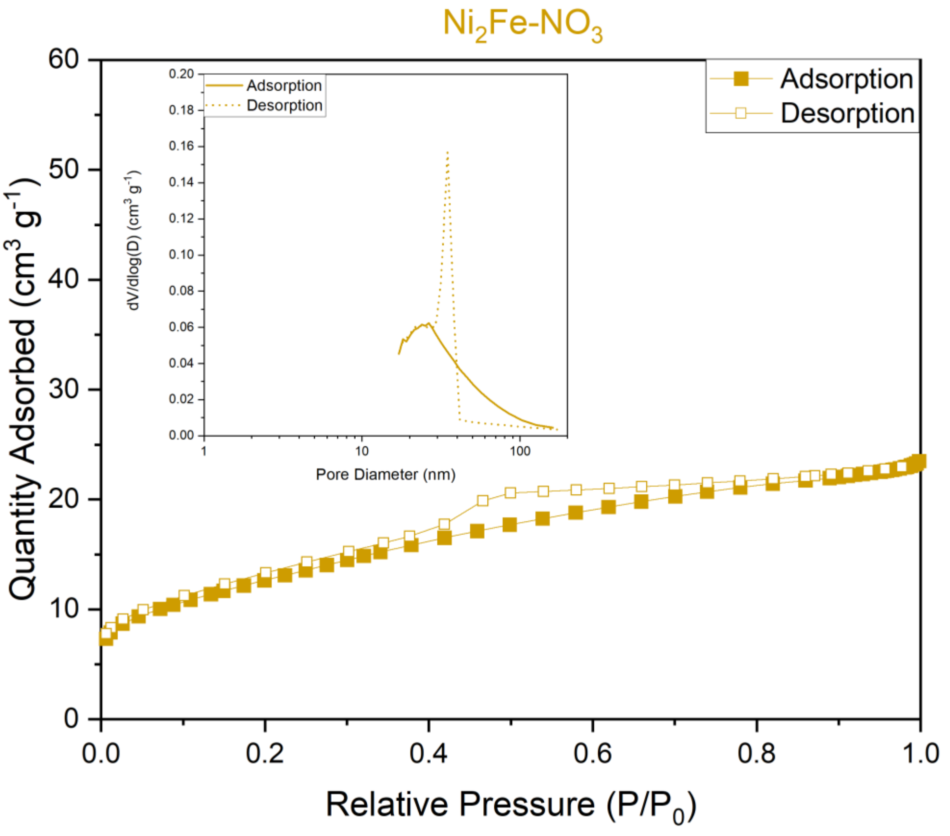

Figure 5.9. N2 adsorption/desorption isotherm of Ni_2Fe-NO_3 and pore size distribution (inset).

The specific surface area of each LDH was calculated using the BET method and can be seen in Table 5.6. All surface areas reported were between 1-100 m^2 g^{-1}, with Mg_2Al-CO_3 having the highest surface area of 90.6 mg g^{-1}. While these surface areas are relatively low compared to the likes of other adsorbents such as MOFs (which can exhibit surface areas as high as 7000 m^2 g^{-1}), [267] it is not necessarily indicative of adsorption performance which is based on a number of different factors.

The BET C value, also seen in Table 5.6, gives a useful indication on isotherm shape. Generally, a BET C value exceeding 150, as seen by Ca_2Al-NO_3, Mg_2Al-CO_3, Zn_2Al-CO_3 and Mg_2Fe-CO_3, is indicative of adsorption on to high-energy surface sites. The C value for Ni_2Al-NO_3 was comparably lower (13.8). A C value below 50 suggests there is overlap between when monolayer and multilayer adsorption, as seen by a less distinct knee at low P/P^0. This makes precise calculation of the monolayer capacity (n_m) and subsequently BET surface area difficult to attain. Therefore the surface area for Ni_2Al-NO_3 calculated may not be a true reflection of its surface area. [186]

Table 5.6. BET specific surface area and isotherm analysis of LDHs

Sample	BET Surface Area / m^2 g^{-1}	BET C Value	Isotherm	Hysteresis
Ca_2Al-NO_3	5.0 ± 0.1	288.6 ± 3.1	Type II	H3
Mg_2Al-CO_3	90.6 ± 4.0	147.2 ± 6.5	Type IVa	H1
Zn_2Al-CO_3	50.5 ± 3.2	187.5 ± 11.9	Type II	H3
Ni_2Al-NO_3	1.3 ± 0.4	13.8 ± 4.1	Type II	H3
Mg_2Fe-CO_3	35.2 ± 1.2	159.9 ± 5.6	Type IVa	H1
Ni_2Fe-NO_3	45.6 ± 2.5	105.4 ± 5.8	Type II	H3

Both Ca_2Al-NO_3 and Zn_2Al-CO_3 portrayed similar surface areas to previous syntheses by CFHS under similar conditions (Table 5.7), indicating LDHs could be repeatably synthesised to produce similar physical properties. In contrast there did appear to be some differences in surface area depending on synthesis method. For example, polyol hydrolysis produced Ni_2Al-NO_3 LDHs of higher surface areas (72 $m^2 g^{-1}$) than by CFHS (1.3 $m^2 g^{-1}$). [268] On the other hand, CFHS synthesis of Mg_2Al-CO_3 had a higher surface area (90.6 $m^2 g^{-1}$) than synthesis by co-precipitation (9.6 $m^2 g^{-1}$) or hydrothermal (15.3 $m^2 g^{-1}$). However, as discussed previously, the physical properties of LDHs are heavily dependent on synthesis conditions such as aging time, temperature, pressure and pH. [20,269] As a result of this, it is difficult to discern whether any differences in surface areas reported are purely down to method, or a product of the conditions utilized during synthesis.

Table 5.7 Synthesis method and surface area of LDHs found in literature

	Synthesis Method	**Surface Area / $m^2 g^{-1}$**	**Ref**
Ca_2Al-NO_3	CFHS	5.0	This Work
Ca_3Al-NO_3	CFHS	4-7	[30]
Ca_2Al-NO_3	Co-Precipitation	21.1	[270]
Mg_2Al-CO_3	CFHS	90.6	This Work
Mg_2Al-CO_3	Co-Precipitation	9.6	[271]
Mg_3Al-CO_3	Hydrothermal	15.3	[162]
Zn_2Al-CO_3	CFHS	50.5	This Work
Zn_2Al-CO_3	CFHS	50.1	[95]
Ni_2Al-NO_3	CFHS	1.3	This Work
Ni_2Al-NO_3	Polyol Hydrolysis	72	[272]
Mg_2Fe-CO_3	CFHS	35.2	This Work
Mg_3Fe-CO_3	Hydrothermal	119	[273]
Ni_2Fe-NO_3	CFHS	45.6	This Work
Ni_4Fe-NO_3	Co-Precipitation	17.8	[143]

5.5. Batch Adsorption of Acid Orange 7

To determine the effectiveness of each LDH for dye remediation, batch adsorption experiments were performed on AO7 (Figure 5.10), an orange sulfonate based azo dye. Acid dyes are available as sodium salts and are commonly used in the textile industry for use with fibres such as polyamide, wool, silk, acrylic and polypropylene. [2]

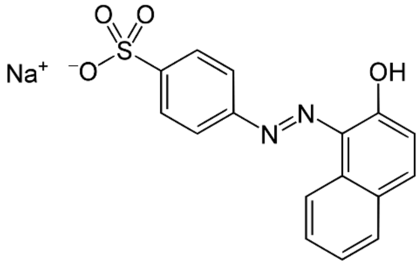

Figure 5.10. Molecular structure of Acid Orange 7 (AO7) dye

5.5.1. Adsorption Kinetics

Adsorption kinetics are vital for adsorbent evaluation to improve understanding of the sorption mechanism and rate of uptake of a pollutant. In addition, understanding of kinetics is important to design columns of different scales. [158] A kinetic experiment to AO7 dye uptake over 24 hours was conducted on all LDHs at 20 °C. The rate of adsorption and equilibrium uptake was analysed through kinetic modelling using the pseudo first order, pseudo second order and intra-particle diffusion models. The pseudo first order and pseudo second order models are most commonly applied to adsorbents. [158] The intra-particle diffusion model, by Weber-Morris, was applied due to its applicability to sorption mechanisms involving diffusion of the sorbent into internal sites, such as ion exchange. [199]

It can be seen in Figure 5.11 that, while the models fit well over the first few hours of analysis, the models appeared to generally under-calculate the maximum uptake of AO7 after 24 hours, with data points deviating far from the trend line. While in $Zn_2Al\text{-}CO_3$ and $Ni_2Al\text{-}NO_3$ this could be attributed to error in the measurements, the deviations in $Mg_2Al\text{-}CO_3$ and $Mg_2Fe\text{-}CO_3$ were significantly larger than the inherent error. This can most likely be attributed to the large time difference between the 4 h and 24 h data points and the fact that the pseudo-first order model tends to fit experimental data well for only the initial period of reaction. While the models for all LDHs showed equilibrium being reached prior to 24 hours (as evidenced by the plateau region), only $Ca_2Al\text{-}NO_3$ appeared to plateau based on its data points. The other five LDHs had a substantial increase in dye uptake from 4 hours to 24 hours.

From linear regression analysis (Table 5.8) it appeared that the pseudo-second order model had a slightly better fit than the pseudo-first order model, as evidenced by greater R^2 values and proximity of calculated equilibrium uptake ($q_{e,cal}$) to experimental ($q_{e,exp}$) . This suggests that of the two, the pseudo-second order is a more appropriate model to fit the adsorption data for all LDHs. This is in agreement with literature where the pseudo-second order model is commonly found to be a better fit for the adsorption of dyes onto LDHs, and suggests the mechanism is based on chemisorption. [34,178]

The two LDHs with the greatest uptake over 24 hours appeared to be $Ca_2Al\text{-}NO_3$ and $Mg_2Fe\text{-}CO_3$ with equilibrium uptakes of 1225 and 1088 mg g^{-1} respectively. While not as high as Ca_2Al and Mg_2Fe, $Mg_2Al\text{-}CO_3$ also had a notable uptake of 518 mg g^{-1}. While there was a large variance between q_e values of the six LDHs (65 – 1225 mg g^{-1}), K_2 values appeared to be of similar magnitude for all LDHs except for $Ni_2Al\text{-}NO_3$, between 1.675 – 3.990 x 10^{-5} g mg^{-1} min^{-1}. This indicated that the choice of M^{2+} and M^{3+} affects sorption capacity but not the speed of uptake. Interestingly, despite its reaction rate being an order of magnitude greater (2.266 x 10^{-4} g mg^{-1} min^{-1}), $Ni_2Al\text{-}CO_3$ had the lowest equilibrium uptake at 65 mg g^{-1}, indicating potential for rapid removal of AO7 in low concentration dye effluent. The large relative errors of $Ni_2Al\text{-}NO_3$ and $Zn_2Al\text{-}CO_3$ data points were attributed to the high initial AO7 concentrations (1500 mg L^{-1}) and low uptake.

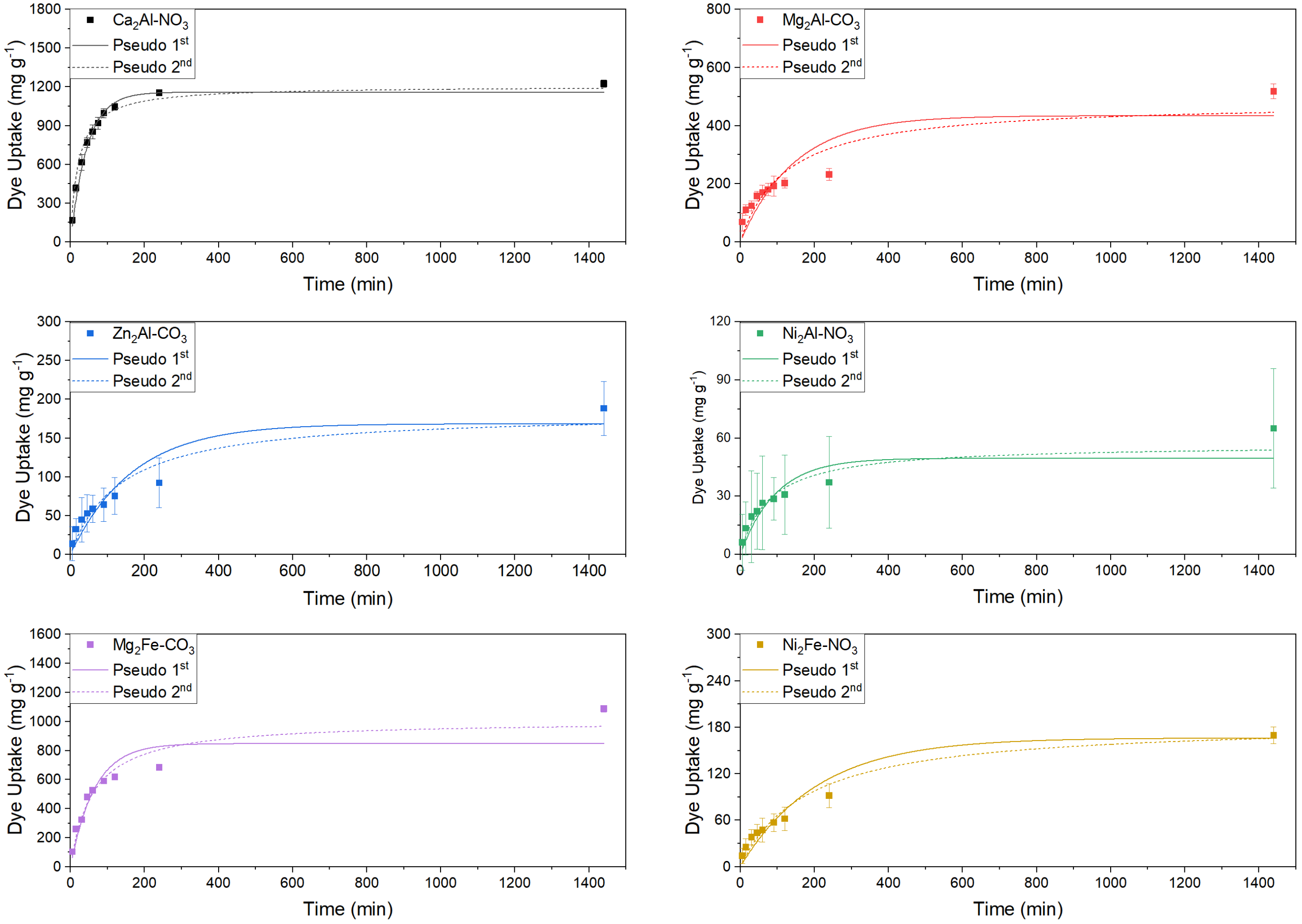

Figure 5.11. Uptake of Acid Orange 7 (AO7) dye over 24 hours, fit with pseudo-first order & pseudo-second order models: $Ca_2Al\text{-}NO_3$ (top left), $Mg_2Al\text{-}CO_3$ (top right), $Zn_2Al\text{-}CO_3$ (centre left), $Ni_2Al\text{-}NO_3$ (centre right), $Mg_2Fe\text{-}CO_3$ (bottom left), $Ni_2Fe\text{-}NO_3$ (bottom right)

Table 5.8. Kinetic constants from pseudo-first and pseudo-second order model fitting

		Pseudo 1st order			**Pseudo 2nd order**		
	$q_{e,exp}$ / mg g^{-1}	**K_1 / min^{-1}**	**$Q_{e,cal}$ / mg g^{-1}**	**R^2**	**K_2 / g mg^{-1} min^{-1}**	**$q_{e,cal}$ / mg g^{-1}**	**R^2**
$Ca_2Al\text{-}NO_3$	1225	0.0223	864	0.878	3.898×10^{-5}	1205	0.923
$Mg_2Al\text{-}CO_3$	518	0.0068	434	0.645	1.715×10^{-5}	482	0.787
$Zn_2Al\text{-}CO_3$	188	0.0060	168	0.804	3.990×10^{-5}	184	0.882
$Ni_2Al\text{-}CO_3$	65	0.0106	50	0.815	2.266×10^{-4}	57	0.909
$Mg_2Fe\text{-}CO_3$	1088	0.0155	847	0.851	1.675×10^{-5}	1004	0.939
$Ni_2Fe\text{-}NO_3$	165	0.0048	166	0.938	2.964×10^{-5}	186	0.962

The intra-particle diffusion model was also applied to experimental kinetic data. The rate of adsorption is complex and dependent on many different factors such as: [199]

- Diffusion of the solute from the solution to the sorbent surface (film diffusion).
- Diffusion from the surface to internal sites (such as the interlayer region).
- Saturation of the sorbent as equilibrium is reached and/or low adsorbate concentrations in solution.[234]

The result of this is that by using linear regression analysis of intra-particle model equation, the sorption mechanism can be split into three distinct regions with different rate limiting processes. This profile with separate rate limiting steps is evident upon looking at the linear intra-particle diffusion plot for Ca_2Al-NO_3 (Figure 5.12, top left). Initially over the first few hours surface adsorption is predominant, with the rate being limited to the diffusion of dye molecules onto the surface (Region A). [9] As the surface becomes saturated, adsorption of the dye molecules into the interlayer becomes the rate limiting step (Region B). Finally, as the state of equilibrium becomes reached through either saturation of adsorption sites or low concentration or sorbate left in solution (Region C). Interestingly, all other LDHs only had two distinct rate limiting processes suggesting that equilibrium saturation was not reached. This can be attributed to the high initial concentrations (~1500 mg L^{-1}) of dye used for the kinetic study when compared to the equilibrium uptake for these LDHs.

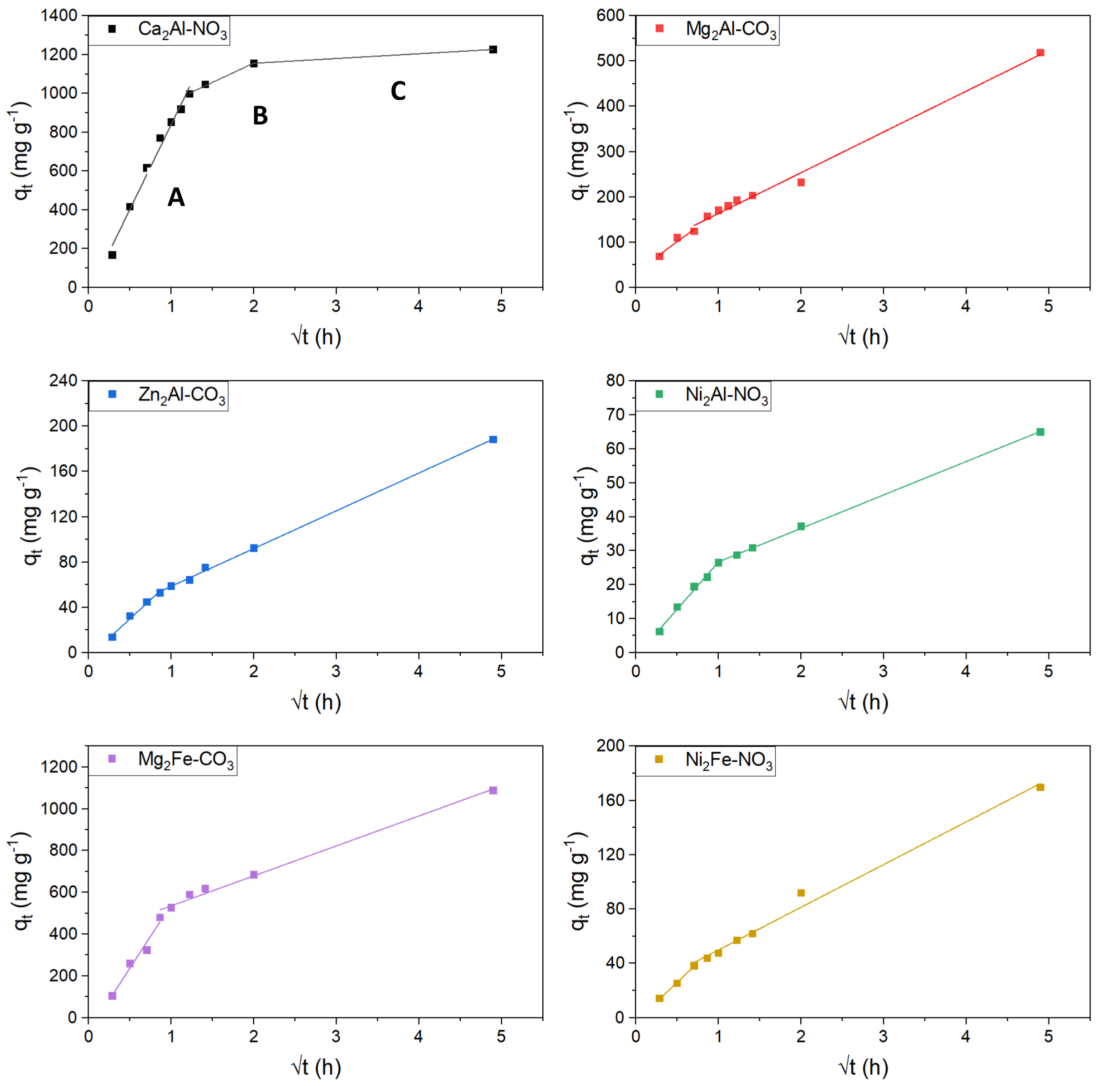

Figure 5.12. Linear intra-particle diffusion plots: Ca_2Al-NO_3 (top left), Mg_2Al-CO_3 (top right), Zn_2Al-CO_3 (centre left), Ni_2Al-NO_3 (centre right), Mg_2Fe-CO_3 (bottom left) and Ni_2Fe-NO_3 (bottom right)

In contrast to the other kinetic models, the rate parameters for the first two rate limiting processes (K_{dA} and K_{dB}), seen in Table 5.9, show that the adsorption rate to be an order of magnitude higher for $Ca_2Al\text{-}NO_3$, $Mg_2Al\text{-}CO_3$ and $Mg_2Fe\text{-}CO_3$ than the other LDHs. In fact, there appeared to be a direct correlation between equilibrium dye uptake (q_e). In addition to K_{id}, C_i values gives information regarding the thickness of boundary layers. If C_i is non-0 this indicates that intra-particle diffusion is the rate limiting step for the entire process. [274] The C_B values varied between 16.9 – 758.2 mg g^{-1} suggesting this is not the case. The negative C_A values during the first stage indicated a retardation of intra-particle diffusion due to the negligible boundary layer. [275] Interestingly the C_b values of $Ca_2Al\text{-}NO_3$ and $Mg_2Fe\text{-}CO_3$ were an order of magnitude greater than the other LDHs suggesting a greater proportion of the adsorption occurs while surface adsorption is predominant. This may indicate why both $Ca_2Al\text{-}NO_3$ and $Mg_2Fe\text{-}CO_3$ have the greatest propensity for AO7 removal as they are able to adsorb greater quantities of AO7 dye onto their surface alongside diffusion into the interlayer. It is evident from the R^2 values that the adsorption kinetics of AO7 onto LDHs is best described by both the pseudo-second order and intra-particle diffusion models.

Table 5.9. Constants from intra-particle diffusion modelling for the adsorption of AO7 onto LDH

LDHs	**Intra-particle diffusion model**								
	K_{dA} (mg $h^{-1/2}$ g^{-1})	**C_A (mg g^{-1})**	**$(R_A)^2$**	**K_{dB} (mg $h^{-1/2}$ g^{-1})**	**C_B (mg g^{-1})**	**$(R_B)^2$**	**K_{dC} (mg $h^{-1/2}$ g^{-1})**	**C_c (mg g^{-1})**	**$(R_C)^2$**
Ca_2Al-NO_3	854.0	-17.0	0.991	199.0	758.2	0.994	24.5	1105.4	0.784
Mg_2Al-CO_3	220.7	1.34	0.998	88.9	77.1	0.993	N/A	N/A	N/A
Zn_2Al-CO_3	63.5	-1.4	0.968	33.7	24.0	0.998	N/A	N/A	N/A
Ni_2Al-NO_3	26.9	-0.5	0.994	9.9	16.9	0.999	N/A	N/A	N/A
Mg_2Fe-CO_3	480.4	-8.0	0.976	143.4	391.7	0.990	N/A	N/A	N/A
Ni_2Fe-CO_3	53.7	-0.7	0.997	31.4	18.4	0.989	N/A	N/A	N/A

5.5.2. Adsorption Isotherms

While kinetic experiments give an idea of both the rate of adsorption and equilibrium uptake, an isotherm study was conducted to discern adsorption capacity. Experimental data was analysed using both the Langmuir and Freundlich models as they are the most widely used models in literature. This is due to both the simplicity of their linear regression methods and generally better R^2/residual sum of squares (SSE) when compared to other adsorption models. [200] The isotherm plots, compared against both the Langmuir and Freundlich models, can be seen in Figure 5.13. Parameters obtained from linear regression analysis can be found in Table 5.10. The correlation coefficients (R^2) show that all LDHs portrayed a greater fit towards the Langmuir model, indicating adsorption sites are homogeneous and that the dye forms a monolayer on the surface with negligible interactions between particles. [20] In contrast, the Freundlich model is an empirical model that suggests adsorption is best described by chemisorption mechanisms onto heterogeneous adsorption sites with differing adsorption energies. This observation was expected as the majority of studies surrounding adsorption of dyes onto LDHs show the Langmuir to be a better model to model adsorption equilibrium. [194]

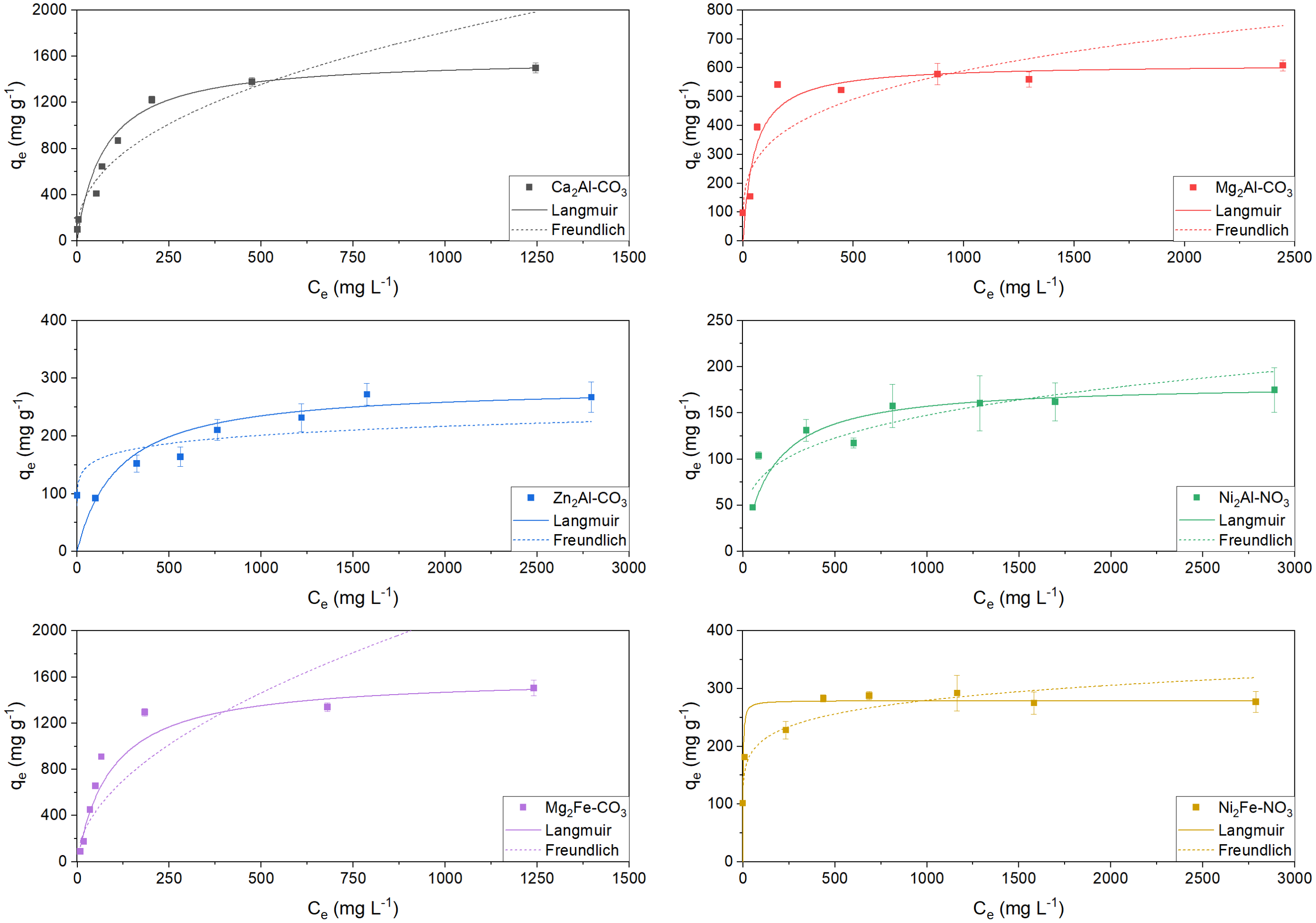

Figure 5.13. Adsorption of AO7 at varying concentration (C_0 = 100 - 3000 mg L^{-1}); V_{dye} = 50 mL; adsorbent loading = 1 g L^{-1}; Ca_2Al-NO_3 (top left), Mg_2Al-CO_3 (top right), Zn_2Al-CO_3 (centre left), Ni_2Al-NO_3 (centre right), Mg_2Fe-CO_3 (bottom left) and Ni_2Fe-NO_3 (bottom right)

Table 5.10. Isotherm parameters for the adsorption of AO7

	Langmuir			**Freundlich**		
	K_L / L mg^{-1}	**Q_m / mg g^{-1}**	**R^2**	**K_F / L$^{1/n}$.mg$^{1-1/n}$.g^{-1}**	**n**	**R^2**
$Ca_2Al\text{-}NO_3$	0.013	1586	0.990	100.6	2.39	0.961
$Mg_2Al\text{-}CO_3$	0.019	612	0.998	95.3	3.79	0.848
$Zn_2Al\text{-}CO_3$	0.004	287	0.981	95.9	9.32	0.617
$Ni_2Al\text{-}CO_3$	0.006	182	0.993	23.9	3.80	0.782
$Mg_2Fe\text{-}CO_3$	0.010	1603	0.992	55.6	1.90	0.793
$Ni_2Fe\text{-}NO_3$	0.619	279	0.999	115.6	7.82	0.899

The largest maximum uptakes (q_m) were once again observed for $Ca_2Al\text{-}NO_3$ and $Mg_2Fe\text{-}CO_3$ at 1586 and 1603 mg g^{-1} respectively, indicating they had the most potential for AO7 removal. Close to 100 % removal was achieved at lower concentrations of 100 and 250 mg L^{-1} (Figure 5.14). In all instances q_m values were larger than the q_e values observed in the kinetic study (Table 5.10), suggesting complete saturation of the sorbents was not achieved at equilibrium (C_0 = 1500 mg L^{-1}). Interestingly the Langmuir constant (k_L) for $Ni_2Fe\text{-}NO_3$ appeared to be over ten-fold greater than the other LDHs. K_L illustrates the ratio of both the adsorption and desorption rate thus suggesting that, despite having considerably lower saturation uptakes of AO7 than the likes of $Ca_2Al\text{-}NO_3$, $Mg_2Fe\text{-}CO_3$ and $Mg_2Al\text{-}CO_3$, $Ni_2Fe\text{-}NO_3$ had a much greater affinity for AO7 dye adsorption.

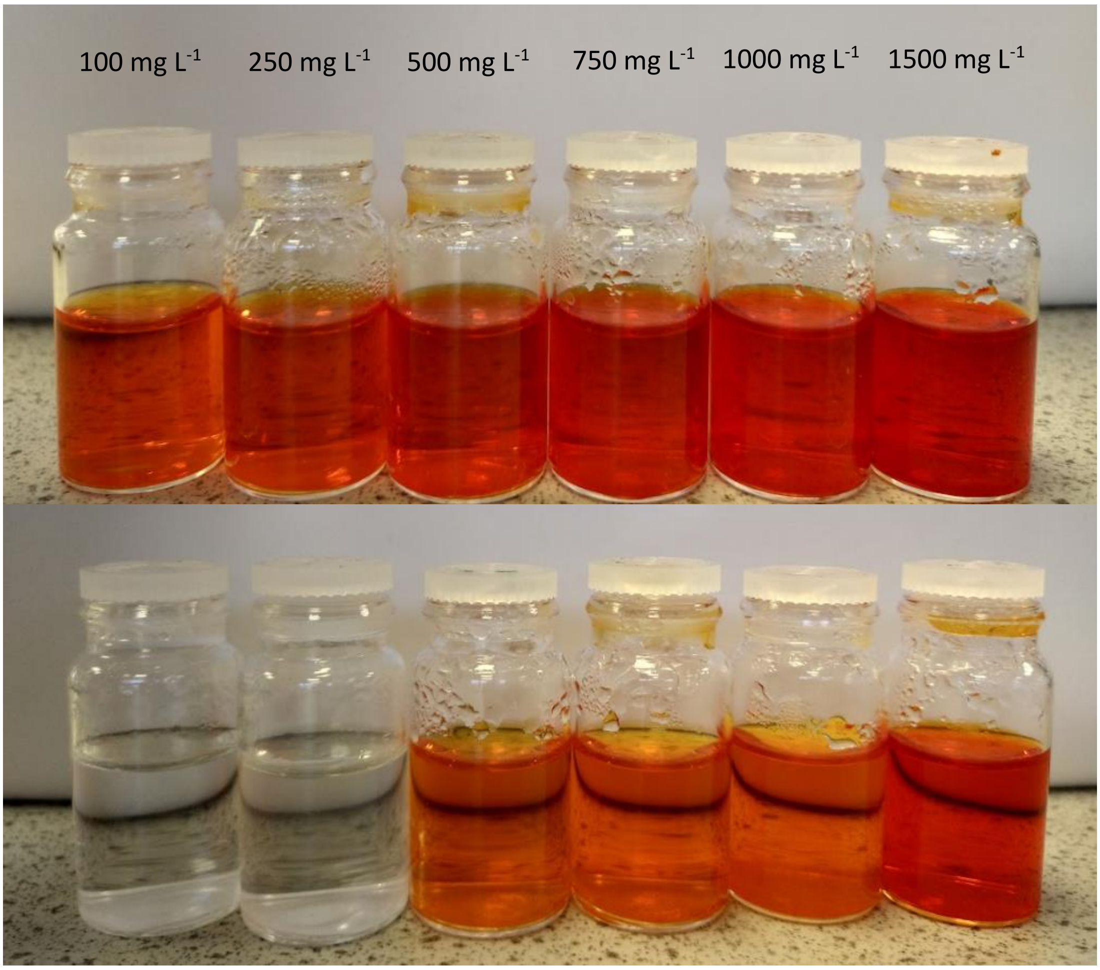

Figure 5.14. The uptake of AO7 onto Ca_2Al-NO_3 over 24 hours at varying initial concentration: Initial concentration (top) and final concentration (bottom)

5.5.3. The Impact of pH on Adsorption of AO7

pH is of great importance for the sorption of dyes onto LDHs as it impacts many phenomena including the sorbent surface charge, degree of ionization, dissociation of functional groups on active sites and the solubility of the dye. [165] Within the literature review it was highlighted that the pH of textile effluents can vary drastically from highly basic to acidic (Section 2.1.4). This was found to be dependent on the specific textile industry, the stage of the dyeing process the effluent was discharged and local legislations/regulations. Therefore the performance of LDHs as sorbents for dyes at varying pH is paramount to ensure application for a wide range of industrial effluents.

Prior to pH analysis, the pH_{PZC} was calculated for each individual LDH to aid in the understanding of the surface charge at different pHs. An interesting phenomenon of LDHs is their ability to pH buffer. While many papers have reported pH dependence for dye sorption, [194] other papers have reported that sorption is independent of pH due to a buffering effect for uncalcined LDHs. [167,168] This is due to hydrogen ions being neutralized by the hydroxyl groups in the brucite layer at low pHs, and deprotonation of the LDH surface at high pH. [20] This buffering phenomenon was observed for all six LDHs studied, buffering in close proximity to their pH_{PZC} regardless of initial pH (Table 5.11), indicating a preference for the LDHs to be charge neutral in solution.

Table 5.11. pH_{PZC} of LDHs and their buffering pH by pH drift method

LDH	pH_{PZC}	Buffering pH	Literature pH_{PZC}	Ref
$Ca_2Al\text{-}NO_3$	10.63 ± 0.34	10.22 – 10.91	7.29	[165]
$Mg_2Al\text{-}CO_3$	8.21 ± 0.12	8.06 – 8.44	11.00, 6.98	[162,167]
$Zn_2Al\text{-}CO_3$	7.60 ± 0.20	7.30 – 8.05	7.58	[15]
$Ni_2Al\text{-}NO_3$	6.79 ± 0.14	6.56 – 6.92	9.70	[178]
$Mg_2Fe\text{-}CO_3$	8.82 ± 0.13	8.70 – 9.11	10.40, 8.00	[162,276]
$Ni_2Fe\text{-}CO_3$	7.39 ± 0.19	7.20 – 7.74	N/A	

Interestingly there appeared to be a correlation between pH_{PZC} of the LDHs and q_m values of AO7 uptake, discussed previously. The pH_{PZC} of $Ca_2Al\text{-}NO_3$ and $Mg_2Fe\text{-}CO_3$ were considerably higher than the other LDHs, at 10.63 and 8.82 respectively, requiring more alkaline conditions to reach neutral surface charge. Similarly, $Ni_2Al\text{-}NO_3$ had both the lowest pH_{PZC} of 6.79 and lowest overall uptake of AO7 (182 mg g^{-1}). Metal hydroxide's surface charge is dependent on the deprotonation and protonation of surface atoms, alongside leaching of charged species into solution and their subsequent readsorption. [277] As the pH_{PZC} of Ca_2Al-NO_3 and Mg_2Fe-CO_3 is greater, this indicates a greater amount of leaching of surface OH^- ions into solution. This could result in a larger positive charge excess within the brucite layer and increase the quantity of anionic species (i.e: AO7 dye) that can be adsorbed.

The pH_{PZC} calculated in this study did not appear to correspond with values observed in literature. For example, one study reported a pH_{PZC} of Ni_2Al-NO_3 of 9.70, while within this work a much lower pH_{PZC} of 6.79 was observed. [178] There also appeared to be discrepancy within literature, with different papers reporting very different values. For example, two separate authors reported vastly different pH_{PZC} of Mg_2Al-CO_3: 11.00 and 6.98. [162,167] Common zeta potential calculations in literature tend to use a zetasizer, however this requires highly stable suspensions for accurate measurements. [158] As LDHs tend to aggregate and settle out of solution this reduces the accuracy and reproducibility of results which may explain the variance of values found. In addition, both synthesis method and physical properties of LDHs likely alter its ability to buffer, with PZC being dependent on crystal structure and elemental constituents, [278] although no papers were found that directly observe this effect.

From Figure 5.15 - Figure 5.20 it can be seen that varying initial pH between 4 – 10 generally has little impact on the overall uptake of acid orange 7, with less than 5 % deviation occurring for Mg_2Al-CO_3, Mg_2Fe-CO_3 and Ni_2Fe-NO_3. This was attributed to the buffering effect discussed earlier. For example, the adsorption of AO7 onto Mg_2Al-CO_3 was maintained around ~610 mg g^{-1}, due to buffering the pH between 8.24 – 8.58 regardless of initial pH. Similarly, the adsorption of AO7 onto Ni_2Al-NO_3 (Figure 5.18) was maintained between 170 – 190 mg g^{-1} between pH 4 -10, with the pH buffering between 6.60 – 6.90 (pH_{PZC} = 6.79). Interestingly, in the few instances where the buffering was not as effective, changes in overall uptake capacity of AO7 were observed. For Ca_2Al-NO_3, there was little change in overall uptake (~1200 mg g^{-1}) with initial pH's of 4,6 and 10 due to the pH buffering to its pH_{PZC} around 10.20-10.40 (Figure 5.15). However, at pH 8 an increase in AO7 uptake to 1353 mg $g-^{1}$ was observed, attributed to a lower pH buffer of 9.25. This pH is considerably lower than the pH_{PZC} of Ca_2Al-NO_3 (pH_{PZC} = 10.63) and would allow for a greater degree of surface adsorption as a result of the positively charged surface that would result.

This suggests that while the pH of solution does play a vital role in adsorption performance, modification of the pH has very limited impact due to the buffering effect that occurs. This implies that these LDH sorbents can be utilised in a variety of wastewater streams, achieving comparable dye removal capacities regardless of the streams pH.

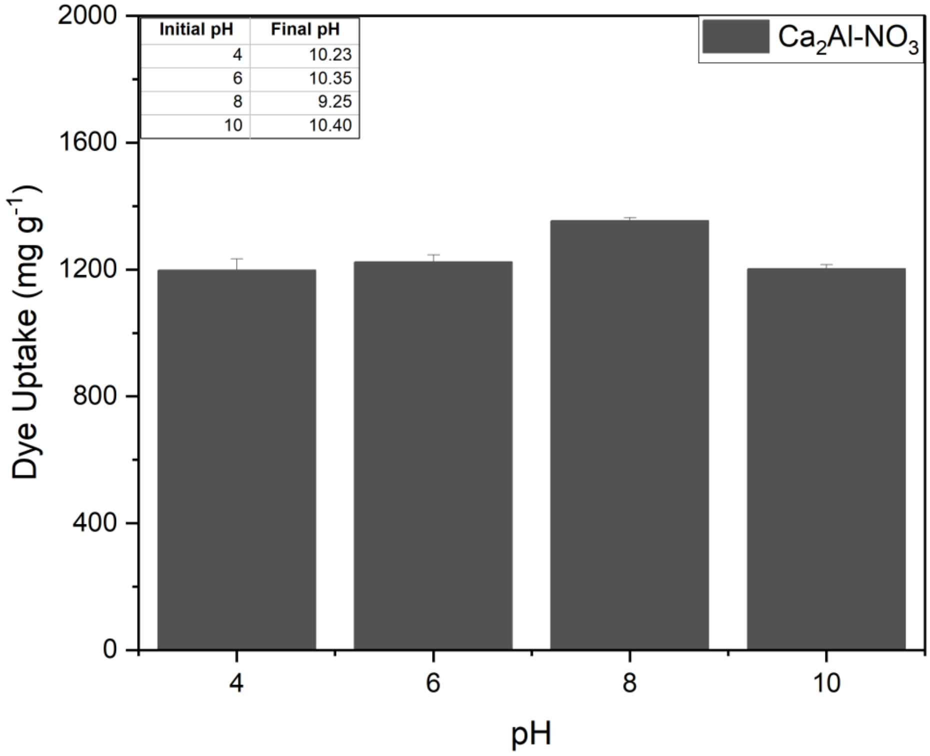

Figure 5.15. The impact of pH on AO7 adsorption onto $Ca_2Al\text{-}NO_3$ LDH

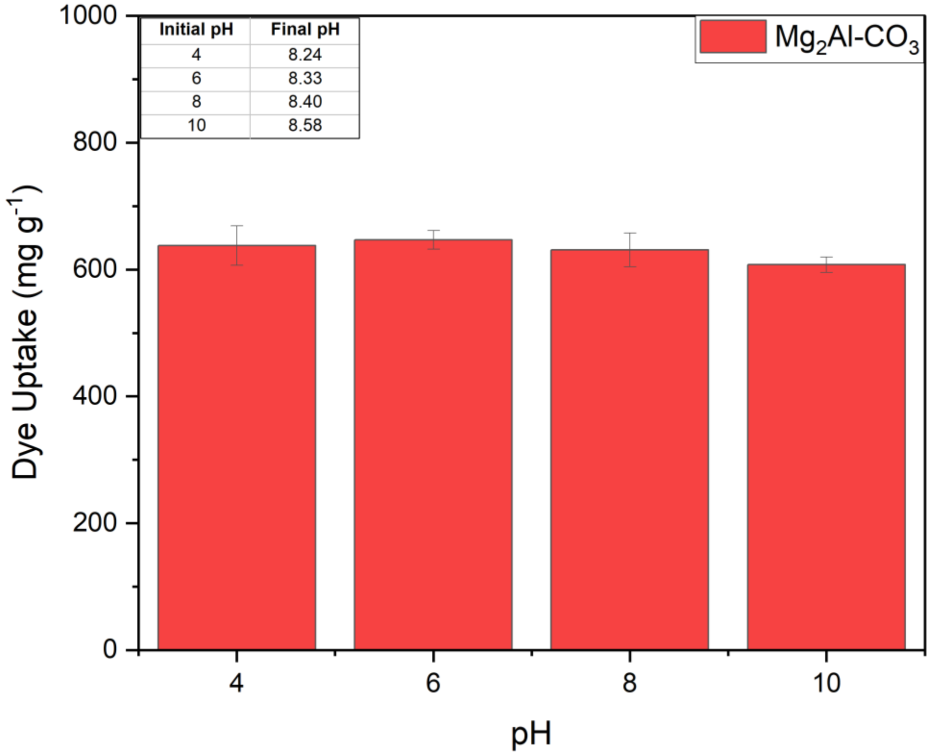

Figure 5.16. The impact of pH on AO7 adsorption onto $Mg_2Al\text{-}CO_3$ LDH

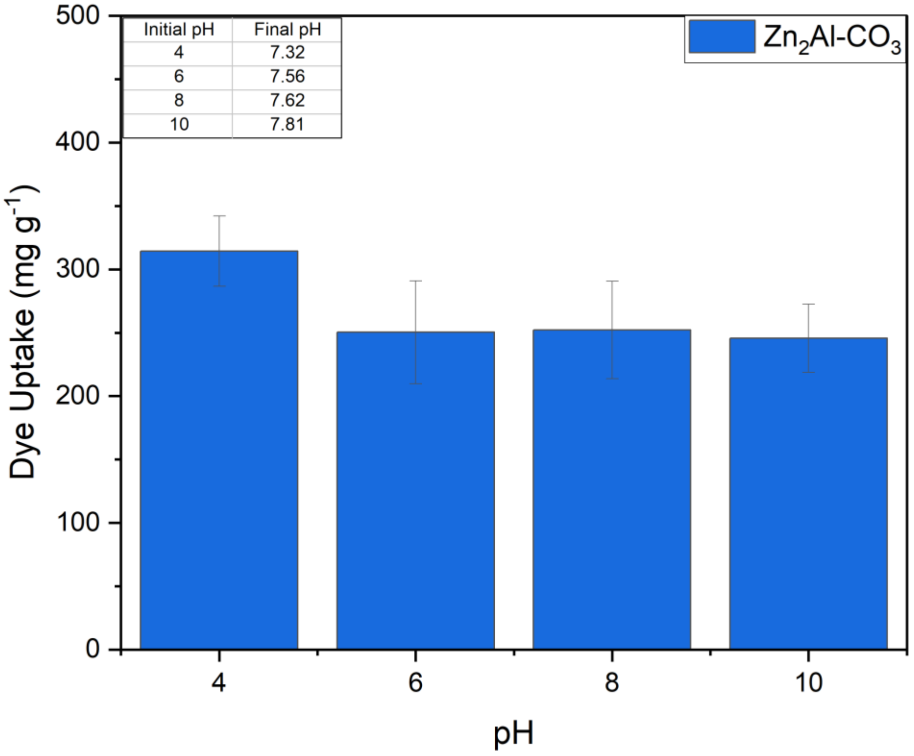

Initial pH	Final pH
4	7.32
6	7.56
8	7.62
10	7.81

Figure 5.17. The impact of pH on AO7 adsorption onto $Zn_2Al\text{-}CO_3$ LDH

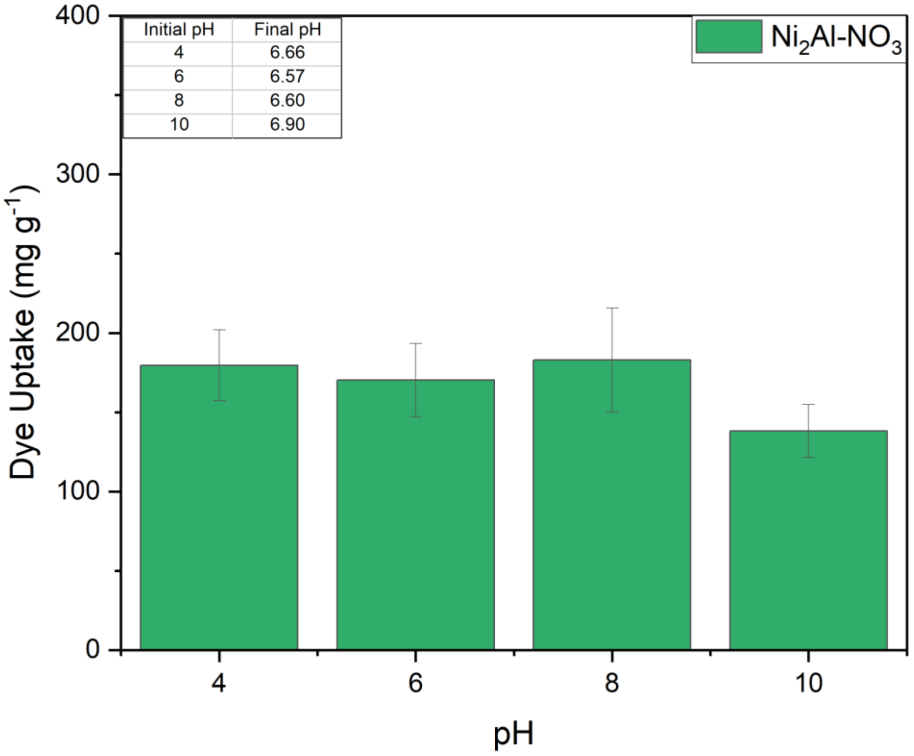

Initial pH	Final pH
4	6.66
6	6.57
8	6.60
10	6.90

Figure 5.18. The impact of pH on AO7 adsorption onto $Ni_2Al\text{-}NO_3$ LDH

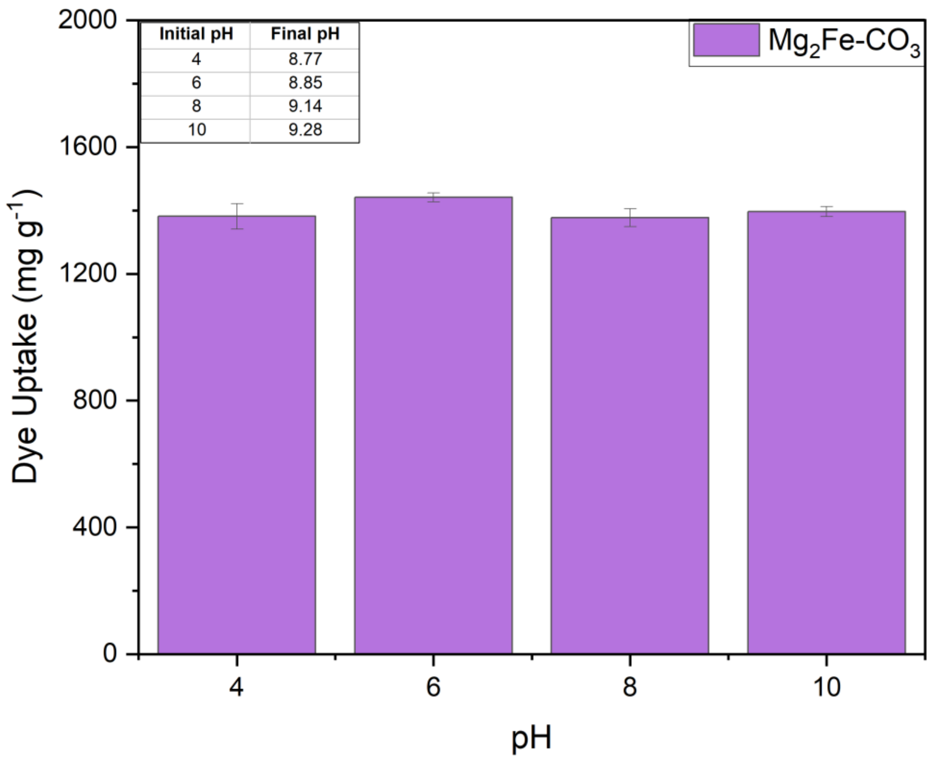

Figure 5.19. The impact of pH on AO7 adsorption onto Mg_2Fe-CO_3 LDH

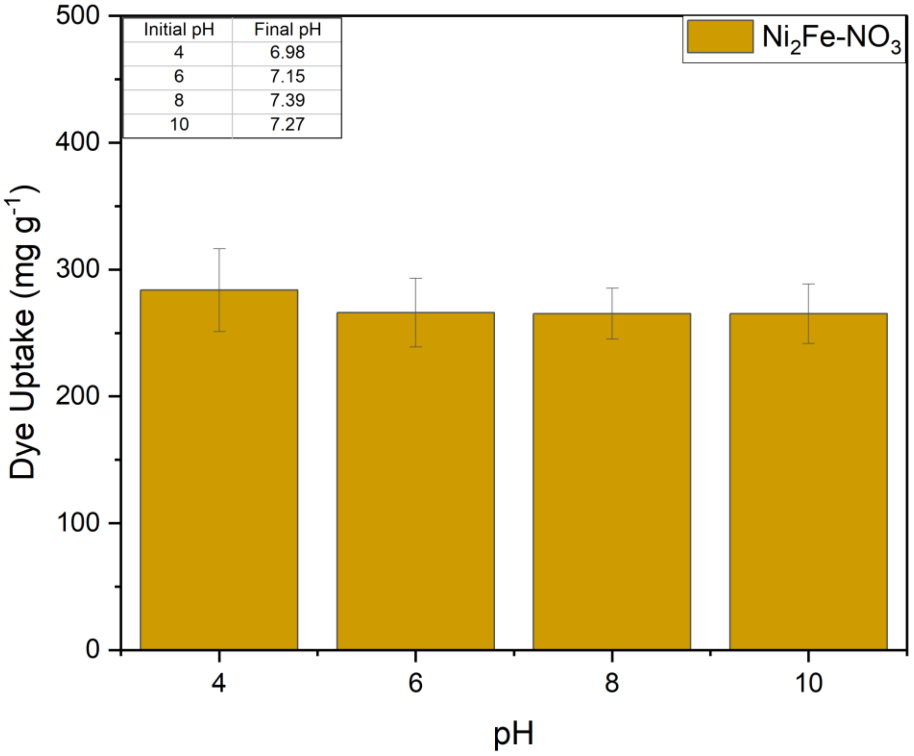

Figure 5.20. The impact of pH on AO7 adsorption onto Ni_2Fe-NO_3 LDH

5.5.4. pH Buffering

Due to its importance for dye sorption a further investigation into the pH buffering effect was conducted; A focus was placed on the speed at which pH buffering occurs, and the effectiveness of buffering over multiple pH ramps. The speed at which pH buffering occurs is important as it will indicate how effective pH modification is at the initial stages of sorption. If the system very rapidly reaches its buffered pH, any modification to pH will have very limited impact on sorption uptake. In contrast, if buffering occurs at a slower rate pH modification may still be able to increase sorption uptake over the initial stages. The effectiveness of buffering over multiple cycles is equally as important as it will play a role in the adsorption cycle after regeneration of the sorbent.

In this study each LDH was placed in a pH modified solution (pH ~4) and monitored every 24 h to determine pH change. After monitoring pH, the solution was immediately acidified (pH ~4) and left to buffer again. During the first cycle the pH change was monitored over the initial hour to determine buffering speed. The impact of these acidification cycles on pH buffering can be seen in Figure 5.21. Upon addition of all LDHs to the acidified solution within 5-10 minutes the pH rose close to that of the buffering pH, where it then levelled off. This suggests that pH modification has a negligible impact on sorption over the initial stages as the system very rapidly restores the pH to the LDHs pH_{PZC}.

When multiple cycles of acidification occurred, it appeared that a steady decline in the buffered pH was observed over seven days for nearly all LDHs. $Ca_2Al\text{-}NO_3$ was the only LDH that was able to continuously buffer back to its pH_{PZC} over all acidification cycles. It should be noted that, while the pH change is shown visually in Figure 5.21 to be a straight line, in reality it is more likely to mimic that of logarithmic decay – plateauing at the buffered pH. Interestingly this analysis suggests that pH modification may have greater potential after multiple adsorption cycles for many LDHs due to their inability to continuously buffer to their pH_{PZC}. For example, after seven days of pH buffering cycle the equilibrium pH of $Mg_2Al\text{-}CO_3$ in solution decreased from its pH_{PZC} of 8.21 to 5.22. At this lower pH, sorption of anionic dyes may become more favourable due to the positively charged surface. However, this is under the assumption that the LDH is water stable, no degradation of the material occurs and that the pH_{PZC} does not change over continuous buffering cycles. As a result, further experimentation is required to test this hypothesis, to understand the relationship between pH buffering and adsorption cycling.

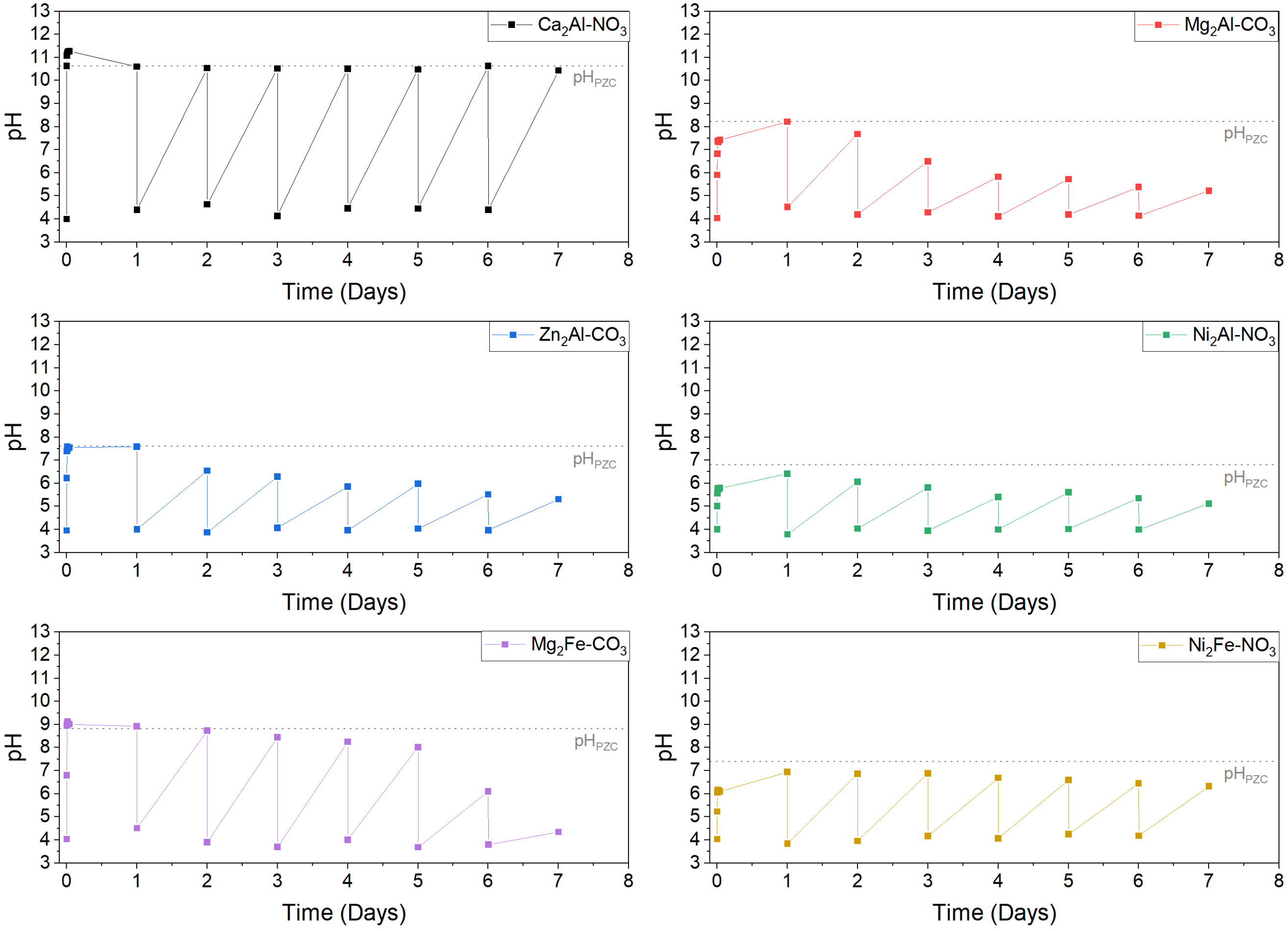

Figure 5.21. The impact of acidification cycles on pH buffering. Ca2Al-NO3 (top left), Mg2Al-CO3 (top right), Zn2Al-CO3 (centre left), Ni2Al-NO3 (centre right), Mg2Fe-CO3 (bottom left) and Ni2Fe-NO3 (bottom right

5.5.5. Comparison of Adsorption Analysis to Physical Properties of LDHs

It is evident from adsorption analysis that changing the M^{2+} and M^{3+} ions within LDH structure had a profound effect on adsorption capacities, with uptake of AO7 varying between 182 – 1603 mg g^{-1}. While both Ca_2Al-NO_3 and Mg_2Fe-CO_3 had the most potential for AO7 removal, with q_m over 1000 mg g^{-1} higher than other LDHs, adsorption analysis did not reveal any direct reasons why this is the case. Despite having vastly different maximum uptakes (q_m) for AO7 the sorption mechanisms were all relatively similar, portraying the best fit for pseudo-second order kinetics and the Langmuir/intra particle diffusion models. It is well documented in literature that some physical characteristics of LDHs play a crucial role in sorption mechanisms. From analysis of the physical properties of LDHs in Section 5.4 it was evident that altering M^{2+}/M^{3+} ions also affected crystallinity, PSD and surface area. As a result of this, a comparison of sorption analysis to physical characteristics was conducted on the six LDHs. Adsorption properties and physical properties are summarised in Table 5.12.

It has been previously discussed that one parameter that goes hand in hand with sorption is the surface area of the sorbent. Increased surface area of sorbents is often followed by increased sorption capacities due to the increased number of adsorption sites. It is one of the main reasons why calcined LDHs have become of significant interest over previous years due to their larger surface areas compared to their uncalcined counterparts. [279] In Chapter 4 it was reported that surface area, altered through variations in synthesis temperature, played a vital role in the adsorption of AO7 onto Co_2Al-CO_3. While in this work the synthesis temperature was constant, it was thought that modifying the M^{2+} and/or M^{3+} ions in the hydroxide sheets may alter the favourability of platelet stacking occurring during synthesis, resulting in different surface areas and sorption capacities. Unfortunately, there did not appear to be any correlation between sorption capacity, surface area or crystal domain length (Table 5.12). While Ca_2Al-NO_3 did possess both the largest maximum uptake of AO7 and largest platelets, it also had one of the lowest surface areas at 5 m^2 g^{-1}. Similarly, despite having a surface area lower than Mg_2Al-CO_3 (91 m^2 g^{-1}), Zn_2Al-CO_3 (51 m^2 g^{-1}) and Ni_2Fe-NO_3 (m^2 g^{-1}), Mg_2Fe-CO_3 had a q_m of 1603 mg g^{-1}. In addition, there was no direct correlation with surface area and crystal domain length in the 003/002 plane suggesting that platelet stacking was not the only phenomena that played a role in surface area of the LDHs. From this it was evident that neither surface area or platelet size were the primary reason for the differences in AO7 adsorption.

Table 5.12. A comparison of sorption analysis to physical characteristics

LDH	**q_m / mg g^{-1}**	**Kinetic Model**	**Isotherm**	**Surface Area / m^2 g^{-1}**	**CDL$_{003}$ / nm**	**M^{2+}:M^{3+} Ratio**	**Interlayer**	**Basal Spacing / nm**
$Ca_2Al\text{-}NO_3$	1586	2nd	L / IPD	5	22.2	1.98	NO_3^-	0.85
$Mg_2Al\text{-}CO_3$	612	2nd	L / IPD	91	11.7	2.61	CO_3^{2-}	0.77
$Zn_2Al\text{-}CO_3$	287	2nd	L / IPD	51	20.6	2.32	CO_3^{2-}	0.76
$Ni_2Al\text{-}NO_3$	182	2nd	L / IPD	1	3.9	2.67	NO_3^-	0.77
$Mg_2Fe\text{-}CO_3$	1603	2nd	L / IPD	35	10.0	1.99	CO_3^{2-}	0.77
$Ni_2Fe\text{-}NO_3$	279	2nd	L / IPD	46	4.6	1.90	NO_3^-	0.78

$$PO_4^{3-} > CO_3^{2-} > SO_4^{2-} > NO_3^{-} > Cl^{-}$$

Figure 5.22. Affinity of common anions into the interlayer region

Another characteristic of LDHs known to impact sorption capacities is the $M^{2+}:M^{3+}$ ratio. For all LDHs synthesised within this study the $M^{2+}:M^{3+}$ ratio was maintained between 1.90 – 2.67. There did not appear to be any correlation between metal ratios and surface area/crystallinity. As the optimal $M^{2+}:M^{3+}$ ratios for only a few LDHs have been reported in literature ($MgFe-CO_3$ and $MgAl-NO_3$) and the ratios for all LDHs was maintained within the 2-4 optimal range it was concluded that metal ratio was also unlikely to be the key factor differentiating changes in q_m observed.

A final comparison was made to determine if the interlayer region was the cause of the increased sorption capacity for Ca_2Al-NO_3 and Mg_2Fe-CO_3 LDHs. LDH materials have a greater affinity towards anions with higher charge density (Figure 5.22). [229] As both NO_3^- and Acid Orange 7 are single valent species they have a lower charge density than CO_3^{2-} and bind less favourably in the interlayer as a result. It was therefore expected that LDHs synthesised with a NO_3^- interlayer would have greater sorption capacities. While this appeared to be the case for Ca_2Al-NO_3, both Mg_2Fe-CO_3 and Mg_2Al-CO_3 had greater sorption capacities than the other NO_3^- intercalated LDHs (Ni_2Al-NO_3 and Ni_2Fe-NO_3).

From this it was concluded that if physical properties are to play a role in sorption potential it is likely to be dependent on a combination of factors that often juxtapose one another. For example, while the high adsorption capacity of Ca_2Al-NO_3 may be attributed to its more favourably exchanged interlayer NO_3^-, these high adsorption capacities are not observed for Ni_2Al-NO_3 or Ni_2Fe-NO_3 as the presence of Ni^{2+} within the structure reduced their inherent crystallinity. Similarly, while the higher surface areas of Mg_2Al-CO_3 and Zn_2Al-CO_3 increase the number of binding sites, adsorption by ion exchange is likely hindered by the strongly bound CO_3^{2-} interlayer anion. This relationship between M^{2+}/M^{3+} choice and numerous LDH properties is not all that surprising when considering that CFHS process variables are interconnected with many different factors. Even a simple change of precursor such as $M(OH)_x$ can have a profound effect on reaction kinetics, mixing regime and conversion rates of product – all of which will affect product composition, morphology, crystallinity, particle sizes and PSD. [127]

A comparison of LDHs within this study to other sorbents in literature, for the adsorption of AO7, can be seen in Table 5.13. Uptake capacities of Ca_2Al-NO_3, Mg_2Al-CO_3 and Mg_2Fe-CO_3 far exceeded most sorbents, with only a chitosan-based sorbent exhibiting a higher uptake capacity (2352 mg g^{-1}). However, it should be noted that the chitosan@Zr composite was synthesised via an arduous co-precipitation method, with long aging times (4h). The LDHs within this study may therefore be a more promising choice for industrial scale-up due to the rapid, continuous nature of the synthesis. The adsorption rates (k_1) of Ca_2Al-NO_3 and Mg_2Fe-CO_3 were also comparable to sorbents such as pumice, bentonite, and chitosan. The pseudo-first order rate constant of a three-dimensional flower-like Mg_2Al-SDS LDH was over an order of magnitude higher at 5.039 min^{-1}, suggesting the adsorption rates of LDH uptake could be further improved upon expansion of the interlayer and changes to morphology.

Table 5.13. Comparison of sorption capacities and rate constants of LDHs, for AO7 adsorption, with other sorbents in literature

Adsorbent	**Maximum Uptake / mg g^{-1}**	**Pseudo-first order rate constant (k_1) / min^{-1}**	**Pseudo-second order rate constant (k_2) / g mg^{-1} min^{-1}**	**Reference**
Ca_2Al-NO_3 LDH	1586	0.0223	3.898×10^{-5}	*This Study*
Mg_2Al-CO_3 LDH	612	0.0068	1.715×10^{-5}	*This Study*
Zn_2Al-CO_3 LDH	287	0.0060	3.990×10^{-5}	*This Study*
Ni_2Al-NO_3 LDH	182	0.0106	2.266×10^{-4}	*This Study*
Mg_2Fe-CO_3 LDH	1603	0.0155	1.675×10^{-5}	*This Study*
Ni_2Fe-NO_3 LDH	279	0.0048	2.964×10^{-5}	*This Study*
Mg_2Al-SDS LDH	485.6	5.039	0.021	[39]
Activated Carbon	440.0	-	0.1809	[238]
ZIF-8 MOF	16.9	-	-	[239]
UiO-66 MOF	106.6	-	-	[239]
Modified Pumice	1.08	0.017	0.007	[240]
TiO_2 Nanotube	137	N/A		[144]
Polymer Modified Bentonite	208.6	0.0301	0.0266	[241]
Magnetic Biochar (sewage Sludge & Woodchip)	110.27	-	0.014	[195]
Zirconium-Chitosan Composite	2352.99	0.0198	3.4×10^{-5}	[242]

5.6. Batch Adsorption of Synthetic Dyes with Ca_2Al-NO_3 and Mg_2Fe-CO_3 LDHs

It is evident from Section 5.5 that both Ca_2Al-NO_3 and Mg_2Fe-CO_3 LDHs have great potential for the adsorption of acid orange 7 dye, evidenced by their greater maximum uptakes (1586 and 1603 mg g^{-1} respectively). This was attributed to multiple factors including interlayer anion and pH buffering effects. However, another factor that plays a vital role on dye adsorption is the dye molecule itself. Different dyes can have vastly different adsorption capacities with LDHs depending on their size, shape, charge and chemical structure. [170] As a result, it would be biased to base the potential of LDHs for dye remediation on their capability of adsorbing a singular dye, AO7. Therefore, the adsorption capacities of Ca_2Al-NO_3 and Mg_2Fe-CO_3 LDHs were compared against four other dyes commonly found in literature: sunset yellow (SY), evan's blue (EB), methylene blue (MB) and safranin-O (Saf-O).

Table 5.14. Chemical properties of dyes.

Dye	Particle Charge		Chemical Structure	Molecular Mass / g mol^{-1}	Λ_{max}	Ref
Acid Orange 7	Anionic	-1	Azo	350.3	485	[238,240]
Sunset Yellow	Anionic	-2	Azo	452.4	480	[165]
Evan's Blue	Anionic	-4	Azo	960.8	608	[149]
Methylene Blue	Cationic	+1	Thiazine	319.9	664	[14,39]
Safranin-O	Cationic	+1	Trimethyl	350.9	520	[197]

These dyes were chosen based on their differing particle charge, chemical structure and molecular mass (Table 5.14). Particle charge, and the functional groups that contribute to charge, are well known to play a role in sorption capacity. It is generally observed that an increase in functional groups that contribute to charge reduces adsorption capacity as they occupy a greater number of active sites. [9] Acid orange 7, sunset yellow and evan's blue were chosen as good candidates to observe this effect as they are all sulfonate based azo dyes with differing numbers of $R-SO_3^-$ functional groups. In addition, increasing the number of $R-SO_3^-$ groups has the consequence of increasing molecular mass, which can also reduce adsorption capacity due to steric hindrance.

As AO7, SY and EB are all anionic dyes, they can be adsorbed by LDHs by both intercalation mechanisms and surface sorption. [20] Methylene blue and safranin-O were therefore chosen due to their cationic nature to determine if they could be adsorbed, despite intercalation into the interlayer being electrostatically unfavourable. In addition to this, both methylene blue and safranin-O have differing chemical structures, with methylene blue being phenothiazine based and safranin-O phenyl diaminophenazine. It was hoped that comparisons of the two when adsorbed by Ca_2Al-NO_3 and/or Mg_2Fe-CO_3 would provide insights into the role of chemical structure for adsorption.

5.6.1. Adsorption Isotherm

An isotherm experiment on all five dyes (AO7, SY, EB, MB and Saf-O) was conducted on Ca_2Al-NO_3 and Mg_2Fe-CO_3. Isotherm plots for each dye can be seen in Figure 5.23. From the linear regression fit (Table 5.15) it appeared that the anionic dyes (AO7, SY and EB) portrayed a greater fit towards the Langmuir model as evidenced by the correlation coefficients ($R^2 > 0.9$). This is in agreement with literature and indicates that adsorption sites are homogeneous and adsorption occurs predominantly by formation of a monolayer on the surface. [20] It was expected that adsorption uptake would follow the trend AO7 > SY > EB due to molecular size and number of sulfonate groups, however this was not the case. While it was expected that AO7 would have the greatest maximum uptake (q_m) for both Ca_2Al-NO_3 and Mg_2Fe-CO_3 (q_m = 1586 mg g^{-1} and 1603 mg g^{-1}) due to having less SO_3^- groups to occupy active sites, SY appeared to have a lower q_m than EB. Despite only having two SO_3^- groups, compared to EB's four, SY had the lowest uptakes for the anionic dyes at 72 and 91 mg g^{-1} for Ca_2Al-NO_3 and Mg_2Fe-CO_3 respectively, suggesting another phenomenon was affecting adsorption uptake onto SY. In addition, uptake of SY was considerably lower than what is observed in literature. For example one author reported a q_m value of 398.41 mg g^{-1} for SY onto Ca_2Al-NO_3, 450 % greater than what was reported herein. [40] K_L values reported were also 4x higher than within this work, suggesting this may be explained in part to be due to weaker interactions between Ca_2Al-NO_3 and SY. It was hoped that this would be further explained by kinetic and pH studies. Previous pH analysis with AO7 adsorption in Section 5.5.3 has shown that buffering pH and pH_{PZC} play an important role in adsorption uptake which may explain why the uptake of SY was lower than expected.

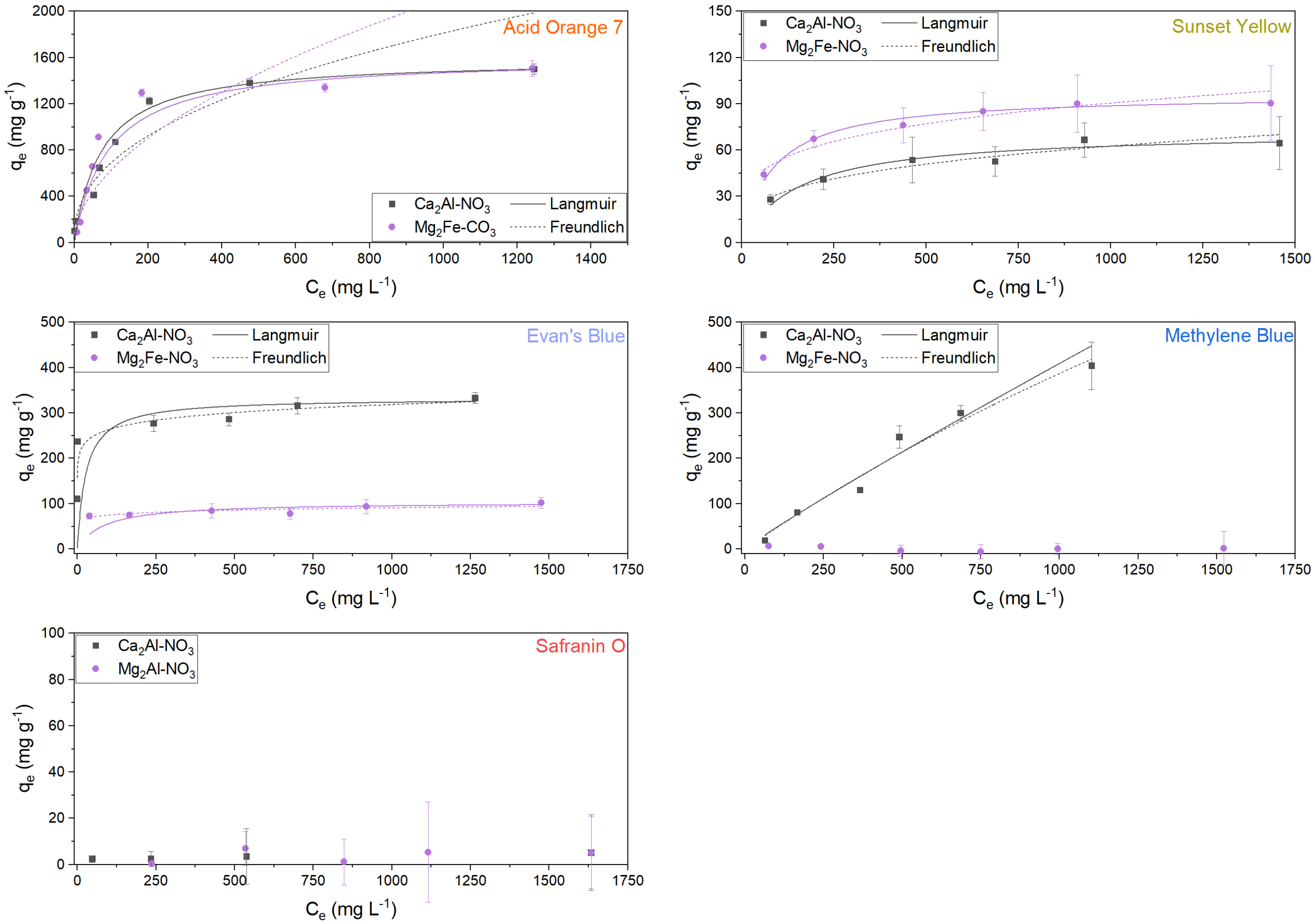

Figure 5.23. Adsorption of dyes onto Ca_2Al-NO_3 and Mg_2Fe-CO_3 at varying concentration (C_0 = 100 - 1500 mg L^{1}); V_{dye} = 50 mL; adsorbent loading = 1 g L^{1}; acid orange 7 (top left), sunset yellow (top right), evan's blue (centre left), methylene blue (centre right) and safranin O (bottom left)

Table 5.15. Isotherm parameters for the adsorption of dyes onto Ca_2Al-NO_3 and Mg_2Fe-CO_3

		Langmuir			**Freundlich**		
		K_L / L mg^{-1}	**q_m / mg g^{-1}**	**R^2**	**K_F / L$^{1/n}$.mg$^{1-1/n}$.g^{-1}**	**n**	**R^2**
Ca_2Al-NO_3	Acid Orange 7	0.013	1586	0.990	100.6	2.39	0.961
	Sunset Yellow	0.007	72	0.987	8.0	3.36	0.951
	Evan's Blue	0.037	332	0.995	180.1	12.13	0.671
	Methylene Blue	0.0002	2069	0.268	0.6	1.07	0.982
	Safranin-O	-0.002	44	0.002	N/A	N/A	N/A
Mg_2Fe-CO_3	Acid Orange 7	0.010	1603	0.992	55.6	1.90	0.793
	Sunset Yellow	0.012	91	0.999	18.3	4.32	0.946
	Evan's Blue	0.012	103	0.981	50.5	11.81	0.711
	Methylene Blue	-0.006	1	0.302	N/A	N/A	N/A
	Safranin-O	0.002	4	0.057	N/A	N/A	N/A

Isotherm analysis of the two cationic dyes (MB and Saf-O) showed negligible dye uptake onto Mg_2Fe-CO_3, evidenced by q_m values of 1 and 4 mg g^{-1} respectively. In addition, there was negligible uptake of Saf-O onto Ca_2Al-NO_3. While linear regression was performed, Freundlich analysis resulted in errors and low R^2 ($R^2 < 0.31$) values were observed for Langmuir fitting because of the negligible uptake, indicating a poor fit to the model. Interestingly, a considerable amount of MB dye uptake (~400 mg g^{-1} at C_0 = 1500 mg L^{-1}) was observed for Ca_2Al-NO_3. Linear regression fitting revealed a greater fit to the Freundlich model, suggesting multilayer adsorption occurs on a heterogeneous surface. This is in agreement with literature for cationic dyes and can be attributed to surface adsorption being the predominant sorption mechanism for cationic dyes. [39] While anionic dyes can be adsorbed both by surface adsorption and ion exchange into the interlayer, ion exchange is unfavourable for cationic dyes due to electrostatic repulsion. [142]

5.6.2. Adsorption Kinetics

A kinetic study was conducted on Ca_2Al-NO_3 and Mg_2Fe-CO_3 to compare adsorption rate of the five dyes. Once again analysis was conducted through kinetic modelling using the pseudo first order, pseudo second order and intra-particle diffusion models. Kinetic plots can be seen in Figure 5.24. From linear regression analysis (Table 5.16) it appeared that pseudo-second order model had a slightly better fit than the pseudo-first order model for the three anionic dyes (AO7, SY and EB), evidenced by greater R^2 values and agreement between $q_{e,exp}$ and $q_{e,cal}$. This is in accordance with anionic dyes found in literature as it suggests the adsorption model is chemisorption based. Similar to the isotherm study (Section 5.6.1) the $q_{e,cal}$ (102 mg g^{-1}) and $q_{e,exp}$ (94 mg g^{-1}) values for SY were lower than expected based on its functionality, suggesting the substantially lower uptake compared to AO7 was not an anomalous result. Previous dye adsorption onto CLDHs suggested that adsorption kinetics is tied to molecular size, with smaller, less bulky dyes pertaining higher reaction rates, due to quicker regeneration of brucite layers. [37] This did not appear to be the case for LDHs, with adsorption rates of AO7, SY and EB being of similar magnitude (1-7 x 10^{-5} g mg^{-1} min^{-1}) for both Ca_2Al-NO_3 and Mg_2Fe-CO_3, presumably due to their similar sulfonate functionality.

While linear regression analysis was performed for MB and Saf-O adsorption onto Mg_2Fe-CO_3, negligible uptake was again observed (< 10 mg g^{-1}) making any conclusions difficult to justify based on the relative errors of each sample point. While a maximum equilibrium uptake of 958 mg g^{-1} was observed for the adsorption of MB onto Ca_2Al-NO_3, only

347 mg g^{-1} was adsorbed after 24 hours suggesting the system was still far from reaching equilibrium. As a result of this, linear regression analysis revealed a greater fit towards a pseudo-first order model (evidenced by R^2 and proximity of $q_{e,cal}$ to $q_{e,exp}$). While this indicates a physisorption-based mechanism this is in disagreement with literature where the pseudo-second order model is more widely reported. [39,280] As the pseudo-first order model tends to have greater fit over the initial stages of adsorption it is possible that it is being favoured within this study due to equilibrium not being reached. [198] For more conclusive analysis it is recommended that kinetic analysis be repeated over a timeframe where equilibrium is reached. However, due to time constraints this was not conducted, as the timeframes of all kinetic studies conducted would have to be extended to limit bias. However, it should be noted that, regardless of whether equilibrium uptake can be reached, the low rate of uptake of MB onto $Ca_2Al\text{-}NO_3$ (k_1 = 0.0003 min^{-1}) is evidence that industrial application is limited due to the low throughputs of wastewater that could be treated.

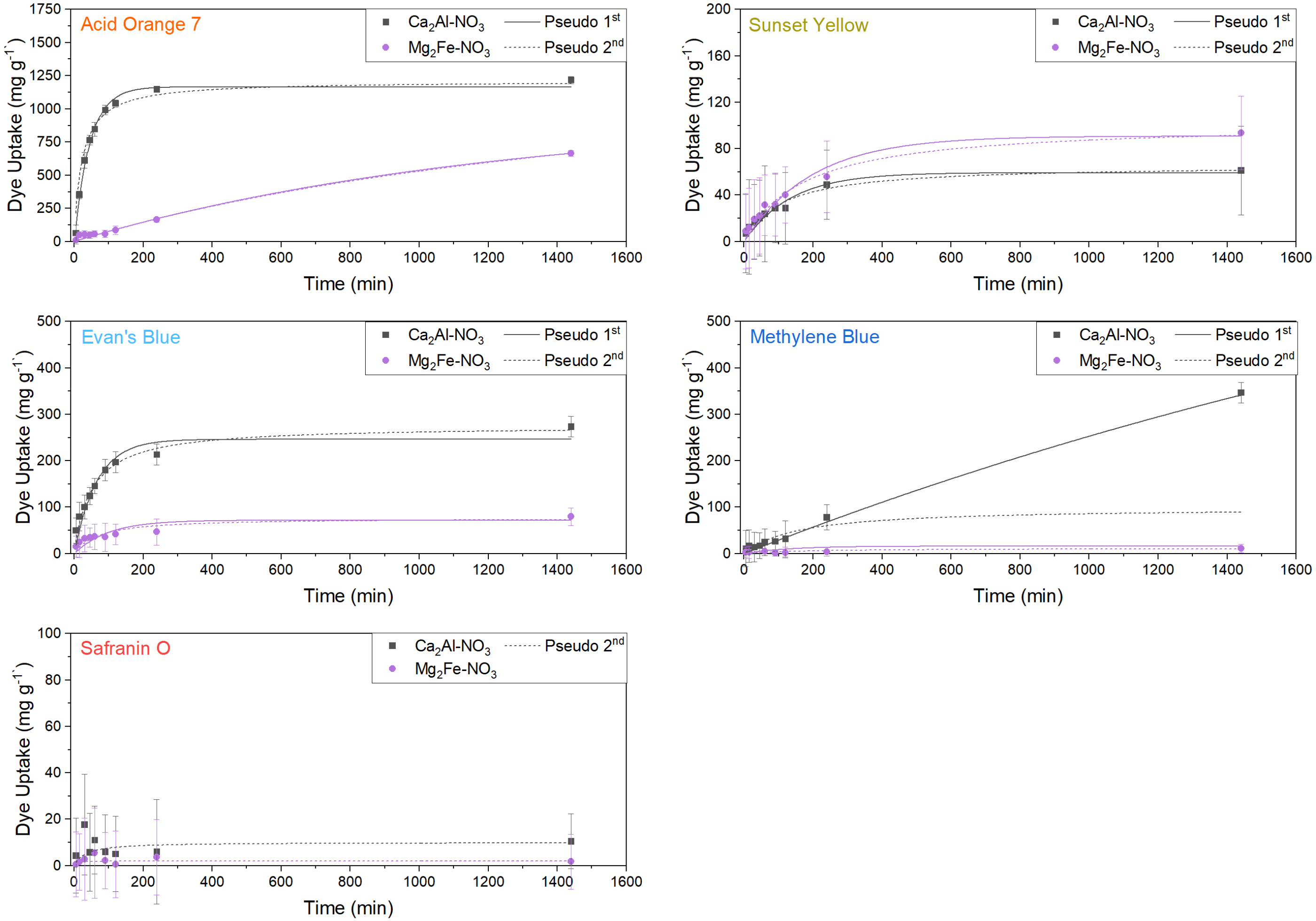

Figure 5.24. Uptake of dyes onto Ca$_2$Al-NO$_3$ and Mg$_2$Fe-CO$_3$ over 24 hours, fit with pseudo-first order & pseudo-second order models: acid orange 7 (top left), sunset yellow (top right), evan's blue (centre left), methylene blue (centre right) and safranin-O (bottom left)

Table 5.16. Kinetic constants from pseudo-first and pseudo-second order model fitting

			Pseudo 1st order			**Pseudo 2nd order**		
		$q_{e,exp}$ / mg g^{-1}	**K_1 / min^{-1}**	**$Q_{e,cal}$ / mg g^{-1}**	**R^2**	**K_2 / g mg^{-1} min^{-1}**	**$q_{e,cal}$ / mg g^{-1}**	**R^2**
Ca_2Al-NO_3	Acid Orange 7	1225	0.0223	864	0.878	3.898×10^{-5}	1205	0.923
	Sunset Yellow	61	0.0074	59	0.936	1.393×10^{-5}	66	0.956
	Evan's Blue	273	0.0150	246	0.919	7.101×10^{-5}	275	0.974
	Methylene Blue	958	0.0003	953	0.999	6.472×10^{-5}	99	0.450
	Safranin-O	9	N/A	N/A	N/A	3.133×10^{-3}	10	0.964
Mg_2Fe-CO_3	Acid Orange 7	1088	0.0155	847	0.851	1.675×10^{-5}	1004	0.939
	Sunset Yellow	94	0.0051	91	0.949	5.657×10^{-5}	102	0.975
	Evan's Blue	80	0.0101	72	0.710	1.918×10^{-4}	77	0.839
	Methylene Blue	11	0.0077	16	0.978	3.859×10^{-4}	12	0.550
	Safranin-O	2	-0.5756	28	0.940	9.992×10^{-2}	2	0.940

In addition to the pseudo-first and pseudo-second order models, the intra-particle diffusion model was applied to kinetic data for AO7, SY and EB dyes. Modelling for MB and Saf-O could not be performed due to negligible uptakes (for saf-O and uptake of MB on $Mg_2Fe\text{-}CO_3$) and equilibrium not reached for the uptake of MB on $Ca_2Al\text{-}NO_3$. The intra-particle diffusion model describes how the processes responsible for rate of adsorption changes as adsorption occurs, eventually reaching equilibrium. Because of this, fitting data that is still far from reaching equilibrium may reduce the accuracy of the results and not fully represent all adsorption processes occurring.

As previously discussed in Section 5.5.1 the uptake of AO7 onto $Ca_2Al\text{-}NO_3$ is split into three rate limiting steps (Figure 5.25): diffusion of dye molecules onto the surface, diffusion of the dye into the interlayer and saturation of interlayer/surface adsorption sites.[199] Only two distinct rate limiting processes were observed for $Mg_2Fe\text{-}CO_3$ suggesting equilibrium saturation had not been reached. Similar observations were observed for the uptake of SY and EB onto $Ca_2Al\text{-}NO_3$ and $Mg_2Fe\text{-}CO_3$ whereby only two distinct rate limiting processes were observed. Interestingly for SY diffusion of the dyes to the sorbent surface appeared to be rate limiting for a larger proportion of time, suggesting that diffusion into the interlayer was limited and/or slow.

Rate parameters and constants from intra-particle diffusion modelling can be seen in Table 5.17. K_{d1} and K_{d2} are indicative of the adsorption rate for surface adsorption (K_{d1}) and interlayer diffusion (K_{d2}). Adsorption rate was an order of magnitude higher for AO7 uptake than SY and EB for both $Ca_2Al\text{-}NO_3$ and $Mg_2Fe\text{-}CO_3$ sorbents. Interestingly C_B was also a magnitude higher for AO7 uptake than SY and EB uptake. As C_i is indicative of the boundary layer thickness this suggests that there was a much greater propensity for surface adsorption for AO7 than SY or EB. Negative C_A values once again indicated that the negligible boundary layer thickness hindered intra-particle diffusion. [275] It should be noted however that, due to interlayer diffusion only occurring for SY at the latter stages of the kinetic study (t = >4 h) and a small number of data points after this point, the calculated value of C_B is unprecise. Further data points (t = >4 h) are required for a more precise estimation of boundary layer thickness.

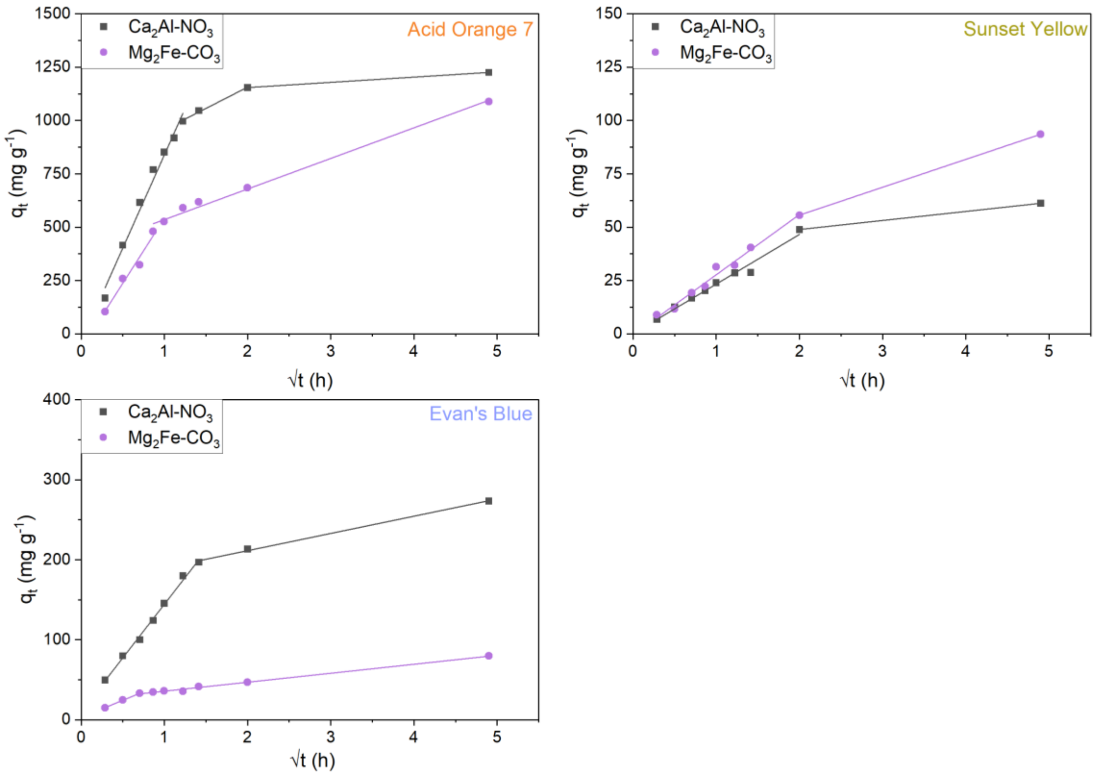

Figure 5.25. Linear intra-particle diffusion plots: acid orange 7 (top left), sunset yellow (top right) and evan's blue (bottom left)

Table 5.17. Rate parameters and constants from intra-particle diffusion modelling for adsorption of dyes

LDHs		**Intra-particle diffusion model**								
		K_{dA} (mg h$^{-1/2}$ g^{-1})	**C_A (mg g^{-1})**	**$(R_A)^2$**	**K_{dB} (mg h$^{-1/2}$ g^{-1})**	**C_B (mg g^{-1})**	**$(R_B)^2$**	**K_{dC} (mg h$^{-1/2}$ g^{-1})**	**C_c (mg g^{-1})**	**$(R_C)^2$**
$Ca_2Al\text{-}NO_3$	Acid Orange 7	854.0	-17.0	0.991	199.0	758.2	0.994	24.5	1105.4	0.784
	Sunset Yellow	20.4	2.1	0.973	4.2*	40.4*	N/A*	N/A	N/A	N/A
	Evan’s Blue	134.1	10.2	0.995	21.5	168.2	0.998	N/A	N/A	N/A
$Mg_2Fe\text{-}CO_3$	Acid Orange 7	480.4	-8.0	0.976	143.4	391.7	0.990	N/A	N/A	N/A
	Sunset Yellow	28.2	-0.58	0.984	13.1*	29.5*	N/A*	N/A	N/A	N/A
	Evan’s Blue	46.8	0.68	0.996	11.2	24.5	0.994	N/A	N/A	N/A

**Unprecise due to a lack of data points*

5.6.3. The Impact of pH on Adsorption of AO7, SY, EB, MB and Saf-O

5.6.3.1. pH Effects involving Anionic Dyes

It was previously discussed in Section 5.5.3 that varying the pH of solution (pH 4 – 10) for the adsorption of AO7 dye onto $Ca_2Al\text{-}NO_3$ and $Mg_2Fe\text{-}CO_3$ resulted in a very minimal effect on adsorption, indicating that the wide range of dye wastewater pH found in literature would not hinder the LDHs performance. This was evidenced by the mean q_e of $Ca_2Al\text{-}NO_3$ remaining constant between 1200 and 1350 mg g^{-3} and q_e of $Mg_2Fe\text{-}CO_3$ between 1350 – 1450 mg g^{-1} at all pHs (Figure 5.26). pH_{PZC} of $Ca_2Al\text{-}NO_3$ and $Mg_2Fe\text{-}CO_3$ were previously calculated in Section 5.5.3 to be 10.63 and 8.82 respectively. This was contributed to a buffering process whereby the LDHs buffered the solution to a pH close to the pH at which it had net zero charge, regardless of initial starting pH.

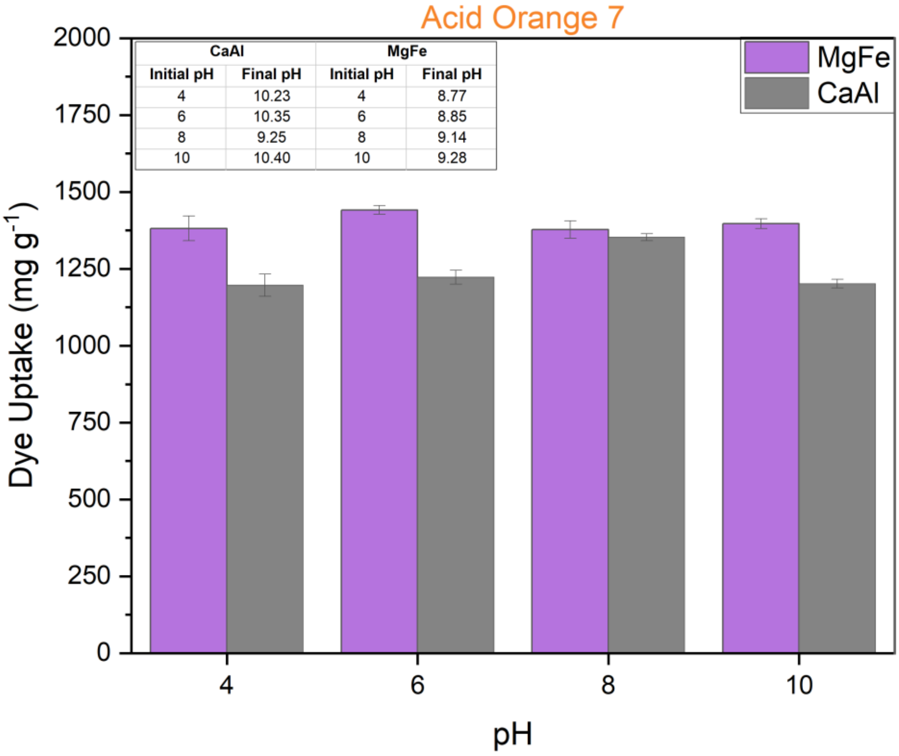

CaAl		MgFe	
Initial pH	Final pH	Initial pH	Final pH
4	10.23	4	8.77
6	10.35	6	8.85
8	9.25	8	9.14
10	10.40	10	9.28

Figure 5.26. The impact of pH on AO7 adsorption onto $Ca_2Al\text{-}NO_3$ and $Mg_2Fe\text{-}CO_3$ LDHs

A similar observation was seen when varying the solution pH during SY adsorption (Figure 5.27). The uptake of SY onto $Ca_2Al\text{-}NO_3$ remained relatively unchanged between pH 4 – 10, evidenced by a mean q_e between 45 – 65 mg g^{-1}. Similarly, for $Mg_2Fe\text{-}CO_3$ uptake remained constant between 75 – 100 mg g^{-1}. Final pH's remained between 9.97 – 10.76 for $Ca_2Al\text{-}NO_3$ and 8.10 – 8.40 for $Mg_2Fe\text{-}CO_3$, suggesting once again the pH was being buffered towards the pH_{PZC}. While initially it was thought from this analysis that pH was unsuccessful in explaining the low adsorption uptake of SY, a paper by Hashem et al. was found highlighting the acid-base equilibria of sunset yellow at varying pH. [281] Depending on pH, the ionic nature of SY can be altered by protonation/deprotonation of sulfonate and hydroxyl groups (eq 5.1).

$$H_4L^+ \xleftrightarrow{-2H^+} H_2L^- \xleftrightarrow{-H^+} HL^{2-} \xleftrightarrow{-H^+} L^{-3} \qquad 5.1$$

pH = (0.4-2.0) (2.5-5.0) (5.5-7.5) (10.0-12.8)

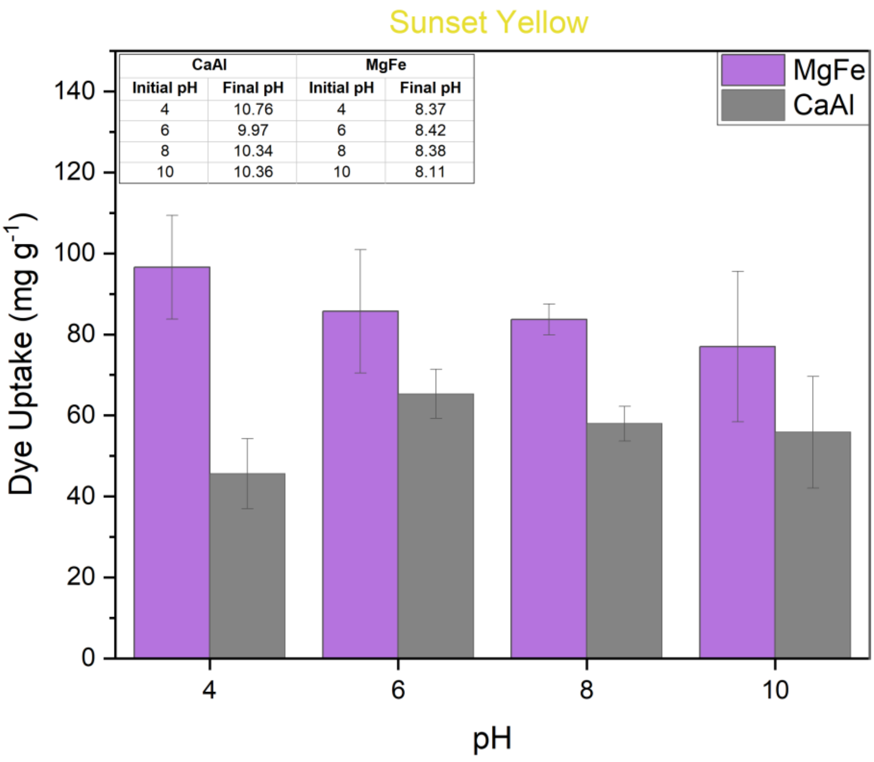

CaAl		MgFe	
Initial pH	Final pH	Initial pH	Final pH
4	10.76	4	8.37
6	9.97	6	8.42
8	10.34	8	8.38
10	10.36	10	8.11

Figure 5.27. The impact of pH on SY adsorption onto $Ca_2Al\text{-}NO_3$ and $Mg_2Fe\text{-}CO_3$ LDHs

In very acidic conditions (pH = 0.4 – 2.0), both R-SO_3H and R-OH within the SY structure are protonated. As the solution tends towards more neutral conditions the structure becomes more anionic due to protonation of sulfonate groups to R-SO_3^-. At very high pH's (pH = 10.0-12.8) further deprotonation of the phenol R-O^- group can occur, resulting in a trivalent anionic species (L^{-3}) becoming dominant. As the buffering pH of Ca_2Al-NO_3 exceeds this pH 10 threshold, SY exists predominantly in this trivalent L^{-3} state during adsorption. Despite Mg_2Fe-CO_3 LDH's buffering pH to be less acidic (8.10 – 8.40) it is likely that SY still exists partially as a trivalent species at this pH, although no speciation diagrams for SY could be found in literature to corroborate this. Therefore, this acid-base equilibria process for SY may explain why its adsorption capacity (q_m) is more analogous to the higher functionality of EB: Its higher anionic charge (L^{-3}) at pH above 10 results in more active sites being occupied per dye molecule. Furthermore, this may explain why a higher adsorption capacity (q_m) of 398.41 mg g^{-1} was reported by Pereira et al. as they reported a lower pH_{PZC} of 7.29. [165] At this pH the divalent HL^{2-} species is dominant, not L^{-3}.

Interestingly for EB sorption onto Ca_2Al-NO_3 the final buffered pH appeared to be lower than its pH_{PZC} (Figure 5.28). While Ca_2Al-NO_3 has a pH_{PZC} of 10.63, the buffered pH varied between 8.39 – 9.72. At this pH the hydrated surface of Ca_2Al-NO_3 becomes positively charged, enhancing the surface sorption of anionic EB. Between pH 4 – 8 the dye uptake remained constant between 280 – 310 mg g^{-1} due to similar buffering pH's around 8.50. At the higher pH 10 dye uptake dropped to 226 mg g^{-1}, which was attributed to a higher buffering pH of 9.72. While no speciation diagrams were found in literature for EB it is unlikely that the dominant tetravalent species (L^{-4}) changes at the buffering pHs observed in Figure 5.28. Sulfonic acids (R-SO_3H) are very strong acids (pKa = ~7) and readily deprotonate to form sulfonates. As a result of this the protonated species (R-SO_3H) is likely to occur only at very low pH. For example the R-SO_3^- species in AO7 only starts to exist in its protonated form in any considerable quantity below pH 3. [282] The dye uptake of EB onto Mg_2Fe-CO_3 during pH analysis remained constant around 70 – 90 mg g^{-1} (Figure 5.28). This lower sorption capacity when compared to Ca_2Al-NO_3 was attributed to the closer proximity of the buffering pH (8.47 – 8.75) to the pH_{PZC} (pH_{PZC} = 8.82), resulting in a comparatively lower net positive charge on the sorbent surface.

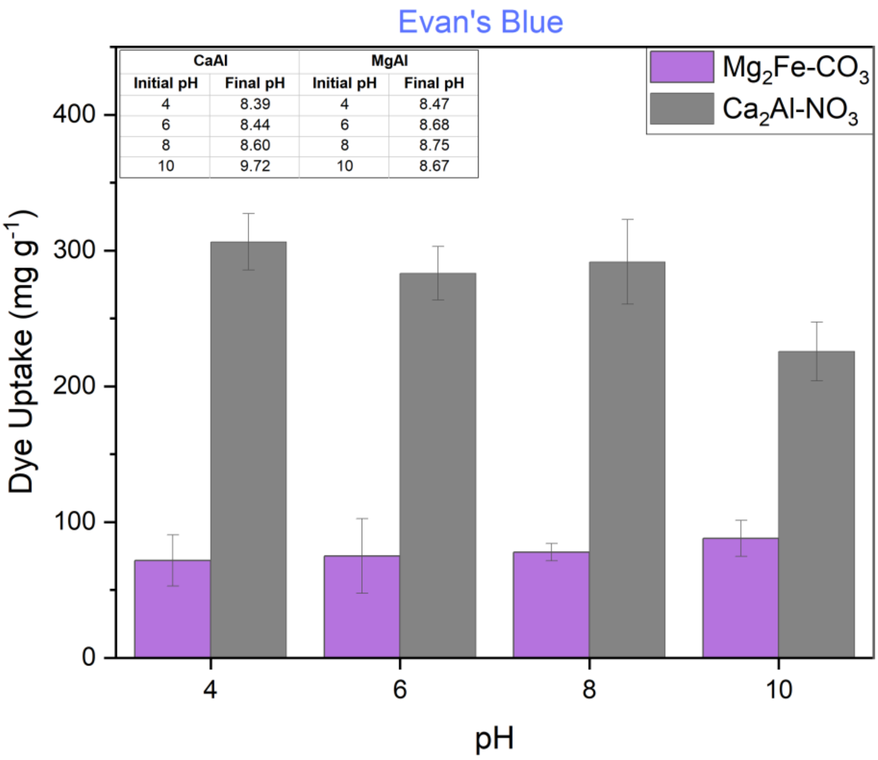

CaAl		MgAl	
Initial pH	Final pH	Initial pH	Final pH
4	8.39	4	8.47
6	8.44	6	8.68
8	8.60	8	8.75
10	9.72	10	8.67

Figure 5.28. The impact of pH on EB adsorption onto Ca_2Al-NO_3 and Mg_2Fe-CO_3 LDHs

5.6.3.1. pH Effects involving Cationic Dyes

pH sorption analysis for MB revealed negligible uptake (< 10 mg g^{-1}) onto Mg_2Fe-CO_3 between pH 4 – 10 (Figure 5.29). As MB is a monovalent cationic dye this was attributed to Mg_2Fe-CO_3 LDH's buffering pH. The main mechanism for cationic dye sorption onto LDHs is via surface sorption. At a pH > pH_{PZC} the LDHs surface is negatively charged, making adsorption electrostatically favourable. As the buffering pH of Mg_2Fe-CO_3 was between 8.00 – 8.90, compared to its pH_{PZC} of 8.82, this suggests that its surface is positively charged making sorption unfavourable. [179] In contrast, the uptake of MB appeared to increase with increasing pH on Ca_2Al-NO_3. At pH 4 the uptake of MB was 113 mg g^{-1}, increasing to a maximum of 377 mg g^{-1} at pH 10. This increase in uptake directly correlated with an increase in the final buffered pH of Ca_2Al-NO_3. When an initial starting pH of 4 was used, the final buffered pH was 10.13 compared to 13.26 at a starting pH of 10, suggesting the buffering effect of Ca_2Al-NO_3 was not as strong in MB solution. Speciation diagrams for MB show that it exists almost exclusively in its monovalent cationic form (MB^+) above pH 6 indicating changes in dye speciation does not play a role in this increase in MB uptake at higher pH. [283] Instead, this was once again attributed to the LDHs surface becoming more negatively charged when pH > pH_{PZC}, favouring sorption of the cationic dye. From this it was evident that the adsorbing capabilities of $Ca_2Al\text{-}NO_3$ for MB would be greatly diminished in wastewater effluents with more acidic pH's.

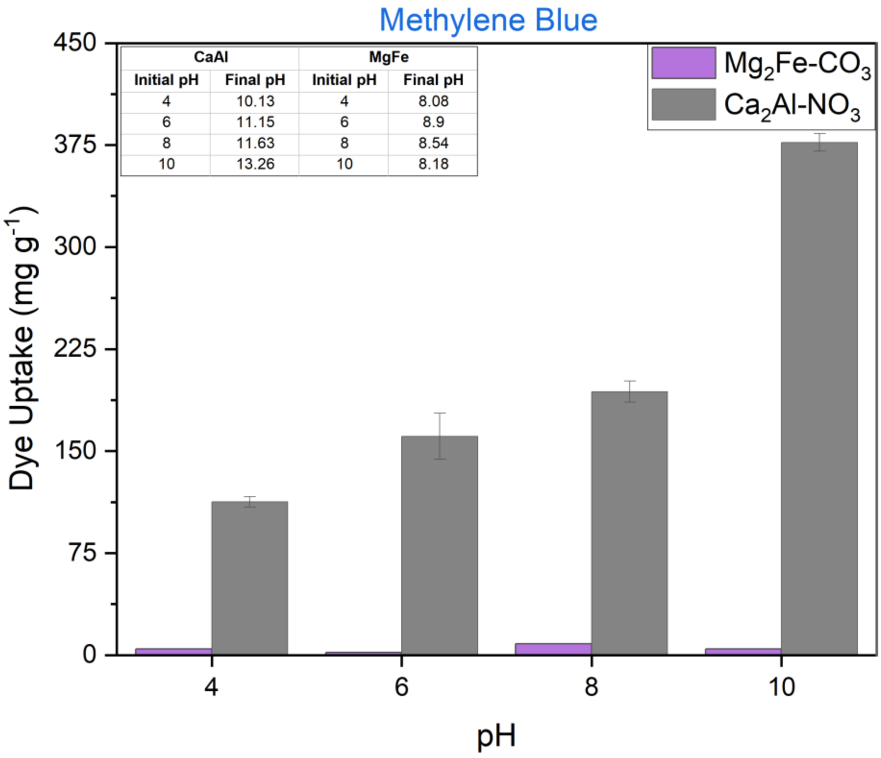

CaAl		MgFe	
Initial pH	Final pH	Initial pH	Final pH
4	10.13	4	8.08
6	11.15	6	8.9
8	11.63	8	8.54
10	13.26	10	8.18

Figure 5.29. The impact of pH on MB adsorption onto $Ca_2Al\text{-}NO_3$ and $Mg_2Fe\text{-}CO_3$ LDHs

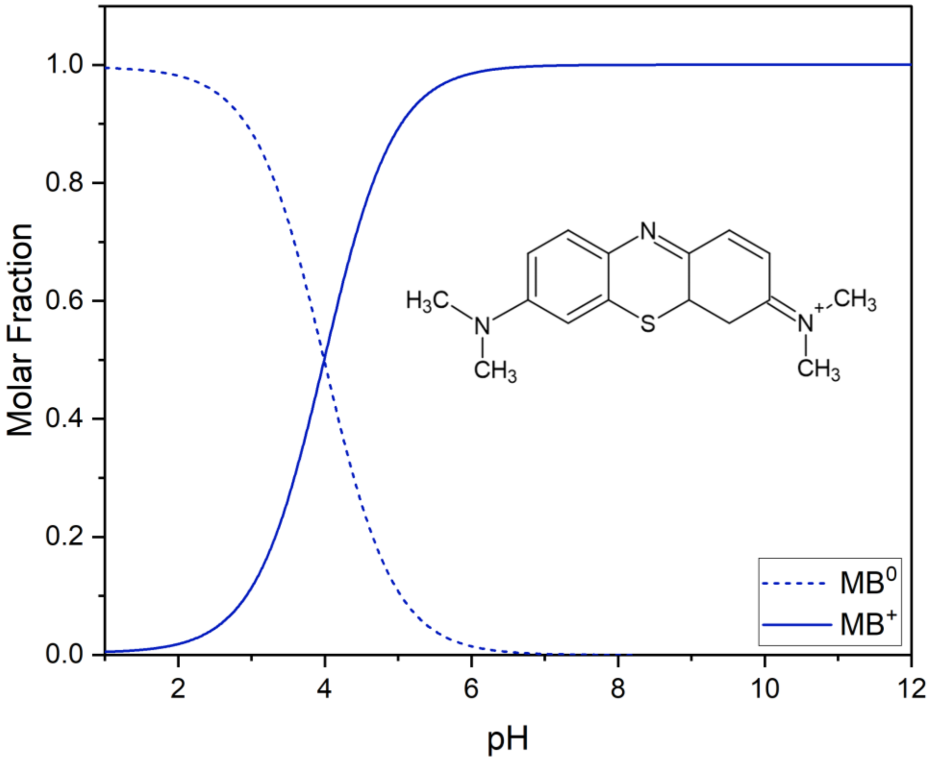

Figure 5.30. MB speciation diagram, adapted from Rabago et al. [283]

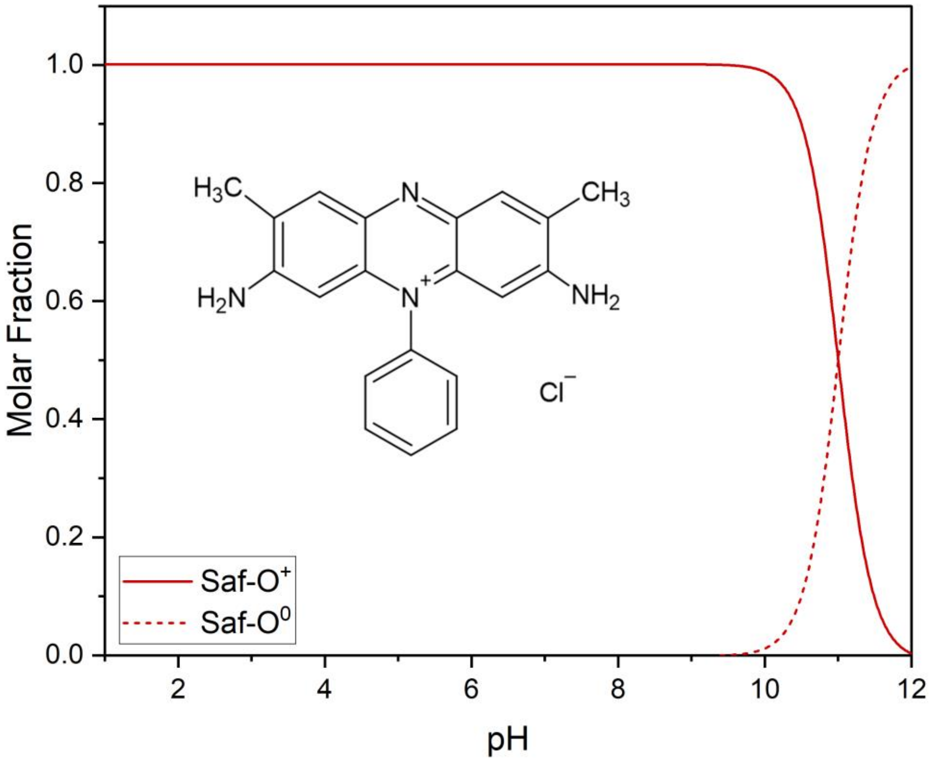

Figure 5.31. Saf-O speciation diagram, adapted from Sieren et al. [82]

Investigation into the speciation of Saf-O prior to pH analysis revealed an interesting juxtaposition with pH_{PZC} effects (Figure 5.31). Below pH 10 Saf-O exists almost exclusively in its monovalent cationic form (Saf-O^+). Above this pH in basic conditions Saf-O is deprotonated, with Saf-O^0 becoming the dominant species above pH 11. [82] As a result, sorption uptake is unlikely to occur above pH 10 due to Saf-O's neutral form. In contrast however sorption of Saf-O at pH's below pH_{PZC} for Ca_2Al-NO_3 and Mg_2Fe-CO_3 (10.63 and 8.82 respectively) is also unfavourable due to protonation of the LDH surface and competition with H^+. Therefore, unsurprisingly negligible uptake was observed for Ca_2Al-NO_3 or Mg_2Fe-CO_3 regardless of pH (Figure 5.32).

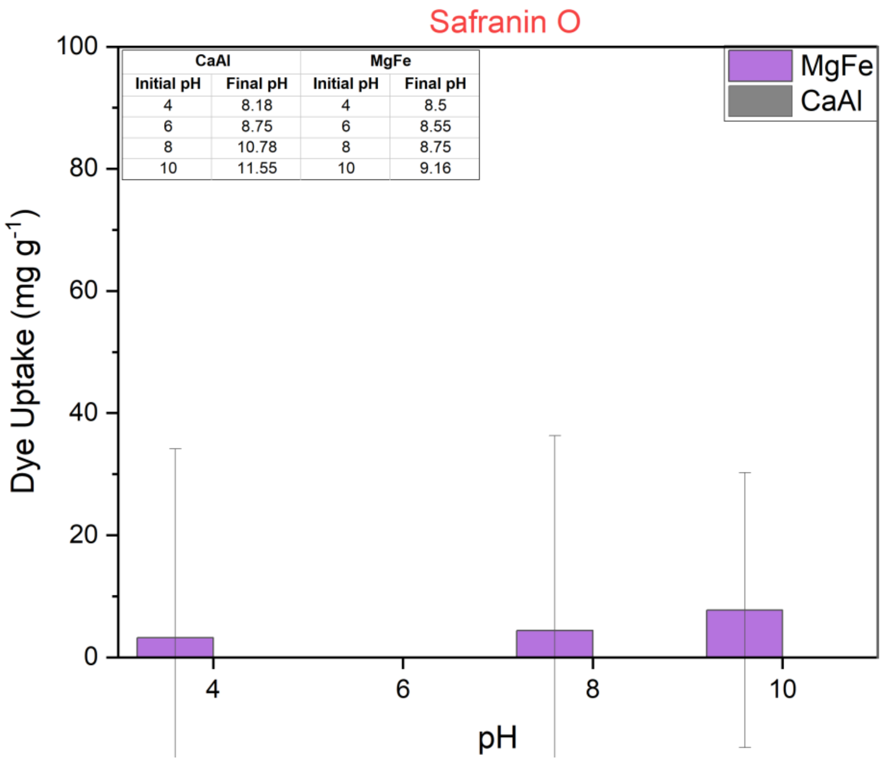

CaAl		MgFe	
Initial pH	Final pH	Initial pH	Final pH
4	8.18	4	8.5
6	8.75	6	8.55
8	10.78	8	8.75
10	11.55	10	9.16

Figure 5.32. The impact of pH on Saf-O adsorption onto Ca_2Al-NO_3 and Mg_2Fe-CO_3 LDHs

5.6.4. Summary of Analysis and Comparisons to Literature

The lower q_m values of SY and EB onto Ca_2Al-NO_3 and Mg_2Fe-CO_3 LDHs, compared with AO7, evidenced that the ionic valency plays an important role in adsorption capacities. However, sorption mechanisms were also found to be heavily dependent on pH related effects such as dye speciation and the pH_{PZC} of the LDH, making any conclusions on the extent of the effect of valency difficult to discern. The molecular size of the anionic dyes did not appear to influence reaction kinetics, with reaction rates of AO7, SY and EB being of similar magnitude onto both LDHs, suggesting dye functionality to be more important in this regard.

As expected from previous analysis, the polarity of the dye (i.e., anionic vs cationic) influenced adsorption mechanisms. Intra-particle diffusion modelling of AO7, SY and EB uptake confirmed adsorption to occur by both intercalation into the interlayer and surface adsorption. In contrast, a greater fit of cationic MB uptake onto Ca_2Al-NO_3 to the Freundlich isotherm model indicated adsorption occurred primarily by surface adsorption. This surface adsorption mechanism of cationic dyes was found to be entirely dependent on pH, with Saf-O having negligible uptake due to its speciation and Ca_2Al-NO_3/Mg_2Fe-CO_3 LDHs buffering the pH below their pH_{PZC}, resulting in a positively charged surface.

Comparison of SY removal to different adsorbents studied in literature, found the dye adsorption capacities of Ca_2Al-NO_3 and Mg_2Fe-CO_3 to be lacklustre (Table 5.18). Many other sorbents such as modified peanut husk (117.7 mg g^{-1}), activated carbon (272 mg g^{-1}), and modified microporous polymers (348.16 mg g^{-1}) all exhibited higher adsorption capacities than the LDHs within this study. [284–286] Although, previous sorption analysis of Ca_2Al-NO_3 synthesised by co-precipitation exhibited a higher uptake of 398.41 mg g^1, indicating SY removal could potentially be improved with further research. Adsorption rates (k_1 and k_2) were also orders of magnitude lower than those found in literature, further invalidating the potential Ca_2Al-NO_3 and Mg_2Fe-CO_3 LDHs have for SY removal.

While few other types of sorbents were found in literature for EB removal, similar observations were found to that of SY uptake onto Mg_2Fe-CO_3 (Table 5.19), with modified bentonite (457.9 mg g^{-1}) and functionalised chitosan (243.9 mg g^{-1}) exhibiting greater EB capacities. [287,288] Interestingly, a Zn_2Al-Cl based LDH was found to have a higher adsorption capacity than both Ca_2Al-NO_3 and Mg_2Fe-CO_3 LDHs within this study, at 491.934 mg g^{-1}. [289] While it is difficult to say for certain due to differences in experimental method and synthesis, this may indicate a ZnAl based LDH has a greater adsorption potential than CaAl or MgFe, despite Zn_2Al-CO_3 exhibiting a lower uptake of AO7 within this study.

As uptakes of MB onto Ca_2Al-NO_3 were still far from reaching equilibrium during adsorption experiments within this work, comparisons of uptakes to literature are hard to justify. However, as discussed previously, the rate of uptake (k_1 = 0.0003 min^{-1}) was orders of magnitude lower than other adsorbents found in literature such as activated carbon and natural zeolite, [198,290] as well as other LDHs such as MgAl, Mgfe and ZnFe, [39,280] limiting the industrial application of Ca_2Al-NO_3 for MB removal. As MB and Saf-O adsorption onto Mg_2Fe-CO_3 was negligible, as well as adsorption of Saf-O onto Ca_2Al-NO_3, comparisons to literature were not conducted. From these findings it was evident that high adsorption capacities of an LDH for one dye, such as AO7, does not necessarily translate over to other dyes, with large variances occurring depending on functionality and ionic nature. Dye speciation and its relationship with pH_{PZC} of the LDH are of utmost importance for discerning the potential of an LDH-dye adsorption system and should be utilized more frequently within literature as a standard protocol for evaluating LDH materials.

Table 5.18. Comparison of sorption capacities and rate constants of LDHs, for SY adsorption, with other sorbents in literature

Adsorbent	**Maximum Uptake / mg g^{-1}**	**Pseudo-first order rate constant (k_1) / min^{-1}**	**Pseudo-second order rate constant (k_2) / g mg^{-1} min^{-1}**	**Reference**
Ca_2Al-NO_3 LDH	72	0.0074	1.393×10^{-5}	*This Study*
Mg_2Fe-CO_3 LDH	91	0.0051	5.657×10^{-5}	*This Study*
Ca_2Al-NO_3 LDH	398.41	-	-	[165]
EDA modified Peanut Husk	117.7	3.2×10^{-3}	4.5×10^{-4}	[284]
Modified Walnut Shell	18.35	4.50×10^{-2}	1.13×10^{-2}	[291]
Alligator Weed Activated Carbon	272	0.0170	8.6×10^{-4}	[285]
Polypyrrole modified Carbon Nanotube	212.1	-	-	[292]
Modified Microporous Polymer	348.16	-	-	[286]

Table 5.19. Comparison of sorption capacities and rate constants of LDHs, for EB adsorption, with other sorbents in literature

Adsorbent	**Maximum Uptake / mg g^{-1}**	**Pseudo-first order rate constant (k_1) / min^{-1}**	**Pseudo-second order rate constant (k_2) / g mg^{-1} min^{-1}**	**Reference**
Ca_2Al-NO_3 LDH	332	0.0150	7.101×10^{-5}	*This Study*
Mg_2Fe-CO_3 LDH	103	0.0101	1.918×10^{-5}	*This Study*
Cu-Al-CO_3 LDH	100	-	-	[293]
Cu-Al CLDH (500 °C)	333.33	-	-	[293]
Zn_3Al-CO_3 LDH	113.64	-	-	[289]
NiFe CLDH	43.5	-	2.3×10^{-3}	[294]
Zn_2Al-Cl LDH	491.93	-	-	[149]
Chitosan Functionalised Fe_3O_4 NP	243.9	-	-	[288]
Rarasaponin-Bentonite	457.9	0.1403	4.458×10^{-4}	[287]

5.6.5. Discussion Regarding Continuous Adsorption of Dyes with LDHs

While bench scale adsorption of dyes by LDHs within this research appeared promising when compared to other sorbents found in literature, there are inherent limitations when considering scaling to continuous removal. As previously discussed in Section 4.6.5. any application of LDHs for wastewater remediation would require the use of continuous processes. This is especially challenging for LDHs due to their nanosize and low porosity hindering their use in fixed-bed columns due to pressure drops and sludge production, requiring immobilization onto larger more porous substrates. [295] In addition to this, previous studies have noted in such systems LDHs can suffer from leaching of precursor metals into solution. [236] This is especially problematic as it, not only results in poorer adsorptive performance, but also further pollutes the wastewater that is being treated. Many metals that are especially common in LDH synthesis such as Calcium, Zinc, Aluminium, Nickel and Cobalt can be toxic to both aquatic and human health when found at high enough concentrations. [296]

This issue of metal leeching goes hand-in-hand with another factor limiting LDHs applicability for wastewater treatment – regenerative capabilities. The most common method of LDH regeneration in literature is through thermal treatment (> 400 °C) to form MMO's. [297] The original LDH structure can then be reformed upon placement into an aqueous solution of desired anions through the memory effect. [298] However, many authors have found that regeneration of LDHs for further dye adsorption tends to only be feasible for a couple cycles due to decreasing LDH crystallinity after reconstruction of the lamellar structure and leeching of metals into solution. [20] Naturally this is problematic as if LDHs are single use this increases both the cumulative energy demand and the environmental impact of the process as saturation of the LDH would require disposal, with fresh LDH to be synthesised to replace it.

Another factor to be considered is the batch nature of the adsorption experiments carried out within this research. While kinetic and isotherm experiments are useful for improving understanding of sorption mechanisms and comparing sorbents, it is not analogous to direct performance in dye-containing environmental wastewater. The dyeing process is very complex and involves the use of many other chemicals such as NaOH, surfactants and soaps for scouring, hydrogen peroxide for bleaching and metals/sorbents for printing. [299] As a result of this, dye wastewater can contain many other anionic and cationic species that can compete with and disrupt adsorption of dye, resulting in poorer performance. While the research above clearly show that solution pH is unlikely to have a substantial impact on LDH dye adsorption capabilities due to a unique buffering phenomenon that LDHs possess, many textile industries use fixing agents such as sodium carbonate to fix pH. [300] It is therefore imperative that, not only are these competing effects well understood for specific LDH/dyebath effluents, but also that relevant water quality analysis is performed on the wastewater streams to understand what species are present in high concentrations. It should however be noted that this problem is not unique to LDHs, rather a generic problem inherent with any wastewater treatment targeting specific pollutants.

6. Results and Discussion: Continuous Hydrothermal Synthesis of Dye-Intercalated LDHs

6.1. Introduction

LDHs have great potential for the remediation of dyes due to their high ion exchange and sorption capacities for both cationic and anionic dyes. Currently, in literature, the predominant sorption mechanisms for dyes involve surface adsorption and anion exchange with other interlayer species. A paper by Liu and Evans reported that the dye acid orange 7 could be directly intercalated into Mg_2Al LDH structure during synthesis. [35] This has potential as an alternative mechanism for wastewater treatment whereby wastewater containing dyes could be used directly as a feedstock to produce a dye intercalated LDH, negating the need for synthesis, washing, and drying steps prior to removal. However, Mg_2Al-AO7 was synthesised by a batch co-precipitation method. Batch processes are not as scalable as their continuous counterparts due to long reaction times, discontinuous operation and variances between batches. [184] In addition, synthesis was conducted at an AO7 concentration equivalent to ~14 000 mg L^{-1}. A case study of environmental wastewater conducted within the literature review (Chapter 2) found that effluents generally had dye concentrations within the range of 10 – 250 mg L^{-1}, considerably lower than the concentrations used by Liu and Evans. Finally, intercalation of only AO7 dye was reported. Over 40 000 different dyes and pigments are used industrially, producing an array of wastewaters containing different dyes. [7] Therefore the scope of dyes that can be removed from solution by this method, and their respective concentrations, needs to be increased if it is to have potential for a wide variety of wastewater feedstocks.

This chapter aimed to build upon Liu and Evans's work by synthesising Mg_2Al-AO7 by CFHS method, a more scalable alternative to typical co-precipitation routes. Experimental conditions were maintained at 93 °C and 1 bar to best replicate previous work. [35] In addition, Mg_2Al-X synthesis was expanded to include other dyes: SY, EB, MB and Saf-O. These were chosen based on their differing ionic nature, charge, and molecular size. Finally, variable AO7-concentration experiments between 100 – 1500 mg L^{-1} were conducted to determine if synthesis of Mg_2Al-AO7 could be conducted at conditions more analogous to those found in environmental dye effluent.

6.2. Highlights

- Based on previous work by Liu and Evans et al., [35] AO7 dye was directly intercalated into LDH structure by CFHS method to form Mg_2Al-AO7.
- Dye-intercalated LDH synthesis was expanded to additional dyes (SY and EB), with the first reported synthesis of Mg_2Al-SY and Mg_2Al-EB.
- Lower concentration synthesis of Mg_2Al-AO7, utilizing AO7 at concentrations typically found in environmental wastewater (100 mg L^{-1}), proved unsuccessful due to low particle-particle interactions.
- A novel method of dye removal by doping traditional Mg_2Al-NO_3 synthesis with small quantities (100 mg L^{1}) of AO7, SY and EB dye resulted in near complete removal of dye from solution.

6.3. Control Experiments

Prior to synthesis, control experiments were conducted on AO7 within the CFHS reactor to ensure any reduction in concentration could be attributed to the formation of either Mg_2Al-AO7 or other solid products. While dyes are typically recalcitrant, degradation can occur by thermal or photocatalytic means. [144] Upon connection of a 1000 mg L^{-1} AO7 downflow solution to the pumps, no visual changes to solution colour were observed for the first four minutes (Figure 6.1). After five minutes the solution became a transparent orange, gradually becoming darker and translucent indicating the presence of dye. No solid precipitates were observed upon centrifugation.

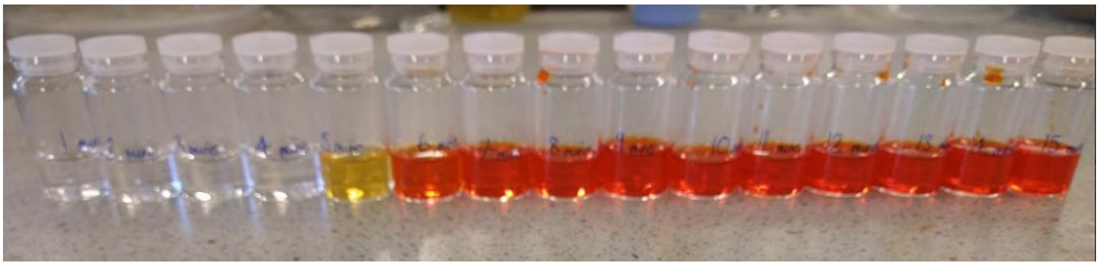

Figure 6.1. Solutions of AO7 dye upon pumping through CFHS reactor (1-15 mins)

This was further confirmed by UV-vis analysis; The concentration of AO7 was negligible until five minutes where it gradually increased, stabilising at 665 – 670 mg L^{-1} after 9 minutes (Figure 6.2). As a 1.5x dilution factor (1000 mg L^{-1} to 666 mg L^{-1}) was expected, as a result of the 20:10 mL min^{-1} ratio of pumps (downflow:upflow), this evidenced that no quantifiable degradation of the dye occurred upon passing through the rig. Despite the downflow having a total residence time of five minutes (inlet to outlet), a uniform concentration of AO7 dye (660 – 670 mg L^{-1}) was not reached for a further four minutes. This was attributed to the presence of stagnant zones throughout the reactor. [133] As these stagnant areas have comparatively lower net flows than the bulk flow, any dye solution trapped in these regions would have an increased residence time. Therefore, collection of any product during subsequent synthesis experiments was not performed during the first ten minutes of a run to ensure homogeneous dispersion of precursor solutions throughout the rig had occurred. Further control experiments conducted with SY, EB, MB and Saf-O confirmed this to be an adequate time for homogeneous dispersion of precursors, with no further changes in concentration occurring after ten minutes (Table 6.1). In addition, all other dyes had dilution factors around 1.5x, indicating no degradation or reactions involving the dyes occurred.

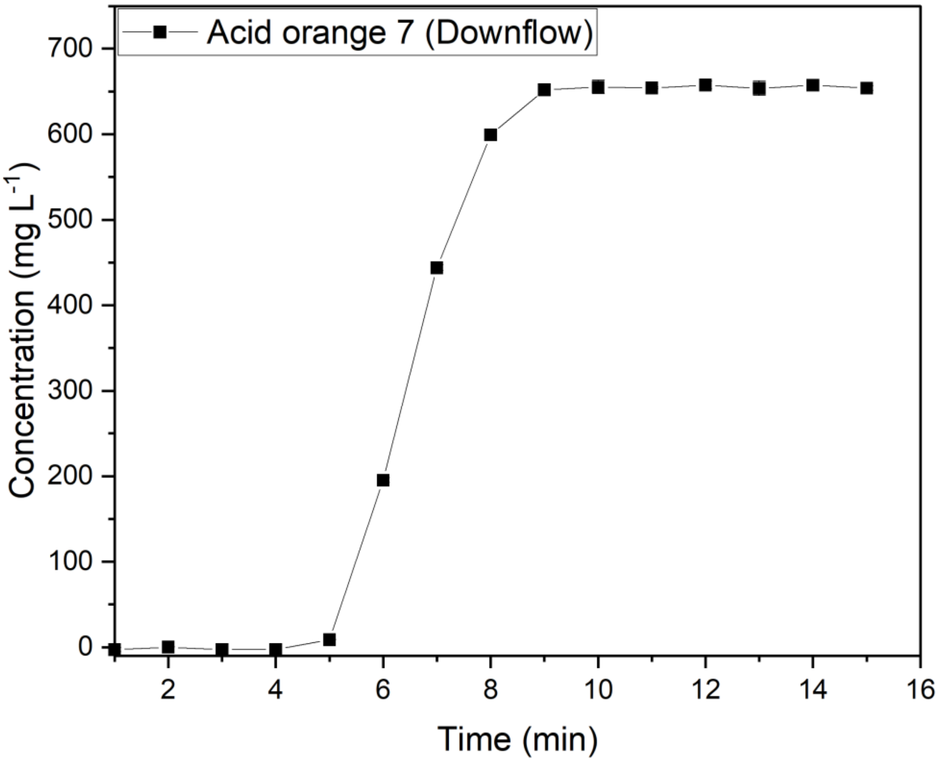

Figure 6.2. Changes in outflow concentration of AO7 dye with time (Initial concentration: 1000 mg L^{-1})

Table 6.1. Changes in dye concentrations upon flowing through the reactor

	Concentration of dye / mg L^{-1}			
	SY	**EB**	**MB**	**Saf-O**
Downflow	101 ± 3	97 ± 2	102 ± 1	101 ± 1
10 mins	65 ± 1	64 ± 1	68 ± 1	64 ± 1
11 mins	65 ± 2	66 ± 2	66 ± 1	66 ± 1
12 mins	63 ± 1	65 ± 1	66 ± 1	67 ± 2
Dilution Factor	1.56 ± 0.03	1.49 ± 0.03	1.52 ± 0.02	1.55 ± 0.04

6.4. Continuous Synthesis of Mg_2Al-AO7

6.4.1. X-Ray Diffraction of Mg_2Al-AO7 and Changes to Interplanar Spacing

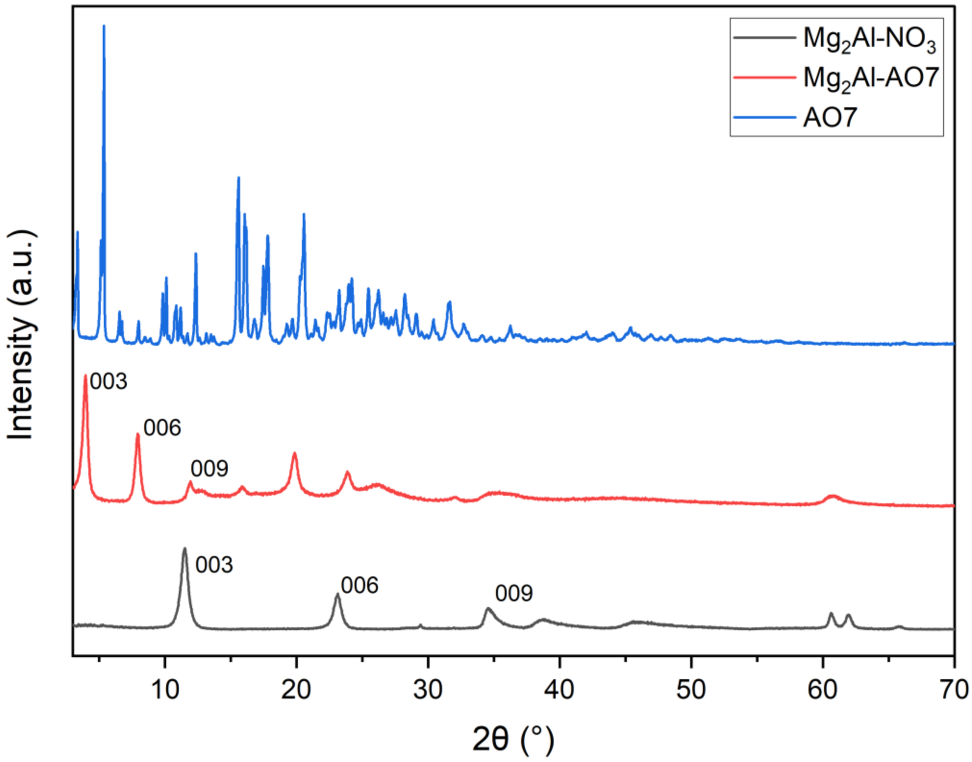

Figure 6.3. XRD spectra of Mg_2Al-CO_3, Mg_2Al-AO7 and AO7 dye

XRD spectra of Mg_2Al-AO7 and Mg_2Al-NO_3 LDHs synthesised by CFHS method, alongside AO7 dye, can be seen in Figure 6.3. LDH formation was evidenced by the presence of intense symmetrical peaks at low 2θ angles, becoming broader and more symmetrical at higher 2θ angles. No diffraction peaks associated with "free" unreacted AO7 dye were present in Mg_2Al-AO7. Specifically of interest was the observation of high intensity and equally spaced 003, 006 and 009 diffraction peaks indicative of the basal spacing and long-range order of brucite sheets. [301] It was apparent in Figure 6.3 that, compared to those of Mg_2Al-NO_3, the 003, 006 and 009 peaks of Mg_2Al-AO7 were heavily shifted to the left. As the scattering angle (θ) is directly correlated to the interplanar spacing (d) this indicated an increase in the interlayer distance for Mg_2Al-AO7, attributed to the larger molecular size of AO7 compared to NO_3^- ions. Using the Bragg Equation, interlayer spacing for NO_3 and AO7 intercalated LDHs were calculated as 0.78 and 2.22 nm respectively (Table 6.2). This was in agreement with previous literature, with Liu and Evans reporting an interplanar spacing of 2.27 nm, suggesting successful intercalation of AO7 into the interlayer region. [35,302]

Table 6.2. 2ϑ, d values and interlayer distances of $Mg_2Al\text{-}NO_3$ and Mg_2Al-AO7 LDHs

LDH	**Diffraction Peaks**						**Interlayer Distance / nm**
	003		**006**		**009**		
	2θ / °	**d / nm**	**2θ / °**	**d / nm**	**2θ / °**	**d / nm**	
$Mg_2Al\text{-}NO_3$	11.53	0.77	23.15	0.38	34.55	0.26	0.77
Mg_2Al-AO7	3.98	2.22	7.93	1.11	11.96	0.74	2.22

6.4.2. Infrared Spectrum of Mg_2Al-AO7

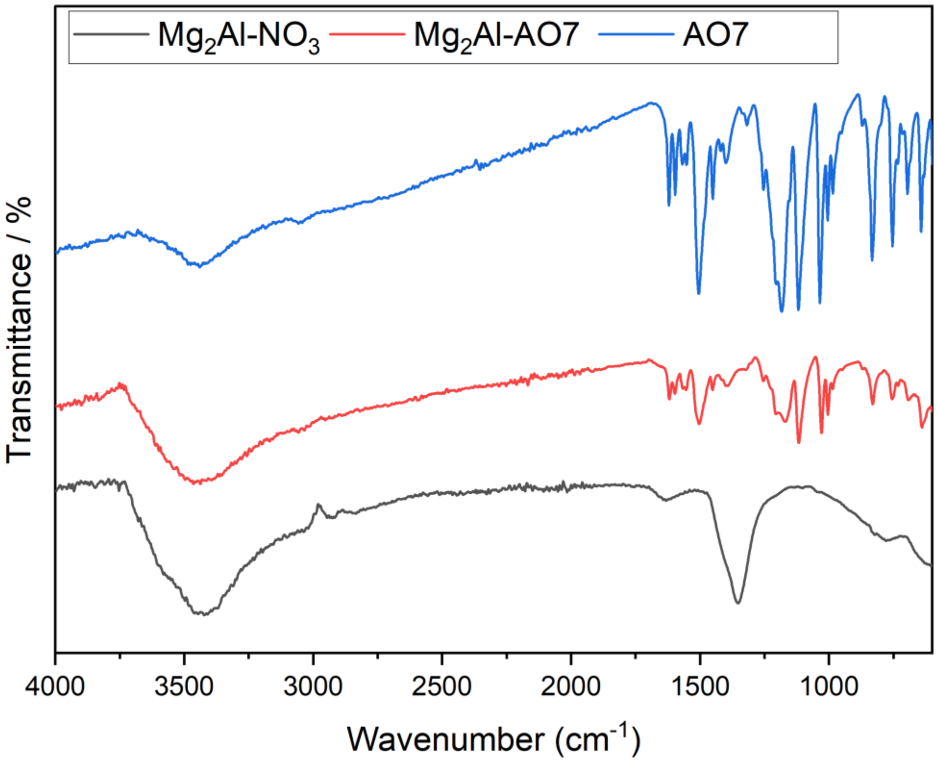

Figure 6.4. FTIR spectra of Mg_2Al-CO_3, Mg_2Al-AO7 and AO7 dye

FTIR analysis was conducted to further confirm the presence of AO7 within the LDH structure (Figure 6.4). For both NO_3 and AO7 intercalated LDHs, a broad peak around 3400 cm^{-1} is observed, associated with hydrogen-bonded O-H stretching peaks from the mixed metal hydroxides within the brucite layer, and interlayer water. [303] A low-intensity peak at 1620 cm^{-1} was also observed for Mg_2Al-NO_3 corresponding to the bending vibration of O-H. [167] The only other intense peak observed in the spectra of Mg_2Al-CO_3 at 1352 cm^{-1} was associated with the symmetrical stretch of N=O within the nitrate species. [35] It was evident from comparison between spectra of Mg_2Al-AO7 and AO7 that peaks below 1750 cm^{-1} were predominantly associated to peaks related to the dye molecule: 1615 – 1450 cm^{-1} (C=C aromatic stretching and C=O stretching) and 1250 – 1000 cm^{-1} (S-O stretching and aromatic C-O stretch). [304] Small shifts (2 – 10 cm^{-1}) in the absorption peak maximums were observed, which have been attributed by previous authors to small changes to the atomic environment upon ionic interactions with the brucite layer. [304] For example, peaks at 1182 and 1034 cm^{-1} in AO7, associated with sulfonate vibrations, shift to 1168 cm^{-1} and 1030 cm^{-1} due to the interactions between SO_3^- and hydroxyls in the brucite layer. [35,305] Interestingly peaks for C=N

(1622 cm^{-1}), C-N (1599 cm^{-1}) and N-H (1452 cm^{-1}) were all present, suggesting both hydrazone and azo forms of AO7 exist in both the unbound dye and the LDH (Figure 6.5). [304]

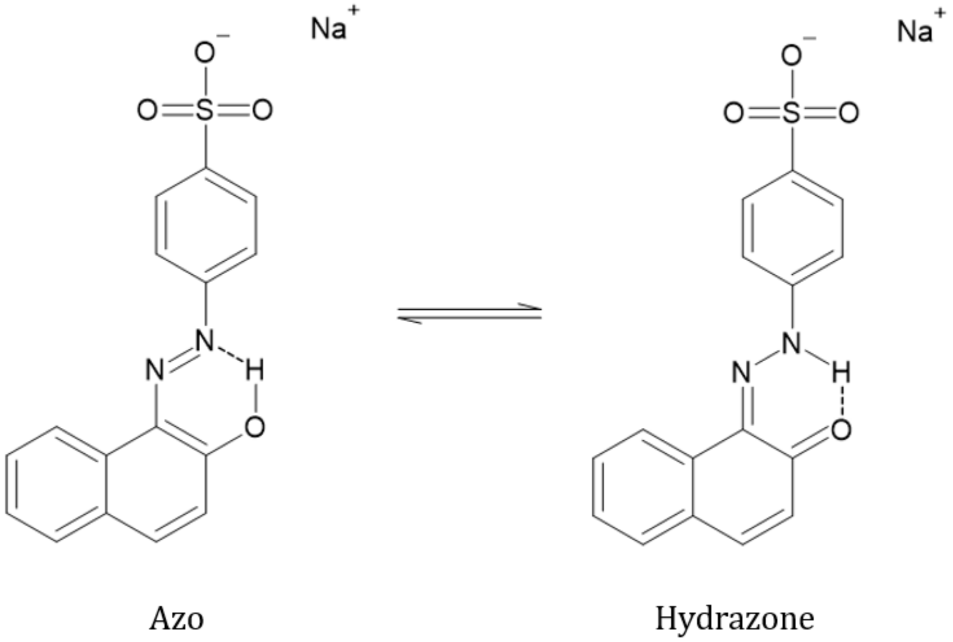

Figure 6.5. Tautomeric forms of AO7

6.4.3. Thermal Stability of Mg_2Al-AO7

The thermal stability of Mg_2Al-AO7 was compared against Mg_2Al-NO_3 and AO7 dye. LDHs generally exhibit three mass loss stages, which were observed in Mg_2Al-NO_3's TGA profile (Figure 6.6, top): [208]

1) Evaporation of surface-bound water (< 200 °C).
2) Dehydroxylation of brucite sheets (300 – 400 °C).
3) Breakdown of the layered structure and evolution of the interlayer anions (> 400 °C).

A total mass loss of 49 % was observed, which was in agreement with the analysis of previously synthesised MgAl-NO_3 LDHs, whereby ~50 % mass loss was reported. [102,306] The most distinguishing feature of AO7's TGA profile was a rapid mass loss at 329 °C due to the combustion of its organic structure (Figure 6.6, bottom). [35] Generally azo dyes start to decompose between 200-300 °C by dissociation of the C-N= bond, forming benzene derivatives such as aniline and naphthalene. [307] However, the thermal degradation of AO7 is stabilised due to intramolecular hydrogen bonding within its hydrazone tautomer. The mass loss of Mg_2Al-AO7 appeared to be a hybrid of both AO7 and Mg_2Al-NO_3 TGA profiles, although no rapid weight loss occurred at 329 °C suggesting incorporation of AO7 into the LDH increases the dyes thermal stability. This was corroborated by previous TG-DTA analyses by Liu and Evan's, where it was considered to be due to host-guest interactions. [35] The higher total mass loss observed for Mg_2Al-NO_3, compared to Mg_2Al-AO7, was attributed to the amounts of surface bound water and differences in interlayer anion (Table 6.3). Previous TGA-MS analysis in Chapter 4 highlighted that CO_3^{-2} and NO_3^- interlayers are evolved as CO_x/NO_x gases, whereas AO7 undergoes combustion to produce a carbon char.

Table 6.3. Total mass loss observed in TGA analysis

	Total Mass Loss / %
Mg_2Al-NO_3	49
Mg_2Al-AO7	43
AO7	48

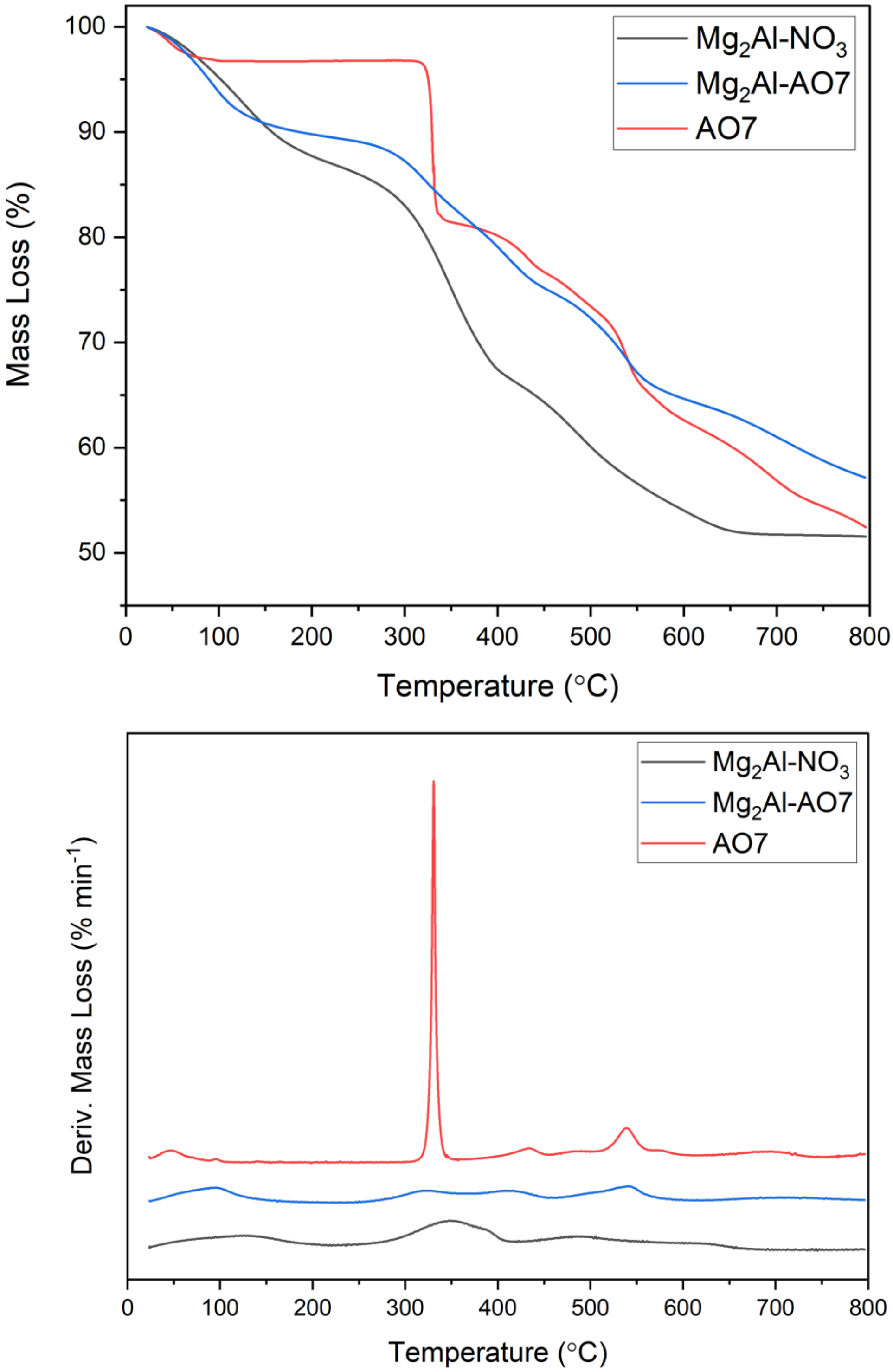

Figure 6.6. Mass loss (top) and derivative mass loss (bottom) profiles of Mg$_2$Al-NO$_3$, Mg$_2$Al-AO7 and acid orange 7

6.4.4. Surface Composition of Mg_2Al-AO7

SEM-EDS imaging was conducted to gain insight into the surface composition of Mg_2Al-AO7 (Figure 6.7). As AO7 is an organic, sulfonate-based dye it can be detected through the presence of both sulphur and carbon elements in EDS.

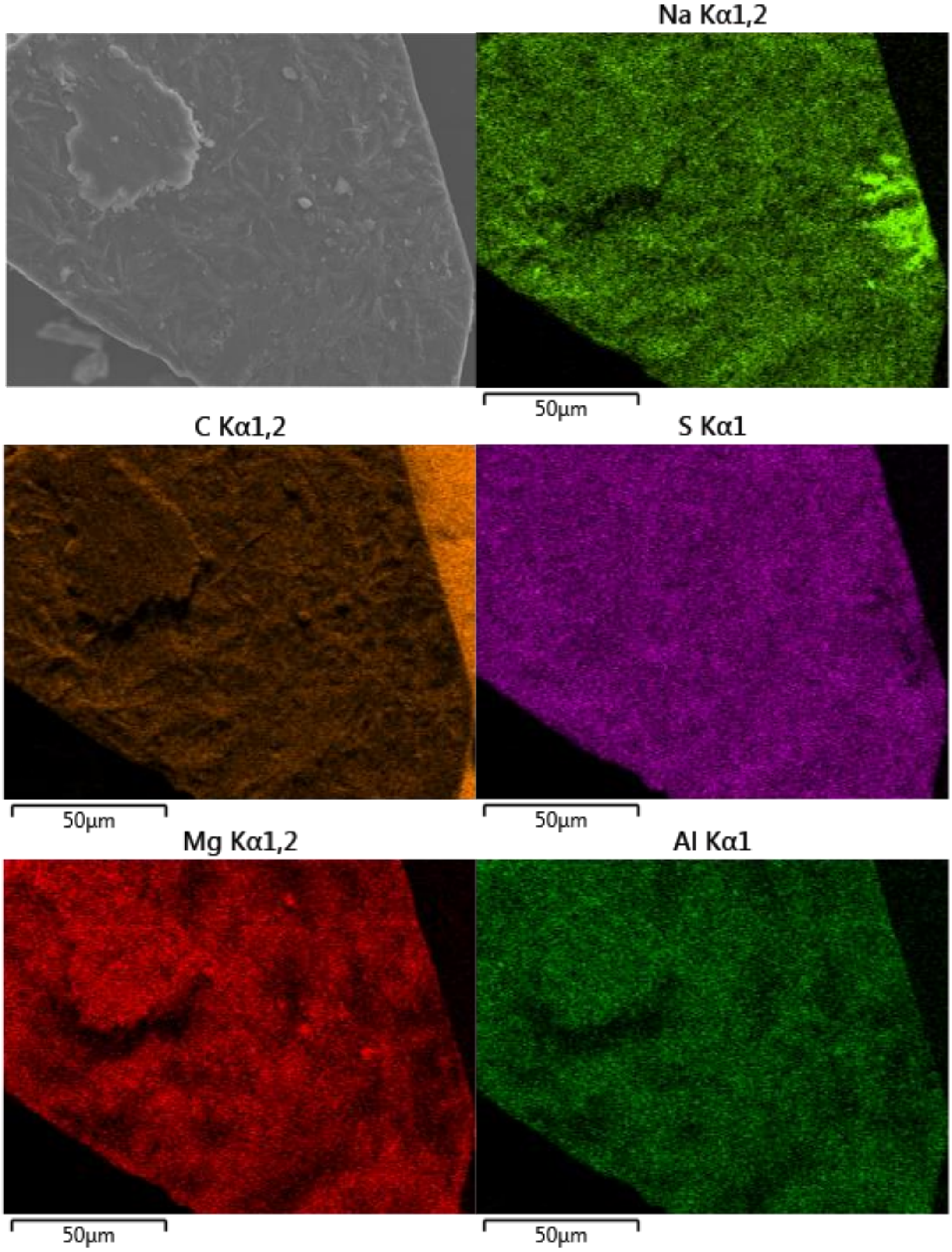

Figure 6.7. SEM-EDS imaging of Mg_2Al-AO7. Original SEM image (top left)

It was apparent from K-alpha emissions of both carbon and sulphur that the dye was well dispersed across the surface. While there were some nanoparticles dispersed across the LDH surface, these did not appear to be due to unbound AO7. Na, O and N intensity in these regions suggested they were instead due to $NaNO_3$, a by-product of LDH synthesis (Eq 6.1), that precipitated on the LDH surface during drying.

$$\begin{aligned}&2NaOH + 0.33AO7 + 0.66\,Mg(NO_3)_2 + 0.33\,Al(NO_3)_3 \\ &\qquad \rightarrow [Mg^{2+}_{0.66}Al^{3+}_{0.33}](AO7)_{0.33} + 2.33\,NaNO_3\end{aligned} \qquad 6.1$$

Quantitative distribution of elements was also attained from EDS analysis (Table 6.4) and compared to theoretical atomic weight distributions, calculated from the expected product based on the reaction equation above (6.1) and molar ratios used. The measured molar ratios between Mg and Al for both Mg_2Al-AO7 and Mg_2Al-CO_3 were 2.11 and 2.17 respectively. As these are close to the expected 2:1 ratio it indicates that both Mg and Al were fully mineralized during synthesis. [308] In Mg_2Al-AO7 LDH, elements associated with AO7 had a higher atomic weight than expected indicating a greater distribution of AO7 on the surface than the bulk solid. For example, C made up approximately 63 % of atomic weight, despite only 53 % calculated from the reaction equation. Similarly, S made up 4.39 % of weight compared to 3.32 % expected. While XRD analysis in Section 6.4.1 confirmed the intercalation of AO7 between brucite layers, this may indicate that AO7 is also removed from the solution by adsorption onto the surface.

Table 6.4. EDS results of Mg_2Al-NO_3 and Mg_2Al-AO7, compared to the theoretical atomic weight

Element	**Atomic Weight / %**		**Theoretical Atomic Weight / %**	
	Mg_2Al-NO_3	**Mg_2Al-AO7**	**Mg_2Al-NO_3**	**Mg_2Al-AO7**
C	65.07 ± 0.33	62.98 ± 0.10	0	53.23
O	22.05 ± 0.41	24.35 ± 0.09	69.37	33.47
S	0.02 ± 0.01	4.39 ± 0.02	0	3.32
Na	1.25 ± 0.06	3.65 ± 0.02	0	0
Mg	3.57 ± 0.08	3.17 ± 0.02	15.31	6.65
Al	1.69 ± 0.04	1.46 ± 0.01	7.66	3.33
N	6.08 ± 0.52	0.00 ± 0.64	7.66	0

Interestingly, despite no carbon sources used during synthesis, over 65 % of Mg_2Al-NO_3 LDH's atomic weight appeared to be due to C. It is well documented in literature that due to the high selectivity of CO_3^{2-} and presence of CO_2 in air and water a nitrogen atmosphere is required to produce a pure nitrate form of LDH. [94] It is therefore possible that a carbonate-based interlayer formed in preference to the more weakly bound NO_3^-. However, a more likely culprit for the high carbon content is due to surface contamination. Carbon has been cited as one of the main culprits of surface contamination in SEM and TEM, whereby layers of carbon can gradually build-up due to CO_2 in the air and cracking of hydrocarbons within the vacuum chamber. [309] In addition, further carbon contamination may occur during sample preparation, whereby samples are adhered to carbon tabs prior to platinum coating. [192] As a result, any quantitative conclusions drawn from the carbon content with LDH samples remain dubious.

6.4.5. Changes in Dye Concentration During Synthesis

Alongside the characteristics of the solid Mg_2Al-AO7 product formed, changes in AO7 concentration within the solution were observed by UV-vis spectrophotometry (Table 6.5). The initial concentration of AO7 (10801 mg L^{-1}) in the downflow agreed with expected values from the 0.033 M AO7 used during synthesis. In addition, the dilution factor of 1.53 observed, upon combination of both the downflow and upflow, was congruent with the flow rates used. After the product had been removed by centrifugation, the concentration of AO7 remained high, exceeding 3500 mg L^{-1}. This corresponded to a 49.8 % removal of dye. This was of notable interest considering 2x excess of AO7 was used during synthesis, based on previous CFHS syntheses of LDHs citing it to be optimal for LDH formation. [30] Under the assumption that all AO7 removed from solution reacted to form Mg_2Al-AO7 LDH, this suggested a 99.6 % conversion of precursors.

Table 6.5. The concentration of AO7 in solution during Mg_2Al-AO7 synthesis

	AO7 Concentration / mg L^{-1}
Downflow	10801 ± 95
Combined flows	7058 ± 66
Centrifuged Product	3549 ± 29

This high conversion rate of precursors was further confirmed upon drying of the unwashed, centrifuged product. XRD analysis revealed it to be a biphasic solution, containing only Mg_2Al-AO7 LDH and reaction byproduct $NaNO_3$ (Figure 6.8). [310] No other diffraction peaks related to precursors such as $Mg(NO_3)_2$, $Al(NO_3)_3$ or AO7 were present in any observable quantity. The presence of high levels of LDH following centrifugation suggests a coagulant may be required if higher levels of product retention are required.

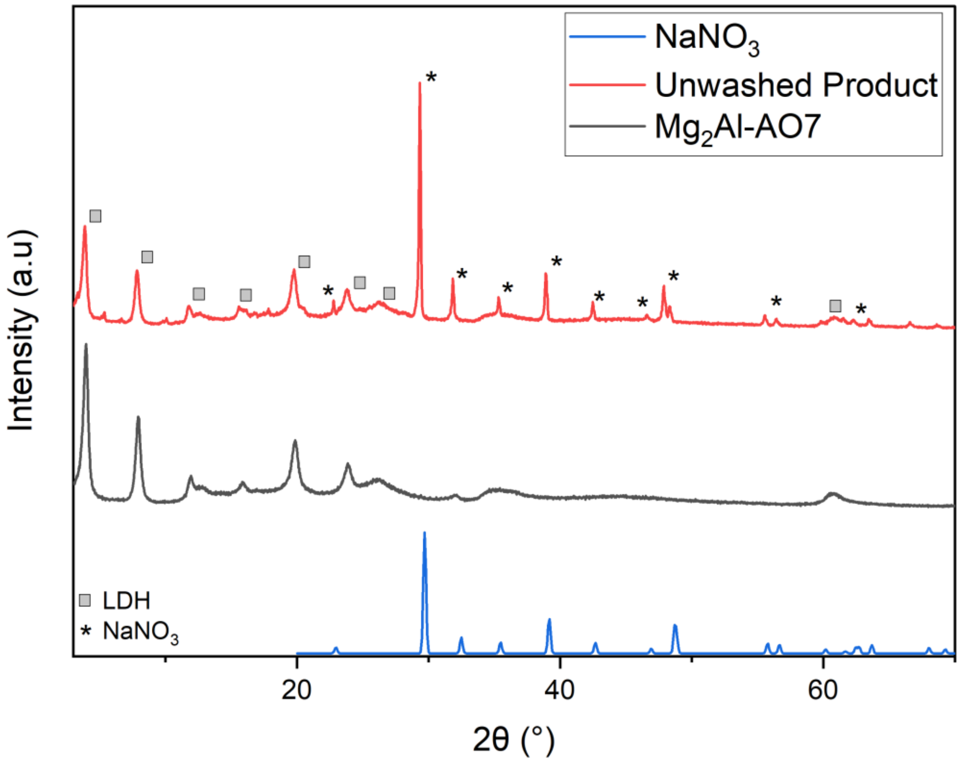

Figure 6.8. XRD analysis of unwashed Mg2Al-AO7, compared to Mg2Al-AO7 and NaNO3

Naturally, if this conversion of precursors could be achieved without 2x excess of AO7, this synthesis method could be utilized for almost complete remediation of dye wastewater containing very high concentrations (5000+ mg L^{-1}) of AO7. As a result, synthesis was repeated using a stoichiometric amount of AO7 (Table 6.6). Unfortunately, only a 54 % conversion of AO7 precursor was achieved, suggesting the excess AO7 was required for higher conversion of precursors. This was in agreement with previous literature, attributed to insufficient nucleation rates at the lower stoichiometric concentration. [87]

Table 6.6. Concentration changes during Mg_2Al-AO7 synthesis using stoichiometric AO7

	AO7 Concentration / mg L^{-1}
Downflow	5369 ± 90
Combined flows	3543 ± 59
Centrifuged Product	1645 ± 41

6.4.6. Stability of Mg_2Al-AO7 in Water

Suspension of Mg_2Al-AO7 in water resulted in instantaneous dissolution of AO7, stabilizing after 24-48 h at 85 mg L^{-1} (Figure 6.9). As previous literature has shown that MMO's reform LDH structure in water due to dissolved CO_2, it was hypothesised that this was due to ion-exchange to form Mg_2Al-CO_3. [95] However, a repeat of the experiment in a solution of CO_3^{2-} ions yielded a similar profile, suggesting this was unlikely to be the case. From this it was deduced that loss of AO7 was likely to occur from surface bound dye, as opposed to any ion-exchange processes.

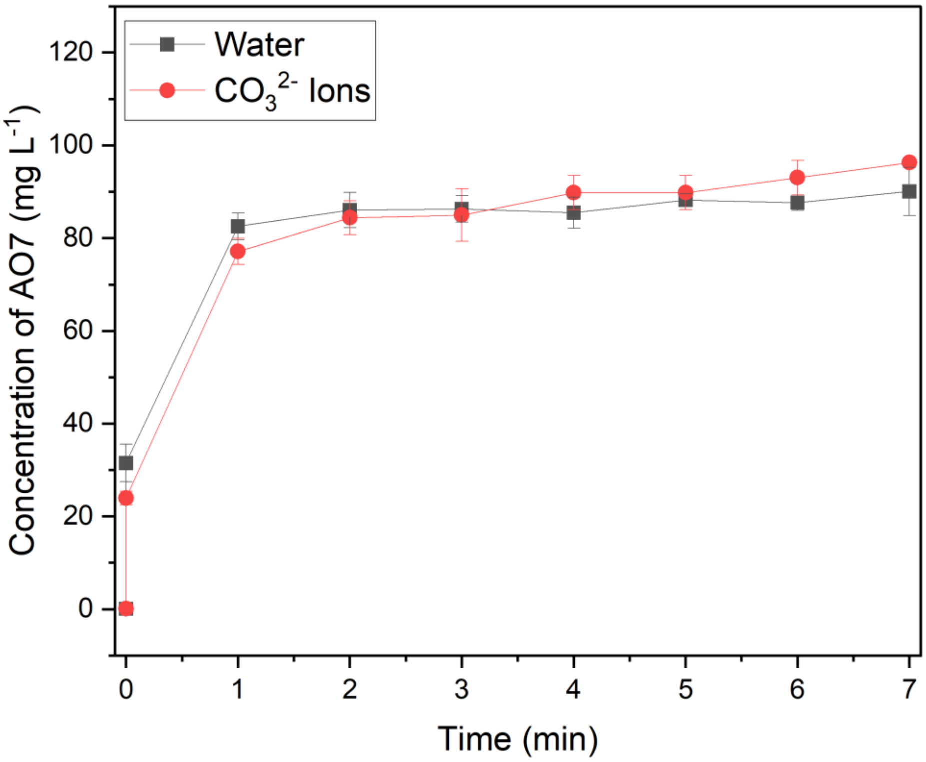

Figure 6.9. Changes in concentration of AO7 over time upon suspension of Mg_2Al-AO7 in solution

This was confirmed upon XRD analysis, whereby no peaks correlating to the formation of Mg_2Al-CO_3 were observed (Figure 6.10). While Mg_2Al-AO7 appeared to remain phase pure after seven days, the reduction in peak intensities suggested that the crystal structure could not be maintained. As a result of this, as well as substantial quantities of AO7 dissolution into water, any solution-based application for Mg_2Al-AO7 is unlikely. Due to the apparent stability of the LDH to ionic species such as CO_3^{2-} in solution, a dye recovery and LDH regeneration mechanism by ion-exchange is also improbable. However, it should be noted that this resistance to ionic species is promising for synthesis of Mg_2Al-AO7 using environmental dye effluent, whereby many other competing anions are present.

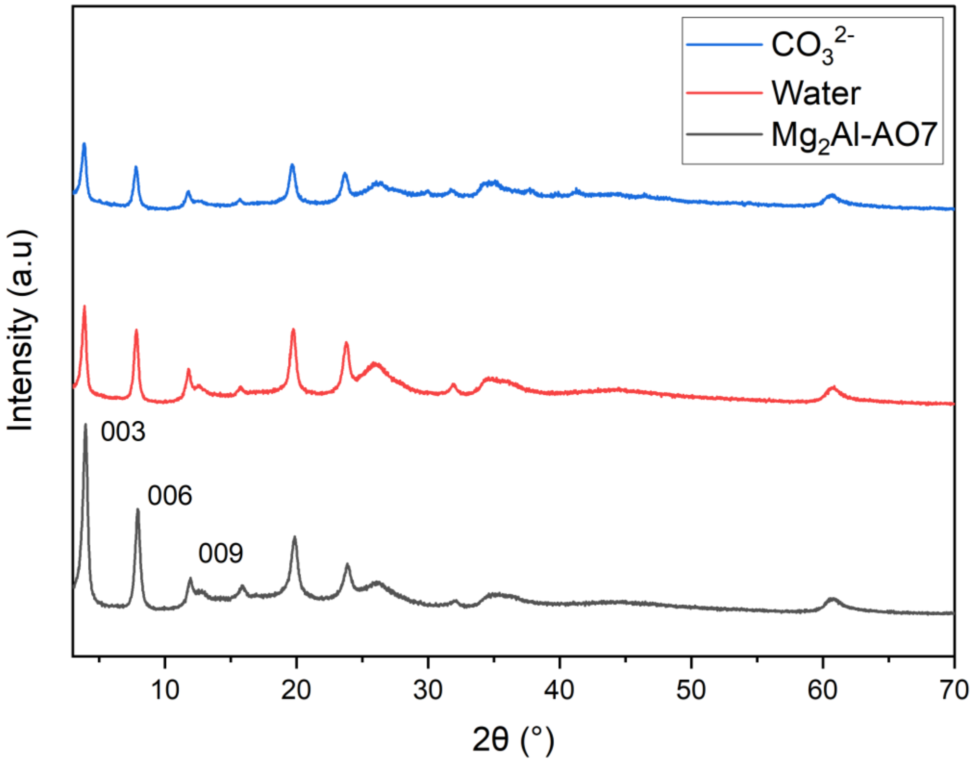

Figure 6.10. Changes in diffraction patterns of Mg_2Al-AO7 upon dispersion in water

6.5. Synthesis of SY, EB, MB and Saf-O Intercalated LDHs

6.5.1. Initial Observations

To determine if CFHS could be utilized for the intercalation of other dyes into LDH structure, synthesis was attempted using four other dyes: SY, EB, MB and Saf-O. These were chosen based on their ionic nature and molecular size (previously discussed in more detail in Chapter 5) replacing the traditional counter ions used in syntheses such as NO_3^- or CO_3^{2-}. While solid precipitates were isolated during Mg_2Al-SY and Mg_2Al-EB synthesis, no product was observed during Mg_2Al-MB and Mg_2Al-Saf-O experiments, indicating unsuccessful synthesis with these dyes. This was further confirmed through UV-vis analysis whereby the only reductions in dye concentrations observed were due to the dilution by combination of both the downflow and upflow (Table 6.7). This result was not unexpected due to the ionic nature of both dyes. Both MB and Saf-O are cationic based dyes of single valency making LDH formation unfavourable due to electrostatic repulsion between brucite sheets and dye. While there are reports of both MB and Saf-O being removed from solution by LDHs in the literature, [82,169,280] these generally occur by surface adsorption processes, not intercalation. [39] As a result, further experimentation on dye intercalated LDH synthesis using cationic dyes was concluded.

Table 6.7. Concentration of MB and Saf-O during LDH synthesis

	MB Concentration / mg L^{-1}	**Saf-O Concentration / mg L^{-1}**
Downflow	9410 ± 62	10417 ± 161
Combined Flows	6220 ± 47	6890 ± 90
Centrifuged Product	6205 ± 59	6940 ± 76

6.5.2. Intercalation of SY and EB into Mg_2Al LDH Structure

In contrast to MB and Saf-O synthesis, a reduction of the dye concentration was observed during both Mg_2Al-SY and Mg_2Al-EB synthesis (Table 6.8). Initial dye concentrations within the precursor solutions corresponded well with the 0.0165 M (SY) and 0.0083 M (EB) used during synthesis. UV-vis analysis revealed removals of 17.5 and 39.0 % respectively (excluding changes in concentration due to dilution by flow combination), considerably lower conversion rates of precursors compared to Mg_2Al-AO7 synthesis. While the exact reason for this was not elucidated, SY's lower conversion was partially attributed to its speciation during synthesis. Due to a high synthesis pH (pH = 11.10), SY exists primarily in its trivalent state (SY^{3-}) due to deprotonation of its phenolic group above pH 10. [281] At this higher anionic charge SY occupies more active sites within the interlayer region per molecule, resulting in a lower incorporation of SY into LDH structure.

Table 6.8. Concentration of SY and EB during LDH synthesis

	SY Concentration / mg L^{-1}	**EB Concentration / mg L^{-1}**
Downflow	7426 ± 59	7920 ± 82
Combined Flows	4901 ± 39	5250 ± 54
Centrifuged Product	4042 ± 63	3202 ± 81

Despite the lower uptakes, XRD analysis did reveal signs of incorporation of both SY and EB into LDH structure. The diffraction patterns of both Mg_2Al-SY and Mg_2Al-EB had no reflections corresponding to free SY or EB dye (Figure 6.11). Much like Mg_2Al-AO7 synthesis, it was expected that intercalation of large SY/EB molecules would increase the interlayer distance, resulting in a left-shift of diffraction peaks associated with this d-spacing. While the diffraction peaks of Mg_2Al-SY and Mg_2Al-EB were very broad and of low intensity, there did appear to be signs of 003, 006 and 009 peaks associated with interlayer spacing at very low 2θ angles (< 10 °). Few papers have discussed intercalation of large anionic species during synthesis, however one author suggested that ion-exchange methods result in LDHs of higher crystallinity as less interlayer expansion occurs. [311] This may explain why the structure of Mg_2Al-SY and Mg_2Al-EB are less crystalline than Mg_2Al-AO7 as their dyes are of larger size, requiring a greater interlayer region to incorporate them. The broad and low intensity of peaks may also be due to other factors such as crystallite size and/or inhomogeneous strain broadening. [147]

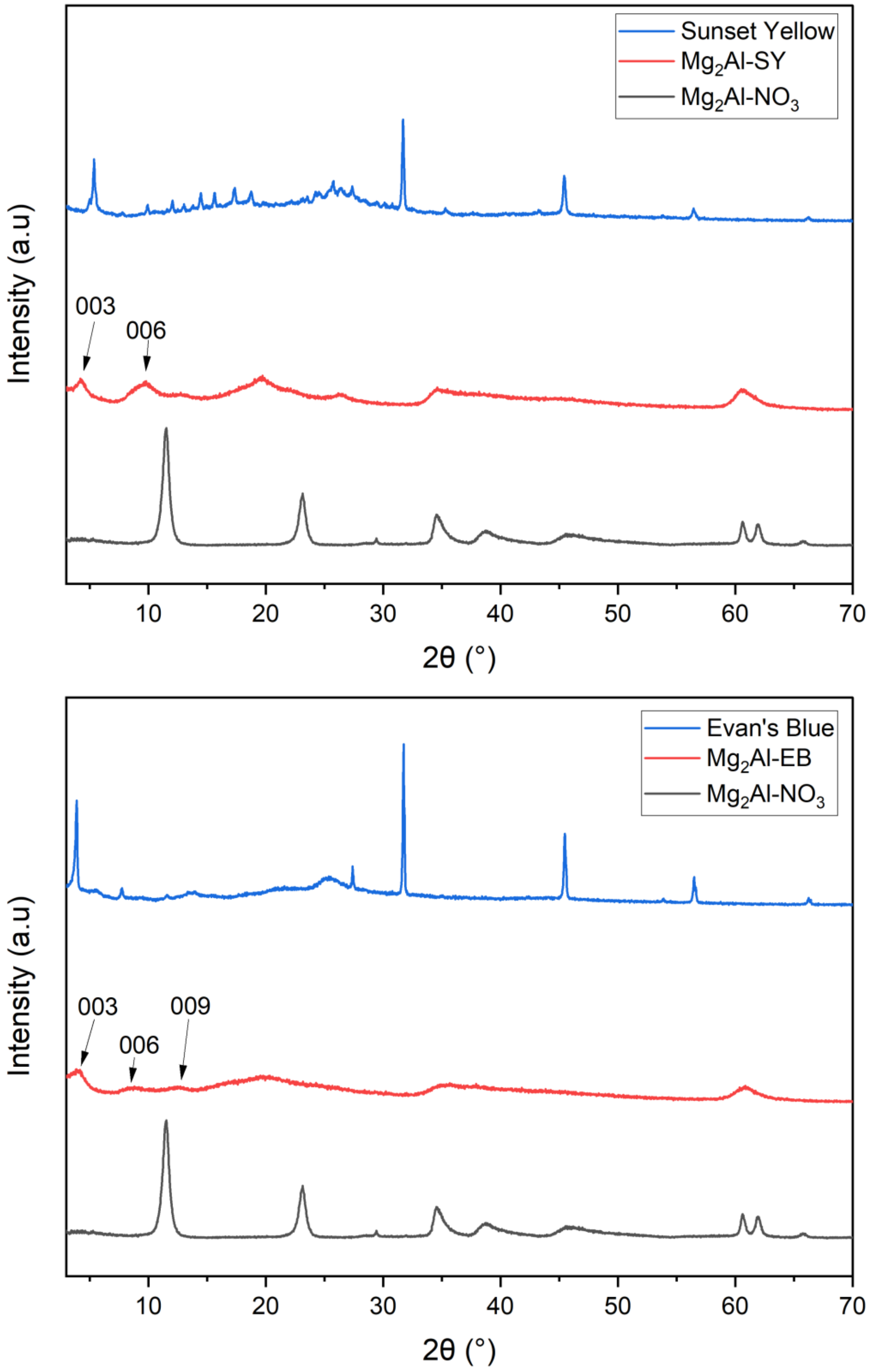

Figure 6.11. Diffraction patterns of Mg_2Al-SY (top) and Mg_2Al-EB (bottom), compared to Mg_2Al-NO_3 and SY/EB dye

Estimations of 2θ positioning of 003, 006 and 009 peaks were used to calculate the interlayer spacing for both LDHs (Table 6.9). D-spacing was calculated at 2.02 and 2.18 nm for Mg_2Al-SY and Mg_2Al-EB respectively, which was in agreement with, albeit slightly smaller than, that of Mg_2Al-AO7 (Section 6.4.1). The comparatively smaller d-spacings of both LDHs, alongside previous UV-vis analysis, may therefore suggest insufficient incorporation of the dyes into the interlayer region. However, it should be noted that there is likely to be considerable error in d-spacing calculations of SY and EB intercalated LDHs due to the broadness and low intensity of peaks.

Table 6.9. 2ϑ, d values and interlayer distances of Mg_2Al-NO_3, Mg_2Al-SY and Mg_2Al-EB

LDH	Diffraction Peaks						Interlayer Distance / nm
	003		006		009		
	2θ / °	d / nm	2θ / °	d / nm	2θ / °	d / nm	
Mg_2Al-NO_3	11.53	0.77	23.15	0.38	34.55	0.26	0.77
Mg_2Al-SY	4.19	2.11	9.44	0.94	12.78	0.69	2.02
Mg_2Al-EB	3.80	2.33	8.53	1.04	12.47	0.71	2.18

6.5.3. Detection of Crystallinity by TEM

Micrographs of Mg_2Al-AO7 and Mg_2Al-SY revealed the presence of small crystallites, less than 100 nm in size (Figure 6.12). Poor image resolution made crystallite sizes difficult to ascertain in Mg_2Al-EB, although similar sizes were assumed. While platelets appeared to be irregularly shaped, with little observation of the indicative hexagonal nature of LDH, lattice fringes along platelet edges indicated crystallinity. A high degree of agglomeration was observed in all LDHs with no distinct order to stacking - both face-to-face and face-to-edge stacking occurred. While this agglomeration in all samples meant that PSD could not be quantified, there did not appear to be any notable visual differences that could attribute to the peak broadening of Mg_2Al-SY and Mg_2Al-EB in XRD.

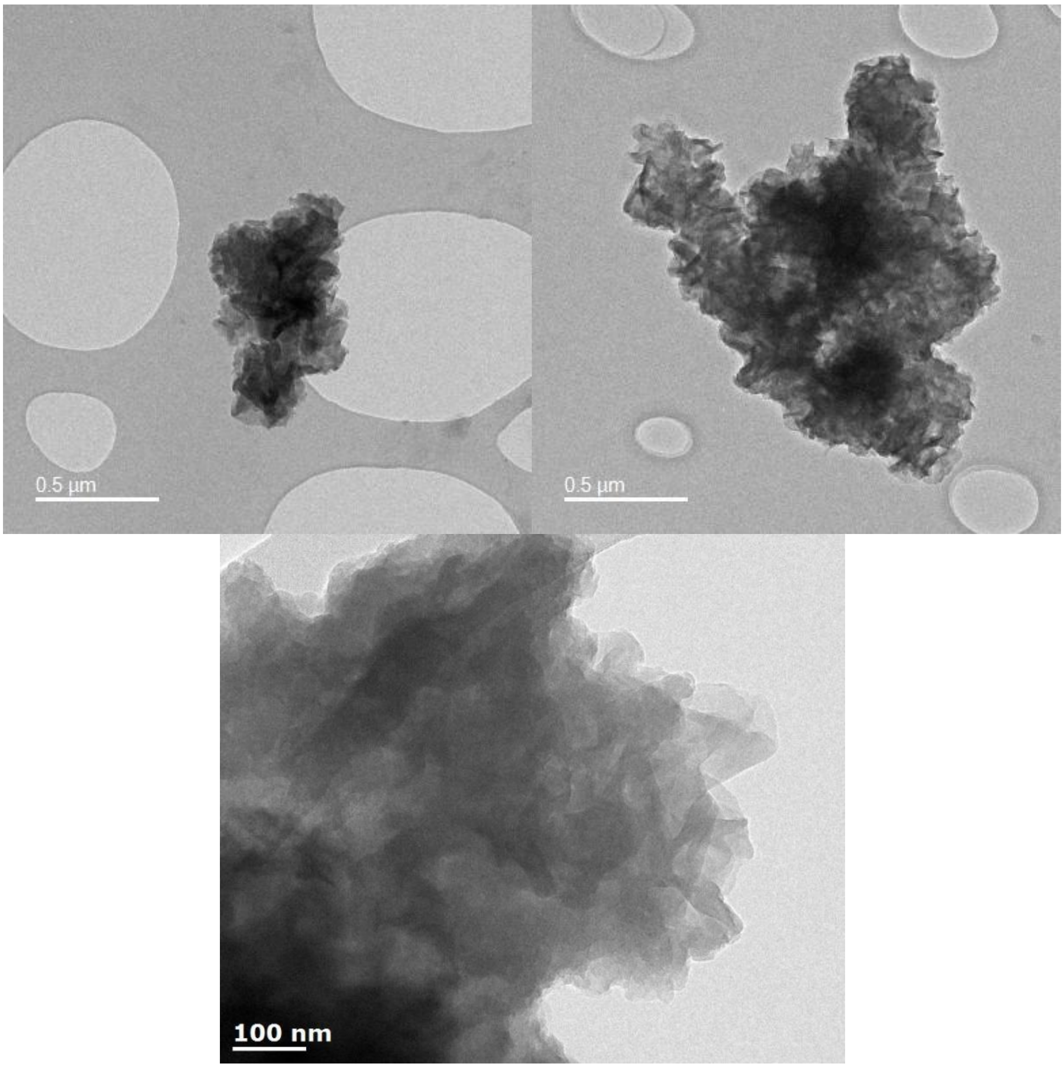

Figure 6.12. TEM imagery of Mg_2Al-AO7 (top left), Mg_2Al-SY (top right) and Mg_2Al-EB (bottom)

Higher magnification images of Mg_2Al-SY and Mg_2Al-EB revealed ordered grain-like parallel lines, further confirming the presence of a crystallographic plane across the sample (Figure 6.13). [193] However, prolonged exposure to the electron beam resulted in the disappearance of these ordered features, suggesting thermal breakdown occurred, thus making it hard to garner how extensive they were. This ordered structure was further confirmed through diffraction analysis, whereby sharp concentric bands were observed due to the regular spacing of Mg ions (Figure 6.14).

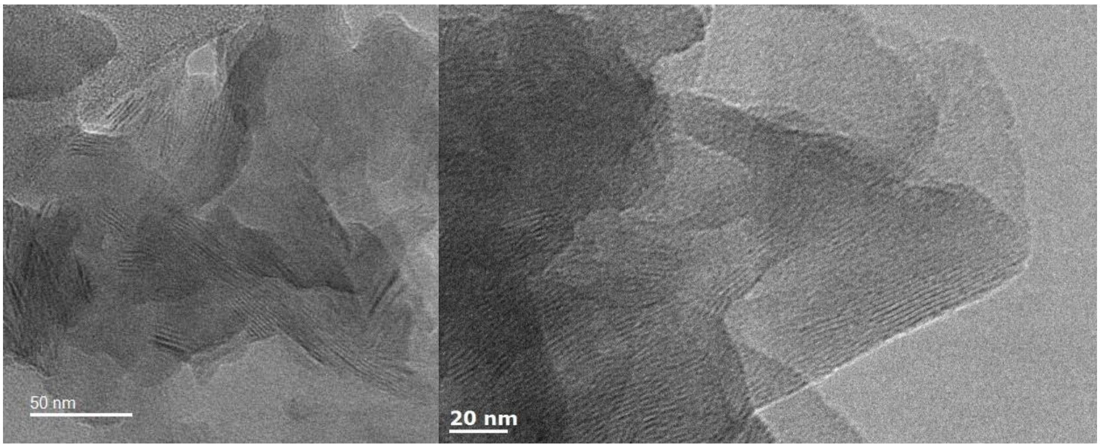

Figure 6.13. Higher magnification TEM images of Mg_2Al-SY (left) and Mg_2Al-EB (right)

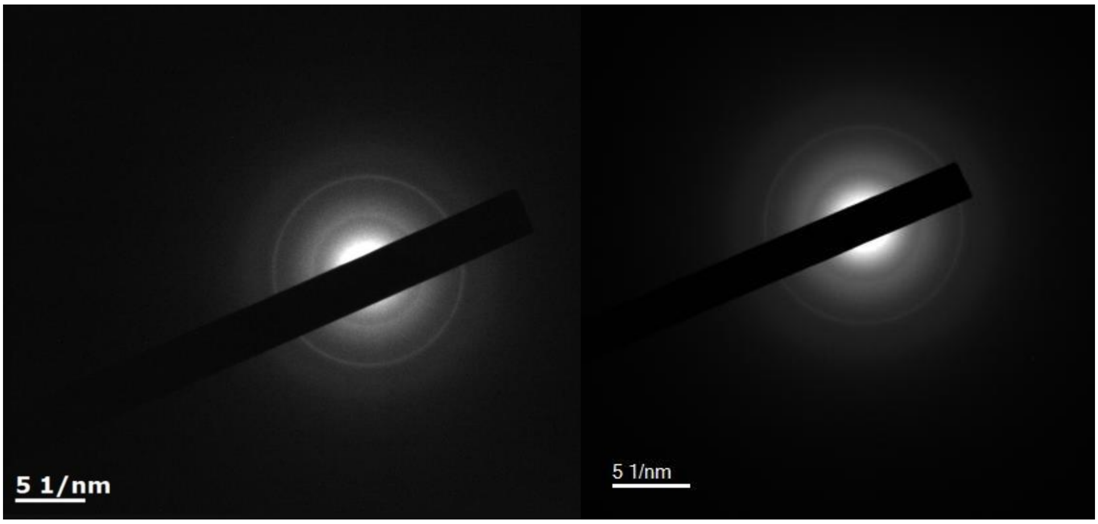

Figure 6.14. TEM Diffraction imaging of Mg2Al-SY (left) and Mg2Al-EB (right)

6.5.4. FTIR Analysis of Mg_2Al-SY and Mg_2Al-EB

FTIR analysis of both Mg_2Al-SY and Mg_2Al-EB confirmed the presence of dyes within the structures (Figure 6.15). This was evidenced by analogous peaks in their spectra to the respective free dyes between 750 – 1750 cm^{-1} and the disappearance of an intense peak at 1352 cm^{-1}, attributed to the symmetrical stretch of N=O in NO_3^- anions. Naturally the intensity of these peaks was reduced compared to the free dye due to the incorporation of the dye into bulk LDH structure. Due to similarities between the structures of AO7, SY and EB, and their subsequent FTIR spectra, in depth analysis of absorption peaks was not repeated (refer back to Section 6.4.2). Much like Mg_2Al-AO7, small shifts in the absorption peak maxima were observed for both Mg_2Al-SY and Mg_2Al-EB, once again highlighting small changes in atomic environment upon intercalation (Table 6.10). [35] As electrons are donated from $-SO_3^-$ groups to the brucite layer bond lengths increase, resulting in a reduction in wavenumber. [303]

Table 6.10. Comparison of the peak maxima of stretching vibrations in LDH and free dye

Stretching Vibration	**Wavenumber / cm^{-1}**			
	Dye		**LDH**	
	SY	**EB**	**Mg_2Al-SY**	**Mg_2Al-EB**
S-O-R	1036	1045	1034	1038
Aromatic C-O	1119	1111	1115	1107
S=O (Symmetric)	1184	1175	1180	1173

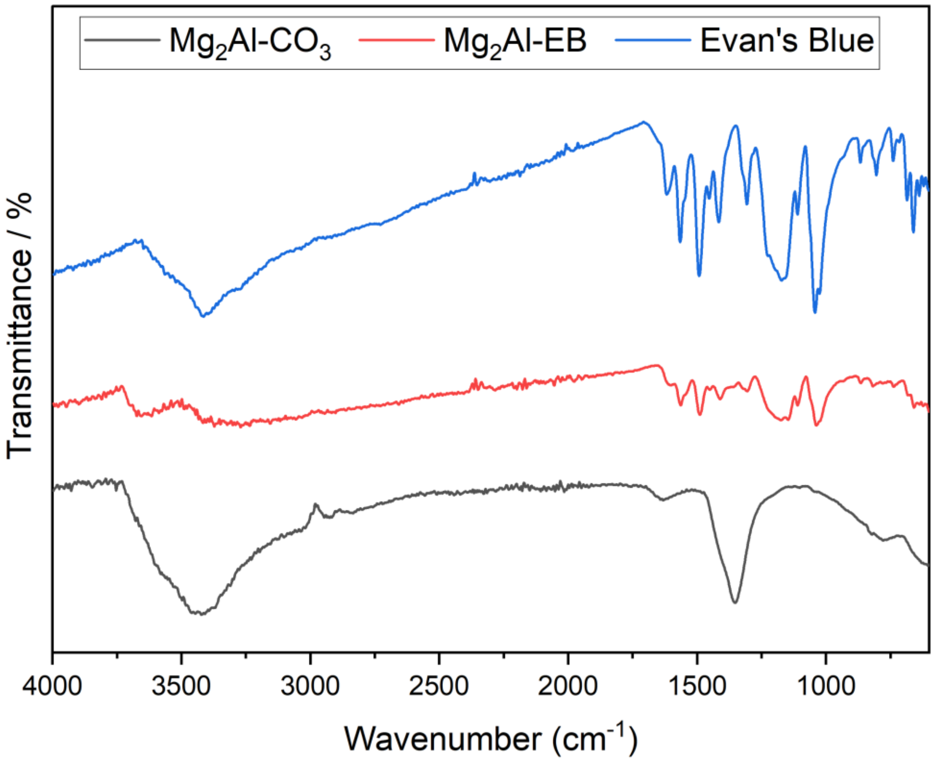

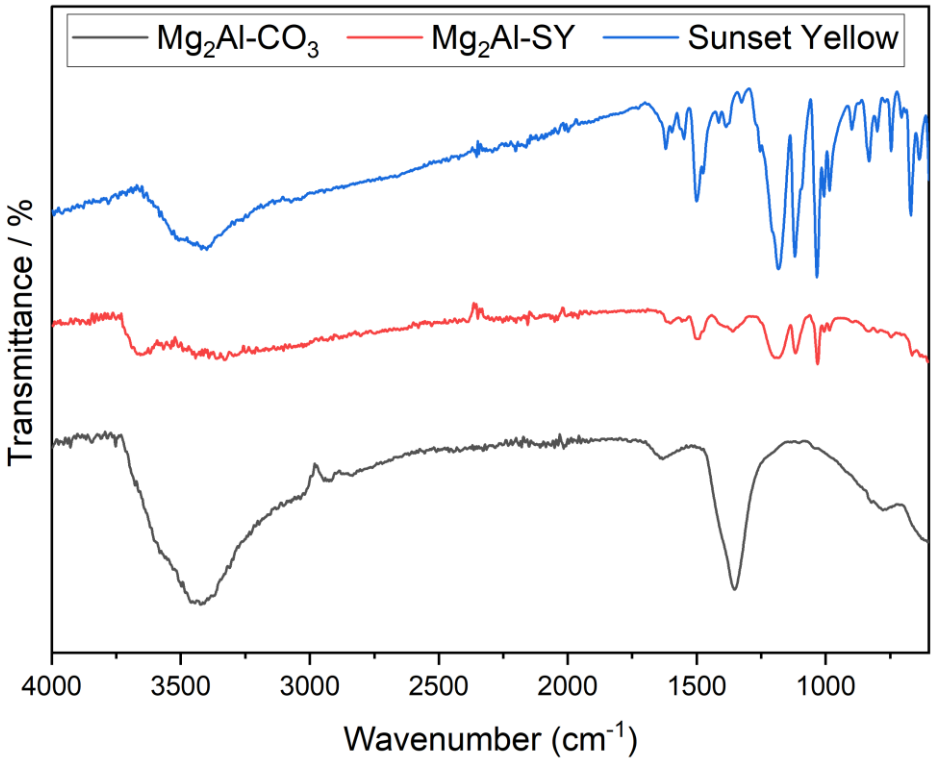

Figure 6.15. FTIR analysis of Mg_2Al-SY (top) and Mg_2Al-EB (bottom), compared to Mg_2Al-NO_3 and SY/EB dye

6.5.5. Thermal Stability of Mg_2Al-SY and Mg_2Al-EB

Much like AO7, both SY and EB dyes pertained thermal stability above 300 °C, exhibiting initial mass loss stages at 383 and 325 °C respectively, due to tautomerisation of the azo bond to hydrazone (Figure 6.16). Broad mass loss regions observed between 30 – 200 °C were observed due to surface bound water. Upon incorporation into LDH structure, unique TGA patterns were observed. Mg_2Al-SY exhibited a TGA profile more analogous to that of conventional LDHs with three different mass loss stages observed akin to evaporation of surface bound water, dehydroxylation and structural breakdown. [93] Much like Mg_2Al-AO7, the thermal stability of SY was increased upon incorporation into LDH structure, evidenced by the disappearance of the initial derivatised peak of SY's decomposition at 383 °C. Interestingly, incorporation of SY into Mg_2Al-SY also appeared to increase the thermal stability of the LDH, with the 2nd dehydroxylation mass loss stage not initiating until 300 °C. The TGA loss profile of Mg_2Al-EB was more complex, exhibiting broad mass loss between 300 – 700 °C. This appeared to be a hybrid of both EB and Mg_2Al-NO_3 profiles. Both Mg_2Al-SY and Mg_2Al-EB exhibited a reduction in total mass loss compared to Mg_2Al-NO_3, attributed to less surface bound water and carbonization of the organic dyes (Table 6.11).

Table 6.11. Total mass losses of Mg_2Al-SY and Mg_2Al-EB during TGA Analysis

	Total Mass Loss / %
Mg_2Al-NO_3	49
Mg_2Al-SY	42
SY	46
Mg_2Al-EB	42
EB	61

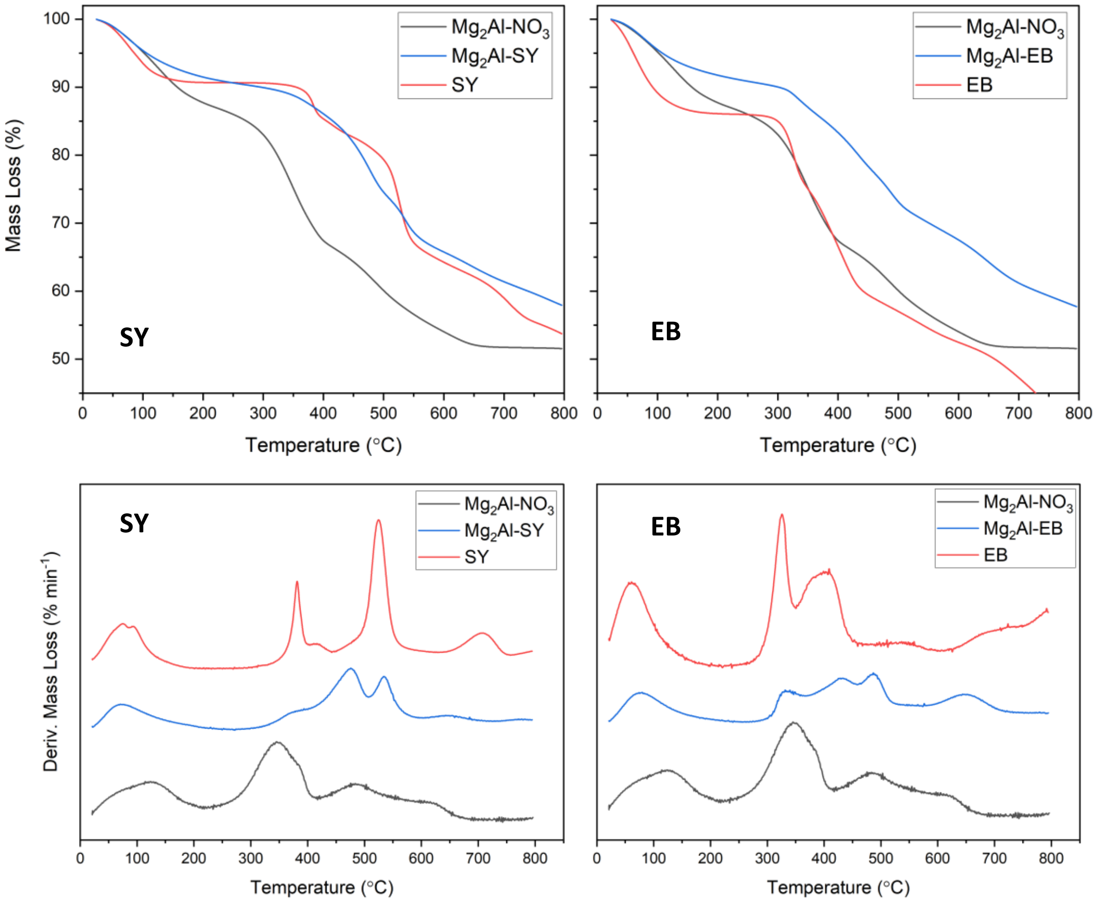

Figure 6.16. Mass loss (top) and derivative mass loss (bottom) of Mg_2Al-SY (left) and Mg_2Al-EB (right)

6.6. Low Dye Concentration Experiments

6.6.1. Scaling down Precursor Concentrations

While the successful synthesis of Mg_2Al-AO7 by CFHS method was reported in Section 6.4, the concentration of AO7 dye used far exceeded those typically found in environmental wastewaters. A previous review by Ateia et al. highlighted that evaluation under realistic conditions is required if further development of sorbents for water treatment is to be achieved. [158] Therefore Mg_2Al-AO7 synthesis using concentrations of AO7 more typical in the environment were attempted. A case study conducted during the literature review (Chapter 2) found that textile wastewater generally containsdye concentrations within the range of 10 – 250 mg L^{-1}. [299] As a result, an AO7 concentration of 100 mg L^{-1} was chosen as the starting point, corresponding to a concentration over 100x lower than used previously. Unfortunately, upon scaling down synthesis concentrations, no LDH product was isolated. UV-vis analysis of precursor and the centrifuged product revealed a 36 % reduction in AO7 concentration, due to dilution by combination of the downflow and upflow solutions (Table 6.12). This was attributed to negligible nucleation, as a result of low particle-particle interactions at these concentrations and the low residence time. [115]

Table 6.12. Concentration of AO7 during low concentration synthesis

	AO7 Concentration / mol dm^{-3}
Downflow	96.9 ± 0.9
Combined flows	62.0 ± 1.3
Centrifuged Product	61.1 ± 0.5

6.6.2. Dye-Doped Mg_2Al-NO_3 Synthesis

Following on from unsuccessful Mg_2Al-AO7 synthesis at low concentrations, an additional idea was formed to dope conventional Mg_2Al-NO_3 with low concentrations of dye. LDH materials have a greater affinity for anions of greater charge density, such as CO_3^{2-} or SO_4^{2-}. [20] It was therefore hypothesised that doping Mg_2Al-NO_3 synthesis with low concentrations of a sulfonate-based dye such as AO7 would result in preferential intercalation of the dye, while still benefiting from the higher concentrations of conventional synthesis. It was immediately evident from visual observations that doping Mg_2Al-NO_3 with

100 mg L^1 AO7 resulted in the removal of dye from solution, as evidenced by discoloration of the centrifuged solution post synthesis (Figure 6.17).

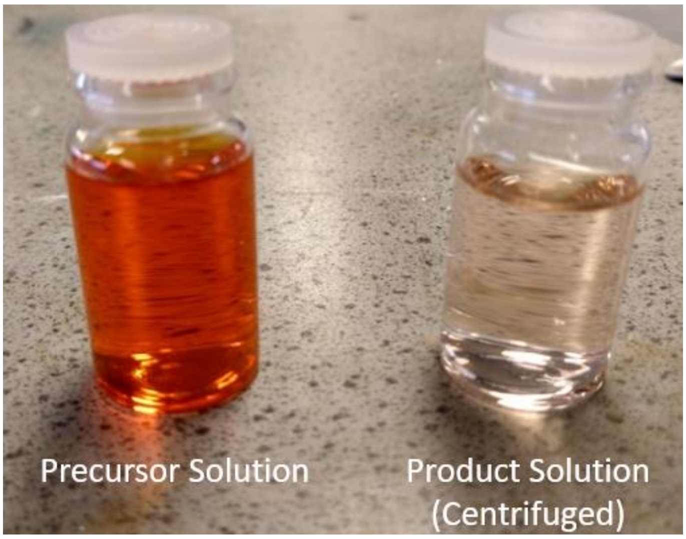

Figure 6.17. Discolouration of AO7 during dye-doped Mg_2Al-NO_3 synthesis

Similar results were seen upon doping Mg_2Al-NO_3 synthesis with SY and EB, where complete discolouration of the dye occurred, producing highly coloured solids (Figure 6.18). These observations were quantitatively confirmed through UV-vis analysis whereby the concentration of AO7 was reduced from 115.9 mg L^{-1} to 1.2 mg L^{-1}, equating to 98.9 % removal (Table 6.13). Concentrations of SY and EB post synthesis were below the limits of detection (LOD), suggesting near complete removal of dye from solution. Interestingly, high levels of dye removal (exceeding 90 %) was also observed for cationic MB-doped synthesis, suggesting the short residence times within the reactor were sufficient enough for surface adsorption to occur. In contrast, negligible uptake of Saf-O was observed, which was attributed to its speciation in solution. At pH 10 Saf-O deprotonation starts to occur, existing predominantly in its neutral form above pH 11. [82] As analysis of its product solution revealed a pH of 11.28, this suggests Saf-O exists predominantly in its neutral form during Mg_2Al-NO_3 synthesis, hindering any surface sorption by ionic interactions. While a similar synthesis pH of 11.31 was observed during MB-doped synthesis, speciation diagrams show it exists as the cationic MB^+ species above pH 6 favouring surface sorption. [283]

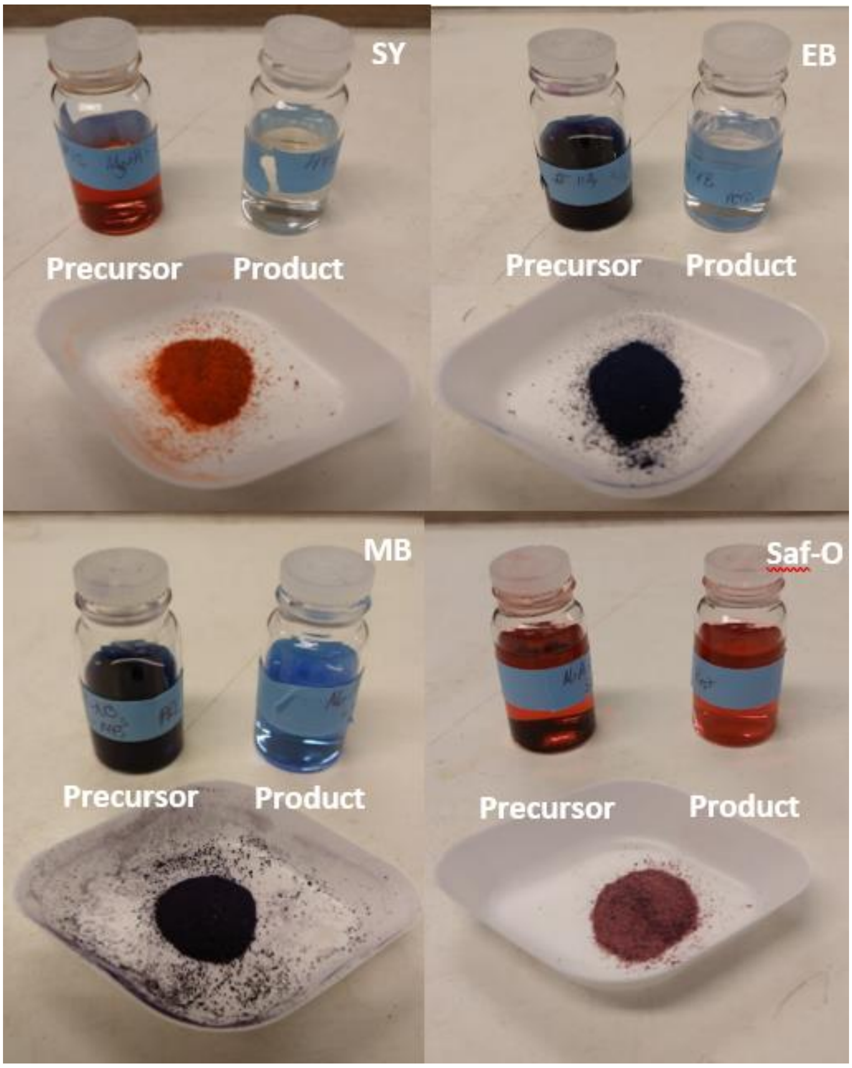

Figure 6.18. Changes in coloration during dye doped synthesis: SY (top left), EB (top right), MB (bottom left) and Saf-O (bottom right)

Table 6.13. Changes in concentration during dye-doped Mg_2Al-NO_3 synthesis

Dopant	**Initial Concentration / mg L^{-1}**	**Final Concentration / mg L^{-1}**	**Dye Removal / %**
AO7	115.9 ± 1.4	1.2 ± 0.1	99%
SY	106.2 ± 2.0	~0 (LOD)	~100 %
EB	107.1 ± 1.1	~0 (LOD)	~100 %
MB	105.5 ± 0.4	7.1 ± 0.9	93.3 %
Saf-O	98.8 ± 3.9	61.2 ± 4.9	38.1 %

LOD – Limits of Detection

XRD analysis of dye-doped LDHs was conducted to determine if the introduction of small quantities of dye had any impact on crystalline structure (Figure 6.19). All LDHs exhibited characteristic patterns of hydrotalcite phase, with minor reflections present due to the presence of $NaNO_3$ impurities for some LDHs. D spacing remained consistently between 0.77 – 0.80 nm, indicative of a nitrate interlayer (Table 6.14). [145] It was expected that incorporation of dye into the interlayer would increase interlayer spacing, due to the larger molecular size. This was not the case, presumably due to the low concentrations of dye (100 mg L^{-1}) used. Interestingly it appeared that dye-doped LDHs produced broader diffraction patterns, as evidenced by the reduction in peak intensities and increase in their FWHM (Table 6.14). This was attributed to reduced order in the structure, due to disruption with stacking of brucite sheets as the dye is adsorbed. [311] Despite this, dye-doped synthesis of $Mg_2Al\text{-}NO_3$ appears to be an effective mechanism for removal of sulfonate-based dyes at low concentrations, more akin to those found in environmental wastewater.

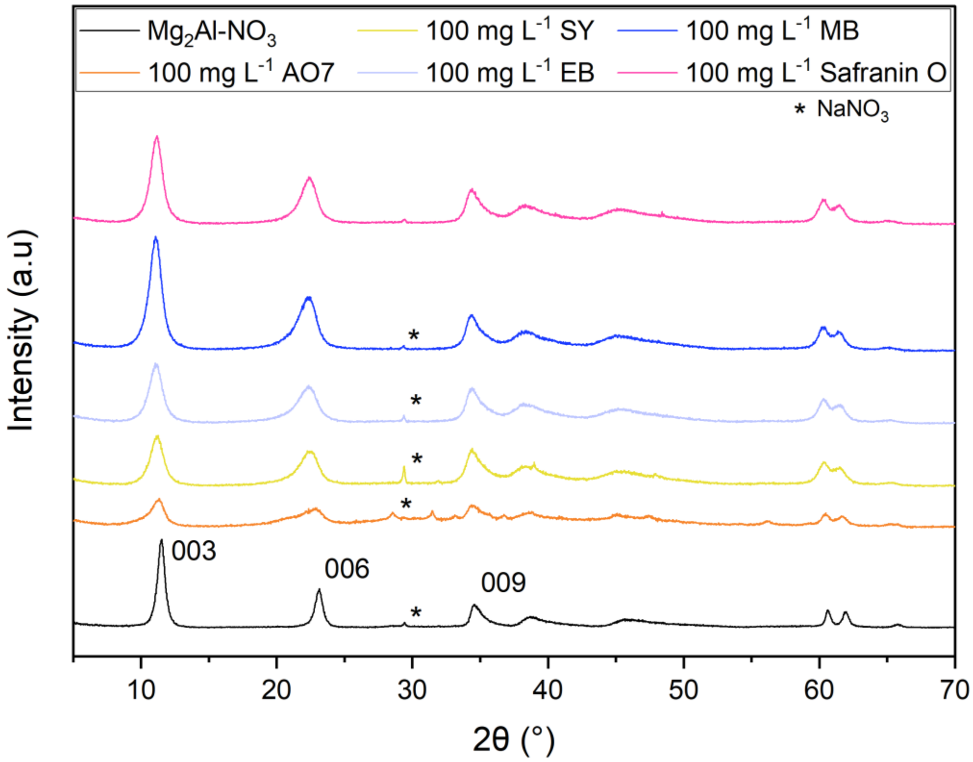

Figure 6.19. X-ray Diffraction patterns of dye-doped $Mg_2Al\text{-}NO_3$ LDHs

Table 6.14. 2ϑ, d values, FWHM and interlayer distances of dye-doped $Mg_2Al\text{-}NO_3$ LDHs

LDH	**Dopant (100 mg L^{-1})**	**Diffraction Peaks**									**Interlayer Distance / nm**
		003			**006**			**009**			
		2θ / °	**d / nm**	**FWHM / °**	**2θ / °**	**d / nm**	**FWHM / °**	**2θ / °**	**d / nm**	**FWHM / °**	
$Mg_2Al\text{-}NO_3$	-	11.49	0.77	0.71	23.11	0.38	0.69	34.74	0.26	1.01	0.77
	AO7	11.20	0.79	1.05	22.52	0.39	1.87	34.30	0.26	-	0.78
	SY	11.16	0.79	1.11	22.36	0.40	1.52	34.61	0.26	1.51	0.79
	EB	11.18	0.80	1.16	22.25	0.40	1.62	34.57	0.26	1.43	0.79
	MB	11.06	0.80	1.16	22.23	0.40	1.63	34.53	0.26	1.33	0.79
	Saf-O	11.14	0.79	1.09	22.34	0.40	1.39	34.54	0.26	1.34	0.79

6.6.3. Varying AO7 Concentration during dye-doped $Mg_2Al\text{-}NO_3$ Synthesis

The nature of environmental textile wastewater is extremely diverse from one effluent to another. Depending on the location, specific industry and local governmental legislations the colouration, BOD levels, COD levels and dye concentrations can vary drastically. [3,52] Therefore to further prove the versatility of dye-doped LDH synthesis as a means for dye removal, additional experiments were conducted at higher AO7 concentrations (100 – 1500 mg L^{-1}). Substantial discoloration of the product solution was observed for $Mg_2Al\text{-}NO_3$ synthesis at all concentrations of doped dye (Figure 6.20). UV-vis analysis revealed negligible quantities of AO7 remained at initial AO7 concentrations of 100, 250 and 500 mg L^{-1} (Table 6.15). While an orange translucency was still visible at higher concentrations (750 – 1500 mg L^{1}), over 90 % of the dye was still removed from solution. From these observations it was evident that dye-doped synthesis of $Mg_2Al\text{-}NO_3$ appears to be extremely effective at dye remediation at a wide variety of AO7 concentrations.

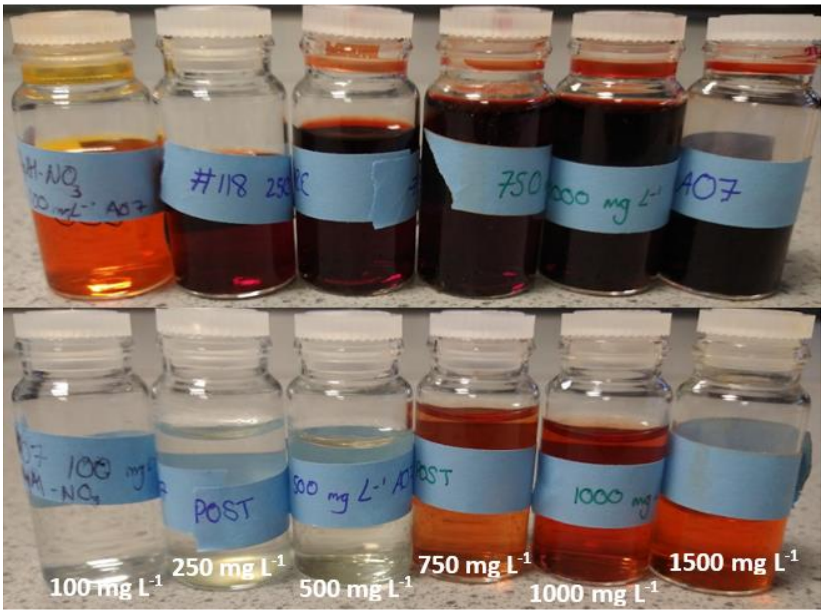

Figure 6.20. Changes in colouration of precursor (top) and product solution (bottom) during AO7-doped Mg2Al-NO3 synthesis

Table 6.15. The effect of AO7 concentration on dye removal during dye-doped Mg2Al-NO3 synthesis

Concentration of doped AO7 / mg L^{-1}	**Final Concentration / mg L^{-1}**	**Dye Removal / %**
128.9 ± 0.4	~0 (LOD)	~100
240.2 ± 0.5	~0 (LOD)	~100
509.4 ± 0.9	~0 (LOD)	~100
745.1 ± 8.9	4.9 ± 0.0	99.4
980.2 ± 6.7	23.4 ± 0.9	97.4
1519 ± 20.2	83.5 ± 1.2	94.5

LOD – Limits of Detection

Due to the low concentrations of dye used during dye-doped synthesis in Section 6.6.2, the mechanism of dye incorporation into Mg_2Al-NO_3 structure could not be elucidated. Therefore, additional XRD analysis was performed on LDHs synthesised with higher initial AO7 concentrations in the hopes that any dye intercalated LDH phases formed would be more prominent. As expected from previous analysis, all concentrations of dye-doping resulted in intense reflections related to the formation of Mg_2Al-NO_3 (Figure 6.21). Upon increasing the concentration of AO7 doped during Mg_2Al-NO_3 synthesis, broad reflections at very low 2θ angles (< 10 °) became more apparent, indicative of Mg_2Al-AO7 phase. The position of these peaks suggested that a biphasic system occurs. If AO7 was homogeneously distributed throughout the interlayer of Mg_2Al-NO_3, a gradual left-shift and broadening of diffractions peaks associated with interlayer spacing would occur as the concentration of AO7 increased, due to a larger quantity of dye intercalation. As this is not the case, it instead indicates that two separate phases of Mg_2Al-NO_3 and Mg_2Al-AO7 form. Similar observations have been reported by other authors, albeit due to incomplete intercalation of dyes during adsorption instead of biphasic synthesis. [28,148] At lower concentrations (< 500 mg L^{-1}) no peaks associated with Mg_2Al-AO7 were observed, suggesting surface sorption onto Mg_2Al-NO_3 is predominant.

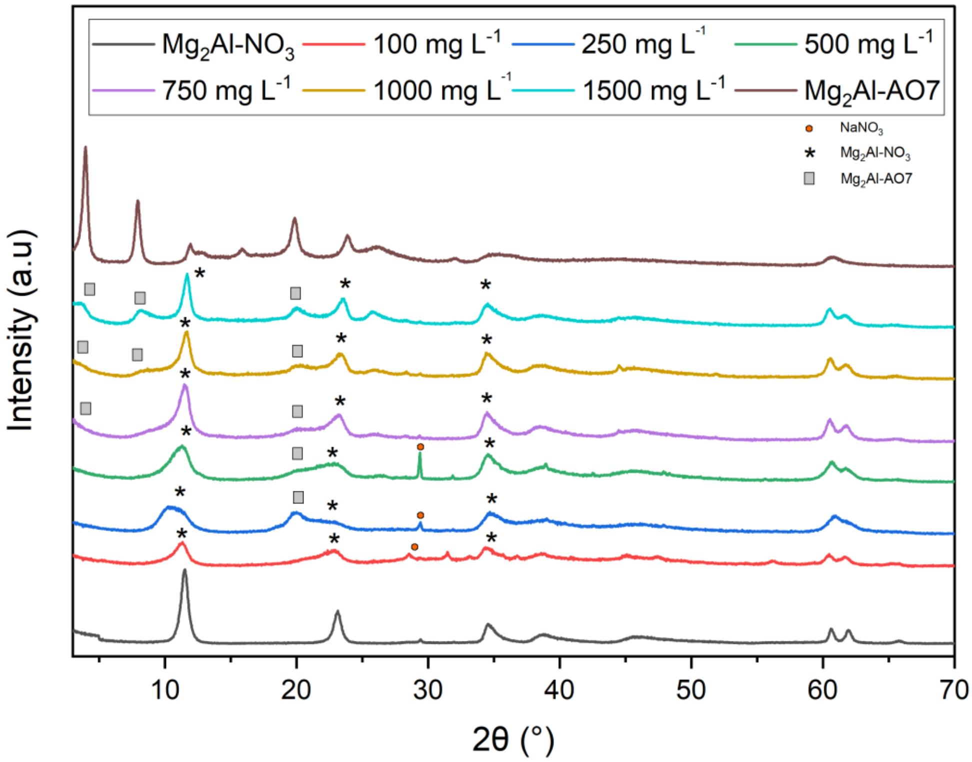

Figure 6.21. Comparison of AO7-doped LDH diffraction patterns to Mg_2Al-NO_3 and Mg_2Al-AO7: 100 - 1500 mg L^{-1} AO7

6.6.4. Feasibility of Mg_2Al-AO7 Using Environmental Wastewater

While the synthesis of Mg_2Al-AO7 via continuous hydrothermal synthesis as a means for dye remediation was successful, its potential application in environmental wastewater is limited for a couple of reasons. The first major hurdle is the diversity of wastewater effluent characteristics with varying pH, varying concentrations of dyes, and the presence of a multitude of other chemical species in solution. Previous analysis in Section 4.3.5. has already highlighted that CFHS is particularly sensitive to additional species in solution, with contamination often resulting in reproducibility issues or lack of product formation entirely. It is therefore entirely likely that similar syntheses conducted in environmental wastewater would have limited success due to differences in synthesis pH and/or other species interfering with synthesis reactions.

In addition to this, currently within literature there is limited research regarding the application of dye-intercalated LDH. While some authors have highlighted their use for applications such as coatings, [312] fluorescent markers, [313] photochromism, [314] and optical sensors, [315] these findings were limited and only discussed between 1995 – 2010, with no further research in recent years. Without an application for dye intercalated LDHs, this process of dye removal is more akin to a chemical precipitation method. While simple, chemical precipitation methods have inherent issues with requiring large volumes of precursor salts and generating sludge that imposes additional cost for its disposal. [74] This problem is further exacerbated when considering that synthesis attempted at lower concentrations (100 mg L^{-1}) more analogous to environmental wastewater concentrations were only successful through further addition of large quantities of precursor salts to produce Mg_2Al-NO_3.

Finally, while CFHS has been shown as a promising method to synthesis nanoparticles at industrial scale, with a reactor system capable of processing 1050 litres of precursor solution per hour, [316] as of yet there is no research to indicate whether this reactor system could be implemented in wastewater treatment facilities that process hundreds of millions of litres of wastewater a day. [317] In addition to this, heating such vast quantities of wastewater to temperatures of 93 °C is likely to massively increase CED and treatment costs when considering many traditional ion-exchange resins and adsorbents treat water under ambient conditions. [318] As a result of these issues, any further research into CFHS as a means for wastewater treatment is unlikely to have any industrial applicability.

7. Conclusions

7.1. The Effect of Synthesis Parameters on Co_2Al-CO_3 Formation

Previous research by Clark et al. has shown that synthesis parameters of the continuous-flow hydrothermal method (temperature, pressure and NaOH concentration) play a vital role in many physical properties such as crystal size and morphology. [87] In this work, Co_2Al-CO_3 LDH has been synthesised for the first time by this continuous method. Subsequently the effect of synthesis temperature, pressure, NaOH concentration and drying method were investigated to determine whether their impact on physical characteristics were comparable to that of Ca_2Al-NO_3 and Mg_2Al-CO_3. [138] In addition brief adsorption studies were conducted using acid orange 7 dye to determine whether synthesis conditions impact dye removal capabilities.

XRD analysis revealed synthesis temperature to play a vital role in the stacking (pillaring) of individual platelets, with a greater degree of stacking occurring at higher temperatures. While TEM analysis showed an increase in average particle size with increased synthesis temperature (up to 150 °C), this came at a cost of an increased distribution of particle sizes. An inverse correlation between SSA and platelet stacking observed in XRD was attributed to reduced surface sites being exposed when platelets are stacked on top of each other. While pressure in of itself did not influence any crystal or surface properties, lower pressures exacerbated the temperature dependence. A similar phenomenon was observed when changing initial NaOH concentration between 0.1 – 1 M whereby increased crystal stacking resulted in lower surface areas at higher NaOH concentrations. No LDH formed at a 1:1 ratio of NaOH and metal salt concentrations. Freeze drying produced larger crystallite sizes and higher surface areas when compared to oven drying.

Upon comparison with literature, many observations within this work did not appear to relate to similar research conducted with Ca_2Al-NO_3 and Mg_2Al-CO_3, suggesting that optimal conditions for LDH synthesis by CFHS are dependent on the individual LDH. As a result of this, a generalised method for LDH synthesis by CFHS is not applicable. Although, high temperatures should generally be avoided due to structural breakdown and preferential synthesis of metal oxides. A maximum uptake of 599 mg g^{-1} was reported for the adsorption of AO7 with calcined Co_2Al-CO_3 LDH. Synthesis temperature appears to play a vital role in sorption, with the highest uptake observed at low temperatures. Despite the high adsorption capacity, Co_2Al-CO_3 was concluded to have minimal potential for dye wastewater treatment due to poor adsorption kinetics as a result of the low surface area and porosity, ineffective scale-up when considering its use in continuous fixed bed adsorption processes and additional energetic demand during synthesis compared to other LDHs as a result of calcination being required.

7.2. The Role of M^{2+}/M^{3+} Ions on Adsorption of Dyes

In this work, six LDHs commonly used in literature for the removal of dyes, were synthesised to determine the role of M^{2+}/M^{3+} ions on physical properties and adsorption of AO7, and expand the list of LDHs that can be synthesised by CFHS method. Experimental conditions were kept as similar as possible for all LDHs to reduce bias. $Ni_2Al\text{-}NO_3$, $Mg_2Fe\text{-}CO_3$ and $Ni_2Fe\text{-}NO_3$ were successfully synthesised by CFHS for the first time. $Ni_2Al\text{-}NO_3$ and $Ni_2Fe\text{-}NO_3$ exhibited lower crystallinity than the other LDHs, as evidenced by relatively lower peak intensities in XRD. This was attributed to smaller crystallite sizes from CDL calculations and TEM imaging, alongside distortions of the layered structure because of Fe^{3+} cations larger atomic radius. Surface areas of all LDHs varied between 1 – 100 m^2 g^{-1}, considerably lower than many other adsorbents found in literature.

To determine the individual potential for dye adsorption, isotherm analysis, kinetic studies and the effect of pH was conducted for the removal of AO7. Pseudo 1st order, pseudo 2nd order and the intra-particle diffusion model were used to determine uptake of AO7 dye. The pseudo 2nd order model appeared to have a greater experimental fit than the pseudo 1st order model. This was in agreement with literature and suggests a chemisorption-based mechanism. $Ca_2Al\text{-}NO_3$ and $Mg_2Fe\text{-}CO_3$ had the greatest uptake over 24 hours, with equilibrium uptakes (q_e) of 1225 and 1088 mg g^1 respectively. Intra-particle diffusion modelling indicated that dye uptake occurred by both intercalation into the interlayer and sorption onto the surface. Langmuir and Freundlich isotherm modelling were conducted to determine adsorption capacity and sorption mechanism. Similar to kinetic studies the maximum saturation uptakes (q_m) were highest for $Ca_2Al\text{-}NO_3$ and $Mg_2Fe\text{-}CO_3$, at 1586 and 1603 mg g^{-1} respectively. The lowest q_m values were observed for both Nickel containing LDHs, $Ni_2Al\text{-}NO_3$ and $Ni_2Fe\text{-}NO_3$ at 182 and 279 mg g^{-1}, attributed to their lower crystallinity. A buffering phenomenon was observed for all LDHs whereby upon suspension in water, pH was buffered near to the LDHs point of zero charge (pH_{PZC}), regardless of initial pH.

The comparison of adsorption characteristics with physical properties did not indicate correlation with any one specific physical attribute. As the adsorption of dyes onto LDH is a complex process it was concluded that differences in adsorption upon changing M^{2+} and/or M^{3+} ions were dependent on a variety of different characteristics: surface area, interlayer ion and changes in crystallinity (caused by distortions of the structure by different metals atomic radii). Due to their higher uptake capacities, further sorption analysis was conducted on Ca_2Al-NO_3 and Mg_2Fe-CO_3 using other dyes. Sunset yellow (SY), evan's blue (EB), methylene blue (MB) and safranin-O (Saf-O) were chosen to determine what impact ionic charge, molecular size and chemical structure had on sorption.

Isotherm and kinetic analysis revealed considerably lower uptake of SY and EB onto both Ca_2Al-NO_3 and Mg_2Fe-CO_3 when compared to AO7, indicating ionic valency plays an important role in adsorption capacity. It was expected that uptake of dye would follow the trend AO7 > SY > EB due to increasing ionic valency however SY had lower uptake than EB onto both LDHs. The lower uptake of SY was attributed to an acid-base equilibria phenomenon that occurs at the buffering pH's of the two LDHs. In addition, EB's dye uptake was assisted by a lower buffering pH ($pH < pH_{PZC}$), resulting in greater surface adsorption. Molecular size did not influence reaction kinetics, with reaction rates of AO7, SY and EB being of similar magnitude onto both Ca_2Al-NO_3 and Mg_2Fe-CO_3. MB had negligible uptake (< 10 mg^{-1}) onto Mg_2Fe-CO_3 despite considerable uptake onto Ca_2Al-NO_3 (~ 400 mg g^{-1}). This was attributed to a greater buffering pH for Ca_2Al-NO_3, compared to its pH_{PZC}, that resulted in a negatively charged surface, making adsorption electrostatically favourable for the cationic MB dye. A greater fit of MB adsorption onto Ca_2Al-NO_3 to the Freundlich isotherm indicated adsorption occurred primarily by surface adsorption. The cationic dye Saf-O had no uptake on either LDH. This was attributed to the juxtaposition of two pH effects that occur, inhibiting adsorption at both low and high pH conditions. It was concluded that both the pH of zero charge and speciation of the dye are vital for ascertaining the potential of any LDH-dye adsorption system and should be utilized more frequently within the literature, as a standard protocol for evaluation of LDH adsorbents.

Comparisons of individual LDHs adsorption properties to literature appeared promising, with both Ca_2Al-NO_3 and Mg_2Fe-CO_3 LDHs possessing adsorption capacities greater than many other adsorbents found in literature, with comparable adsorption kinetics. However, further discussion analysing the potential scale-up and application of LDHs found it to be challenging due to many factors:

- Issues with metal leaching and poor performance in continuous fixed-bed systems due to low porosity and the requirement for immobilization onto other substrates.
- Limited regenerative capability increasing CED and environmental impact.
- Limited research regarding LDHs use in environmental wastewater laden with competing species.

7.3. Synthesis of Dye Intercalated LDHs

Mg_2Al-AO7 was successfully produced directly by a continuous hydrothermal synthesis method, negating the need for traditional ion-exchange methods for AO7 intercalation post-synthesis. This was evidenced by an increased interplanar spacing of 2.22 nm, considerably larger than CO_3^{2-} or NO_3^{2-} intercalated LDHs. Incorporation of AO7 was further proved by FTIR, where peaks associated with AO7 bonds were shifted slightly to lower wavenumbers due to intercalation. Incorporation of AO7 into the LDH interlayer improved its thermal stability, which was in agreement with previously synthesised Mg_2Al-AO7. [35] While SEM-EDS analysis suggested a large proportion of AO7 was bound to LDH surface, results were inconclusive due to a considerable amount of carbon contamination. Higher degrees of precursor conversion were achieved when excess AO7 was used, attributed to lower degrees of LDH nucleation with stoichiometric AO7.

Additional dye-intercalated synthesis by CFHS was attempted with four additional dyes: SY, EB, MB and Saf-O. Due to their cationic nature, no product was observed upon synthesis of Mg_2Al-MB and Mg_2Al-Saf-O. Synthesis of Mg_2Al-SY and Mg_2Al-EB had more success, with considerable quantities of dye removal occurring. There was evidence for dye intercalation upon XRD analysis, due to the presence of low intensity broad peaks at very low 2θ angles. Interplanar spacing was estimated at 2.02 and 2.18 nm for both Mg_2Al-SY and Mg_2Al-EB respectively. TEM micrographs revealed highly agglomerated, irregularly shaped crystallites ~100 nm in size. Despite broad peaks in XRD, crystallinity was confirmed through the presence of ordered structures at high magnification and TEM-diffraction analysis. Much like Mg_2Al-AO7, intercalation of SY and EB into LDH structure increased the thermal stability of the dyes.

The concentrations used during dye intercalated LDH synthesis were much higher than those found in typical environmental wastewater. However, synthesis attempted at lower AO7 concentrations (100 mg L^{-1}) resulted in no LDH formation due to negligible particle-particle interactions. Doping traditional Mg_2Al-NO_3 synthesis with low concentrations of dye had better success, with near complete removal of AO7, SY and EB from solution at an initial concentration of 100 mg L^{-1}. Over 90 % of MB was also removed at these concentrations, suggesting the short residence times were sufficient for removal by surface adsorption. No removal of Saf-O occurred, due to its neutral speciation at the synthesis pH. Further dye-doped $Mg_2Al\text{-}NO_3$ synthesis was conducted with variable concentrations of AO7 (100 – 1500 mg L^{-1}) to discern the mechanism of dye removal. Dye-doped synthesis was just as effective at higher initial concentrations, with > 99 % AO7 removal between 100 – 750 mg L^{-1}. XRD analysis confirmed the removal of AO7 by intercalation mechanism at high concentrations (> 500 mg L^{-1}), evidenced by a biphasic diffractogram consisting of $Mg_2Al\text{-}NO_3$ and $Mg_2Al\text{-}AO7$. At lower concentrations (< 500 mg L^{-1}) only peaks associated to $Mg_2Al\text{-}NO_3$ were observed indicating surface sorption predominated.

Upon discussion of CFHS as a means for dye remediation it was ultimately concluded to have limited industrial merit due to:

- Contaminant species hindering synthesis in environmental wastewater.
- Lack of application for $Mg_2Al\text{-}AO7$ product making the process more akin to chemical precipitation
- Uncertainties regarding the scale-up and CED of CFHS to process the volumes of wastewater typical in treatment facilities.

8. Recommendations for Future Work

8.1. Synthesis of LDH Materials by CFHS

While this research has further expanded the scope of LDHs synthesised by CFHS method, there is still room for a larger catalogue of LDHs to be made. So far, the focus of LDH synthesis by CFHS has been for their utilization as sorbents in water, however many other LDHs have potential for other applications including catalysis, photocatalysis and drug delivery (Table 8.1). Therefore, further research into synthesising LDHs for these alternative applications via a continuous and scalable means (CFHS), would help justify their potential as a commercialized nanomaterial.

Table 8.1. Potential applications of other types of LDHs

LDH	Application	Ref
Co-Mn	Photocatalytic degradation of dyes	319
Cu-Al/Cu-Mg-Al/Cu-Zn-Al-Cu/Zn-Cr	Catalysis of the water-gas shift reaction for Hydrogen production	91
Ni-Co	Use in supercapacitors for energy storage	320
Cu-Al	Controlled release of drugs	321
Li-Al	Detection of organic-coating degradation	298

Another facet that has also been relatively unexplored thus far is the production of LDH composites by CFHS. Previous research has shown that incorporation of other structures such as MOFs, [322] metal oxides, [169,323] graphene, [175] and magnetite can enhance the adsorptive properties/recoverability of LDHs. [324] However, generally the synthesis of these composite materials requires time consuming multi-step, batch processes. However, research by Clark et al. has shown that a sequential counter current flow system, containing two reactors, could be utilized for the synthesis of a $ZnO@Mg_2Al-CO_3$ composite by a one-step continuous process. [325] While the core-shell material produced was not phase pure, further optimisation of this synthesis process, alongside application to other LDH-nanomaterial systems, could open the door to an efficient and scalable method for a wide range of LDH-composite materials.

8.2. Application of LDHs as Sorbents

Within this research, when analysing the sorption of dyes onto LDHs, focus was put on three adsorption analysis techniques: Kinetic analysis to ascertain the speed and mechanism of uptake, isotherm studies for the determination of maximum uptake capacities, and pH analysis to determine pH-specific phenomena. While these properties are important, there are many other criteria to be considered when reviewing LDHs for wastewater remediation. These include the impact of temperature, adsorbent dose, adsorbent modification, the role of competitive anions (selectivity), adsorbent regeneration and the M^{2+}:M^{3+} ratio. Of these, selectivity and adsorbent regeneration are arguably the most relevant and understudied properties in literature. It has also been highlighted that due to their low surface area and porosity, alongside their nanosize, LDHs have inherent issues when scaling to continuous fixed-bed adsorption systems due to pressure drops and sludge production. As a result additional work should be conducted to observe their adsorptive performance when immobilized to larger more porous substrates such as PFA. [236]

Generally, the literature, including the work herein, highlights the use of LDHs for dye adsorption in controlled synthetic solutions of dye. While this is useful for gaining an increased understanding of sorption mechanisms, it is not analogous to dye-containing environmental wastewater. The dyeing process is very complex and involves the use of many other chemicals such as NaOH, surfactants and soaps for scouring, hydrogen peroxide for bleaching and metals/solvents for printing. [299] As a result of this, dye wastewater can contain many other anionic and cationic species that can compete with and disrupt adsorption of dye. It is therefore imperative that, not only are these competing effects well understood for specific LDH/dyebath effluents, but also that relevant water quality analysis is performed on the wastewater streams to understand what species are present in high concentrations.

In addition to LDH selectivity, the regeneration capabilities of each LDH are important for industrial use. The economic viability of LDHs as sorbents is dependent on their ability to regenerate their original structure for multiple cycles after adsorption. The most common method of LDH regeneration in literature is through thermal treatment (> 400 °C) to form MMO's. [297] The original LDH structure can then be reformed upon placement into an aqueous solution of desired anions through the memory effect. [298] However, many authors have found that regeneration of LDHs for further dye adsorption tends to only be feasible for a couple cycles due to decreasing LDH crystallinity after reconstruction of the lamellar structure. [20] Therefore further research is recommended to improve the regenerative capabilities of the most promising LDHs.

8.3. Environmental Concerns, Sustainable Synthesis and Technoeconomic Assessments

In the United Kingdom, employers are required to control hazardous samples through the Control of Substances Hazardous to Health (COSHH) law. [326] These hazards are compiled through Safety Data Sheets (SDS) and allow employers to complete risk assessments to determine the probability of any hazards that may arise when using nanomaterials. Due to the application and synthesis of LDH materials still being within the R&D phase of development, their respective hazards are not yet known. While many analogous chemicals used in the synthesis of LDHs, such as aluminium hydroxide, iron oxide hydroxide and magnesium hydroxide are not listed as hazardous substances according to regulation (EC) no. 1272/2008, [327–329] other hydroxide materials are more hazardous (Table 8.2) . For example, both calcium hydroxide and zinc hydroxide are listed as causing serious eye damage, skin irritation and specific target organ toxicity upon exposure. [330,331] Nickel hydroxide is especially hazardous upon use, containing ten H-statements related to causing harm and toxicity to both humans and aquatic life in some way. [332] As LDHs are essentially mixed metal hydroxide sheets containing interlayer anions it is likely that they contain similar hazard statements as their respective hydroxide precursors. Therefore, industrial use of LDHs would require a safety assessment to, not only determine if any additional safety measures are required upon handling, but also to determine if LDH nanomaterials are likely to have any inherent toxicity to aquatic life if they remain in wastewater post-treatment.

Table 8.2. Hazard statements for chemicals used in LDH synthesis

Chemical	H-statements	Ref
Aluminium Hydroxide	None according to regulation No. 1272/2008	327
Calcium Hydroxide	H315, H318, H335	330
Iron Oxide Hydroxide	None according to regulation No. 1272/2008	328
Magnesium Hydroxide	None according to regulation No. 1272/2008	329
Nickel Hydroxide	H302, H315, H317, H332, H334, H341, H350i, H360, H372, H410	332
Zinc Hydroxide	H315, H318, H335	331

Alongside health concerns, general environmental sustainability is an additional factor that is of utmost importance to ensure both socio-economic and environment conservation. Life cycle analyses (LCA) of continuous-flow syntheses for titania and silver sulphide (Ag_2S) nanoparticles have already shown them to be less environmentally impactful, both in terms of cumulative energy demand (CED) and global warming potential (GWP), than other synthesis methods such as precipitation, hydrothermal and solvothermal synthesis. [333,334] Generally processes with fewer productions steps, and less organic solvent use have lower environmental impacts. While this suggests CFHS of LDHs is likely to be a more sustainable synthesis when compared to respective batch synthesis methods, an LCA should be conducted to quantify this. A previous ex-ante LCA has been conducted on the use of LDH composites for application as agricultural films, however its analysis was limited to only MgAl and ZnAl based LDH-composites. [335] For a thorough environmental impact investigation into the use of LDHs for wastewater remediation, the LCA should include:

- A comparison of common synthesis methods (e.g: CFHS, hydrothermal and precipitation)
- The role of the precursor (e.g: metal chlorides, oxides and hydroxides)
- A comparison of individual LDHs (CaAl, MgAl, ZnAl, NiFe etc.)

In addition to this, techno-economic assessments would highlight if there any economic benefits to LDH synthesised by CFHS. A previous study has shown that, due to both production quality and method scalability, CFHS for NP production is highly competitive when compared to other batch syntheses methods. [336] However, LDHs were not included in this study. For commercial use of LDHs for water remediation to be viable these assessments should, not only be extended to LDHs, but also include a comparison to other common sorbents such as AC and zeolites.

8.4. Dye-Intercalated LDH Synthesis

Within Chapter 5.6.5 the syntheses of dye intercalated Mg_2Al LDHs as a means for dye remediations were discussed. While It was overall concluded that the method have little merit for industrial application due to uncertainties with scale up and product application, herein further work has been discussed, highlighting solutions that would need solving if this method were to ever be pursued. Much like sorption, the applicability of this method for wastewater treatment is highly dependent on its performance using environmental dye effluents as a feedstock. While a dye-doped Mg_2Al-NO_3 synthesis was found to be applicable for dye removal at concentrations analogous to those found in environmental systems, the temperature, pH, composition and competing anions within the effluents are also likely to affect synthesis. As a result, further research should be conducted to determine the effect of these parameters on Mg_2Al-Dye synthesis. A direct synthesis attempt using dye effluent as a precursor would provide rapid proof of concept of this method, while a systematic approach to understanding the effects of parameters discussed would allow for utilization of a wide range of dyebath effluents further down the line.

Another factor required to determine the feasibility of this method is valorisation of the product. Without an application for the Mg_2Al-Dye produced, this synthesis method is more akin to chemical precipitation, which is often regarded as an inferior wastewater treatment method due to high chemical consumptions and large sludge volumes produced. [337] Previous research has shown that incorporation of dyes into LDH structure could be utilized for coatings, [312] fluorescent markers, [313] photochromism, [314] and optical sensors. [315] This is attributed to the enhanced photochemical and thermal stability of the dye upon intercalation. [338] Naturally, further work should therefore be conducted on the application of Mg_2Al-AO7, Mg_2Al-SY and Mg_2Al-EB LDH materials.

References

1 K. Hunger, *Industrial Dyes: Chemistry, Properties, Applications*, WILEY-VCH, Germany, 2003.

2 A. Gürses, M. Açikyildiz, K. Güneş and M. Gürses, *Dyes and Pigments*, Springer Briefs in Molecular Science, 2016.

3 C. Hessel, C. Allegre, M. Maisseu, F. Charbit and P. Moulin, Guidelines and legislation for dye house effluents, *J Environ Manage*, 2007, **83**, 171–180.

4 Y. Doruk ARACAGÖK and N. CİHANGİR, Decolorization of Reactive Black 5 by *Yarrowia lipolytica* NBRC 1658, *Am J Microbiol Res*, 2013, **1**, 16–20.

5 L. Pereira and M. Alves, Dyes-environmental impact and remediation, *Environmental Protection Strategies for Sustainable Development*, 2012, 111–162.

6 F. Uddin, Environmental hazard in textile dyeing wastewater from local textile industry, *Cellulose*, 2021, **28**, 10715–10739.

7 N. Puvaneswari, J. Muthukrishnan and P. Gunasekaran, Toxicity assessment and microbial degradation of azo dyes, *Indian J Exp Biol*, 2006, **44**, 618–626.

8 W. Hajjaji, R. C. Pullar, J. A. Labrincha and F. Rocha, Aqueous Acid Orange 7 dye removal by clay and red mud mixes, *Appl Clay Sci*, 2016, **126**, 197–206.

9 I. Clark, J. Smith, R. L. Gomes and E. Lester, Continuous Synthesis of Zn2Al-CO3 Layered Double Hydroxides for the Adsorption of Reactive Dyes from Water, *J Environ Chem Eng*, 2019, **7**, 103–175.

10 N. Y. Donkadokula, A. K. Kola, I. Naz and D. Saroj, A review on advanced physico-chemical and biological textile dye wastewater treatment techniques, *Rev Environ Sci Biotechnol*, 2020, **19**, 543–560.

11 F. Kehinde and H. A. Aziz, Textile Waste Water and the advanced Oxidative Treatment Process, an Overview, *Int J Innov Res Sci Eng Technol*, 2014, **03**, 15310–15317.

12 I. M. Banat, P. Nigam, D. Singh and R. Marchant, Microbial decolorization of textile-dye-containing effluents: A review, *Bioresour Technol*, 1996, **58**, 217–227.

13 N. Mohan, N. Balasubramanian and V. Subramanian, Electrochemical treatment of simulated textile effluent, *Chem Eng Technol*, 2001, **24**, 749–753.

14 M. T. Yagub, T. K. Sen, S. Afroze and H. M. Ang, *Adv Colloid Interface Sci*, 2014, 209, 172–184.

15 A. El Khanchaoui, M. Sajieddine, M. Mansori, A. Essoumhi and U. Sultan Moulay Slimane, Anionic dye adsorption on ZnAl hydrotalcite-type and regeneration studies based on ‘memory effect’, , DOI:10.1080/03067319.2020.1772769.

16 K. Y. Foo and B. H. Hameed, An overview of dye removal via activated carbon adsorption process, *Desalination Water Treat*, 2010, **19**, 255–274.

17 S. Babel and T. A. Kurniawan, Low-cost adsorbents for heavy metals uptake from contaminated water: a review., *J Hazard Mater*, 2003, **97**, 219–243.

18 S. Syafalni, I. Abustan, I. Dahlan, C. K. Wah and G. Umar, Treatment of dye wastewater using granular activated carbon and zeolite filter, *Mod Appl Sci*, 2012, **6**, 37–51.

19 H. Han, M. K. Rafiq, T. Zhou, R. Xu, O. Mašek and X. Li, A critical review of clay-based composites with enhanced adsorption performance for metal and organic pollutants, *J Hazard Mater*, 2019, **369**, 780–796.

20 Z. Yang, F. Wang, C. Zhang, G. Zeng, X. Tan, Z. Yu, Y. Zhong, H. Wang and F. Cui, *RSC Adv*, 2016, 6, 79415–79436.

21 E. E. Gaskell, T. Ha and A. R. Hamilton, Ibuprofen intercalation and release from different layered double hydroxides, *Ther Deliv*, 2018, **9**, 653–666.

22 E. M. Seftel, E. Popovici, M. Mertens, K. De Witte, G. Van Tendeloo, P. Cool and E. F. Vansant, Zn-Al layered double hydroxides: Synthesis, characterization and photocatalytic application, *Microporous and Mesoporous Materials*, 2008, **113**, 296–304.

23 F. L. Theiss, G. A. Ayoko and R. L. Frost, Synthesis of layered double hydroxides containing Mg2+, Zn2+, Ca2+ and Al3+ layer cations by co-precipitation methods—A review, *Appl Surf Sci*, 2016, **383**, 200–213.

24 F. Li, X. Jiang, D. G. Evans and X. Duan, Structure and basicity of mesoporous materials from Mg/Al/In layered double hydroxides prepared by separate nucleation and aging steps method, *Journal of Porous Materials*, 2005, **12**, 55–63.

25 S. Bai, T. Li, H. Wang, L. Tan, Y. Zhao and Y. F. Song, Scale-up synthesis of monolayer layered double hydroxide nanosheets via separate nucleation and aging steps

method for efficient CO2 photoreduction, *Chemical Engineering Journal*, 2021, **419**, 129390.

26 G. Hu and D. O'Hare, Unique layered double hydroxide morphologies using reverse microemulsion synthesis, *J Am Chem Soc*, 2005, **127**, 17808–17813.

27 G. Hu, N. Wang, D. O'Hare and J. Davis, Synthesis of magnesium aluminium layered double hydroxides in reverse microemulsions, *J Mater Chem*, 2007, **17**, 2257–2266.

28 Q. Wang, S. V. Y. Tang, E. Lester and D. O'Hare, Synthesis of ultrafine layered double hydroxide (LDHs) nanoplates using a continuous-flow hydrothermal reactor, *Nanoscale*, 2013, **5**, 114–117.

29 P. W. Dunne, C. L. Starkey, M. Gimeno-Fabra and E. H. Lester, The rapid size- and shape-controlled continuous hydrothermal synthesis of metal sulphide nanomaterials, *Nanoscale*, 2014, **6**, 2406–2418.

30 I. Clark, P. W. Dunne, R. L. Gomes and E. Lester, Continuous hydrothermal synthesis of Ca2Al-NO3 layered double hydroxides: The impact of reactor temperature, pressure and NaOH concentration on crystal characteristics, *J Colloid Interface Sci*, 2017, **504**, 492–499.

31 O. Williams, I. Clark, R. L. Gomes, T. Perehinec, J. L. Hobman, D. J. Stekel, R. Hyde, C. Dodds and E. Lester, Removal of copper from cattle footbath wastewater with layered double hydroxide adsorbents as a route to antimicrobial resistance mitigation on dairy farms, *Science of The Total Environment*, 2019, **655**, 1139–1149.

32 S. M. Ashekuzzaman and J.-Q. Jiang, Study on the sorption–desorption–regeneration performance of Ca-, Mg- and CaMg-based layered double hydroxides for removing phosphate from water, *Chemical Engineering Journal*, 2014, **246**, 97–105.

33 J. Mittal, Recent progress in the synthesis of Layered Double Hydroxides and their application for the adsorptive removal of dyes: A review, *J Environ Manage*, 2021, **295**, 113017.

34 S. M. Gidado and İ. Akanyeti, Comparison of Remazol Brilliant Blue Reactive Adsorption on Pristine and Calcined ZnAl, MgAl, ZnMgAl Layered Double Hydroxides, *Water Air Soil Pollut*, , DOI:10.1007/s11270-020-04522-0.

35 L. Y. Liu, M. Pu, L. Yang, D. Q. Li, D. G. Evans and J. He, Experimental and theoretical study on the structure of acid orange 7-pillared layered double hydroxide, *Mater Chem Phys*, 2007, **106**, 422–427.

36 S. H. He, M. Pu, J. N. Li, J. He and D. G. Evans, Assembly, structure and properties of acid orange 7-pillared Zn/Al hydrotalcite, *Wuli Huaxue Xuebao/ Acta Physico - Chimica Sinica*, 2010, **26**, 259–264.

37 I. Clark, J. Smith, R. L. Gomes and E. Lester, Continuous Synthesis of Zn2Al-CO3 Layered Double Hydroxides for the Adsorption of Reactive Dyes from Water, *J Environ Chem Eng*, , DOI:10.1016/j.jece.2019.103175.

38 X. He, X. Qiu, C. Hu and Y. Liu, Treatment of heavy metal ions in wastewater using layered double hydroxides: A review, *J Dispers Sci Technol*, 2018, **39**, 792–801.

39 X. Pan, M. Zhang, H. Liu, S. Ouyang, N. Ding and P. Zhang, Adsorption behavior and mechanism of acid orange 7 and methylene blue on self-assembled three-dimensional MgAl layered double hydroxide: Experimental and DFT investigation, *Appl Surf Sci*, , DOI:10.1016/j.apsusc.2020.146370.

40 F. Pereira De Sá, B. N. Cunha and L. M. Nunes, Effect of pH on the adsorption of Sunset Yellow FCF food dye into a layered double hydroxide (CaAl-LDH-NO 3), , DOI:10.1016/j.cej.2012.11.024.

41 A. R. Auxilio, P. C. Andrews, P. C. Junk, L. Spiccia, D. Neumann, W. Raverty and N. Vanderhoek, Adsorption and intercalation of Acid Blue 9 on Mg-Al layered double hydroxides of variable metal composition, *Polyhedron*, 2007, **26**, 3479–3490.

42 P. A. Agudo, *Risks and impacts of the commodification and financialization of water on the human rights to safe drinking water and sanitation*, 2021, vol. 76th sessi.

43 X. C. Jin, G. Q. Liu, Z. H. Xu and W. Y. Tao, Decolorization of a dye industry effluent by Aspergillus fumigatus XC6, *Appl Microbiol Biotechnol*, 2007, **74**, 239–243.

44 B. Lellis, C. Z. Fávaro-Polonio, J. A. Pamphile and J. C. Polonio, Effects of textile dyes on health and the environment and bioremediation potential of living organisms, *Biotechnology Research and Innovation*, 2019, **3**, 275–290.

45 F. Copaciu, O. Opriş, V. Coman, D. Ristoiu, Ü. Niinemets and L. Copolovici, Diffuse water pollution by anthraquinone and azo dyes in environment importantly alters

foliage volatiles, carotenoids and physiology in wheat (Triticum aestivum), *Water Air Soil Pollut*, , DOI:10.1007/s11270-013-1478-4.

46 S. Boubakri, M. A. Djebbi, Z. Bouaziz, P. Namour, N. Jaffrezic-Renault, A. B. H. Amara, M. Trabelsi-Ayadi, I. Ghorbel-Abid and R. Kalfat, Removal of two anionic reactive textile dyes by adsorption into MgAl-layered double hydroxide in aqueous solutions, *Environmental Science and Pollution Research*, 2018, **25**, 23817–23832.

47 M. A. Barakat, New trends in removing heavy metals from industrial wastewater, *Arabian Journal of Chemistry*, 2011, **4**, 361–377.

48 B. Gordon, P. Callan and C. Vickers, WHO guidelines for drinking-water quality., *WHO Chron*, 2008, **38**, 564.

49 The Council of the European Union, Council Directive 98/83/EC of 3 November 1998 on the quality of water intended for human consumption, *Official Journal of the European Communities*, 1998, **L330**, 32–54.

50 B. Said, R. Souad M' and E. H. Ahmed, A review on classifications, recent synthesis and applications of textile dyes, *Inorg Chem Commun*, 2020, 107891.

51 C. Li, X. Yang, R. Chen, J. Pan, H. Tian, H. Zhu, X. Wang, A. Hagfeldt and L. Sun, Anthraquinone dyes as photosensitizers for dye-sensitized solar cells, *Solar Energy Materials and Solar Cells*, 2007, **91**, 1863–1871.

52 D. A. Yaseen and M. Scholz, *Textile dye wastewater characteristics and constituents of synthetic effluents: a critical review*, Springer Berlin Heidelberg, 2019, vol. 16.

53 F. Qian, X. Sun and Y. Liu, Removal characteristics of organics in bio-treated textile wastewater reclamation by a stepwise coagulation and intermediate GAC/O3 oxidation process, *Chemical Engineering Journal*, 2013, **214**, 112–118.

54 G. S. Harpreet Kaur, Removal of Dyes from Textile Industry Effluent: A Review, *Journal of the Textile Association*, 2015, 59–63.

55 M. C. Tomei, J. Soria Pascual and D. Mosca Angelucci, Analysing performance of real textile wastewater bio-decolourization under different reaction environments, *J Clean Prod*, 2016, **129**, 468–477.

56 P. T. Almazán-Sánchez, I. Linares-Hernández, M. J. Solache-Río and V. Martínez-Miranda, Textile wastewater treatment using iron-modified clay and copper-modified

carbon in batch and column systems, *Water Air Soil Pollut*, , DOI:10.1007/s11270-016-2801-7.

57 A. Bes-Piá, B. Cuartas-Uribe, J. A. Mendoza-Roca and M. I. Alcaina-Miranda, Study of the behaviour of different NF membranes for the reclamation of a secondary textile effluent in rinsing processes, *J Hazard Mater*, 2010, **178**, 341–348.

58 J. Yimrattanabovorn, S. Nopkhuntod and S. Dararat, Removal of reactive dyes from wastewater by shale, *Songklanakarin Journal of Science and Technology*, 2012, **34**, 117–123.

59 *Methods for chemical analysis of water and wastes*, Washington, D.C., 1983.

60 T. Dawson, Progress towards a greener textile industry, *Coloration Technology*, 2012, **128**, 1–8.

61 P. Anastas and N. Eghbali, Green Chemistry: Principles and Practice, *Chem Soc Rev*, 2010, **39**, 301–312.

62 E. Forgacs, T. Cserháti and G. Oros, Removal of synthetic dyes from wastewaters: A review, *Environ Int*, 2004, **30**, 953–971.

63 S. Sakthivel, B. Neppolian, M. V. Shankar, B. Arabindoo, M. Palanichamy and V. Murugesan, Solar photocatalytic degradation of azo dye: Comparison of photocatalytic efficiency of ZnO and TiO2, *Solar Energy Materials and Solar Cells*, 2003, **77**, 65–82.

64 W. Z. Tang and Huren An, UV/TiO2 photocatalytic oxidation of commercial dyes in aqueous solutions, *Chemosphere*, 1995, **31**, 4157–4170.

65 J. Kiwi, Role of oxygen at the TiO2 interface during photodegradation of biologically difficult-to-degrade anthraquinone-sulfonate dyes, *Environ Toxicol Chem*, 1994, **13**, 1569–1575.

66 D. Georgiou, Destruction of Azo-Reactive Dyes by Ozonation and the Synergetic Effect of a Radio-Frequency Alternating Electric Field Inductance Device, *Current Trends in Fashion Technology & Textile Engineering*, 2017, **1**, 42–47.

67 S. Samuchiwal, D. Gola and A. Malik, Decolourization of textile effluent using native microbial consortium enriched from textile industry effluent, *J Hazard Mater*, 2021, **402**, 123835.

68 P. Kanekar and S. Sarnaik, An activated sludge process to reduce the pollution load of a dye-industry waste, *Environmental Pollution*, 1991, **70**, 27–33.

69 G. M. Didier de Vasconcelos, J. Mulinari, S. M. de Arruda Guelli Ulson de Souza, A. A. Ulson de Souza, D. de Oliveira and C. J. de Andrade, Biodegradation of azo dye-containing wastewater by activated sludge: a critical review, *World J Microbiol Biotechnol*, 2021, **37**, 1–12.

70 K. A. Shaul, G.M. Holdsworth, T.J. Dempsey, C.R. Dostal, Fate of Water Soluble Azo Dyes in the Activated Sludge Process, *Chemosphere*, 1991, **22**, 107–119.

71 J. Marszałek and R. Żyłła, Recovery of water from textile dyeing using membrane filtration processes, *Processes*, , DOI:10.3390/pr9101833.

72 H. Afanga, H. Zazou, F. E. Titchou, Y. Rakhila, R. A. Akbour, A. Elmchaouri, J. Ghanbaja and M. Hamdani, Integrated electrochemical processes for textile industry wastewater treatment: System performances and sludge settling characteristics, *Sustainable Environment Research*, 2020, **30**, 1–11.

73 T. H. Kim, C. Park, E. B. Shin and S. Kim, Decolorization of disperse and reactive dyes by continuous electrocoagulation process, *Desalination*, 2002, **150**, 165–175.

74 T. A. Kurniawan, G. Y. S. Chan, W. H. Lo and S. Babel, Physico-chemical treatment techniques for wastewater laden with heavy metals, *Chemical Engineering Journal*, 2006, **118**, 83–98.

75 B. Shi, G. Li, D. Wang, C. Feng and H. Tang, Removal of direct dyes by coagulation: The performance of preformed polymeric aluminum species, *J Hazard Mater*, 2007, **143**, 567–574.

76 A. Szyguła, E. Guibal, M. Ruiz and A. M. Sastre, The removal of sulphonated azo-dyes by coagulation with chitosan, *Colloids Surf A Physicochem Eng Asp*, 2008, **330**, 219–226.

77 F. Mcyotto, Q. Wei, D. K. Macharia, M. Huang, C. Shen and C. W. K. Chow, Effect of dye structure on color removal efficiency by coagulation, *Chemical Engineering Journal*, , DOI:10.1016/j.cej.2020.126674.

78 C. X. H. Su, L. W. Low, T. T. Teng and Y. S. Wong, Combination and hybridisation of treatments in dye wastewater treatment: A review, *J Environ Chem Eng*, 2016, **4**, 3618–3631.

79 S. Papić, N. Koprivanac, A. Lončarić Božić and A. Meteš, Removal of some reactive dyes from synthetic wastewater by combined Al(III) coagulation/carbon adsorption process, *Dyes and Pigments*, 2004, **62**, 291–298.

80 F. K. Yuen and B. H. Hameed, Recent developments in the preparation and regeneration of activated carbons by microwaves, *Adv Colloid Interface Sci*, 2009, **149**, 19–27.

81 T. A. Kurniawan, G. Y. S. Chan, W. H. Lo and S. Babel, Physico-chemical treatment techniques for wastewater laden with heavy metals, *Chemical Engineering Journal*, 2006, **118**, 83–98.

82 Z. Sieren, B. Baker, J. Wang, X. Rozzoni, S. J. Carlson, K. McBain, A. Kerstan, D. Allen, L. Liao, L. Li, Sorptive Removal of Color Dye Safranin O by Fibrous Clay Minerals and Zeolites, *Advances in Materials Science and Engineering*, 2020, **2020**, 1–12.

83 T. A. Kurniawan, G. Y. S. Chan, W. H. Lo and S. Babel, Physico-chemical treatment techniques for wastewater laden with heavy metals, *Chemical Engineering Journal*, 2006, **118**, 83–98.

84 M. S. Armagan, B. Turan, M. Celik, Equilibrium studies on the adsorption of reactive azo dyes into zeolite, *Desalination*, 2004, **170**, 33–39.

85 S. Babel and T. A. Kurniawan, Low-cost adsorbents for heavy metals uptake from contaminated water: a review., *J Hazard Mater*, 2003, **97**, 219–243.

86 T. Ngulube, J. R. Gumbo, V. Masindi and A. Maity, An update on synthetic dyes adsorption onto clay based minerals: A state-of-art review, *J Environ Manage*, 2017, **191**, 35–57.

87 I. Clark, P. W. Dunne, R. L. Gomes and E. Lester, Continuous hydrothermal synthesis of Ca2Al-NO3 layered double hydroxides: The impact of reactor temperature, pressure and NaOH concentration on crystal characteristics, *J Colloid Interface Sci*, 2017, **504**, 492–499.

88 F. L. Theiss, G. A. Ayoko and R. L. Frost, Synthesis of layered double hydroxides containing Mg2+, Zn2+, Ca2+ and Al3+ layer cations by co-precipitation methods—A review, *Appl Surf Sci*, 2016, **383**, 200–213.

89 E. E. Gaskell, T. Ha and A. R. Hamilton, Ibuprofen intercalation and release from different layered double hydroxides, *Ther Deliv*, 2018, **9**, 653–666.

90 V. Rives and M. Angeles Ulibarri, Layered double hydroxides (LDH) intercalated with metal coordination compounds and oxometalates, *Coord Chem Rev*, 1999, **181**, 61–120.

91 D. Li, Y. Cai, Y. Ding, R. Li, M. Lu and L. Jiang, Layered double hydroxides as precursors of Cu catalysts for hydrogen production by water-gas shift reaction, *Int J Hydrogen Energy*, 2015, **40**, 10016–10025.

92 S. Saha, S. Ray, S. Ghosh and J. Chakraborty, pH-dependent facile synthesis of CaAl-layered double hydroxides and its effect on the growth inhibition of cancer cells, *Journal of the American Ceramic Society*, 2018, **101**, 3924–3935.

93 M. v. Bukhtiyarova, A review on effect of synthesis conditions on the formation of layered double hydroxides, *J Solid State Chem*, 2019, **269**, 494–506.

94 Z. Rezvani, F. Khodam, A. Mokhtari and K. Nejati, Amine-Assisted Syntheses of Carbonate-Free and Highly Crystalline Nitrate-Containing Zn-Al Layered Double Hydroxides, *Z Anorg Allg Chem*, 2014, **640**, 2203–2207.

95 I. Clark, 2018.

96 F. Cavani, F. Trifirò and A. Vaccari, Hydrotalcite-type anionic clays: Preparation, properties and applications., *Catal Today*, 1991, **11**, 173–301.

97 Y. Zhao, F. Li, R. Zhang, D. G. Evans and X. Duan, Preparation of layered double-hydroxide nanomaterials with a uniform crystallite size using a new method involving separate nucleation and aging steps, *Chemistry of Materials*, 2002, **14**, 4286–4291.

98 A. A. Sertsova, E. N. Subcheva and E. V. Yurtov, Synthesis and study of structure formation of layered double hydroxides based on Mg, Zn, Cu, and Al, *Russian Journal of Inorganic Chemistry*, 2015, **60**, 23–32.

99 K. Abderrazek, N. Frini Srasra and E. Srasra, Synthesis and Characterization of [Zn-Al] Layered Double Hydroxides: Effect of the Operating Parameters, *Journal of the Chinese Chemical Society*, 2017, **64**, 346–353.

100 J. Y. Lee, G. H. Gwak, H. M. Kim, T. Il Kim, G. J. Lee and J. M. Oh, Synthesis of hydrotalcite type layered double hydroxide with various Mg/Al ratio and surface charge under controlled reaction condition, *Appl Clay Sci*, 2016, **134**, 44–49.

101 Y. Zhao, J. Liang, F. Li and X. Duan, Selectivity of crystal growth direction in layered double hydroxides, *Tsinghua Sci Technol*, 2004, **9**, 672–675.

102 M. Khitous, Z. Salem and D. Halliche, Effect of interlayer anions on chromium removal using Mg-Al layered double hydroxides: Kinetic, equilibrium and thermodynamic studies, *Chin J Chem Eng*, 2016, **24**, 433–445.

103 R. Rojas, M. R. Perez, E. M. Erro, P. I. Ortiz, M. A. Ulibarri and C. E. Giacomelli, EDTA modified LDHs as Cu2+ scavengers: Removal kinetics and sorbent stability, *J Colloid Interface Sci*, 2009, **331**, 425–431.

104 M. A. González, I. Pavlovic, R. Rojas-Delgado and C. Barriga, Removal of Cu2+, Pb2+ and Cd2+ by layered double hydroxide–humate hybrid. Sorbate and sorbent comparative studies, *Chemical Engineering Journal*, 2014, **254**, 605–611.

105 W. Chen, J. Xing, Z. Lu, J. Wang, S. Yu, W. Yao, A. M. Asiri, K. A. Alamry, X. Wang and S. Wang, Citrate-modified Mg–Al layered double hydroxides for efficient removal of lead from water, *Environ Chem Lett*, 2018, **16**, 561–567.

106 L. Y. Liu, M. Pu, L. Yang, D. Q. Li, D. G. Evans and J. He, Experimental and theoretical study on the structure of acid orange 7-pillared layered double hydroxide, *Mater Chem Phys*, 2007, **106**, 422–427.

107 G. Huang, D. Wang, S. Ma, J. Chen, L. Jiang and P. Wang, A new, low-cost adsorbent: Preparation, characterization, and adsorption behavior of Pb(II) and Cu(II), *J Colloid Interface Sci*, 2015, **445**, 294–302.

108 L. Ma, Q. Wang, S. M. Islam, Y. Liu, S. Ma and M. G. Kanatzidis, Highly Selective and Efficient Removal of Heavy Metals by Layered Double Hydroxide Intercalated with the MoS 4 2− Ion, , DOI:10.1021/jacs.6b00110.

109 J. Ali, H. Wang, J. Ifthikar, A. Khan, T. Wang, K. Zhan, A. Shahzad, Z. Chen and Z. Chen, Efficient, stable and selective adsorption of heavy metals by thio-functionalized layered double hydroxide in diverse types of water, *Chemical Engineering Journal*, 2018, **332**, 387–397.

110 H. Asiabi, Y. Yamini, M. Shamsayei and E. Tahmasebi, Highly selective and efficient removal and extraction of heavy metals by layered double hydroxides intercalated with the diphenylamine-4-sulfonate: A comparative study, *Chemical Engineering Journal*, 2017, **323**, 212–223.

111 D. G. Evans and X. Duan, Preparation of layered double hydroxides and their applications as additives in polymers, as precursors to magnetic materials and in biology and medicine, *Chemical Communications*, 2006, 485–496.

112 Y. Zhao, F. Li, R. Zhang, D. G. Evans and X. Duan, Preparation of Layered Double-Hydroxide Nanomaterials with a Uniform Crystallite Size Using a New Method Involving Separate Nucleation and Aging Steps, , DOI:10.1021/cm020370h.

113 M. Yang, E. Tuckley, J. C. Buffet and D. O'Hare, Rapid, efficient phase pure synthesis of Ca2AlNO3 layered double hydroxide, *J Mater Chem A Mater*, 2015, **4**, 500–504.

114 D. Tichit, G. Layrac and C. Gérardin, *Chemical Engineering Journal*, 2019, 369, 302–332.

115 S. Abelló, S. Mitchell, M. Santiago, G. Stoica and J. Pérez-Ramírez, Perturbing the properties of layered double hydroxides by continuous coprecipitation with short residence time, *J Mater Chem*, 2010, **20**, 5878–5887.

116 Z. Chang, D. G. Evans, X. Duan, C. Vial, J. Ghanbaja, V. Prevot, M. de Roy and C. Forano, Synthesis of [Zn-Al-CO3] layered double hydroxides by a coprecipitation method under steady-state conditions, *J Solid State Chem*, 2005, **178**, 2766–2777.

117 D. Tichit, G. Layrac and C. Gérardin, *Chemical Engineering Journal*, 2019, 369, 302–332.

118 V. S. Shirure, B. P. Nikhade and V. G. Pangarkar, Intensification of Precipitation Using Narrow Channel Reactors: Case Study of Hydrotalcite Precipitation, , DOI:10.1021/ie060371.

119 A. Flegler, M. Schneider, J. Prieschl, R. Stevens, T. Vinnay and K. Mandel, Continuous flow synthesis and cleaning of nano layered double hydroxides and the potential of the route to adjust round or platelet nanoparticle morphology, *RSC Adv*, 2016, **6**, 57236–57244.

120 Q. Wang, S. V. Y. Tang, E. Lester and D. O'Hare, Synthesis of ultrafine layered double hydroxide (LDHs) nanoplates using a continuous-flow hydrothermal reactor, *Nanoscale*, 2013, **5**, 114–117.

121 T. Adschiri, Y. Hakuta and K. Arai, Hydrothermal synthesis of metal oxide fine particles at supercritical conditions, *Ind Eng Chem Res*, 2000, **39**, 4901–4907.

122 I. Clark, R. L. Gomes, C. Crawshaw, L. Neve, R. Lodge, M. Fay, C. Winkler, M. Hull and E. Lester, Continuous synthesis of Zn2Al-CO3 layered double hydroxides: A comparison of bench, pilot and industrial scale syntheses, *React Chem Eng*, 2019, **4**, 663–666.

123 J. Sierra-Pallares, T. Huddle, J. García-Serna, E. Alonso, F. Mato, I. Shvets, O. Luebben, M. J. Cocero and E. Lester, Understanding bottom-up continuous hydrothermal synthesis of nanoparticles using empirical measurement and computational simulation, *Nano Res*, 2016, **9**, 3377–3387.

124 X. Yang, K. Zhanghao, H. Wang, Y. Liu, F. Wang, X. Zhang, K. Shi, J. Gao, D. Jin and P. Xi, Versatile Application of Fluorescent Quantum Dot Labels in Super-resolution Fluorescence Microscopy, *ACS Photonics*, 2016, **3**, 1611–1618.

125 N. Baig, I. Kammakakam, W. Falath and I. Kammakakam, Nanomaterials: A review of synthesis methods, properties, recent progress, and challenges, *Mater Adv*, 2021, **2**, 1821–1871.

126 V. Sebastian, M. Arruebo and J. Santamaria, Reaction engineering strategies for the production of inorganic nanomaterials, *Small*, 2014, **10**, 835–853.

127 E. Lester, G. Aksomaityte, J. Li, S. Gomez, J. Gonzalez-Gonzalez and M. Poliakoff, Controlled continuous hydrothermal synthesis of cobalt oxide (Co 3O 4) nanoparticles, *Progress in Crystal Growth and Characterization of Materials*, 2012, **58**, 3–13.

128 E. Lester, P. Blood, J. Denyer, D. Giddings, B. Azzopardi and M. Poliakoff, Reaction engineering: The supercritical water hydrothermal synthesis of nano-particles, *Journal of Supercritical Fluids*, 2006, **37**, 209–214.

129 F. Cansell, B. Chevalier, A. Demourgues, J. Etourneau, C. Even, Y. Garrabos, V. Pessey, S. Petit, A. Tressaud and F. Weill, Supercritical fluid processing: A new route for materials synthesis, *J Mater Chem*, 1999, **9**, 67–75.

130 L. J. Cote, A. S. Teja, A. P. Wilkinson and Z. J. Zhang, *Continuous hydrothermal synthesis and crystallization of magnetic oxide nanoparticles*, 2002.

131 V. Pessey, R. Garriga, F. Weill, B. Chevalier, J. Etourneau and F. Cansell, Submicronic particles synthesis by a supercritical way, *High Press Res*, 2001, **20**, 289–298.

132 P. J. Blood, J. P. Denyer, B. J. Azzopardi, M. Poliakoff and E. Lester, A versatile flow visualisation technique for quantifying mixing in a binary system: Application to continuous supercritical water hydrothermal synthesis (SWHS), *Chem Eng Sci*, 2004, **59**, 2853–2861.

133 J. Sierra-Pallares, T. Huddle, E. Alonso, F. A. Mato, J. García-Serna, M. J. Cocero and E. Lester, Prediction of residence time distributions in supercritical hydrothermal reactors working at low Reynolds numbers, *Chemical Engineering Journal*, 2016, **299**, 373–385.

134 H. Hobbs, S. Briddon and E. Lester, The synthesis and fluorescent properties of nanoparticulate ZrO2 doped with Eu using continuous hydrothermal synthesis, *Green Chemistry*, 2009, **11**, 484–49.

135 A. S. Munn, P. W. Dunne, S. V. Y. Tang and E. H. Lester, Large-scale continuous hydrothermal production and activation of ZIF-8, *Chemical Communications*, 2015, **51**, 12811–12814.

136 M. Gimeno-Fabra, A. S. Munn, L. A. Stevens, T. C. Drage, D. M. Grant, R. J. Kashtiban, J. Sloan, E. Lester and R. I. Walton, Instant MOFs: Continuous synthesis of metal–organic frameworks by rapid solvent mixing, *Chemical Communications*, 2012, **48**, 10642–10644.

137 P. W. Dunne, E. Lester and R. I. Walton, Towards scalable and controlled synthesis of metal-organic framework materials using continuous flow reactors, *React Chem Eng*, 2016, **1**, 352–360.

138 Q. Wang, S. V. Y. Tang, E. Lester and D. O'Hare, Synthesis of ultrafine layered double hydroxide (LDHs) nanoplates using a continuous-flow hydrothermal reactor, *Nanoscale*, 2013, **5**, 114–117.

139 C. Prasad, H. Tang, Q. Q. Liu, S. Zulfiqar, S. Shah and I. Bahadur, An overview of semiconductors/layered double hydroxides composites: Properties, synthesis, photocatalytic and photoelectrochemical applications, *J Mol Liq*, , DOI:10.1016/j.molliq.2019.111114.

140 L. Zhang, Z. Xiong, L. Li, R. Burt and X. S. Zhao, Uptake and degradation of Orange II by zinc aluminum layered double oxides, *J Colloid Interface Sci*, 2016, **469**, 224–230.

141 A. Guzmán-Vargas, E. Lima, G. A. Uriostegui-Ortega, M. A. Oliver-Tolentino and E. E. Rodríguez, Adsorption and subsequent partial photodegradation of methyl violet 2B on Cu/Al layered double hydroxides, *Appl Surf Sci*, 2016, **363**, 372–380.

142 A. L. Johnston, E. Lester, O. Williams and R. L. Gomes, Understanding Layered Double Hydroxide properties as sorbent materials for removing organic pollutants from environmental waters, *J Environ Chem Eng*, 2021, **9**, 105197.

143 Y. Lu, B. Jiang, L. Fang, F. Ling, J. Gao, F. Wu and X. Zhang, High performance NiFe layered double hydroxide for methyl orange dye and Cr(VI) adsorption, *Chemosphere*, 2016, **152**, 415–422.

144 S. Xu, J. Ng, X. Zhang, H. Bai and D. D. Sun, Adsorption and photocatalytic degradation of Acid Orange 7 over hydrothermally synthesized mesoporous TiO2 nanotube, *Colloids Surf A Physicochem Eng Asp*, 2011, **379**, 169–175.

145 R. Trujillano, I. González-García, A. Morato and V. Rives, Controlling the Synthesis Conditions for Tuning the Properties of Hydrotalcite-Like Materials at the Nano Scale, *ChemEngineering*, 2018, **2**, 31.

146 S. Moriyama, K. Sasaki and T. Hirajima, Effect of freeze drying on characteristics of Mg–Al layered double hydroxides and bimetallic oxide synthesis and implications for fluoride sorption, *Appl Clay Sci*, 2016, **132–133**, 460–467.

147 Y. Waseda, E. Matsubara and K. Shinoda, X-Ray Diffraction Crystallography, *X-Ray Diffraction Crystallography*, , DOI:10.1007/978-3-642-16635-8.

148 P. Zhang, G. Qian, H. Shi, X. Ruan, J. Yang and R. L. Frost, Mechanism of interaction of hydrocalumites (Ca/Al-LDH) with methyl orange and acidic scarlet GR, , DOI:10.1016/j.jcis.2011.08.064.

149 R. Marangoni, M. Bouhent, C. Taviot-Guého, F. Wypych and F. Leroux, Zn 2 Al layered double hydroxides intercalated and adsorbed with anionic blue dyes: A physico-chemical characterization, *J Colloid Interface Sci*, 2009, **333**, 120–127.

150 L. Lv, J. He, M. Wei, D. G. Evans and X. Duan, Factors influencing the removal of fluoride from aqueous solution by calcined Mg-Al-CO3 layered double hydroxides, *J Hazard Mater*, 2006, **133**, 119–128.

151 Gopal. Monash, Purushothaman. Pugazhenthi, Utilization of Calcined Ni-Al Layered Double Hydroxide (LDH) as an Adsorbent for Removal of Methyl Orange Dye from Aqueous Solution, *Environ Prog Sustain Energy*, 2014, **33**, 676–680.

152 R. M. M. dos Santos, R. G. L. Gonçalves, V. R. L. Constantino, L. M. da Costa, L. H. M. da Silva, J. Tronto and F. G. Pinto, Removal of Acid Green 68:1 from aqueous solutions by calcined and uncalcined layered double hydroxides, *Appl Clay Sci*, 2013, **80–81**, 189–195.

153 R. E. Johnsen and P. Norby, A comparative in situ Rietveld refinement study: Thermal decomposition and transformation of CoAl and CoZnAl layered double hydroxides, *J Appl Crystallogr*, 2008, **41**, 991–1002.

154 B. Li, Y. Zhang, X. Zhou, Z. Liu, Q. Liu and X. Li, Different dye removal mechanisms between monodispersed and uniform hexagonal thin plate-like MgAl-CO32--LDH and its calcined product in efficient removal of Congo red from water, *J Alloys Compd*, 2016, **673**, 265–271.

155 Y. Guo, Z. Zhu, Y. Qiu and J. Zhao, Enhanced adsorption of acid brown 14 dye on calcined Mg/Fe layered double hydroxide with memory effect, *Chemical Engineering Journal*, 2013, **219**, 69–77.

156 C. Lei, X. Zhu, B. Zhu, C. Jiang, Y. Le and J. Yu, Superb adsorption capacity of hierarchical calcined Ni/Mg/Al layered double hydroxides for Congo red and Cr(VI) ions, *J Hazard Mater*, 2017, **321**, 801–811.

157 H. Zaghouane-Boudiaf, M. Boutahala and L. Arab, Removal of methyl orange from aqueous solution by uncalcined and calcined MgNiAl layered double hydroxides (LDHs), *Chemical Engineering Journal*, 2012, **187**, 142–149.

158 M. Ateia, D. E. Helbling and W. R. Dichtel, Best practices for evaluating new materials as adsorbents for water treatment, *ACS Mater Lett*, 2020, **2**, 1532–1544.

159 K.-H. Goh, T.-T. Lim and Z. Dong, Application of layered double hydroxides for removal of oxyanions: A review, *Water Res*, 2008, **42**, 1343–1368.

160 N. K. Lazaridis, T. D. Karapantsios and D. Georgantas, Kinetic analysis for the removal of a reactive dye from aqueous solution onto hydrotalcite by adsorption, *Water Res*, 2003, **37**, 3023–3033.

161 Y. Li, B. Gao, T. Wu, B. Wang and X. Li, Adsorption properties of aluminum magnesium mixed hydroxide for the model anionic dye Reactive Brilliant Red K-2BP, *J Hazard Mater*, 2009, **164**, 1098–1104.

162 I. Jurado Dávila, M. Rosset, O. Perez Lopez and L. Amaral Féris, Removal of reactive red 120 in aqueous solution using mg-hydrotalcites as adsorbents solids: Kinetics and isotherms, *Revista Internacional de Contaminacion Ambiental*, 2020, **36**, 443–453.

163 K. Nejati, Z. Rezvani, M. Mansurfar, A. Mirzaee and M. Mahkam, Adsorption of metanil yellow azoic dye from aqueous solution onto Mg-Fe-NO3 layered double hydroxide, *Z Anorg Allg Chem*, 2011, **637**, 1573–1579.

164 N. Drici Setti, N. Jouini and Z. Derriche, Sorption study of an anionic dye - benzopurpurine 4B - on calcined and uncalcined Mg-Al layered double hydroxides, *Journal of Physics and Chemistry of Solids*, 2010, **71**, 556–559.

165 F. P. De Sá, B. N. Cunha and L. M. Nunes, Effect of pH on the adsorption of Sunset Yellow FCF food dye into a layered double hydroxide (CaAl-LDH-NO3), *Chemical Engineering Journal*, 2013, **215–216**, 122–127.

166 Y. Chen, C. Jing, X. Zhang, D. Jiang, X. Liu, B. Dong, L. Feng, S. Li and Y. Zhang, Acid-salt treated CoAl layered double hydroxide nanosheets with enhanced adsorption capacity of methyl orange dye, *J Colloid Interface Sci*, 2019, **548**, 100–109.

167 L. Ai, C. Zhang and L. Meng, Adsorption of Methyl Orange from Aqueous Solution on Hydrothermal Synthesized Mg-Al Layered Double Hydroxide, *J. Chem. Eng. Data*, 2011, **56**, 4217–4225.

168 A. R. Auxilio, P. C. Andrews, P. C. Junk and L. Spiccia, Adsorption of ink-jet inks and anionic dyes onto Mg-Al-NO3 layered double hydroxides of variable Mg:Al molar ratio, *Aust J Chem*, 2010, **63**, 83–91.

169 R. R. Shan, L. G. Yan, K. Yang, S. J. Yu, Y. F. Hao, H. Q. Yu and B. Du, Magnetic Fe3O4/MgAl-LDH composite for effective removal of three red dyes from aqueous solution, *Chemical Engineering Journal*, 2014, **252**, 38–46.

170 P. Huang, J. Liu, F. Wei, Y. Zhu, X. Wang, C. Cao and W. Song, Size-selective adsorption of anionic dyes induced by the layer space in layered double hydroxide hollow microspheres, *Mater Chem Front*, 2017, **1**, 1550–1555.

171 H. Gao, R. Cao, X. Xu, J. Xue, S. Zhang, T. Hayat, N. S. Alharbi and J. Li, Surface Area- and Structure-Dependent Effects of LDH for Highly Efficient Dye Removal, , DOI:10.1021/acssuschemeng.8b04476.

172 M. A. Nazir, N. A. Khan, C. Cheng, S. S. A. Shah, T. Najam, M. Arshad, A. Sharif, S. Akhtar and A. ur Rehman, Surface induced growth of ZIF-67 at Co-layered double hydroxide: Removal of methylene blue and methyl orange from water, *Appl Clay Sci*, 2020, **190**, 105564.

173 N. D. Mu’azu, N. Jarrah, M. Zubair, M. S. Manzar, T. S. Kazeem, A. Qureshi, S. A. Haladu, N. I. Blaisi, M. H. Essa and M. A. Al-Harthi, Mechanistic aspects of magnetic MgAlNi barium-ferrite nanocomposites enhanced adsorptive removal of an anionic dye from aqueous phase, *Journal of Saudi Chemical Society*, 2020, **24**, 715–732.

174 H. Palza, K. Delgado and J. Govan, Novel magnetic CoFe2O4/layered double hydroxide nanocomposites for recoverable anionic adsorbents for water treatment, *Appl Clay Sci*, 2019, **183**, 105350.

175 H. Pang, Y. Wu, X. Wang, B. Hu and X. Wang, Recent Advances in Composites of Graphene and Layered Double Hydroxides for Water Remediation: A Review, *Chem Asian J*, 2019, **14**, 2542–2552.

176 Eny. Mamat, Mazidah. Abdullah, Mohd Aidil Adhha. Kadir, Maisara Abdul. Jaafar, Adila Mohamad. Kusrini, Preparation of layered double hydroxides with different divalent metals for the adsorption of methyl orange dye from aqueous solutions, *International Journal of Technology*, 2018, **6**, 1103–1111.

177 D. Bharali and R. C. Deka, Adsorptive removal of congo red from aqueous solution by sonochemically synthesized NiAl layered double hydroxide, , DOI:10.1016/j.jece.2017.04.012.

178 C. Zhang, S. Yang, H. Chen, H. He and C. Sun, Adsorption behavior and mechanism of reactive brilliant red X-3B in aqueous solution over three kinds of hydrotalcite-like LDHs, *Appl Surf Sci*, 2014, **301**, 329–337.

179 Z. Shi, Y. Wang, S. Sun, C. Zhang and H. Wang, Removal of methylene blue from aqueous solution using Mg-Fe, Zn-Fe, Mn-Fe layered double hydroxide, , DOI:10.2166/wst.2020.313.

180 O. Williams, I. Clark, R. L. Gomes, T. Perehinec, J. L. Hobman, D. J. Stekel, R. Hyde, C. Dodds and E. Lester, Removal of copper from cattle footbath wastewater with layered double hydroxide adsorbents as a route to antimicrobial resistance mitigation on dairy farms, *Science of The Total Environment*, 2019, **655**, 1139–1149.

181 Y.-M. Zheng, N. Li and W.-D. Zhang, Preparation of nanostructured microspheres of Zn-Mg-Al layered double hydroxides with high adsorption property, *Physicochem. Eng. Aspects*, 2012, **415**, 195–201.

182 E. Lester, P. Blood, J. Denyer, D. Giddings, B. Azzopardi and M. Poliakoff, Reaction engineering: The supercritical water hydrothermal synthesis of nano-particles, *Journal of Supercritical Fluids*, 2006, **37**, 209–214.

183 Promethean Particles, https://prometheanparticles.co.uk/, (accessed 25 January 2022).

184 Q. Wang, S. V. Y. Tang, E. Lester and D. O’Hare, Synthesis of ultrafine layered double hydroxide (LDHs) nanoplates using a continuous-flow hydrothermal reactor, *Nanoscale*, 2013, **5**, 114–117.

185 G. Caglioti, A. Paoletti and F. P. Ricci, Choice of collimators for a crystal spectrometer for neutron diffraction, *Nuclear Instruments*, 1958, **3**, 223–228.

186 M. Thommes, K. Kaneko, A. V. Neimark, J. P. Olivier, F. Rodriguez-Reinoso, J. Rouquerol and K. S. W. Sing, Physisorption of gases, with special reference to the evaluation of surface area and pore size distribution (IUPAC Technical Report), *Pure and Applied Chemistry*, 2015, **87**, 1051–1069.

187 S. Lowell and J. E. Shields, *Powder Surface Area and Porosity*, Springer Netherlands, 1984.

188 H. K. Livingston and Z. Nv, The Cross-Sectional Areas of Molecules Adsorbed on Solid Surfaces.

189 Perkin Elmer, A Beginner’s Guide to Thermogravimetric Analysis (TGA), *Perkin Elmer*, 2004, 3–19.

190 Agilent, ICP-OES Principles, Instrument and Analysis, https://www.agilent.com/en/support/atomic-spectroscopy/inductively-coupled-plasma-optical-emission-spectroscopy-icp-oes/icp-oes-instruments/icp-oes-faq.

191 S. H. Baek, G. H. Nam and I. K. Park, Morphology controlled growth of ZnAl-layered double hydroxide and ZnO nanorod hybrid nanostructures by solution method, *RSC Adv*, 2015, **5**, 59823–59829.

192 T. Oku, *Structure Analysis of Advanced Nanomaterials: Nanoworld by high-Resolution Electron Microscopy*, De Gruyter, Inc., Berlin/Boston, 2014.

193 J. M. Fultz, B. Howe, *Transmission Electron Microscopy and Diffractometry of Materials*, Springer, Berlin, 2001.

194 I. Clark, J. Smith, R. L. Gomes and E. Lester, Continuous Synthesis of Zn2Al-CO3 Layered Double Hydroxides for the Adsorption of Reactive Dyes from Water, *J Environ Chem Eng*, 2019, **7**, 103175.

195 C. Santhosh, E. Daneshvar, K. M. Tripathi, P. Baltrėnas, T. Kim, E. Baltrėnaitė and A. Bhatnagar, Synthesis and characterization of magnetic biochar adsorbents for the removal of Cr(VI) and Acid orange 7 dye from aqueous solution, *Environmental Science and Pollution Research*, , DOI:10.1007/s11356-020-09275-1.

196 B. R. Lee, K. Il Joo, E. S. Choi, J. Jahng, H. Kim and E. Kim, Evans blue dye-enhanced imaging of the brain microvessels using spectral focusing coherent anti-Stokes Raman scattering microscopy, *PLoS One*, 2017, **12**, 1–16.

197 M. K. Sahu, U. K. Sahu and R. K. Patel, Adsorption of safranin-O dye on CO2 neutralized activated red mud waste: Process modelling, analysis and optimization using statistical design, *RSC Adv*, 2015, **5**, 42294–42304.

198 J. Lin and L. Wang, Comparison between linear and non-linear forms of pseudo-first-order and pseudo-second-order adsorption kinetic models for the removal of methylene blue by activated carbon, *Frontiers of Environmental Science and Engineering in China*, 2009, **3**, 320–324.

199 F. Ramirez-Rodriguez, T. Landa Castillo-Alvarado, Application of the intra-particle diffusion model for activated carbon fibers in an aqueous medium, *Materials Research Society*, 2012, **1373**, 149–155.

200 J. Wang and X. Guo, *Chemosphere*, 2020, 258, 127279.

201 H. S. Panda, R. Srivastava and D. Bahadur, Synthesis and in situ mechanism of nuclei growth of layered double hydroxides, *Bulletin of Materials Science*, 2011, **34**, 1599–1604.

202 G. Wang and Z. Jin, Oxygen-vacancy-rich cobalt-aluminium hydrotalcite structures served as high-performance supercapacitor cathode, *J Mater Chem C Mater*, 2021, **9**, 620–632.

203 R. E. Johnsen, F. Krumeich and P. Norby, Structural and microstructural changes during anion exchange of CoAl layered double hydroxides: An in situ X-ray powder diffraction study, *J Appl Crystallogr*, 2010, **43**, 434–447.

204 D. Li, Y. Cai, Y. Ding, R. Li, M. Lu and L. Jiang, Layered double hydroxides as precursors of Cu catalysts for hydrogen production by water-gas shift reaction, *Int J Hydrogen Energy*, 2015, **40**, 10016–10025.

205 A. V. Radha, P. V. Kamath and C. Shivakumara, Order and disorder among the layered double hydroxides: combined Rietveld and DIFFaX approach, *Acta Crystallogr B*, 2007, **63**, 243–250.

206 Yoshio. Sasaki, Satoshi. Fujino, Kiyoshi. Takeuchi, X-Ray Determination of Electron-Density Distributions in Oxides, MgO, MnO, CuO, and NiO, and Atomic Scattering Factors of their Constituent Atoms, *Proc Jpn Acad*, 1979, **55**, 43–48.

207 F. Li, X. Liu, Q. Yang, J. Liu, D. G. Evans and X. Duan, Synthesis and characterization of Ni1-xZnxFe 2O4 spinel ferrites from tailored layered double hydroxide precursors, *Mater Res Bull*, 2005, **40**, 1244–1255.

208 I. Clark, P. W. Dunne, R. L. Gomes and E. Lester, Continuous hydrothermal synthesis of Ca2Al-NO3 layered double hydroxides: The impact of reactor temperature, pressure and NaOH concentration on crystal characteristics, *J Colloid Interface Sci*, 2017, **504**, 492–499.

209 J. W. Genck, Temperature effects on growth and nucleation rates in mixed suspension crystallization.

210 G. Madras and B. J. McCoy, Temperature effects during Ostwald ripening, *Journal of Chemical Physics*, 2003, **119**, 1683–1693.

211 K. S. W. Sing and R. T. Williams, Physisorption hysteresis loops and the characterization of nanoporous materials, *Adsorption Science and Technology*, 2004, **22**, 773–782.

212 G. Y. Kang, Y. Chen and J. J. Li, Comparison on structure and electrochemical performances of NiAl-LDH, CoAl-LDH and NiCoAl-LDH, *Wuji Cailiao Xuebao/Journal of Inorganic Materials*, 2016, **31**, 1230–1236.

213 E. Lester, P. Blood, J. Denyer, D. Giddings, B. Azzopardi and M. Poliakoff, Reaction engineering: The supercritical water hydrothermal synthesis of nano-particles, *Journal of Supercritical Fluids*, 2006, **37**, 209–214.

214 M. Haraketi, K. Hosni and E. Srasra, Intercalation behavior of salicylic acid into calcined Cu-Al-layered double hydroxides for a controlled release formulation, *Surface Engineering and Applied Electrochemistry*, 2017, **53**, 360–370.

215 F. Rouquerol, J. Rouquerol, K. S. W. Sing, P. Llewellyn and G. Maurin, *Adsorption by powders and porous solids*, 2014.

216 M. V. Bukhtiyarova, A review on effect of synthesis conditions on the formation of layered double hydroxides, *J Solid State Chem*, 2019, **269**, 494–506.

217 K. F. Ortega, D. Rein, C. Lüttmann, J. Heese, F. Özcan, M. Heidelmann, J. Folke, K. Kähler, R. Schlögl and M. Behrens, Ammonia Decomposition and Synthesis over Multinary Magnesioferrites: Promotional Effect of Ga on Fe Catalysts for the Decomposition Reaction, *ChemCatChem*, 2017, **9**, 659–671.

218 F. L. Theiss, G. A. Ayoko and R. L. Frost, Synthesis of layered double hydroxides containing Mg2+, Zn2+, Ca2+ and Al3+ layer cations by co-precipitation methods—A review, *Appl Surf Sci*, 2016, **383**, 200–213.

219 A. A. Sertsova, E. N. Subcheva and E. v. Yurtov, Synthesis and study of structure formation of layered double hydroxides based on Mg, Zn, Cu, and Al, *Russian Journal of Inorganic Chemistry*, 2015, **60**, 23–32.

220 J. T. Kloprogge, L. Hickey and R. L. Frost, The effects of synthesis pH and hydrothermal treatment on the formation of zinc aluminum hydrotalcites, *J Solid State Chem*, 2004, **177**, 4047–4057.

221 V. Rives, *Layered Double Hydroxides: Present and Future*, Nova Science Publishers, Huntington, N.Y., 2001.

222 S. Moriyama, K. Sasaki and T. Hirajima, Effect of freeze drying on characteristics of Mg–Al layered double hydroxides and bimetallic oxide synthesis and implications for fluoride sorption, *Appl Clay Sci*, 2016, **132–133**, 460–467.

223 K. El Hassani, H. Jabkhiro, D. Kalnina, B. H. Beakou and A. Anouar, Effect of drying step on layered double hydroxides properties: Application in reactive dye intercalation, *Appl Clay Sci*, 2019, **182**, 105246.

224 A. S. Mujumdar, *Handbook of industrial drying*, CRC Press, 4th edn., 1987.

225 A. Conde-Islas, M. Jiménez-Fernández, D. Cantú-Lozano, G. Urrea-García and G. Luna-Solano, Effect of the Freeze-Drying Process on the Physicochemical and Microbiological Properties of Mexican Kefir Grains, *Processes*, 2019, **7**, 127.

226 C. de Torres, M. C. Díaz-Maroto, I. Hermosín-Gutiérrez and M. S. Pérez-Coello, Effect of freeze-drying and oven-drying on volatiles and phenolics composition of grape skin, *Anal Chim Acta*, 2010, **660**, 177–182.

227 Z. Pakowski, Modern methods of drying nanomaterials, *Transp Porous Media*, 2007, **66**, 19–27.

228 S. J. Olusegun, E. T. F. Freitas, L. R. S. Lara, H. O. Stumpf and N. D. S. Mohallem, Effect of drying process and calcination on the structural and magnetic properties of cobalt ferrite, *Ceram Int*, 2019, **45**, 8734–8743.

229 S. Boubakri, M. A. Djebbi, Z. Bouaziz, P. Namour, N. Jaffrezic-Renault, A. B. H. Amara, M. Trabelsi-Ayadi, I. Ghorbel-Abid and R. Kalfat, Removal of two anionic reactive textile dyes by adsorption into MgAl-layered double hydroxide in aqueous solutions, *Environmental Science and Pollution Research*, 2018, **25**, 23817–23832.

230 R. Extremera, I. Pavlovic, M. R. Pérez and C. Barriga, Removal of acid orange 10 by calcined Mg/Al layered double hydroxides from water and recovery of the adsorbed dye, *Chemical Engineering Journal*, 2012, **213**, 392–400.

231 W. L. Smith, A. D. Hobson and IUCr, The structure of cobalt oxide, Co3O4, *urn:issn:0567-7408*, 1973, **29**, 362–363.

232 F. Ling, L. Fang, Y. Lu, J. Gao, F. Wu, M. Zhou and B. Hu, A novel CoFe layered double hydroxides adsorbent: High adsorption amount for methyl orange dye and fast removal of Cr(VI), *Microporous and Mesoporous Materials*, 2016, **234**, 230–238.

233 T. R. Sahoo and B. Prelot, Adsorption processes for the removal of contaminants from wastewater: the perspective role of nanomaterials and nanotechnology, *Nanomaterials for the Detection and Removal of Wastewater Pollutants*, 2020, 161–222.

234 J. Zhou, S. Yang, J. Yu and Z. Shu, Novel hollow microspheres of hierarchical zinc-aluminum layered double hydroxides and their enhanced adsorption capacity for phosphate in water, *J Hazard Mater*, 2011, **192**, 1114–1121.

235 Q. Yang, Y. Zhong, X. Li, X. Li, K. Luo, X. Wu, H. Chen, Y. Liu and G. Zeng, Adsorption-coupled reduction of bromate by Fe(II)-Al(III) layered double hydroxide in fixed-bed column: Experimental and breakthrough curves analysis, *Journal of Industrial and Engineering Chemistry*, 2015, **28**, 54–59.

236 G. Nie, L. Wu, S. Qiu, Z. Xu and H. Wang, Preferable phosphate sequestration using polymer-supported Mg/Al layered double hydroxide nanosheets, *J Colloid Interface Sci*, 2022, **614**, 583–592.

237 B. Stieberova, M. Zilka, M. Ticha, F. Freiberg, P. Caramazana-González, J. McKechnie and E. Lester, Sustainability assessment of continuous-flow hydrothermal synthesis of nanomaterials in the context of other production technologies, *J Clean Prod*, , DOI:10.1016/j.jclepro.2019.118325.

238 S. Aber, N. Daneshvar, S. M. Soroureddin, A. Chabok and K. Asadpour-Zeynali, Study of acid orange 7 removal from aqueous solutions by powdered activated carbon and modeling of experimental results by artificial neural network, *Desalination*, 2007, **211**, 87–95.

239 S. Yoon, J. J. Calvo and M. C. So, Removal of Acid Orange 7 from Aqueous Solution by Metal-Organic Frameworks, *Crystals (Basel)*, , DOI:10.3390/cryst9010017.

240 M. Ahmadian, N. Yosefi, A. Toolabi, N. Khanjani, S. Rahimi and A. Fatehizadeh, Adsorption of direct yellow 9 and acid orange 7 from aqueous solutions by modified pumice, *Asian Journal of Chemistry*, 2012, **24**, 3094–3098.

241 L. Wang, F. Meng, M. Pei, W. Guo, G. Liu and S. Du, Synthesis of a Cationic Polymer-Bentonite Composite Utilizing a Simple and Green Process for the Adsorption of Acid Orange 7 from Aqueous Solution) Synthesis of a Cationic Polymer-Bentonite Composite Utilizing a Simple and Green Process for the Adsorption of Acid Orange 7 from Aqueous Solution Synthesis of a Cationic Polymer-Bentonite Composite Utilizing a Simple and Green Process for the Adsorption of Acid Orange 7 from Aqueous Solution, , DOI:10.1080/00222348.2019.1644788.

242 L. Zhang, L. Chen, X. Liu and W. Zhang, Effective removal of azo-dye orange II from aqueous solution by zirconium-based chitosan microcomposite adsorbent, *RSC Adv*, 2015, **5**, 93840–93849.

243 G. Zhang, C. Liu, J. Zhao, J. Z. Zhou and G. Qian, Effective Removal of Anionic Dye by Ni-Zn-Cr-Ldhs Prepared from Electroplating Wastewater via Accelerated Carbonation, 2012, **2**, 25–34.

244 Y.-M. Zheng, N. Li and W.-D. Zhang, Preparation of nanostructured microspheres of Zn-Mg-Al layered double hydroxides with high adsorption property, *Physicochem. Eng. Aspects*, 2012, **415**, 195–201.

245 M. V. Bukhtiyarova, A review on effect of synthesis conditions on the formation of layered double hydroxides, *J Solid State Chem*, 2019, **269**, 494–506.

246 S. A. Speakman, Introduction to X-Ray Powder Diffraction Data Analysis, http://prism.mit.edu/xray/Introduction to XRPD Data Analysis.pdf, (accessed 22 October 2021).

247 G. Renaudin and M. François, The lamellar double-hydroxide (LDH) compound with composition 3CaO·Al2O3·Ca(NO3) 2·10H2O, *Acta Crystallogr C*, 1999, **55**, 835–838.

248 M. Bellotto, B. Rebours, O. Clause, J. Lynch, D. Bazin and E. Elkaı, *A Reexamination of Hydrotalcite Crystal Chemistry*, 1996.

249 G. M. Lombardo, G. C. Pappalardo, F. Punzo, F. Costantino and U. Costantino, A novel integrated X-ray Powder Diffraction (XRPD) and Molecular Dynamics (MD) approach for modelling mixed-metal (Zn, Al)-Layered Double Hydroxides (LDHs), *Eur J Inorg Chem*, 2005, 5026–5034.

250 S. J. Mills, P. S. Whitfield, A. R. Kampf, S. A. Wilson, G. M. Dipple, M. Raudsepp and G. Favreau, Contribution to the crystallography of hydrotalcites: the crystal structures of woodallite and takovite, *Journal of Geosciences*, 2012, **57**, 273–279.

251 L. Ingram and H. F. W. Taylor, The crystal structures of sjögrenite and pyroaurite, *Mineralogical Magazine and Journal of the Mineralogical Society*, 1967, **36**, 465–479.

252 S. A. de Waal and E. A. Viljoen, Nickel minerals from Barberton, South Africa: IV. Reevesite, a member of the hydrotalcite group, *Am Mineral*, 1971, **56**, 1077–1081.

253 G. Renaudin and M. François, The lamellar double-hydroxide (LDH) compound with composition 3CaO·Al2O3·Ca(NO3) 2·10H2O, *Acta Crystallogr C*, 1999, **55**, 835–838.

254 M. Bellotto, B. Rebours, O. Clause, J. Lynch, D. Bazin and E. Elkaı, *A Reexamination of Hydrotalcite Crystal Chemistry*, 1996.

255 G. M. Lombardo, G. C. Pappalardo, F. Punzo, F. Costantino and U. Costantino, A novel integrated X-ray Powder Diffraction (XRPD) and Molecular Dynamics (MD) approach for modelling mixed-metal (Zn, Al)-Layered Double Hydroxides (LDHs), *Eur J Inorg Chem*, 2005, 5026–5034.

256 S. J. Mills, P. S. Whitfield, A. R. Kampf, S. A. Wilson, G. M. Dipple, M. Raudsepp and G. Favreau, Contribution to the crystallography of hydrotalcites: the crystal structures of woodallite and takovite, *Journal of Geosciences*, 2012, **57**, 273–279.

257 L. Ingram and H. F. W. Taylor, The crystal structures of sjögrenite and pyroaurite, *Mineralogical Magazine and Journal of the Mineralogical Society*, 1967, **36**, 465–479.

258 S. A. De Waal and E. A. Viljoen, Nickel minerals from Barberton, South Africa: IV. Reevesite, a member of the hydrotalcite group, *Am Mineral*, 1971, **56**, 1077–1081.

259 D. Li, Y. Cai, Y. Ding, R. Li, M. Lu and L. Jiang, Layered double hydroxides as precursors of Cu catalysts for hydrogen production by water-gas shift reaction, *Int J Hydrogen Energy*, 2015, **40**, 10016–10025.

260 E. E. Gaskell, T. Ha and A. R. Hamilton, Ibuprofen intercalation and release from different layered double hydroxides, *Ther Deliv*, 2018, **9**, 653–666.

261 M. A. Ahmed, A. A. Brick and A. A. Mohamed, An efficient adsorption of indigo carmine dye from aqueous solution on mesoporous Mg/Fe layered double hydroxide nanoparticles prepared by controlled sol-gel route, , DOI:10.1016/j.chemosphere.2017.01.147.

262 A. I. Tsyganok, T. Tsunoda, S. Hamakawa, K. Suzuki, K. Takehira and T. Hayakawa, Dry reforming of methane over catalysts derived from nickel-containing Mg-Al layered double hydroxides, *J Catal*, 2003, **213**, 191–203.

263 L. Deng, Z. Yang, Z. Fu, Y. Rong and J. Wu, Synthesis of ZnAl-LDH and biomass carbon composites and its application as anode material with long cycle life for zinc-nickel secondary battery, , DOI:10.1007/s11581-020-03732-0/Published.

264 Y. Lu, B. Jiang, L. Fang, F. Ling, J. Gao, F. Wu and X. Zhang, High performance NiFe layered double hydroxide for methyl orange dye and Cr(VI) adsorption, *Chemosphere*, 2016, **152**, 415–422.

265 H. Gao, R. Cao, X. Xu, J. Xue, S. Zhang, T. Hayat, N. S. Alharbi and J. Li, Surface Area- and Structure-Dependent Effects of LDH for Highly Efficient Dye Removal, *ACS Sustain Chem Eng*, 2019, **7**, 905–915.

266 A. V Neimark, F.-O.-X. Coudert, A. Boutin and A. H. Fuchs, Stress-Based Model for the Breathing of Metal-Organic Frameworks, *J. Phys. Chem. Lett*, 2010, **1**, 445–449.

267 O. K. Farha, I. Eryazici, N. C. Jeong, B. G. Hauser, C. E. Wilmer, A. A. Sarjeant, R. Q. Snurr, S. T. Nguyen, A. Ö. Yazaydin and J. T. Hupp, Metal-organic framework materials with ultrahigh surface areas: Is the sky the limit?, *J Am Chem Soc*, 2012, **134**, 15016–15021.

268 V. Prevot, C. Forano and J. P. Besse, Hydrolysis in polyol: New route for hybrid-layered double hydroxides preparation, *Chemistry of Materials*, 2005, **17**, 6695–6701.

269 S. Möhmel, I. Kurzawski, D. Uecker, D. Müller and W. Ge, The influence of a hydrothermal treatment using microwave heating on the crystallinity of layered double hydroxides, *Crystal Research and Technology*, 2002, **37**, 359–369.

270 Y. Kuwahara and H. Yamashita, Synthesis of Ca-based Layered Double Hydroxide from Blast Furnace Slag and Its Catalytic Applications, *ISIJ International*, 2015, **55**, 1531–1537.

271 G. Huang, D. Wang, S. Ma, J. Chen, L. Jiang and P. Wang, A new, low-cost adsorbent: Preparation, characterization, and adsorption behavior of Pb(II) and Cu(II), *J Colloid Interface Sci*, 2015, **445**, 294–302.

272 V. Prevot, C. Forano and J. P. Besse, Hydrolysis in polyol: New route for hybrid-layered double hydroxides preparation, *Chemistry of Materials*, 2005, **17**, 6695–6701.

273 I. Jurado Dávila, M. Rosset, O. Perez Lopez and L. Amaral Féris, Removal of reactive red 120 in aqueous solution using mg-hydrotalcites as adsorbents solids: Kinetics and isotherms, *Revista Internacional de Contaminacion Ambiental*, 2020, **36**, 443–453.

274 D. Chen, Y. Li, J. Zhang, W. Li, J. Zhou, L. Shao and G. Qian, Efficient removal of dyes by a novel magnetic Fe3O4/ZnCr-layered double hydroxide adsorbent from heavy metal wastewater, *J Hazard Mater*, 2012, **243**, 152–160.

275 F. C. Wu, R. L. Tseng and R. S. Juang, Initial behavior of intraparticle diffusion model used in the description of adsorption kinetics, *Chemical Engineering Journal*, 2009, **153**, 1–8.

276 M. A. Ahmed, A. A. Brick and A. A. Mohamed, An efficient adsorption of indigo carmine dye from aqueous solution on mesoporous Mg/Fe layered double hydroxide nanoparticles prepared by controlled sol-gel route, , DOI:10.1016/j.chemosphere.2017.01.147.

277 M. Kosmulski, Isoelectric points and points of zero charge of metal (hydr)oxides: 50 years after Parks' review, *Adv Colloid Interface Sci*, 2016, **238**, 1–61.

278 M. Yu, N. Du and W. Hou, Model prediction of the point of zero net charge of layered double hydroxides and clay minerals, *Colloids Surf A Physicochem Eng Asp*, , DOI:10.1016/j.colsurfa.2020.125860.

279 K.-H. Goh, T.-T. Lim and Z. Dong, Application of layered double hydroxides for removal of oxyanions: A review, *Water Res*, 2008, **42**, 1343–1368.

280 Z. Shi, Y. Wang, S. Sun, C. Zhang and H. Wang, Removal of methylene blue from aqueous solution using Mg-Fe, Zn-Fe, Mn-Fe layered double hydroxide, *Water Science and Technology*, 2020, **81**, 2522–2532.

281 E. Y. Hashem, M. S. Saleh, N. O. A. Al-Salahi and A. K. Youssef, Advanced Spectrophotometric Analysis of Sunset Yellow Dye E110 in Commercial Food Samples, *Food Anal Methods*, 2017, **10**, 865–875.

282 K. Bourikas, M. Stylidi, D. I. Kondarides and X. E. Verykios, Adsorption of Acid Orange 7 on the surface of titanium dioxide, *Langmuir*, 2005, **21**, 9222–9230.

283 J. J. Salazar-Rabago, R. Leyva-Ramos, J. Rivera-Utrilla, R. Ocampo-Perez and F. J. Cerino-Cordova, Biosorption mechanism of Methylene Blue from aqueous solution onto White Pine (Pinus durangensis) sawdust: Effect of operating conditions, *Sustainable Environment Research*, 2017, **27**, 32–40.

284 Y. Song, H. Xu and J. Ren, Adsorption study for removal of sunset yellow by ethylenediamine-modified peanut husk, *Desalination Water Treat*, 2016, **57**, 17585–17592.

285 Q. Kong, Q. Liu, M. S. Miao, Y. Z. Liu, Q. F. Chen and C. S. Zhao, Kinetic and equilibrium studies of the biosorption of sunset yellow dye by alligator weed activated carbon, *Desalination Water Treat*, 2017, **66**, 281–290.

286 J. Fan, Y. Ling, C. Gao and H. Lyu, A high efficiency and rapid adsorbent for removing sunset yellow fcf by amine-modified microporous polymer, *Desalination Water Treat*, 2018, **124**, 326–335.

287 I. K. Chandra, Y. H. Ju, A. Ayucitra and S. Ismadji, Evans blue removal from wastewater by rarasaponin-bentonite, *International Journal of Environmental Science and Technology*, 2013, **10**, 359–370.

288 S. Y. Lee, H. E. Shim, J. E. Yang, Y. J. Choi and J. Jeon, Continuous flow removal of anionic dyes in water by chitosan-functionalized iron oxide nanoparticles incorporated in a dextran gel column, *Nanomaterials*, , DOI:10.3390/nano9081164.

289 M. Shamim and K. Dana, Efficient removal of Evans blue dye by Zn–Al–NO3 layered double hydroxide, *International Journal of Environmental Science and Technology*, 2018, **15**, 1275–1284.

290 R. Han, J. Zhang, P. Han, Y. Wang, Z. Zhao and M. Tang, Study of equilibrium, kinetic and thermodynamic parameters about methylene blue adsorption onto natural zeolite, *Chemical Engineering Journal*, 2009, **145**, 496–504.

291 S. Yinghua, P. Rong, G. Lili and Y. Mei, Removal of sunset yellow by methanol modified walnut shell, *Iranian Journal of Chemistry and Chemical Engineering*, 2021, **40**, 1095–1104.

292 R. S. Aliabadi and N. O. Mahmoodi, Synthesis and characterization of polypyrrole, polyaniline nanoparticles and their nanocomposite for removal of azo dyes; sunset yellow and Congo red, *J Clean Prod*, 2018, **179**, 235–245.

293 F. Kefif, K. Ezziane, A. Bahmani, N. Bettahar and S. Mayouf, Evans Blue dye removal from contaminated water on calcined and uncalcined Cu-Al-CO3 layered double hydroxide materials prepared by coprecipitation, *Bulletin of Materials Science*, 2019, **42**, 1–11.

294 F. B. D. Saiah, B. L. Su and N. Bettahar, in *Macromolecular Symposia*, 2008, vol. 273, pp. 125–134.

295 H. Patel, Fixed-bed column adsorption study: a comprehensive review, *Appl Water Sci*, 2019, **9**, 1–17.

296 M. Jaishankar, T. Tseten, N. Anbalagan, B. B. Mathew and K. N. Beeregowda, Toxicity, mechanism and health effects of some heavy metals, *Interdiscip Toxicol*, 2014, **7**, 60–72.

297 M. A. Ulibarri, I. Pavlovic, M. C. Hermosín and J. Cornejo, Hydrotalcite-like compounds as potential sorbents of phenols from water, *Appl Clay Sci*, 1995, **10**, 131–145.

298 F. Wong and R. G. Buchheit, Utilizing the structural memory effect of layered double hydroxides for sensing water uptake in organic coatings, *Prog Org Coat*, 2004, **51**, 91–102.

299 D. A. Yaseen and M. Scholz, Textile dye wastewater characteristics and constituents of synthetic effluents: a critical review, *International Journal of Environmental Science and Technology*, 2019, **16**, 1193–1226.

300 D. A. Yaseen and M. Scholz, *Textile dye wastewater characteristics and constituents of synthetic effluents: a critical review*, Springer Berlin Heidelberg, 2019, vol. 16.

301 M. A. González, I. Pavlovic, R. Rojas-Delgado and C. Barriga, Removal of Cu2+, Pb2+ and Cd2+ by layered double hydroxide–humate hybrid. Sorbate and sorbent comparative studies, *Chemical Engineering Journal*, 2014, **254**, 605–611.

302 R. Trujillano, I. González-García, A. Morato and V. Rives, Controlling the Synthesis Conditions for Tuning the Properties of Hydrotalcite-Like Materials at the Nano Scale, *ChemEngineering*, 2018, **2**, 31.

303 J. R. Lampman, G.M. Pavia, D. L. Kriz, G. S. Vyvyan, *Spectroscopy*, Brooks/Cole, Cengage Learning, Belmont, CA, 4th edn., 2010.

304 S. J. Zhang, H. Q. Yu and Q. R. Li, Radiolytic degradation of Acid Orange 7: A mechanistic study, *Chemosphere*, 2005, **61**, 1003–1011.

305 C. Bauer, P. Jacques and A. Kalt, Investigation of the interaction between a sulfonated azo dye (AO7) and a TiO2 surface, *Chem Phys Lett*, 1999, **307**, 397–406.

306 T. Bujdosó, Á. Patzkó, Z. Galbács and I. Dékány, Structural characterization of arsenate ion exchanged MgAl-layered double hydroxide, *Appl Clay Sci*, 2009, **44**, 75–82.

307 T. L. Nguyen and M. A. Saleh, Thermal degradation of azobenzene dyes, *Results Chem*, 2020, **2**, 100085.

308 P. Li, P. Chen, Z. Liu, S. Nie, X. Wang, G. Wang, W. Zhang, H. Chen and L. Wang, Highly efficient elimination of uranium from wastewater with facilely synthesized Mg-Fe layered double hydroxides: Optimum preparation conditions and adsorption kinetics, *Ann Nucl Energy*, 2020, **140**, 107140.

309 A. J. V. Griffiths and T. Walther, Quantification of carbon contamination under electron beam irradiation in a scanning transmission electron microscope and its suppression by plasma cleaning, *J Phys Conf Ser*, 2010, **241**, 4–7.

310 Y. V. Nelyubina, A. A. Korlyukov, K. A. Lyssenko and I. V. Fedyanin, Transferable Aspherical Atom Modeling of Electron Density in Highly Symmetric Crystals: A Case Study of Alkali-Metal Nitrates, *Inorg Chem*, 2017, **56**, 4688–4696.

311 E. E. Gaskell, T. Ha and A. R. Hamilton, Ibuprofen intercalation and release from different layered double hydroxides, *Ther Deliv*, 2018, **9**, 653–666.

312 P. Tang, Y. Feng and D. Li, Fabrication and properties of Acid Yellow 49 dye-intercalated layered double hydroxides film on an alumina-coated aluminum substrate, *Dyes and Pigments*, 2011, **91**, 120–125.

313 Z. Sun, L. Jin, W. Shi, M. Wei and X. Duan, Preparation of an anion dye intercalated into layered double hydroxides and its controllable luminescence properties, *Chemical Engineering Journal*, 2010, **161**, 293–300.

314 T. Kuwahara, H. Tagaya and K. Chiba, Photochromism of spiropyran dye in LiAl layered double hydroxide, *Microporous Materials*, 1995, **4**, 247–250.

315 L. Jin, Z. Guo, Z. Sun, A. Li, Q. Jin and M. Wei, Assembly of 8-aminonaphthalene-1,3,6-trisulfonate intercalated layered double hydroxide film for the selective detection of Mg 2+, *Sens Actuators B Chem*, 2012, **161**, 714–720.

316 I. Clark, R. L. Gomes, C. Crawshaw, L. Neve, R. Lodge, M. Fay, C. Winkler, M. Hull and E. Lester, Continuous synthesis of Zn2Al-CO3 layered double hydroxides: A comparison of bench, pilot and industrial scale syntheses, *React Chem Eng*, 2019, **4**, 663–666.

317 T. Water, The Sewage Treatment Process, https://www.thameswater.co.uk/about-us/responsibility/education/the-sewage-treatment-process.

318 M. T. Yagub, T. K. Sen, S. Afroze and H. M. Ang, *Adv Colloid Interface Sci*, 2014, 209, 172–184.

319 X. Zhao, C. Niu, L. Zhang, H. Guo, X. Wen, C. Liang and G. Zeng, Co-Mn layered double hydroxide as an effective heterogeneous catalyst for degradation of organic dyes by activation of peroxymonosulfate, *Chemosphere*, 2018, **204**, 11–21.

320 R. Patel, A. I. Inamdar, B. Hou, S. N. Cha, A. T. Ansari, J. L. Gunjakar, H. Im and H. Kim, Solvothermal synthesis of high-performance Ni-Co layered double hydroxide nanofoam electrode for electrochemical energy storage, *Current Applied Physics*, 2017, **17**, 501–506.

321 M. Haraketi, K. Hosni and E. Srasra, Intercalation behavior of salicylic acid into calcined Cu-Al-layered double hydroxides for a controlled release formulation, *Surface Engineering and Applied Electrochemistry*, 2017, **53**, 360–370.

322 F. Wang and Z. Guo, Insitu growth of ZIF-8 on Co[sbnd]Al layered double hydroxide/carbon fiber composites for highly efficient absorptive removal of hexavalent chromium from aqueous solutions, *Appl Clay Sci*, 2019, **175**, 115–123.

323 D. Chen, Y. Li, J. Zhang, W. Li, J. Zhou, L. Shao and G. Qian, Efficient removal of dyes by a novel magnetic Fe3O4/ZnCr-layered double hydroxide adsorbent from heavy metal wastewater, *J Hazard Mater*, 2012, **243**, 152–160.

324 X. L. Wu, L. Wang, C. L. Chen, A. W. Xu and X. K. Wang, Water-dispersible magnetite-graphene-LDH composites for efficient arsenate removal, *J Mater Chem*, 2011, **21**, 17353–17359.

325 I. Clark, J. Smith, R. L. Gomes and E. Lester, Towards the continuous hydrothermal synthesis of zno@mg2 al-co3 core-shell composite nanomaterials, *Nanomaterials*, 2020, **10**, 1–15.

326 The Control of Substances Hazardous to Health Regulations 2002.

327 Sigma-Aldrich, Aluminium Hydroxide [Materials Safety Data Sheet], https://www.sigmaaldrich.com/GB/en/sds/mm/1.01091.

328 Sigma-Aldrich, Iron oxide hydroxide [Materials Safety Data Sheet], https://www.sigmaaldrich.com/GB/en/sds/aldrich/796093, (accessed 12 October 2021).

329 Sigma-Aldrich, Magnesium hydroxide [Materials Safety |Data Sheet], https://www.sigmaaldrich.com/GB/en/sds/sial/63081, (accessed 12 October 2021).

330 Sigma-Aldrich, Calcium Hydroxide [Materials Safety Data Sheet], 2021, 1–10.

331 Inc. Santa Cruz Biotechnology, Zinc Hydroxide [Materials Safety Data Sheet], https://datasheets.scbt.com/sds/aghs/en/sc-362090.pdf, (accessed 12 October 2021).

332 Sigma-Aldrich, Nickel (II) Hydroxide [Materials Safety Data Sheet], https://www.sigmaaldrich.com/GB/en/sds/aldrich/283622, (accessed 12 October 2021).

333 P. Caramazana-González, P. W. Dunne, M. Gimeno-Fabra, M. Zilka, M. Ticha, B. Stieberova, F. Freiberg, J. McKechnie and E. H. Lester, Assessing the life cycle environmental impacts of titania nanoparticle production by continuous flow solvo/hydrothermal syntheses, *Green Chemistry*, 2017, **19**, 1536–1547.

334 P. Caramazana, P. Dunne, M. Gimeno-Fabra, J. McKechnie and E. Lester, A review of the environmental impact of nanomaterial synthesis using continuous flow hydrothermal synthesis, *Curr Opin Green Sustain Chem*, 2018, **12**, 57–62.

335 D. L. Schrijvers, F. Leroux, V. Verney and M. K. Patel, Ex-ante life cycle assessment of polymer nanocomposites using organo-modified layered double hydroxides for potential application in agricultural films, *Green Chemistry*, 2014, **16**, 4969–4984.

336 B. Stieberova, M. Zilka, M. Ticha, F. Freiberg, P. Caramazana-González, J. McKechnie and E. Lester, Sustainability assessment of continuous-flow hydrothermal synthesis of nanomaterials in the context of other production technologies, *J Clean Prod*, , DOI:10.1016/j.jclepro.2019.118325.

337 F. Fu and Q. Wang, Removal of heavy metal ions from wastewaters: A review, *J Environ Manage*, 2011, **92**, 407–418.

338 C. Chakraborty, K. Dana and S. Malik, Intercalation of perylenediimide dye into LDH clays: Enhancement of photostability, *Journal of Physical Chemistry C*, 2011, **115**, 1996–2004.

Appendix

UV-vis Limits of Detection (LoD) and Calibration Curves

Limit of detection (LoD) for the UV-vis spectrophotometer was determined through analysis of blank samples. Twenty blank samples were analysed at λ = 485 nm, the adsorption maximum for AO7. [195] The LoD was taken as as a multiple of three times the standard deviation. LoD was calculated as 0.002.

Appendix A. Calibration absorbance data for AO7

Dye Concentration / mg L^{-1}	**Absorbance 1**	**Absorbance 2**	**Absorbance 3**	**Average**
0.2	0.0146	0.0147	0.0144	0.0146
0.5	0.0290	0.0286	0.0282	0.0286
2.5	0.1629	0.1613	0.1681	0.1641
5.0	0.3288	0.3298	0.3404	0.3330
7.5	0.4867	0.4894	0.4991	0.4917
10	0.6471	0.6580	0.6493	0.6515
15	0.9718	0.9716	0.9715	0.9716

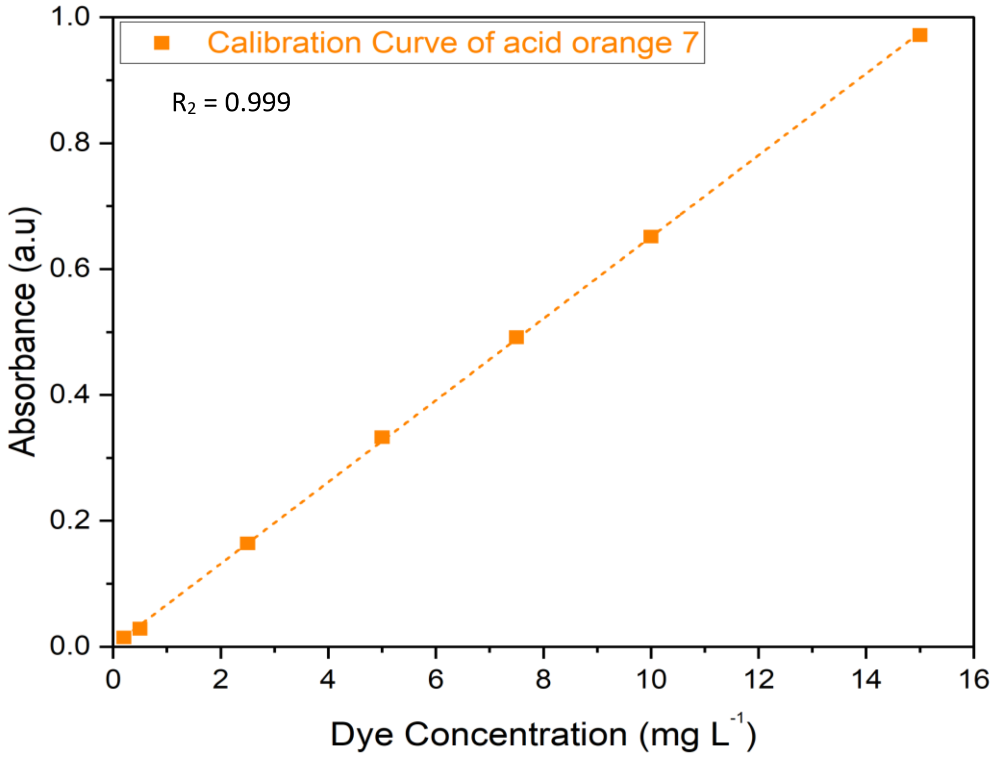

Appendix B. Calibration curve of AO7

Appendix C. Calibration absorbance for SY

Dye Concentration / mg L^{-1}	Absorbance 1	Absorbance 2	Absorbance 3	Average
0.2	0.0103	0.0102	0.0106	0.0104
0.5	0.0272	0.0267	0.0274	0.0271
2.5	0.1360	0.1329	0.1366	0.1351
5.0	0.2657	0.2610	0.2664	0.2644
7.5	0.3813	0.3773	0.3841	0.3809
10	0.5149	0.5085	0.5139	0.5124
15	0.7816	0.7774	0.7856	0.7815

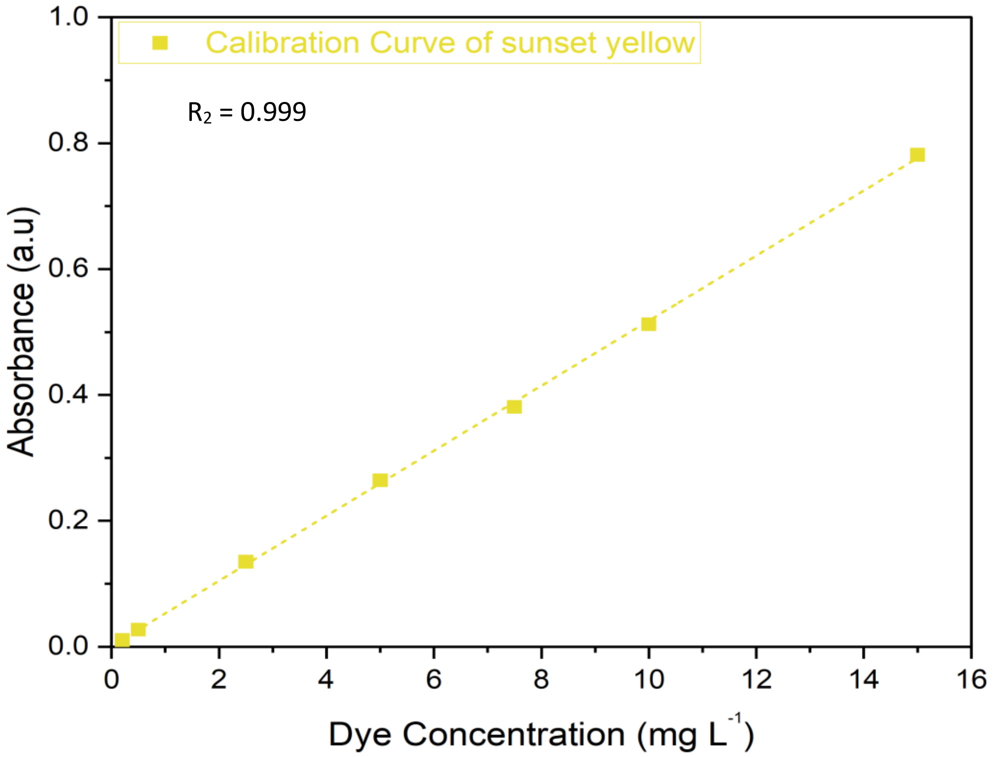

Appendix D. Calibration curve of SY

Appendix E. Calibration absorbance for EB

Dye Concentration / mg L^{-1}	**Absorbance 1**	**Absorbance 2**	**Absorbance 3**	**Average**
0.2	0.0185	0.0190	0.0176	0.0184
0.5	0.0463	0.0476	0.0440	0.0549
2.5	0.1997	0.1937	0.1965	0.1966
5.0	0.4078	0.3959	0.4125	0.4054
7.5	0.6104	0.6001	0.6007	0.6037
10	0.8074	0.8000	0.8092	0.8055
15	1.2554	1.2528	1.2540	1.2540

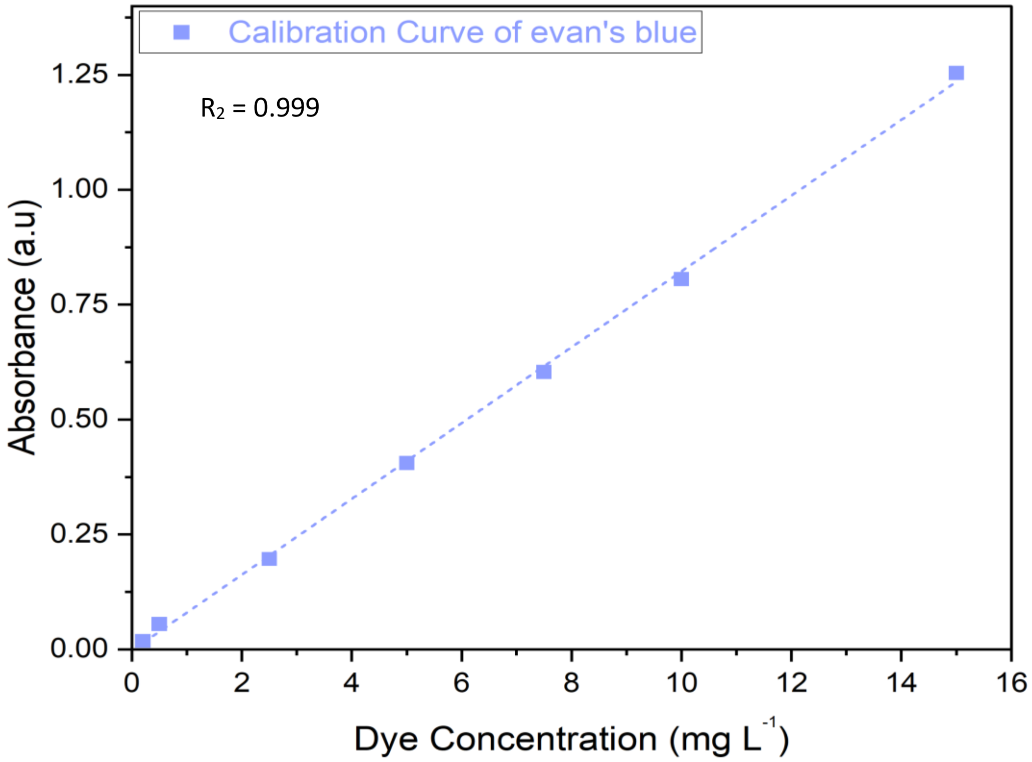

Appendix F. Calibration curve of EB

Appendix G. Calibration absorbance data for MB

Dye Concentration / mg L^{-1}	Absorbance 1	Absorbance 2	Absorbance 3	Average
0.2	0.0442	0.0437	0.0439	0.0440
0.5	0.1222	0.1185	0.1247	0.1218
1	0.2314	0.2287	0.2207	0.2269
2	0.4613	0.4579	0.4605	0.4599
3	0.6623	0.6574	0.6683	0.6627
4	0.8735	0.8681	0.8783	0.8733
6	1.3186	1.3144	0.3220	1.3183

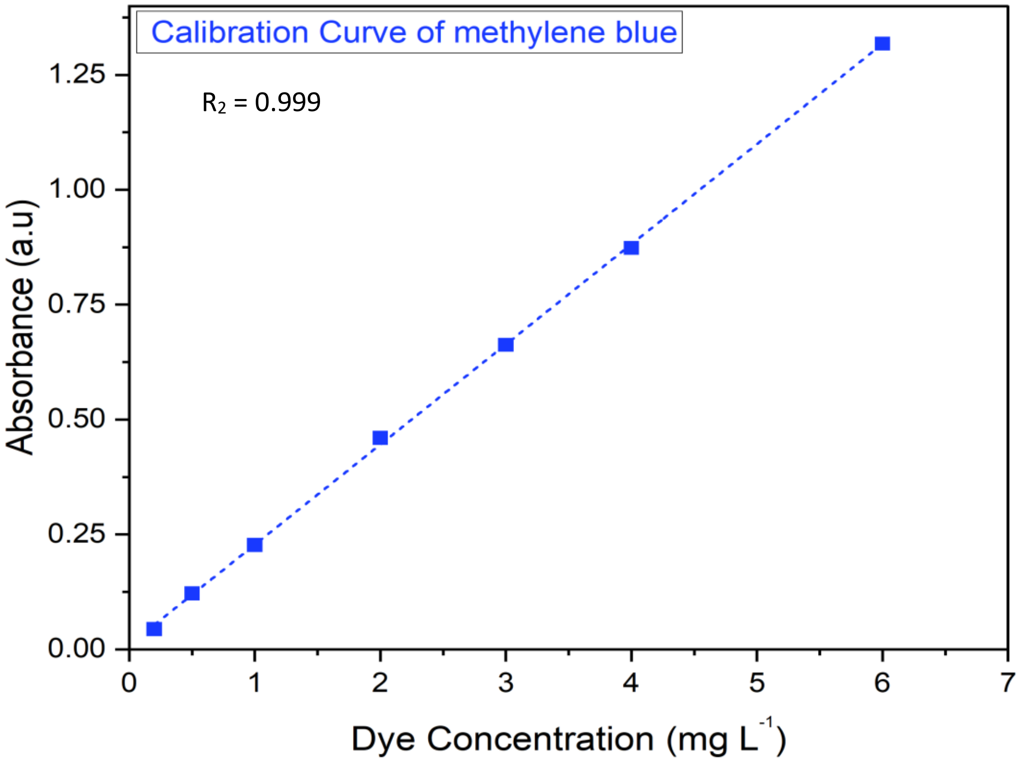

Appendix H. Calibration curve of MB

Appendix I. Calibration absorbance data for Saf-O

Dye Concentration / mg L^{-1}	**Absorbance 1**	**Absorbance 2**	**Absorbance 3**	**Average**
0.2	0.0242	0.0237	0.0239	0.0440
0.5	0.0587	0.0584	0.0584	0.0585
2.5	0.2911	0.2904	0.2899	0.2905
5.0	0.5734	0.5750	0.5732	0.5739
7.5	0.8552	0.8604	0.8594	0.8583
10	1.0470	1.0414	1.0524	1.0469
15	1.5194	1.5184	1.5120	1.5166

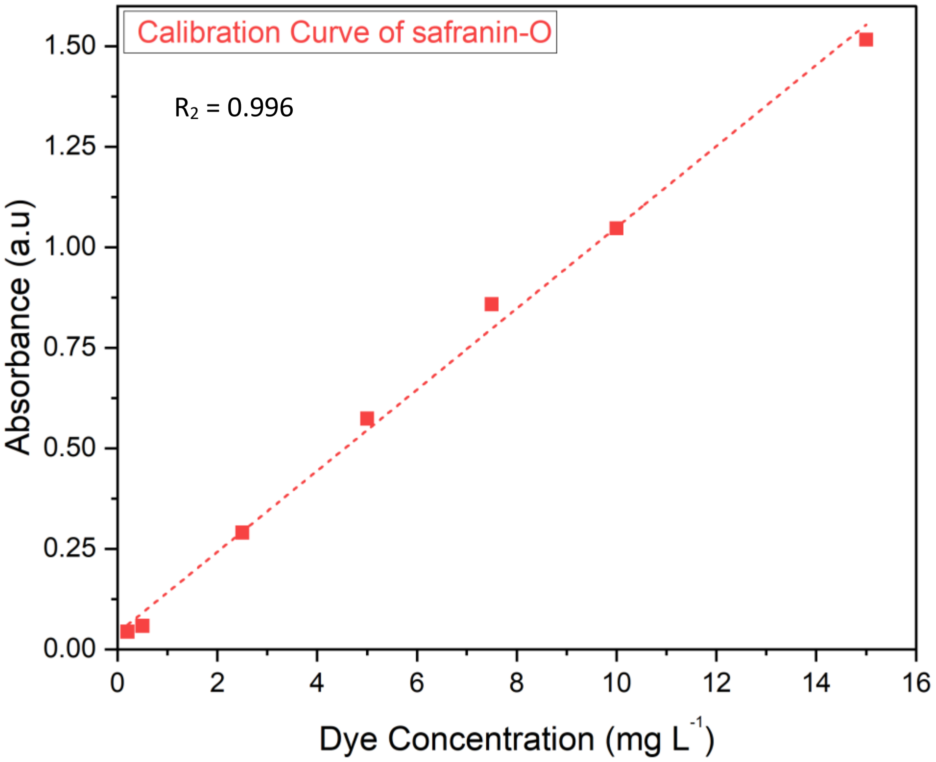

Appendix J. Calibration curve of Saf-O

SEM-EDX Analysis of Contaminated $Mg_2Al\text{-}CO_3$

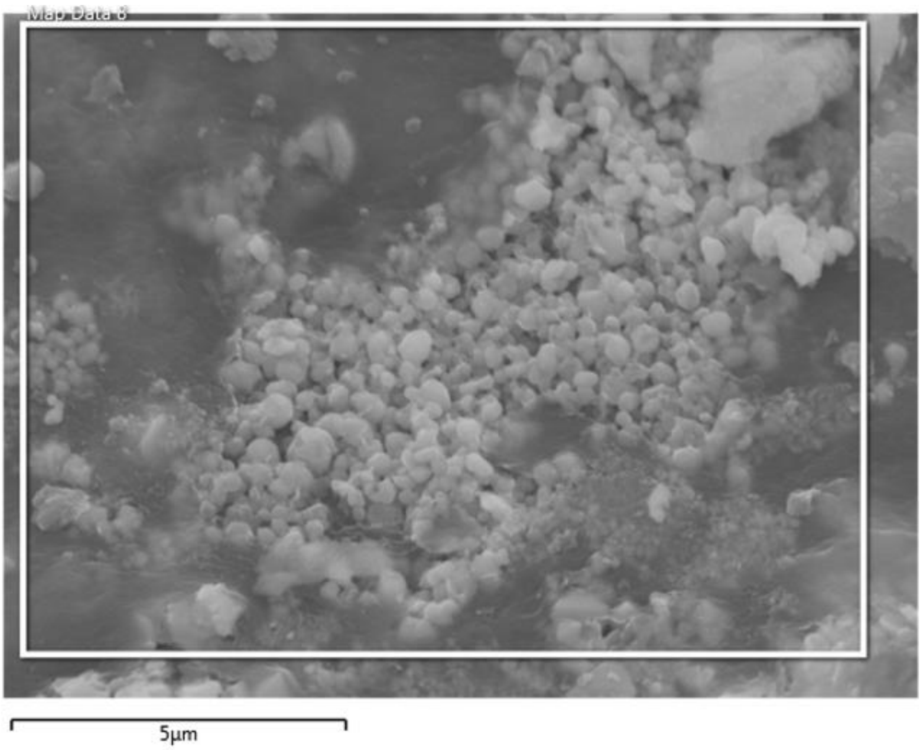

Appendix K. SEM imaging of Fe_3O_4 particles on the surface of $Mg_2Al\text{-}CO_3$

Appendix L. SEM-EDX analysis of $Mg_2Al\text{-}CO_3$

Element Signal	Weight / %	Std Dev (σ)
O	52.01	0.11
C	21.59	0.10
Mg	8.43	0.03
Fe	6.78	0.03
Al	2.97	0.01
Ba	2.06	0.04
Ce	1.78	0.03
Na	1.12	0.02
Cr	0.98	0.01
Ti	0.82	0.02
S	0.28	0.28